Characterisation and modelling of Taylor flow in small circular channels for the purpose of sequential screening.

Wa'el Salman

University College London
April, 2005

Thesis submitted to the University of London for the degree of Doctor of Philosophy

ProQuest LLC
789 East Eisenhower Parkway
P.O. Box 1346
Ann Arbor, MI 48106-1346

To my parents..

ACKNOWLEDGMENTS

This work wouldn't have been possible without the support and friendship of many people. I wish to express my gratitude to my principal supervisor Dr Panagiota Angeli and my second supervisor Prof. Asterios Gavriilidis. I also thank the EU commission for sponsoring this work under the "Key Elements for the Application of Microreactors in Multiphasic Catalytic Chemistries (KEMiCC)" project.

Carlos Amador, who has worked with me on the KEMiCC project, deserves a special mention for his advise, companionship and true friendship. Dr. Marcello Murru also deserves a special thanks for his advice and support (not to mention the long chats and countless biscuits). I would like to also thank my other colleagues in Prof. Gavriilidis' group for their help: Dr. Enhong Cao, Xiuyan Sun, Dr. Monica Zanfir, Dr. Key Kin Yeong and Nan Shao.

Of the many close friends I would like to mention: Jason Lum whose fortitude and good nature despite his grievous illness shall forever be in my memory. Jackie Lo for his friendship and Giovanna Bruni with her sunny personality and cheerful outlook.

Finally, I dedicate this PhD to my family. To my parents for their generosity and love, may I always have their blessing. To my Brother Shadi and my sister Hoda for their infinite patience.

ABSTRACT

This work focuses on the characterisation of a commonly encountered flow pattern, Taylor flow, for the purpose of using it in high throughput experimentation (HTE). Taylor flow consists of elongated gas bubbles of equivalent diameter larger than the tube diameter separated by liquid slugs. The bubbles adopt a characteristic capsular shape almost entirely filling the channel cross section. This configuration enhances the mixing within the liquid slugs and significantly decreases axial mixing along the liquid compared to single phase liquid flow.

In this work, the characterisation of a Taylor flow reactor was divided into three parts: The first part deals with the hydrodynamics of the flow, identifying the dimensionless parameter governing Taylor flow and the size of forming bubbles in a coaxial inlet arrangement. One of the findings was that a minimum channel size 100 μm exists below which the Taylor flow may becomes non-periodic or unstable.The experimentally observed mechanisms of Taylor bubble formation are reported and a simple model is provided for predicting the most common of the mechanisms.

In the second part, two models were developed which enable the prediction of axial mixing and the residence time distribution curves of the Taylor flow reactor. The first model is applicable when Peclet numbers $Pe > 100$. It was used to evaluate existing literature models and then for determining the rate of mixture injection in HTE. The second model is a special extension of the first applicable when $Pe < 1000$ and accounts for forward as well as back mixing.

In the third part a model was developed for identifying the flow rates and channel and slug lengths in the Taylor reactor which allow its use for determining kinetics of chemical reactions. An important finding from both axial and the kinetics models is that the slug lengths should be kept to the minimum possible size for best reactor performance.

CONTENTS

LIST OF FIGURES

LIST OF TABLES

1. THESIS INTRODUCTION

High throughput experimentation (HTE) has become ubiquitous in companies conducting research in advanced materials, drugs, catalysts and polymers. Its adoption has led to new products, reduced product innovation cycle time and increased return on research and development investment [1]. High levels of spending on R&D typical of the electronics, chemical and pharmaceutical sectors and the presence of companies dedicated to developing, marketing and facilitating implementation of HTE (e.g. Symyx, Avantium and HTE) have aided the shift to this paradigm from the traditional serial discovery process. This development was also enabled by the convergence of several technologies, computer software (data warehousing and query engines, molecular modelling, machine control software and statistics) running on more cost effective computers; robotics; and MEMS (microelectromechanical systems) technologies and sensors.

In the context of catalyst screening experimentation, high throughput screening (HTS) like all HTE techniques is invariably based on a two-step approach (Fig. 1.1) comprising of primary screening of a large number of candidates (discovery stage) followed by optimisation of a small number of leads. In the discovery stage, thousands or even tens of thousands of catalysts may be tested, but often only one binary parameter is scanned. If that parameter outperforms a set standard, it is considered a "hit". In the optimisation stage the process is repeated on the "hits" with different standards resulting in "Leads".

Most of the efforts for screening catalyst libraries have been in the field of heterogeneous catalysis, especially for gas-solid processes. Less studied are homogeneous and particularly biphasic (liquid-liquid or gas-liquid) homogenous catalysis[1] (such as chiral organometallic catalysts in hydrofomylation, hydrocyanation, carbonylations to name a few). One of the practical issues that arise when characterising the libraries is the design to be adopted for the parallel catalytic test reactor. The required characteristics are listed by de Bellefon [2] as:

[1] Biphasic refers to both processes where the reaction reagents are naturally in two phases or where the reaction is designed so that the catalyst is only present in one of the phase for easy recovery.

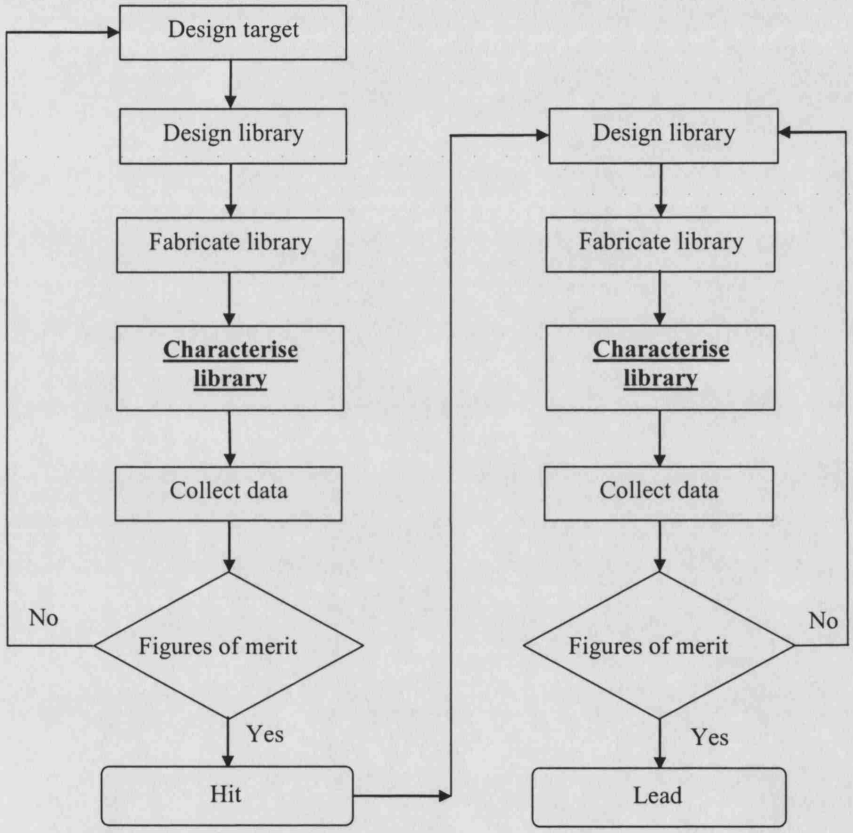

Fig. 1.1: Typical steps in high throughput experimentation. The "characterise library" step has been underlined as it is where this work fits into the general scheme [1].

1. Multiphase capabilities: The reactor must allow contact between the several phases, gas-solid, gas-liquid, gas-liquid-solid and liquid-liquid.
2. No mass and heat transfer limitations. This is to ensure intrinsic kinetics are under evaluation.
3. Ideal hydrodynamics (flow pattern) for easy reactor modelling.
4. Flexible residence (reaction time).
5. Flexible range of operating conditions (pressure,temperature).
6. Sample catalyst inventory from milligrams down to micrograms.
7. Significant throughput testing frequency (>100/day).
8. Easy and inexpensive automation (sampling)

For homogeneous catalysis, the commercial HTE equipment, consisting of racks of miniature agitated batch reactors for liquid, gas-liquid, liquid-liquid and gas-liquid-solid, proved problematic because of the difficulty in characterising the resulting agitation [3]. A new concept for HTS of catalysts based on dynamic sequential operation with a combination of pulse injections and a micromachined contacting devices was developed by de Bellefon et al. [3, 4]. Sequential screening of both liquid-liquid (isomerization of allyl alcohol derivatives) and gas-liquid reactions (hydrogenation of Z-(α)-acetamidocinnamic methyl ester) using a micromixer contacting device connected to a capillary. The flow in the capillary reactor consisted of a gas-liquid dispersion (termed hexagonal flow) generated continuously by the so-called "slit interdigital micromixer" [5]. Large interfacial areas, of the order of $5000 m^2/m^3$, for gas-liquid mass transfer were achieved. Other devices such as a micro-helicoidal-falling film reactor for gas-liquid hydrogenations and micro-mesh contactor devices for liquid-liquid and gas-liquid-solid catalysis have been tested and led to the conclusion that microreactors satisfy the above listed requirements [2]. Again, the development of the microreactor technology had reached a stage that allows HTE to be carried out in such devices.

de Bellefon et al [6] used the micromixer contacting device and pulse injection setup described above for screening, to perform kinetic studies on the asymmetric hydrogenation of methyl Z-(α)-acetamidocinamate catalysed by rhodium/(S,S-BDPPTS) in aqueous phase. Although a large number of tests were performed in a short time, with a small inventory of Rh/test, comparison with traditional batch

reactor system showed differences in the values of the estimated kinetics parameters. These discrepancies were attributed to problems resulting from poor temperature and residence time control in the setup. A similar setup has also been used for synthesis [7]. The use of the same apparatus for screening, for determining kinetics and for small initial production can be complemented by the concept of "scale-out" which drives some of the research into microreactors allowing an integrated approach from characterisation to (potentially) large scale production.

The work documented in this thesis has been carried out in the context of an EU funded project entitled "Key Elements for the application of Microreactors in multiphasic Catalytic Chemistries" (KEMICC) which aimed to demonstrate and facilitate the capabilities of microreactor based systems in implementing "high speed chemistry" which combines:

1. HTE, enabling screening of catalysts and extraction of kinetics and fast optimisation of multiphase chemistries in addition to fast reagent and catalyst loading and fast subsequent analysis.

2. Implementation of new chemical synthesis through either microreactor "scale-out" or classical "scale-up".

One of the objectives of this project was the development of instrumented multiphase (liquid-liquid and gas-liquid or gas-liquid-solid) analytical microreactors and sufficient models to enable the extraction of high quality quantitative reaction kinetics. This thesis addresses the modelling and characterisation of a gas-liquid microreactor arrangement in which the flow is known as Taylor flow. It is a two-phase pattern where gas bubbles of larger equivalent diameter than the tube diameter flow alternately with liquid slugs. Its segmenting behaviour, natural stability, gas-liquid mass transfer and reproducible periodicity make it a suitable system for performing HTE studies and a possible alternative to hexagonal flow.

The work can be grouped into three broad parts, the first, comprising chapters 2-4, deals with the hydrodynamics of the flow. A literature review of small scale phenomena and the associated mathematical modelling equations is reported in chapter 2 with illustrations of their effects on the observed multiphase flow patterns. Chapter 3 specifically focusses on Taylor flow, lists the dimensionless equations governing its behaviour and the dimensionless parameters that can be used to characterise it. Experimental and theoretical work on this flow pattern is reviewed and important issues resulting from the modelling of its hydrodynamics are highlighted. Chapter

4 examines the length of the bubble formed depending on the prevailing conditions at a coaxial inlet of the Taylor flow reactor and the gas and liquid flow rates.

The second part, chapters 5-7, deals with axial mixing along the microreactor channel. The time available for a reaction and the number of sequential reactions that can be achieved depends on the reactants' residence time in the Taylor flow reactor. Chapter 7 is a special case of the general model of chapter 5 where diffusion dominates enough to deviate from the closed vessel assumptions of Chapter 5.

Part three, chapter 8, deals specifically with the use of Taylor flow reactor arrangement for extraction of kinetic data. It identifies the conditions necessary for the kinetic regime to exist where conversion data at the end of the reactor yield kinetic data.

An important point to note throughout this work is the use of circular channels rather than the familiar rectangular channels typical of the microreactor microfabrication processes. The reason for this is three fold, firstly analysis of axi-symmetric channels simplifies the computation to a manageable level. The methodology can then be further extended to rectangular channels, with further computational effort. Secondly Taylor flow in circular microchannels has been far more studied and characterised than Taylor flow in rectangular channels and as such there is more information to draw on when formulating the different models. Finally and importantly, Taylor flow in circular channels has better segmentation features because of the absence of liquid filled corners typical of polygonal channels making it superior in terms of dispersion and reaction.

2. THE HYDRODYNAMICS AND SURFACE PHENOMENA OF TWO-PHASE FLOW IN SMALL CAPILLARIES

Nomenclature

a	Molecular size	m
Bo	Bond number $\frac{(\rho_\beta - \rho_\alpha) g d^2}{\gamma}$	
c	Contaminant concentration	$\mathrm{kg/m^3}$
c_s^*	Subsurface bulk concentration	$\mathrm{kg/m^3}$
Ca	Capillary number	
D	Diffusivity of contaminant	$\mathrm{m^2/s}$
g	Acceleration due to gravity	$\mathrm{m/s^2}$
k	Boltzman constant	$\mathrm{J\,K^{-1}}$
k_L^a	Adsorption rate coefficient	s^{-1}
k_L^d	Desorption rate coefficient	s^{-1}
Kn	Knudsen number $\frac{\text{Mean free length}}{\text{Characteristic length}}$	
n	Gas density	$\mathrm{mol/m^3}$
$\mathbf{n}_b$	Interface unit normal vector	
$\mathbf{n}_t$	Interface unit tangent vector	
p	Pressure	$\mathrm{N/m^2}$
$\mathbf{q}$	Contaminant sorption flux	$\mathrm{kg\,m^{-2}\,s^{-1}}$
R	Universal gas constant	$\mathrm{J\,mol^{-1}\,K^{-1}}$
T	Temperature	K
$\mathbf{T}$	Stress Tensor	$\mathrm{N/m^2}$
$\mathbf{u}$	Velocity field	m/s
U	Superficial velocity	m/s
We_{GS}, We_{LS}	Gas and Liquid Weber number based on superfical velocities $\frac{\rho_\alpha U_{GS}^2 d}{\gamma}$ and $\frac{\rho_\beta U_{LS}^2 d}{\gamma}$	
Greek symbols		
Γ	Surface concentrations	$\mathrm{kg/m^2}$
γ	Interfacial tension	N/m

μ	Viscocity	$\mathrm{N\,s\,m^{-2}}$
σ_{sg}, σ_{sl}	Gas solid and solid liquid surface energy	$\mathrm{N/m}$
λ	slip length	m
ρ	Density	$\mathrm{kg/m^3}$
τ	Deviatoric stress	$\mathrm{N/m^2}$
θ	Contact angle	
Subscripts		
α	Gas phase	
β	Liquid phase	
w	Wall property	
s	Interfacial property	
sat	Saturation	
Superscripts		
T	Transpose	

2.1 Introduction

With the continuous miniaturisation of flow devices, the decreasing scales and increasing surface area to volume ratio result in an increase of the significance of surface forces and associated surface phenomena. Microfluid flows can be manipulated using different kinds of external fields (pressure, electric, magnetic and so on). Such manipulations of flows can be achieved either by forces applied macroscopically, at inlets and outlets, or locally within the microchannel by integrated components [8]. In this thesis only pressure will be considered as a means of moving the fluids, while surface tension gradients arising naturally from hard to remove trace contaminant in the liquid are considered in relation to experimental variations and deviations from theoretical predictions.

In this chapter the general issues related to the modelling of hydrodynamics of two-phase flows in microchannels are introduced. Particular studies on the Taylor flow pattern will be considered in detail in chapter 3. An outline is presented of the application of the classical Navier-Stokes theory to two-phase flow and of the appropriate boundary conditions to be used at these small scales. Some topics discussed, such as the Marangoni effects and modelling of contact lines, are complex in nature and still very much a field of active research well beyond practical implementation. They were included for completeness and as a background to some discussions of assumptions and phenomena that appear later in this thesis.

2.2 Mathematical representation of hydrodynamics of two-phase systems

Fluid-liquid multiphase flows are usually treated using classical fluid mechanics. Very small length scales however bring into question the continued validity of the classical continuum approach at small scale. Some experimental evidence demonstrates that such a description is valid for simple liquids down to $50nm$ scale [9], other evidence suggests that it may be valid to a scale of the order of 10 molecular diameters [10]. For a gas, the continuum approach is valid as long as the channel dimension is larger than the mean free path. A typical size of the cross-section of a microchannel lies between $1\mu m$ and $1mm$. On the other hand, the mean free path of ideal gasses is given by equation 2.1[11].

$$\text{mean free path}=\frac{1}{\sqrt{2}\pi n a^2} = \frac{kT}{\sqrt{2}\pi p a^2} \tag{2.1}$$

where n is the number density, a is the molecular size, k the Boltzman constant, p is the pressure and T the absolute temperature. At 270 K and atmospheric pressure, the mean free path is on the order of $70nm$ [12].

The continuum theory is not valid for Knudsen number $Kn < 0.1$ where Kn is the ratio of the mean free path to the characteristic dimension, which for the above example would give a channel dimension of the order of $700nm$ (close to the $1\mu m$ limit). Higher temperatures and low pressures may cause the gas to behave as a rarefied gas and not as a continuum fluid at the limit of $1\mu m$. The continuum approach can therefore be considered valid for the range of microreactor scales used in this work.

In a general two-phase flow of two immiscible Newtonian fluids in a tube any differential control volume at any point in a general two-phase flow (Fig. 2.1) can be of three different types. Any conservation equation derived will consequently have a form appropriate to the element it is describing. The types are:

1. Differential volume containing gas phase α
2. Differential volume containing liquid phase β
3. Differential volume containing an interface between the two phases.

2.2.1 Conservation of Mass

The conservation of mass equations in a differential form are:

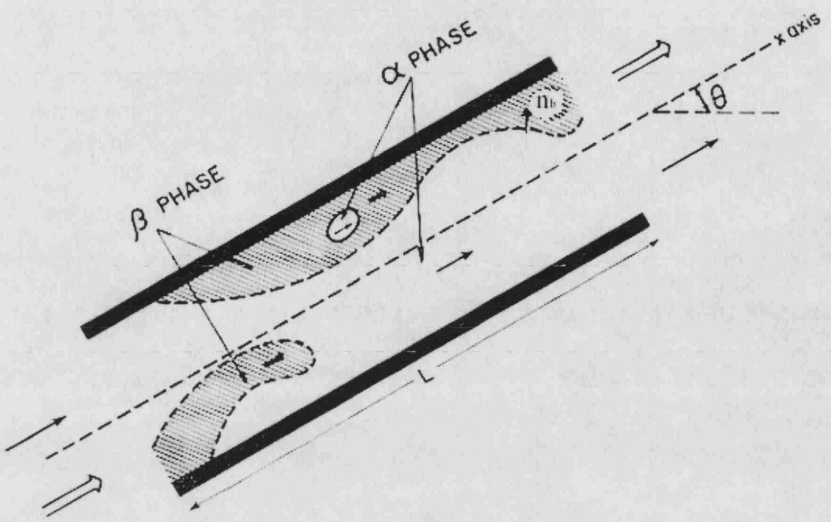

Fig. 2.1: Schematic diagram for equation for the flow of a two-phase system.

For phase α:

$$\frac{\partial \rho_\alpha}{\partial t} + \boldsymbol{\nabla} \cdot (\rho_\alpha \mathbf{u}_\alpha) = 0 \tag{2.2}$$

similarly for phase β:

$$\frac{\partial \rho_\beta}{\partial t} + \boldsymbol{\nabla} \cdot (\rho_\beta \mathbf{u}_\beta) = 0 \tag{2.3}$$

for the interface:

$$\rho_\alpha (\mathbf{u}_\alpha - \mathbf{u}_b) \cdot \mathbf{n}_b + \rho_\beta (\mathbf{u}_\beta - \mathbf{u}_b) \cdot \mathbf{n}_b = 0 \tag{2.4}$$

Equation 2.4 decomposes into equations 2.5 and 2.6 when there is no boiling or mass transfer through the interface:

$$\rho_\alpha (\mathbf{u}_\alpha - \mathbf{u}_b) \cdot \mathbf{n}_b = 0 \tag{2.5}$$

$$\rho_\beta (\mathbf{u}_\beta - \mathbf{u}_b) \cdot \mathbf{n}_b = 0 \tag{2.6}$$

2.2.2 *Conservation of Momentum*

The equation of conservation of momentum equations in differential form are:

For phase α:

$$\frac{\partial(\rho_\alpha \mathbf{u}_\alpha)}{\partial t} + \nabla \cdot (\rho_\alpha \mathbf{u}_\alpha \mathbf{u}_\alpha) = \rho_\alpha \mathbf{g} + \nabla \cdot \mathbf{T}_\alpha \tag{2.7}$$

Similarly phase β:

$$\frac{\partial(\rho_\beta \mathbf{u}_\beta)}{\partial t} + \nabla \cdot (\rho_\beta \mathbf{u}_\beta \mathbf{u}_\beta) = \rho_\beta \mathbf{g} + \nabla \cdot \mathbf{T}_\beta \tag{2.8}$$

At the interface between the two phases α and β we obtain:

$$\begin{aligned} 0 \;=\; & +\{\rho_\alpha \mathbf{u}_\alpha (\mathbf{u}_\alpha - \mathbf{u}_b) + \mathbf{T}_\alpha\} \cdot \mathbf{n}_b - \{\rho_\beta \mathbf{u}_\beta (\mathbf{u}_\beta - \mathbf{u}_b) + \mathbf{T}_\beta\} \cdot \mathbf{n}_b \\ & + [\nabla\gamma - \gamma \mathbf{n}_b (\nabla \cdot \mathbf{n}_b)] \end{aligned} \tag{2.9}$$

where for an incompressible Newtonian fluid:

$$\begin{aligned} \mathbf{T}_\alpha &= -p_\alpha \mathbf{I} + \boldsymbol{\tau}_\alpha \\ \mathbf{T}_\beta &= -p_\beta \mathbf{I} + \boldsymbol{\tau}_\beta \end{aligned}$$

$\boldsymbol{\tau}_\alpha$ and $\boldsymbol{\tau}_\beta$ are given by:

$$\begin{aligned} \boldsymbol{\tau}_\alpha &= 2\mu_\alpha \mathbf{E}_\alpha \\ \boldsymbol{\tau}_\beta &= 2\mu_\beta \mathbf{E}_\beta \end{aligned}$$

and $\mathbf{E}$ is the rate of strain tensor:

$$\begin{aligned} \mathbf{E}_\alpha &= \frac{1}{2}\left(\nabla \mathbf{u}_\alpha + \nabla \mathbf{u}_\alpha^T\right) \\ \mathbf{E}_\beta &= \frac{1}{2}\left(\nabla \mathbf{u}_\beta + \nabla \mathbf{u}_\beta^T\right) \end{aligned}$$

When there is no boiling or mass transfer through the interface, equation 2.9 reduces to 2.10:

$$(\mathbf{T}_\alpha - \mathbf{T}_\beta) \cdot \mathbf{n}_b + [\nabla\gamma - \gamma \mathbf{n}_b (\nabla \cdot \mathbf{n}_b)] = 0 \tag{2.10}$$

Equation 2.10 can be decomposed into two parts when there is no mass transfer or

boiling between the two phases, namely a direction normal to the interface, equation 2.11 and another tangential to it, equation 2.12.

$$-(p_\alpha - p_\beta) + [(\boldsymbol{\tau}_\alpha - \boldsymbol{\tau}_\beta) \cdot \mathbf{n}_b] \cdot \mathbf{n}_b - \gamma(\boldsymbol{\nabla} \cdot \mathbf{n}_b) = 0 \tag{2.11}$$

$$[(\boldsymbol{\tau}_\alpha - \boldsymbol{\tau}_\beta) \cdot \mathbf{n}_b] \cdot \mathbf{n}_t + (\boldsymbol{\nabla}\gamma) \cdot \mathbf{n}_t = 0 \tag{2.12}$$

As a special case of equation 2.11, when there is no shear stress, the Young-Laplace equation is obtained:

$$p_\alpha - p_\beta = -\gamma(\boldsymbol{\nabla} \cdot \mathbf{n}_b) \tag{2.13}$$

2.3 Boundary conditions

2.3.1 "Slip"/"no-slip" boundary conditions

In classical fluid mechanics it is considered that liquids do not slip on solid surfaces. The physical justification assumes that attractive Van der Waal interaction forces tend to link fluid atomic layers next to the solid wall to the wall, preventing slip from occurring. Experimental and theoretical investigation of this assumption revealed many conditions in which the "no-slip" is not obeyed:

Using molecular dynamics simulations of Pouiseuille flow, Koplik et. al. [13] found that liquids that have strong interaction with the wall behave in almost all respects like a continuum fluid even for scales as small as $40 - 100$ Å. The macroscopic flow properties were found to be still valid at such a small scale and the liquid velocity field was found to vanish at the fixed solid boundaries in agreement with the "no-slip" boundary condition for a viscous fluid flowing past a solid wall. Their investigation of moving interfacial contact lines showed that the "no-slip" boundary condition did not hold near the contact line. The breakdown is expected from the singularity arising when the classical hydrodynamic theory is applied at that point. Thompson and Robbins [14] found similarly the "no-slip" boundary condition to hold in a Couette flow arrangement. The solid fluid interaction induced a degree of order in the adjacent liquid layers which in turn influences the degree of momentum transfer.

The "no-slip" boundary is mathematically expressed as:

$$\mathbf{u}_\alpha = \mathbf{u}_\beta = 0 \tag{2.14}$$

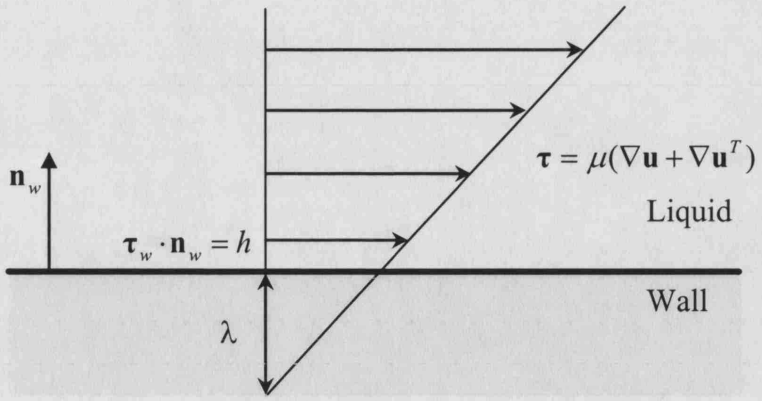

Fig. 2.2: Slip length λ for a Newtonian liquid. The velocity at the wall is finite and the length λ can be obtained from a linear extrapolation to a point where the velocity would be zero.

Barrat and Bocquet [15] using molecular dynamics simulations showed that when the liquid-solid interactions are weak the boundary conditions can drastically differ (at a microscopic level) from the "no-slip" assumption. A model of "slip" at the wall is illustrated in Fig. 2.2. It should be noted that for an ideally smooth solid surface, the "slip" can be related to wetting behaviour as both depend on the strength of the interactions [16]. A typical boundary condition adopted instead of the "no-slip" is given by equation 2.15. It is characterised by a slip length λ independent of local shear rate (Fig. 2.2). Barrat and Bocquet [15] reported slip lengths exceeding 30 molecular diameters for a contact angle of 140°, characteristic of mercury on glass.

$$\mathbf{u}_w = \lambda \left.\frac{\partial \mathbf{u}}{\partial n}\right|_w \tag{2.15}$$

"Slip" has also been experimental demonstrated by various workers [9, 17, 18, 19, 20] and slip lengths experimentally correlated to the measurements. Results indicate that slip length λ is of the order of micrometers, or fractions of a micrometer, sometimes much larger than the characteristic dimension of the liquid region studied . Thompson and Troian [21] demonstrated, using molecular dynamics of Newtonian fluids under shear, a non-linear relationship between λ and the local shear rate at solid surface. Studies on the effect of surface roughness show that slip length increases with increasing roughness, contrary to the usual notion of friction increasing with surface roughness [20]. It has been suggested that a gaseous layer nucleating at the interface between the fluid and the solid increases the slippage, and this has been validated experimentally by observation of nano-bubbles [22] and in theoretical molecular dynamic simulation for surfaces patterned on the micrometer scale [16].

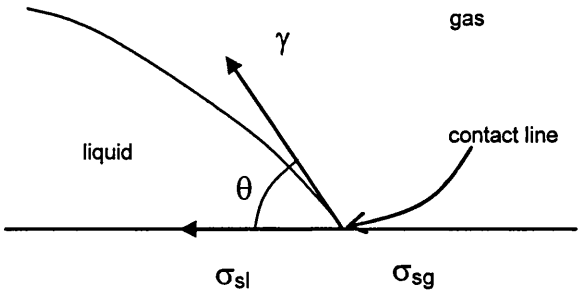

Fig. 2.3: Horizontal static forces must balance at the contact line.

It can therefore be concluded that for most of the range of length scales used in microreactors and any liquid wall interactions, the "no-slip" boundary condition is a sufficient approximation. For a hydrophobic channel wall of a $100\mu m$ or more diameter channel a slip length of the order of 1μ is not going to change the resulting flow field appreciably. Errors however become more significant with decreasing channel size and a model of slip needs to be introduced. In this thesis, only the "no-slip" boundary condition will be considered.

2.3.2 Contact point treatment

Whenever a contact line between three phases (Fig. 2.3) is stationary, a horizontal force balance gives the Young equation, equation 2.16.

$$\gamma \cos\theta = \sigma_{sg} - \sigma_{sl} \tag{2.16}$$

However, when the interface moves, the shear stress in the liquid causes an imbalance of the forces and a change in the observed contact angle. A comprehensive description of the dynamic contact angle requires detailed hydrodynamics and an understanding of what happens at the contact point. The classic model of "no-slip" always yields a singularity at the contact line because it leads to infinite shear stress. Pismen [23] reviews existing approaches that deal with moving contact lines. Two broad approaches are available: the first introduces phenomenological corrections, such as effective slip at the solid interface in the vicinity of the three-phase boundary, special rheological properties at the interface or an empirical velocity dependence of the contact angle. The second has a more physical basis replacing the continuum approach by molecular dynamics simulations in the immediate vicinity of the contact line. Unfortunately the second approach cannot be incorporated into

the general continuum approach. Pismen [23] proposes a formulation of continuous models which include intermolecular forces. The field remains a point of active research and is beyond the scope of this thesis.

2.3.3 Marangoni effects

Surface tension is a thermodynamic property and depends on temperature, external electric field and surface active agents. Gradients of temperature, external electric fields and surface active agents cause gradients of surface tension to develop and the effects this causes on the flow are referred to as Marangoni effects. Only surface active agents are considered here. When they are uniformly distributed in space, these agents increase or decrease the surface tension values and hence only influence the value of γ in equation 2.11. In the case of non-uniform spatial distribution along interfaces surface tension gradients develop. This non uniform distribution may be desirable, and can be exploited for controlling fluid flow and imposed externally [8]. However, the presence of surface tension gradients due to contaminants in the liquid is usually uncontrollable, difficult to account for and causes unexpected deviations from theoretical results. Equation 2.12 accounts for surface tension gradients, but predicting these gradients is difficult and depends on the flow dynamics, nature of the contaminants, and local contaminant concentration at the surface.

The difficulty in the detailed analysis of the Marangoni effect is due to the complexity of the surfactant transport problem and the coupling between surfactant transport and fluid motion through equation 2.12. For a gas-liquid system with the surfactant present in the liquid phase the advection and diffusion of surfactant in the bulk needs to be known.

$$\frac{\partial (c_\beta)}{\partial t} + \nabla \cdot (c_\beta \mathbf{u}_\beta) = D_\beta \nabla^2 c_\beta \tag{2.17}$$

where c_β is the surfactant concentration and D_β is the diffusivity in phase β.

The local interface concentration Γ will depend on the rates of adsorption and desorption of the surfactant onto the interface and its mobility on the interface. The governing equation is [24]:

$$\frac{\partial \Gamma}{\partial t} + \nabla_s \cdot (\Gamma \mathbf{u}_s) - D_s \nabla_s^2 \Gamma + \Gamma \nabla_s \cdot \mathbf{n}(u \cdot \mathbf{n}) = -\mathbf{n} \cdot \mathbf{q}_\beta \tag{2.18}$$

Which is a form of convection-diffusion equation for the surfactant on the surface. The subscript s denotes surface operators and surface values of properties and fields, $\mathbf{q}_\beta$ denotes the net sorption flux. Adsorpotion/desorption to/from the interface

follows first order kinetic laws [25].

$$-\mathbf{n} \cdot \mathbf{q}_\beta = k_L^a c_s^* \left[\Gamma_{sat} - \Gamma\right] - k_L^d \Gamma \tag{2.19}$$

Assuming that the concentration of surfactant adsorbed at the free surface is much smaller than the maximum interfacial concentration Γ_{sat}, an expression for the relationship between the surfactant concentration and surface tension is the linearised Frumkin equation [26, 27]:

$$\gamma = \gamma_0 - (RT\Gamma_{sat}) \frac{\Gamma}{\Gamma_{sat}} \quad \text{for} \quad 0 \leq \Gamma \ll \Gamma_{sat} \tag{2.20}$$

where γ_0 is the surface tension of the uncontaminated surface and Γ_{sat} is the saturation solute surfactant concentration.

2.4 Gas-Liquid flow in small channels

Multiphase flow patterns in small channels have been studied by many researchers and are reviewed in numerous papers. The same classifications and terminology as those in much larger tubes are most commonly used. Apart from flow regime maps [28, 29, 30, 31, 32, 33, 34] frictional pressure drop and void fraction are also given [28, 35, 36, 37, 38], researchers often discuss deviations from the predictions of general correlations and models which are used in large tubes, such the Armand-type correlation for void fraction, and homogeneous, Lockhart-Martinelli or Friedel type correlations for pressure drop.

Channels are generally regarded as small when surface tension forces dominate over gravitational forces. A measure of the relative values of the two forces is given by the Bond number:

$$Bo = \frac{\left(\rho_\beta - \rho_\alpha\right) g d^2}{\gamma} \tag{2.21}$$

As a result the dominant stratified flow pattern in large channels is absent from small channels. Brauner and Moalem-Maron [39] use the limit of stability and well posedness of unidirectional continuity and momentum equations that describe stratified flow in pipes as a criterion for defining small channels and they propose $Bo \leq (2\pi)^2$. Substituting the appropriate values for an air-water system, the tube 'small' diameter can be calculated to be $\sim$ 17 mm. Suo and Griffith [32] do not observe any effects of Bo on the velocity ratio of a Taylor bubble moving through a horizontal tube and suggest that at least $Bo < 0.88$, which is the maximum Bo

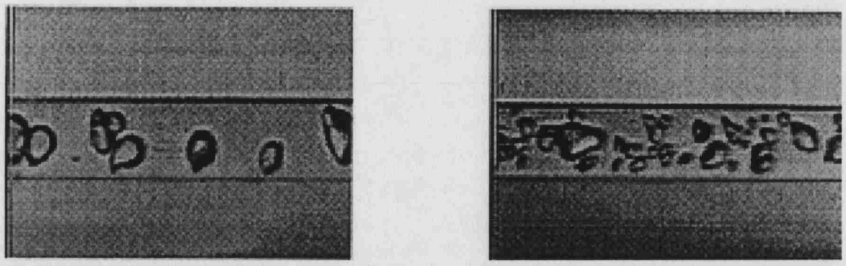

Fig. 2.4: Bubbly flow. Air-water flow in 1.1mm circular pyrex capillary [31]. It is characterised by distinct (sometimes non-spherical) bubbles, generally considerably smaller than the channel diameter. Increasing U_{gs}, the gas inlet velocity, increases void fraction and the increased number of the bubbles in the capillary eventually leads to the development of slug flow.

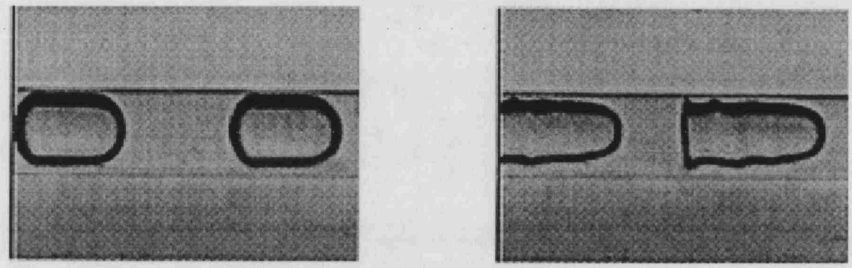

Fig. 2.5: Taylor flow (also known as slug flow/bubble train flow). Air-water flow in 1.1mm circular pyrex capillary [31]. It is characterised by elongated cylindrical bubbles. The bubbles occupy most of the channel cross-section and have an equivalent bubble diameter larger than the tube diameter.

number they investigated in these experiment as a sufficient criterion for smallness. Another criterion can also be deduced based on Bretherton's [40] observation that for a Bond number range of $Bo \lesssim 3.37$, a Taylor bubble no longer rises spontaneously in a water filled circular capillary under the effect of gravity. For an air-water system the maximum 'small' tube diameter is now calculated to be ~ 5 mm.

Interestingly, there is a large body of literature on low gravity two-phase flows [41, 42, 43, 44, 45], which were carried out using 'large' diameter tubes, under reduced gravity, but which may be classified as 'small' tube studies because with reduced gravity the Bo number satisfies the criterion for smallness. It can be concluded that for the cases of microgravity and 'small' tube normal gravity multiphase flows only surface tension, viscous and inertial forces are important.

The flow patterns generally observed in small channels are given in Figs. 2.4-2.8. The conditions at which these patterns are usually observed are summarised in flow maps which are given for the specific fluids and for the specific channel sizes and

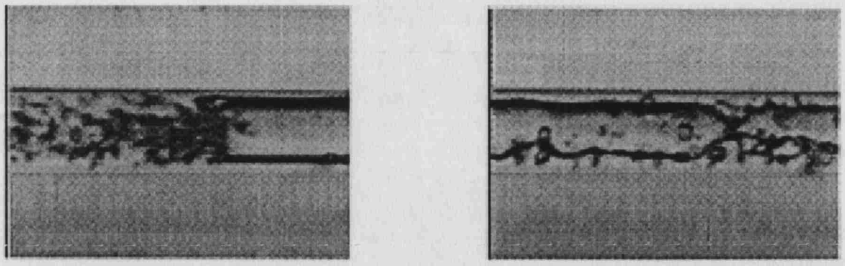

Fig. 2.6: Churn flow. Air-water flow in 1.1mm circular pyrex capillary [31]. It appears at high total flow rates. For conditions which have a relatively large liquid flow, the bubbles in the Taylor flow pattern become unstable near their trailing ends, leading to their disruption (sometimes referred to as bubbly slug flow). In others with higher relative gas flow rates, flooding type churn flow periodically disrupts an apparently wavy-annular flow.

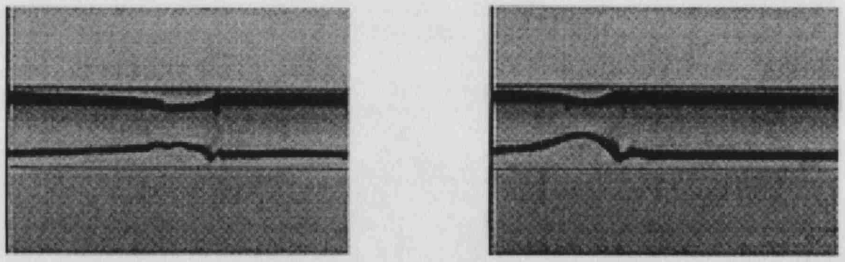

Fig. 2.7: Taylor-annular flow (also known as slug- annular or wavy annular) Air-water flow in 1.1mm circular pyrex capillary [31]. At relatively low liquid superficial velocities increasing the mixture volumetric flux leads to longer bubbles and shorter liquid slugs; eventually, the elongated bubbles merge and the slug-annular flow pattern establishes. It takes the appearance of annular flow with large solitary waves.

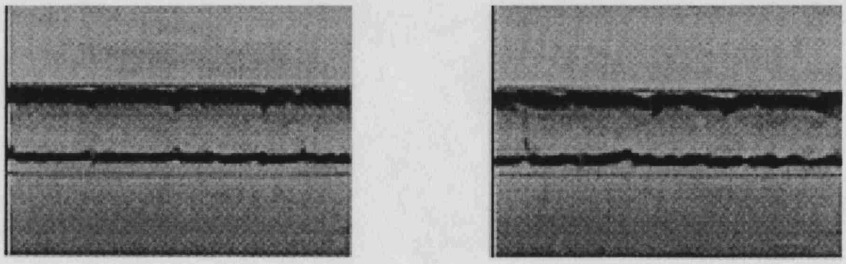

Fig. 2.8: Annular flow. Air-water flow in 1.1mm circular pyrex capillary [31]. With further increasing gas flow rates, the long waves observed in slug-annular flow disappear.

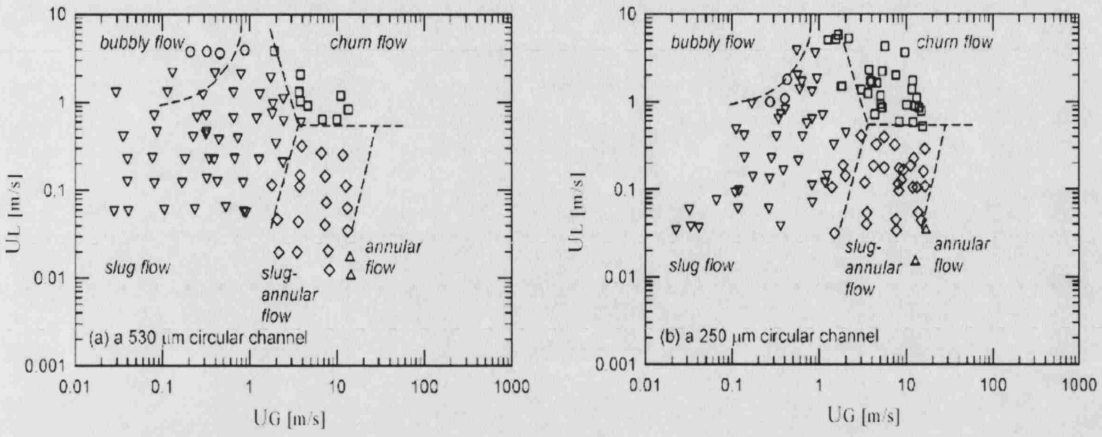

Fig. 2.9: Flow pattern data from nitrogen-water flow in fused silica capillaries with polyamide coating and diameters (a) 530 μm and (b)250 μm capillaries [28]. Reasonable agreement is found with the flow regime transition lines from the work Triplett et al.[31] for 1 mm channels and air-water mixture.

shapes (Fig. 2.9). Empirical transition lines are used to separate regions of different flow patterns.

The position of the transition lines in a flow pattern map is a strong function of the properties of the fluids used. Suo and Griffith [32] observed, by changing the liquid from water to heptane, a dependence of the transition lines from slug to annular and from bubbly Taylor to Taylor flow on the Capillary number, Ca. A more general (and intuitive) approach in analysing flow maps is based on the dominant force classification, which is based on studies in microgravity two-phase flow [41, 43, 44]. By comparing the characteristic force ratios in the flow regime map, the flow maps are divided into three regions (elaborated to four by Akbar et al. [46]):

1. Surface tension-dominated region, including bubbly and Taylor flow.

2. Inertia-dominated zone 1, including annular and wavy-annular regimes.

3. Inertia-dominated zone 2, including the dispersed flow regimes.

4. Transition zone.

Since it is the inertia-surface tension ratio that is important for regime transitions, Akbar et al. [46] proposed plotting the flow map diagrams using the gas and

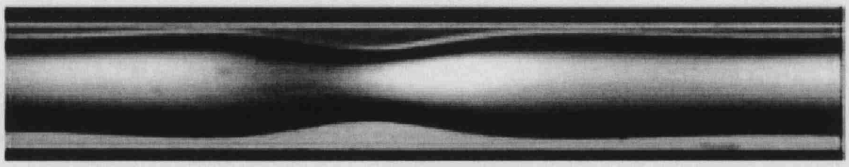

Fig. 2.10: Liquid ring flow for air-water in a 100 μm quartz tube [49]. This pattern occurs when gas velocity increases in Taylor flow. The bubbles increase in size until they connect, leaving 'liquid rings'. It differs in description from Taylor-Annular flow (Fig. 2.7) by being symmetrical and equispaced.

liquid Weber numbers, We_{GS} and We_{LS} respectively based on superficial velocities. The transition lines were then given in the form $We_{GS} = We_{LS}^{\eta}$, where η is an empirical power. Akbar et al. [46] fitted this expression to literature results for gas-water in channels of diameter $\sim 1mm$, but did not check them against other experimental data using different fluids. Chung and Kawaji [28] investigated different sizes (530, 250, 100 and 50 μm) and concluded that the larger two diameters investigated (530 and 250μm) showed similar behaviour to that observed on the $1mm$ scale (Fig. 2.9). In the smaller capillary diameters (100 and 50 μm), however, considerable deviation and dominance of Taylor flow were found. They concluded that for the same fluids, apart from the transition occurring between 250μm and 100μm, transition lines are weak functions of the channel diameter.

Additional flow patterns/variations of flow patterns have been identified for capillary diameters smaller than 100μm (Figs. (2.10)-(2.12)). These patterns may be viewed as variations of Taylor-annular which have only been observed in microscale tubes. Chung and Kawaji [28] and Kawahara et al. [47] reported varying flow patterns with time, and adopted a probabilistic approach for mapping their observations (Fig. 2.13). The new patterns and the time variation of observed patterns may be attributed to phenomena related to surface tension gradients and gas-liquid-solid contact which become important at small scale and increasingly so with further scale decrease.

There is limited discussion of the influence of surface tension gradients or contact angle on flow pattern maps. Barajas and Panton [48] examined the effect of surface wettability on flow patterns in 1.6 mm tubes. For partially wetting fluid-solid combinations (contact angles smaller than 90°) flow pattern maps were found to be similar and only a new pattern, rivulet flow, occurred in tests with 61 and 74° contact angles and its domain expanded with increased contact angle (Fig. 2.16). With partially non-wetting liquid (contact angle =106°), the rivulet flow pattern re-

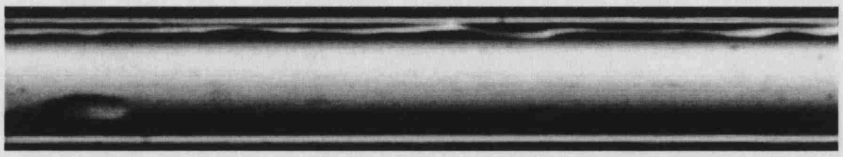

Fig. 2.11: Liquid Lump flow. Air-Water flow in a 25 μm silica tube [49]. Further increasing the gas flow rate in liquid ring flow results in this flow pattern where the liquid phase in the form of liquid drops slides along the wall of the tube. This is similar in appearance to what Tripplett et al.[31] term Taylor annular flow however, the strong surface tension forces prevent the liquid from wetting the walls.

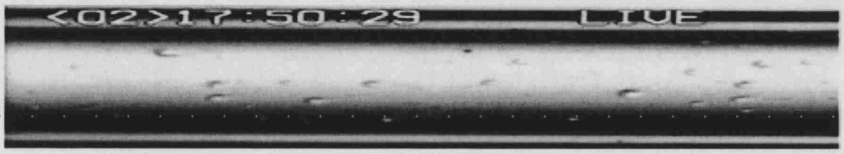

Fig. 2.12: Droplet flow. Air-Water flow in a 100 μm quartz tube [49]. With further increase in gas flow rate, rather than single large liquid droplets as in liquid lump flow, many small liquid drops are seen.

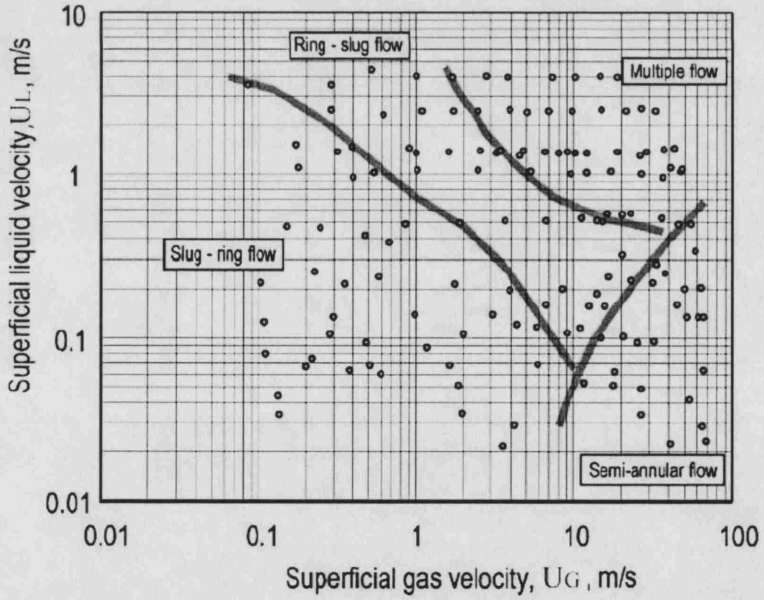

Fig. 2.13: Two-phase flow regime map for a 100 μm microchannel. Slug-ring flow regions show predominantly Taylor but with occasional ring flow, while the ring-slug flow region indicates the opposite. Semi-annular flow indicates a region which includes annular and wavy annular. Multiple flow shows a mixture of all flow patterns. Air-Water flow in a 100 μm fused silica tube [47].

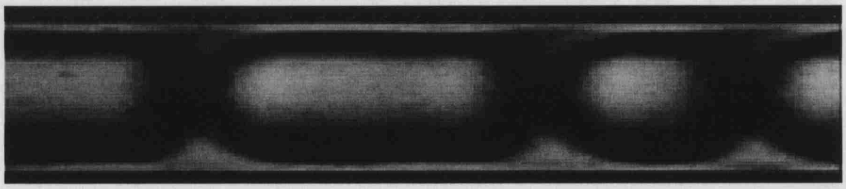

Fig. 2.14: Yakitori Flow (colourfully named after Japanese Skewered barbeque and also sometimes confusingly called bubble train flow): where several bubbles of various sizes are flowing in series, with only a clear interface separating the bubbles. This flow pattern is not unique to microchannels and has been also observed in 1mm channels [29], and also in microgravity studies [41].

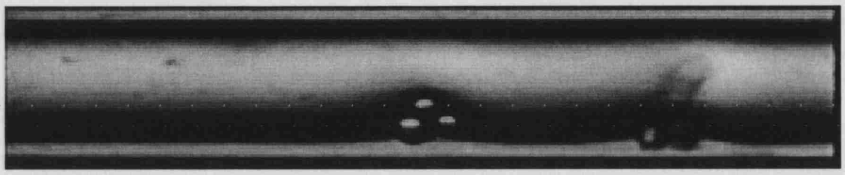

Fig. 2.15: Frothy annular flow: small bubbles were trapped within the thin liquid film flow on the tube wall.

gion was considerably wider, and in comparison to the partially wetting experiments some of the flow regime transition lines were noticeably displaced. Serizawa et al. [49], for air-water flow, after performing their first set of experiments, subjected the tube to a thorough cleaning procedure and used high purity distilled water in their second set of experiments. They found bubbly, Yakitori (Fig. 2.14) , frothy annular (Fig. 2.15) and Rivulet flows (Fig. 2.16), which were not observed in the first set of experiments for the same conditions. The changes were attributed to the improved wettability of the wall leading to the conclusion that the surface contamination is a key parameter which dominates two-phase flow pattern transitions.

Dreyfus et. al. [50] carried out experiments in oil-water flow in etched silicon rectangular microchannels ($20\,\mu$m $\times$ $200\,\mu$m) with glass anodically bonded to the top. The contact angles and surface tension were modified by introducing surface

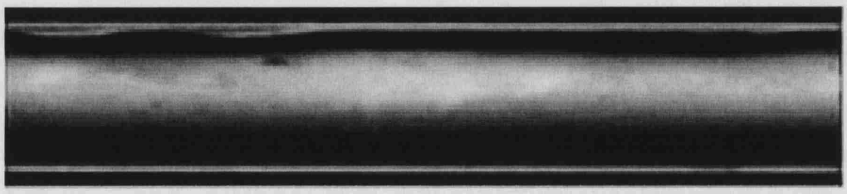

Fig. 2.16: Rivulet flow

active agents into the flow which decreased the wetting of the water and the surface tension between the liquids. High surfactant concentrations, well beyond the critical micellar concentration, caused complete oil wetting of the walls and resulted in varied but regular patterns. Interestingly varying the inlet configuration resulted in some difference in the phase diagrams leading the researchers to conclude that the flow pattern diagram substantially depends on the the entry conditions. In contrast at low surfactant concentration, where the oil was only partially wetting, irregular, erratic and sometime random flow patterns were formed..

Most recently, Cubaud et. al. [51], investigated flow patterns in etched silicon rectangular microchannels ($250\,\mu$m $\times$ $525\,\mu$m) with glass anodically bonded to the top and bottom of the silicon which was subsequently treated with surface modifiers to create hydrophobic surfaces. Their results illustrate the surface effects on the observed flow patterns (Figs. 2.17 and 2.18).

This section concluded with two observations specifically relevant to this thesis. First, in small capillaries and tubes, Taylor flow not only occupies a large portion of the flow map but specifically the region where the residence times for most reactions of interest lie for realistic capillary lengths (Appendix A). Second, surface forces and surface tension gradients play an important role in determining the phenomena observed in small channels, with regular flow generally observed in the larger liquid-wetting microchannels.

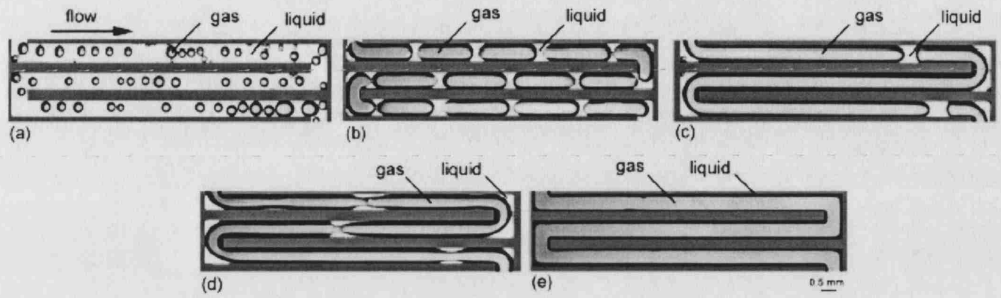

Fig. 2.17: Pure water/air flow patterns in hydrophilic channels ($\theta_{silicon} \approx 9°$,$\theta_{glass} \approx 25°$). (a) bubbly flow, (b)Taylor-Yakatori flow, (c) Taylor flow, (d) Wavy annular flow, (e) Annular flow. From Cubaud et al. [51] with flow patterns reclassified by author.

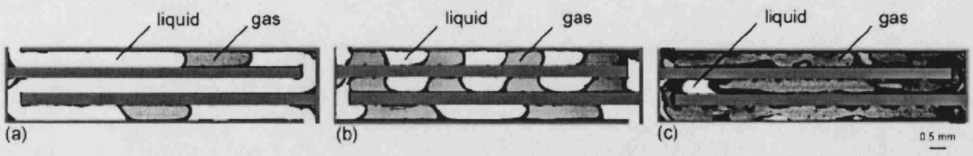

Fig. 2.18: Pure water/air flow patterns in hydrophobic channels (treated with Teflon® to produce a static contact angle $\theta \approx 120°$). Flow low to high void fraction, (a,b) asymmetric Taylor flow, (c) lumped liquid flow. From Cubaud et al. [51], flow patterns reclassified by author.

3. TAYLOR FLOW AND ITS HYDRODYNAMICS

Nomenclature

Bo	Bond number $\frac{(\rho_\beta - \rho_\alpha)gd^2}{\gamma}$	
c	Contaminant concentration	$\mathrm{kg/m^3}$
c_s^*	Subsurface bulk concentration	$\mathrm{kg/m^3}$
c_0	Downstream bulk concentration	$\mathrm{kg/m^3}$
Ca	Capillary number $\frac{\mu U_b}{\gamma}$	
Ca'	Capillary number $\frac{\mu U_{ls}}{\gamma}$	
d	Tube diameter	$\mathrm{m^2/s}$
D	Diffusivity of contaminant	$\mathrm{m^2/s}$
D_s	Surface diffusivity of contaminant	$\mathrm{m^2/s}$
El	Elasticity number $\frac{RT\Gamma_{sat}}{\gamma_0}$	
g	Acceleration due to gravity	$\mathrm{m/s^2}$
l_b	Taylor bubble length	m
l_s	Liquid slug length	m
L_b	Dimensionless Taylor bubble length $\frac{l_b}{d}$	
L_s	Dimensionless liquid slug $\frac{l_s}{d}$	
Mo	Morton number $\frac{g\mu_\beta^4}{\rho\gamma^3}$	
m	Relative slip $\frac{U_b - U_{ls}}{U_b}$	
$\mathbf{n}_b$	Interface unit normal vector	
N_f	Dimensionless Inverse Viscosity $\sqrt{\frac{\rho_\beta^2 g d^3}{\mu_\beta^2}}$	
$\mathbf{n}_g$	Unit vector in the direction of the gravity	
$\mathbf{n}_t$	Interface unit tangent vector	
p	Pressure	$\mathrm{N/m^2}$
$\tilde{p}$	Viscosity non-dimensionalised pressure $\frac{d\,p}{\mu U_b}$	
$\hat{p}$	Inertia non-dimensionalised pressure $\frac{p}{\rho U_b^2}$	
$\bar{p}$	Surface tension non-dimensionalised pressure $\frac{pd}{\gamma}$	
Pe	Bulk Peclet number $\frac{U_b d}{D}$	

Pe_s	Surface Peclet number $\frac{U_b d}{D_s}$	
q_{lf}	Film flow rate in moving reference frame	m^3/s
R	Universal gas constant	$\mathrm{J\,mol^{-1}\,K^{-1}}$
Re	Reynolds number $\frac{\rho U_b d}{\mu}$	
r_0	radial position of vortex centre	m
r_1	radial position of streamline separating vortex and film regions in slug	m
St_a	Adsorption Stanton number $\frac{k^a d}{U_b}$	
St_d	Desorption Stanton number $\frac{k^d d}{U_b}$	
T	Temperature	K
$\mathbf{u}$	Velocity field	$\mathrm{m/s}$
U_0	bubble rise velocity in stagnant liquid	$\mathrm{m/s}$
U_b	Bubble velocity	$\mathrm{m/s}$
U_{ls}	Average liquid velocity in slug	$\mathrm{m/s}$
We	Weber number $\frac{\rho U_b^2 d}{\gamma}$	
Greek symbols		
δ	Film thickness	m
ψ	Slip $\frac{U_{ls}}{U_b}$	
Γ	Surface concentrations	$\mathrm{kg/m^2}$
γ	Interfacial tension	$\mathrm{N/m}$
γ_0	Contaminant free interfacial tension	$\mathrm{N/m}$
μ	Viscosity	$\mathrm{N\,s\,m^{-2}}$
λ	Adsorption depth $\frac{\Gamma_{sat}}{c_0 d}$	
ρ	Density	$\mathrm{kg/m^3}$
θ	Equilibrium contact angle	
θ_A	Dynamic advancing contact angle	
θ_R	Dynamic receding contact angle	
Superscripts		
$\bar{x}$	Barred symbols are non-dimensionalised	
Subscripts		
α	Gas phase	
β	Liquid phase	
w	Wall property	
s	Interfacial property	
sat	Saturation	

3.1 Introduction

Taylor flow in microscale channels has appears in numerous applications such as flow of blood cells in blood vessels [52], foam flow in porous media for oil recovery operations [53], three-phase monolith reactors [54] and most recently, with increased miniturisation of unit operations in chemical engineering, microreactor devices [55]. Taylor flow is defined as the gas-liquid flow pattern where the liquid is segmented in slugs by elongated bubbles with size larger than the channel size that are only separated by a thin film from the channel wall. However, this definition neglects distinctions which are present within the flow for different flow rates, channel geometries and sizes. In this work only circular straight channels are considered. The prevailing flow fields in the liquid slugs, the shape and stability of the bubbles as well the stability of the flow structures[1], are presented in relation to characteristic dimensionless numbers.

3.2 Theory of Taylor bubbles

The fact that stable Taylor flow structure shows a movement of all bubbles at constant velocity U_b allows the simplification in its analysis by introducing a moving frame of reference moving with velocity U_b . Under such conditions the bubbles can be treated as stationary and all equations can be solved for steady state. Another common concept when analysing Taylor flow is that of a *unit cell.* A unit cell amounts to a single bubble and a single slug (see Fig. 3.1). When the unit cell repeats, Taylor flow is said to be periodic with the unit cell comprising a single period. The entire flow can then be analysed from the analysis of a single unit cell. The flow field and the bubble shape are considered to be the same in all identical unit cells.

A close problem to the movement of a single Taylor bubble in a tube is that of the semi infinite bubble (Fig. 3.2), which has practical importance in many applications: painting, printing, emulsion deposition in photographic industry and air displacement in wetted porous media [56]. The thickness of the deposited film left behind a gas bubble displacing the liquid at a fixed flow velocity is the important parameter to be determined from this problem. The undisturbed flow field at a sufficient distance from the cap of the semi infinite bubble has a parabolic profile. The front profile and film thickness of a sufficiently long Taylor bubble, with suffi-

[1] The stability of the structure refers to absence of bubble breakup and coalescence of adjacent Taylor bubbles.

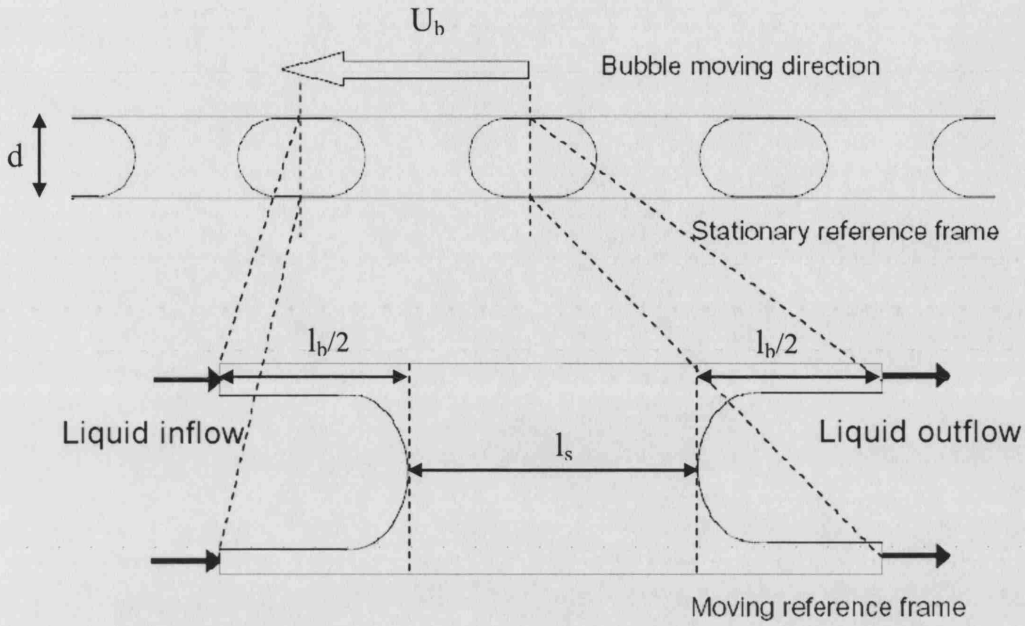

Fig. 3.1: A unit cell usually contains a bubble and a slug. When the flow is periodic the slug and bubble can also be taken as two half bubbles and a slug.

cient separation between the bubbles, can be approximated by that of a semi-infinite bubble.

3.2.1 Mass balance on semi-infinite bubble

In a cylindrical tube with the Taylor bubble front or a semi infinite bubble (Fig. 3.2), given a film thickness δ and bubble speed U_b the flow rate in the film q_{lf} can be calculated by simple mass balance to give:

$$q_{lf} = (U_b - U_{ls})\frac{\pi d^2}{4} \tag{3.1}$$

Where $U_{ls} = \frac{4(Q_\alpha + Q_\beta)}{\pi d^2}$ is the mean flow velocity in the liquid calculated from the two-phase flow rates. The difference in the speed between the bubble and the liquid slug is therefore dependent on the flow in the liquid film. The film would have a flow associated with the shearing action of the wall caused by its relative motion to the bubble. Other possible forces such as pressure or gravity, for non-horizontal tubes or thermal or surfactant induced surface tension gradients cause can also cause additional flow in the liquid film. In the absence of such gradients only pressure and gravity remain. If gravity and pressure are neglected (valid assumption when the

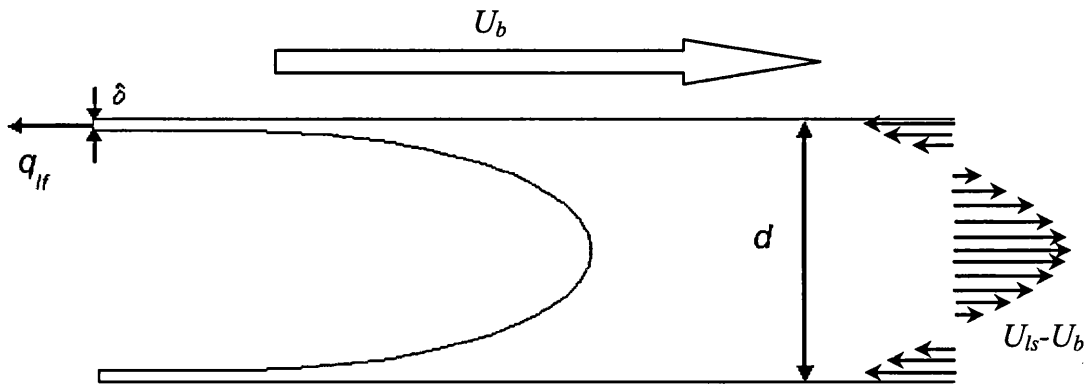

Fig. 3.2: Schematic of semi infinite bubble as seen from a frame moving with the bubble. U_{ls} is the average liquid slug velocity in a stationary frame.

film is very thin), the "no-slip" assumed at the wall, the relationship between bubble velocity and the film thickness is given by:

$$U_b = U_{ls}\frac{d^2}{(d-2\delta)^2} \tag{3.2}$$

The effect of slip would be to reduce the value of q_{lf} associated with wall shear and hence reduces the film thickness. Pressure and gravity induced flow in the film would increase the bubble velocity when it is counter to the bubble flow direction and decrease it when is in the same direction as bubble flow. In this simple analysis we have neglected any variation in the film thickness caused by the additional acting forces.

The treatment is identical for sufficiently long Taylor bubbles where the film develops into the constant thickness profile. The film thickness and therefore the bubble velocity cannot be determined without first investigating the hydrodynamics carefully.

A special case would arise if the flow conditions were such that a film does not develop, and a contact line exists instead. In such a case $U_b = U_{ls}$. Whether a film develops or not will be discussed in section 3.3.5.

3.2.2 Dimensional analysis of the hydrodynamics of a Taylor flow system

The general system of transient equations 2.2-2.13 can be non-dimensionalised for the case of a semi-infinite bubble moving in a liquid to obtain the important dimensionless numbers involved. The scaling dimensions are:

Velocity	U_b bubble terminal velocity
Length	d is the diameter
Time	d/U_b

The non-dimensional velocity $\bar{\mathbf{u}} = \frac{\mathbf{u}}{U_b}$ can then be used to rewrite equations 2.2 and 2.3 as:

$$\bar{\nabla} \cdot \bar{\mathbf{u}}_\alpha = 0 \tag{3.3}$$

$$\bar{\nabla} \cdot \bar{\mathbf{u}}_\beta = 0 \tag{3.4}$$

The time dependent term is removed from the system because in the bulk of the phases the density is constant. At the interface, the mass conservation equation 2.4 becomes:

$$\frac{\rho_\alpha}{\rho_\beta} (\bar{\mathbf{u}}_\alpha - \bar{\mathbf{u}}_b) \cdot \mathbf{n}_b + (\bar{\mathbf{u}}_\beta - \bar{\mathbf{u}}_b) \cdot \mathbf{n}_b = 0 \tag{3.5}$$

For no mass transfer across the interface, the dimensionless equivalent of equations 2.5 and 2.6 are:

$$(\bar{\mathbf{u}}_\beta - \bar{\mathbf{u}}_b) \cdot \mathbf{n}_\beta = 0 \tag{3.6}$$

$$(\bar{\mathbf{u}}_\beta - \bar{\mathbf{u}}_b) \cdot \mathbf{n}_\beta = 0 \tag{3.7}$$

There are three possible approaches for non-dimensionalising p:

Surface tension dominant	$p = \frac{\gamma}{d}\bar{p}$
Viscous stresses dominant	$p = \frac{\mu U_b}{d}\tilde{p}$
Inertia dominant	$p = \rho U_b^2 \hat{p}$

Converting between the three is straightforward by multiplying by the Capillary or the Weber numbers:

$$\bar{p} = \underbrace{\frac{\mu \mathbf{U_b}}{\gamma}}_{Ca} \tilde{p} = \underbrace{\frac{\rho U_b^2 d}{\gamma}}_{We=CaRe} \hat{p} \tag{3.8}$$

The base case for the non-dimensionalisation in small scales is the surface tension dominant pressure. The momentum equations can also be rewritten for phase α as:

$$\frac{\partial \bar{\mathbf{u}}_\alpha}{\partial \bar{t}} + \bar{\mathbf{u}}_\alpha \cdot \bar{\boldsymbol{\nabla}} \bar{\mathbf{u}}_\alpha = \frac{1}{Fr^2}\mathbf{n}_g + \left(- \left(\frac{\rho_\beta}{\rho_\alpha} \right) \frac{1}{We_\beta} \bar{\boldsymbol{\nabla}} \bar{p}_\alpha + \frac{1}{\mathrm{Re}_\alpha} \bar{\boldsymbol{\nabla}}^2 \bar{\mathbf{u}}_\alpha \right) \tag{3.9}$$

and for phase β as:

$$\frac{\partial \bar{\mathbf{u}}_\beta}{\partial \bar{t}} + \bar{\mathbf{u}}_\beta \cdot \bar{\boldsymbol{\nabla}} \bar{\mathbf{u}}_\beta = \frac{1}{Fr^2}\mathbf{n}_g + \left(- \frac{1}{We_\beta} \bar{\boldsymbol{\nabla}} \bar{p}_\beta + \frac{1}{\mathrm{Re}_\beta} \bar{\boldsymbol{\nabla}}^2 \bar{\mathbf{u}}_\beta \right) \tag{3.10}$$

At the interface between the two phases α and β:

$$\begin{aligned} 0 \;=\; & \left[\left(-\bar{p}_\alpha \mathbf{I} + \frac{We_\beta}{\mathrm{Re}_\alpha} \left(\frac{\rho_\alpha}{\rho_\beta} \right) \left[\bar{\boldsymbol{\nabla}} \bar{\mathbf{u}}_\alpha + \bar{\boldsymbol{\nabla}} \bar{\mathbf{u}}_\alpha^T \right] \right) \cdot \mathbf{n}_b - \left(-\bar{p}_\beta \mathbf{I} + Ca_\beta \left[\bar{\boldsymbol{\nabla}} \bar{\mathbf{u}}_\beta + \bar{\boldsymbol{\nabla}} \bar{\mathbf{u}}_\alpha^T \right] \right) \cdot \mathbf{n}_b \right] \\ & - \left[\bar{\boldsymbol{\nabla}} \left(\frac{\gamma}{\gamma_0} \right) - \left(\frac{\gamma}{\gamma_0} \right) \mathbf{n}_b \left(\bar{\boldsymbol{\nabla}} \cdot \mathbf{n}_b \right) \right] \end{aligned} \tag{3.11}$$

The normal component of equation 3.11 is:

$$\begin{aligned} 0 \;=\; & \left[\left(-\bar{p}_\alpha \mathbf{I} + \frac{We_\beta}{\mathrm{Re}_\alpha} \left(\frac{\rho_\alpha}{\rho_\beta} \right) \left[\bar{\boldsymbol{\nabla}} \bar{\mathbf{u}}_\alpha + \bar{\boldsymbol{\nabla}} \bar{\mathbf{u}}_\alpha^T \right] \right) \cdot \mathbf{n}_b \cdot \mathbf{n}_b - \left(\bar{p}_\beta \mathbf{I} + Ca_\beta \bar{\boldsymbol{\nabla}} \bar{\mathbf{u}}_\beta \right) \cdot \mathbf{n}_b \cdot \mathbf{n}_b \right] \\ & + \left(\frac{\gamma}{\gamma_0} \right) \left(\bar{\boldsymbol{\nabla}} \cdot \mathbf{n}_b \right) \end{aligned} \tag{3.12}$$

While the tangential component of equation 3.11 is:

$$\begin{aligned} 0 \;=\; & \left(\left[\left(\frac{We_\beta}{\mathrm{Re}_\alpha} \left(\frac{\rho_\alpha}{\rho_\beta} \right) \left[\bar{\boldsymbol{\nabla}} \bar{\mathbf{u}}_\alpha + \bar{\boldsymbol{\nabla}} \bar{\mathbf{u}}_\alpha^T \right] \right) - Ca_\beta \left[\bar{\boldsymbol{\nabla}} \bar{\mathbf{u}}_\beta + \bar{\boldsymbol{\nabla}} \bar{\mathbf{u}}_\alpha^T \right] \right] \cdot \mathbf{n}_b \right) \cdot \mathbf{n}_t \\ & + \bar{\boldsymbol{\nabla}} \left(\frac{\gamma}{\gamma_0} \right) \cdot \mathbf{n}_t \end{aligned} \tag{3.13}$$

when there are no surface tension gradients components equation 3.12 becomes:

$$\begin{aligned} 0 \;=\; & \left[\left(-\bar{p}_\alpha \mathbf{I} + \frac{We_\beta}{\mathrm{Re}_\alpha} \left(\frac{\rho_\alpha}{\rho_\beta} \right) \left[\bar{\boldsymbol{\nabla}} \bar{\mathbf{u}}_\alpha + \bar{\boldsymbol{\nabla}} \bar{\mathbf{u}}_\alpha^T \right] \right) \cdot \mathbf{n}_b \cdot \mathbf{n}_b - \left(\bar{p}_\beta \mathbf{I} + Ca_\beta \bar{\boldsymbol{\nabla}} \bar{\mathbf{u}}_\beta \right) \cdot \mathbf{n}_b \cdot \mathbf{n}_b \right] \\ & + \left(\bar{\boldsymbol{\nabla}} \cdot \mathbf{n}_b \right) \end{aligned}$$

The independent dimensionless groups that appear from the governing differential equations are listed in Table 3.1. The range of the parameters of interest is given in Appendix A. Interestingly, because of the $\frac{We_\beta}{\mathrm{Re}_\alpha} \left(\frac{\rho_\alpha}{\rho_\beta} \right) = \frac{\mathrm{Re}_\beta Ca_\beta}{\mathrm{Re}_\alpha} \left(\frac{\rho_\alpha}{\rho_\beta} \right)$ scaling factor

1. $\frac{\rho_\alpha}{\rho_\beta}$	2. $\frac{\rho_\alpha U_b d}{\mu_\alpha} = \mathrm{Re}_\alpha$
3. $\frac{\rho_\beta U_b d}{\mu_\beta} = \mathrm{Re}_\beta$	4. $\frac{\mu_\beta U_b}{\gamma} = Ca_\beta$
5. $\frac{U_b}{\sqrt{gd}} = Fr$	6. $L_s = \frac{l_s}{d}$
7. $L_b = \frac{l_b}{d}$	

Tab. 3.1: Dimensionless groups governing Taylor flow

of the phase α shear stresses in equations 3.12 and 3.13, these terms can in general be neglected giving equations 3.14 and 3.15 respectively:

$$0 = \left(\left(\bar{p}_\alpha - \bar{p}_\beta\right)\mathbf{I} + Ca_\beta\left[\bar{\nabla}\bar{\mathbf{u}}_\alpha + \bar{\nabla}\bar{\mathbf{u}}_\alpha^T\right]\right)\cdot\mathbf{n}_b\cdot\mathbf{n}_b + \left(\frac{\gamma}{\gamma_0}\right)\mathbf{n}_b\left(\bar{\nabla}\cdot\mathbf{n}_b\right)\cdot\mathbf{n}_b \tag{3.14}$$

$$0 = -Ca_\beta\left[\bar{\nabla}\bar{\mathbf{u}}_\alpha + \bar{\nabla}\bar{\mathbf{u}}_\alpha^T\right]\cdot\mathbf{n}_b\cdot\mathbf{n}_t - \bar{\nabla}\left(\frac{\gamma}{\gamma_0}\right)\cdot\mathbf{n}_t \tag{3.15}$$

Other non-dimensional variables arise when considering and entire Taylor bubbles and liquid slugs such as the dimensionless bubble and slug lengths (Table 3.1).

3.3 Theoretical and experimental investigation of Taylor flow

3.3.1 Bubble rise in a stagnant liquid

Early analyses of Taylor flow focussed on the study of a single gas bubble rising through a stagnant liquid. Researchers attempted to describe the bubble behaviour by identifying forces that may be either dominant or unimportant under particular conditions. White [57], Wallis [58] and later Fabre and Liné [59] determined experimentally these different regimes for vertical circular tubes. The dimensionless groups used were the Bo, N_f, Mo and Fr numbers, see Table 3.2. The terms in Table 3.2 are a recombination of the Re, the Fr and the Ca numbers obtained in Table 3.1 such that the bubble velocity only appears in the Fr term. Fr is then correlated to the different dimensionless numbers [57, 59]. The regimes of force dominance are given in Table 3.3.

With different tube inclination, including horizontal tubes, there are different bubble terminal velocities U_0. For a horizontal tube, this terminal velocity corresponds to that of a semi-infinite air bubble displacing the liquid in an emptying tube

Bond Number	$Bo = \frac{\rho_\beta g d^2}{\gamma} = \frac{Ca_\beta Re_\beta}{Fr^2}$	Buoyancy to surface tension force ratio
Morton Number	$Mo = \frac{g\mu_\beta^4}{\rho\gamma^3} = \frac{Ca_\beta^3}{Re_\beta Fr^2}$	
Dimensionless Inverse Viscosity	$N_f = \sqrt{\frac{\rho_\beta^2 g d^3}{\mu_\beta^2}}$	Buoyancy to viscous forces ratio

Tab. 3.2: Alternative dimensionless numbers used to characterise rising bubbles in stagnant liquid

Inertia Dominant	$N_f > 300$ $N_f > 300$	$Bo > 100$ $Bo > 100$	$Fr = 0.345$ $Fr = 0.351$	[58] [59]
Inertia Negligible			$Fr < 0.05$	[57]
Viscosity dominant	$N_f < 2$	$Bo > 100$	$Fr = 0.01 N_f$	[58]
Surface Tension Dominant	$N_f^2 = 6.2/Mo^2$	$Bo = 3.37$		[40]
Surface Tension Negligible		$Bo > 70$		[57]

Tab. 3.3: 2 A summary of predominant forces for a single bubble rising through a vertical circular pipe in stagnant liquid.

[60]. The terminal velocity is a maximum at an inclination [61].

Increased surface tension results in the reduction of the bubble velocity [57]. When surface tension becomes dominant, the continuity of the liquid phase is disrupted, i.e. there is no liquid film around the bubble, and the bubble does not move at all in a circular tube. This happens for $Bo = 3.37$ as derived by Bretherton [40]. Most practical microscale applications would be with $Bo < 3.37$ (see the example in section 2.4) and hence the bubble would not move spontaneously. In polygonal tubes however, investigations by Bi and Zhao [62] suggest that the bubbles always rise because liquid always occupies the corners of the polygons, a phenomenon known as the Gregorig effect.

3.3.2 Bubble movement in a flowing liquid

When the liquid flows as well, the drift-flux model of Wallis [58] is used to correlate the bubble velocity, U_b, to the liquid slug average velocity, U_{ls}, and a bubble rise velocity in stagnant liquid, U_0:

$$U_b = \psi U_{ls} + U_0 \tag{3.16}$$

where ψ is an experimentally determined coefficient. The values and meanings of the terms ψ and U_0 for large tubes vary with the inclination of the pipe [69]. In a

m	Range	Method	Reference
$1.0Ca^{\frac{1}{2}}$	$7.5 \times 10^{-5} \leq Ca \leq 0.014$	Conductimetry	[63]
0.58	$Ca \rightarrow \infty$	Conductimetry	[63]
0.6	$Ca \rightarrow \infty$	Theory	[64]
$1.29(3Ca)^{\frac{2}{3}} \pm 5\%$	$Ca < 0.003$	Volumetry	[40]
$1.29(3Ca)^{\frac{2}{3}} \pm 10\%$	$Ca < 0.0005$	Volumetry	[40]

Tab. 3.4: Correlations of m in literature

δ	Range	Method	Reference
$0.25Ca'^{\frac{1}{2}}$	$5 \times 10^{-5} \leq Ca' \leq 3 \times 10^{-4}$	Conductimetry	[65]
$\left[0.445 - 0.025/U_g^{\frac{1}{2}}\right] Ca'^{\frac{1}{2}}$ (U_g is in cm/s)	$7 \times 10^{-6} \leq Ca' \leq 2 \times 10^{-4}$	Conductimetry	[66]
$\frac{1.34}{2}Ca^{2/3}$	$10^{-3} \leq Ca \leq 10^{-2}$	Volumetry	[40]
$0.18\left[1 - e^{\left(-3.08(Ca'^{0.54})\right)}\right]$	$10^{-3} \leq Ca' \leq 1.9$	Colourimetry	[67]
$\frac{\frac{1}{2}\left(1.34Ca^{2/3}\right)}{1+2.5\left(1.34Ca^{2/3}\right)}$	$10^{-3} \leq Ca \leq 1.4$	Volumetry	[68]

Tab. 3.5: Correlations of film thickness in literature. For convenience, Ca' is defined using the average slug velocity

vertical tube the bubble drift velocity is taken equal to the bubble rising (terminal) velocity in stagnant liquid. For small capillaries, the bubble rise velocity is usually very small or zero because of the surface tension effects, and usually negligible in comparison with the liquid slug velocity contribution. This reduces equation 3.16 to:

$$\frac{U_b}{U_{ls}} = \psi \tag{3.17}$$

A further term m can be defined from 3.17:

$$m = 1 - \frac{1}{\psi} \tag{3.18}$$

Experimental investigations of Taylor flow either give results in terms of m (Table 3.4), or film thickness $\bar{\delta}$ (Table 3.5). Interestingly, all these correlations feature only Ca or Ca'.

Bretherton [40] in his classic paper on Taylor flow, assumed creeping flow in the bulk, lubrication in the film and inviscid Taylor bubble with spherical caps in a moving coordinate system. The Taylor bubble was divided into five distinct regions, the two bubble cap, a film of constant thickness δ in the middle and two transition regions connecting the two caps to the film. Using perturbation theory

Bretherton calculated the bubble profile for the front transition region by matching the static film to the spherical front caps and the static film thickness δ. The shape of the bubble at the transition region in the back showed undulations which (within the range the perturbation method) were found to become more prominent with increasing film thickness. The film thickness was found to correlate to $Ca_\beta^{2/3}$ and to depend on the analysis of the front of the bubble alone (thus the link between the semi infinite and Taylor bubbles). The pressure required to push the bubble was also found to correlate with $Ca_\beta^{2/3}$. The results are supposed to be valid for small Ca_β. It was noted however, that experimental results agreed better with the theory at the range for $Ca \sim 10^{-3}$ than at the asymptotic limit as $Ca \to 0$, where the theory should exactly hold. No explanation was given as to the reason of the deviation. The theoretical equation obtained and the observed error margins are listed in Table 3.4.

Extension and theoretical validations of Bretherton's theory was done by either numerical methods or using other asymptotic expansions to including other forces:

For the creeping flow limit, Reinelt and Saffman [70] developed a finite difference method for obtaining the shape and film thickness of a semi-infinite bubble at $10^{-4} \leq Ca \leq 0.1$. Shen and Udell [71] used a deformable grid and a finite element method to obtain the shape of the bubbles and film thickness in semi-infinite bubbles. The Stokes equations and the bubble shape equations were solved sequentially and iteratively until the final shape and flow field were obtained. The maximum Ca_β considered was $Ca_\beta = 0.2$. Lu and Chang [72] used a boundary integral method for $10^{-4} \leq Ca_\beta \leq 1$. The method of Shen and Udell for calculating the bubble profile was extended by Martinez and Udell [73] using a boundary element method for both the front and back of the bubble separately (two semi-infinite bubble analyses). They reported film thickness and pressure drop values at $10^{-2} \leq Ca_\beta \leq 10$ for the leading bubble end and $10^{-2} \leq Ca_\beta \leq 1.5$ for the back end. Westborg and Hassager [74] simultaneously solved for the profile of the complete Taylor bubble and flow field using a finite element method for $10^{-2} \leq Ca_\beta \leq 1$. All above numerical solutions agreed with the theory of Bretherton for low Ca_β, deviating from Bretherton's solution at around $Ca > 10^{-1}$ while agreeing with the correlation of Fairbrother and Stubbs [63] for higher Ca_β. For $Ca > 10^{-1}$ the caps of the bubble can no longer be regarded as spherical [74] and one of the assumptions in Bretherton's analysis is no longer valid.

Ratulowski and Chang [75] calculated the film thickness and pressure drop for isolated bubbles and bubble trains using an arclength-angle formulation of a com-

posite lubrication equation which allowed the extension of Bretherton's analysis for circular capillaries to higher capillary numbers. Finite bubble are shown to resemble infinitely long bubbles in film thickness and pressure drop if their lengths exceed the channel width.

Edvinsson and Irandoust [76] were the first to solve for the entire bubble shape and flow field simultaneously, including the inertia terms in the calculations . A transient finite element analysis of a complete Taylor bubble was used to obtain bubble velocity, shape and the film thickness for $0.001 \leq Ca_\beta \leq 0.06$ and $500 \leq Re_\beta \leq 2000$. From their analysis of the film undulations, the limit at which the lubrication theory fails was estimated to be $Ca_\beta = 0.005$. The dependence of the film thickness had so far been mainly correlated to Ca_β, however, in their numerical simulations Edvinsson and Irandoust [76] showed the dependence of the film thickness on Fr and Re as well. For a co-current upward flow it was found that film thickness and bubble velocity increased with decreasing Fr. This trend reversed for co-current downward flow. The effect of Fr decreased with decreasing Ca_β to become negligible for $Ca_\beta < 10^{-3}$. Increasing Re causes an increase in the wave length at the rear of the bubble. They also reported qualitatively a slight thickening of the liquid film. Interestingly, for some short bubbles they observe a lack of existence of a constant liquid film for the higher Re. The longest bubbles length simulated were eight diameters. They reported that the length of bubble had little or no effect on m as long as the length of the bubble was sufficiently long to reach a constant film thickness.

Giavedoni and Saita in two works analysed separately the front of a Taylor bubble (the semi infinite problem)[77] and its back [78]. For the front the range of Ca_β was $(10^{-5} < Ca_\beta < 10)$ while for Re_β it was $Re_\beta < 70$. They obtained the limiting $m = 0.6$ at $Ca_\beta = 10$ confirming the result of Cox [82]. The final film thickness becomes 0.361. For $Re_\beta = 0$ the study of the trailing bubble cap shows the undulation in the meniscus to disappear for $Ca_\beta \geq 0.5$. The continuous increase in Ca_β also leads to an increase in concavity of the rear cap of the bubble which becomes flat for $Ca_\beta \cong 0.75$ and changes from convex to a concave shape for $Ca_\beta \cong 1 - 1.8$. They limit their studies to $Ca_\beta \leq 8$ based on the observations of Olbricht and Kung [79] that bubble break up would occur at the back for $Ca_\beta > 8$. They note that any numerical solution beyond this Ca_β might be unstable. Analysis of the caps show that they are very close to hemispherical for $Ca_\beta < 0.01$ but the transition region between the constant film and the back cap contained undulations. The authors attribute the presence of these undulations to the pressure jump associated with

the expanding channel encountered by the liquid in the film as it enters the slug and which has to be be balanced by a change of surface curvature. As $Ca_\beta \rightarrow 0$ the pressure jump is likely to be small as compared to that associated with the cap curvature and the undulations tend to diminish in amplitude.

The inertial investigations of Giavedoni and Saita are limited to $Re_\beta < 70$ on the erroneous assumptions that higher values are not feasible in practice, see Appendix A. The influence of increasing Re_β on film thickness was reported to be slight but non-monotonic, where an initially small decrease was followed by an increase. The Ca for the transition to the concave cap shape decreases with increasing Re_β. The authors also reported the undulation to have increased amplitude and frequency in the tail transition region with increasing Re. For $Ca \leq 10^{-3}$ the influence of Re on the bubble shape diminished.

Heil [80] extended the range of Re_β studied to $Re_\beta < 280$ for the front cap and observed a continuing trend of increasing film thickness with increasing Re_β after $Re_\beta = 70$.

Aussillous and Quéré [68] studied the film thickness deposited by a semi-infinite bubble. Using scaling arguments they divided Taylor flow into three different limiting regimes. For the first, the visco-capillary regime, where the viscous and capillary forces are comparable, they fitted the results of Taylor [81] and their own experimental results using viscous liquids to a correlation which reduces to the form of Bretherton's equation with decreasing Ca, (Table 3.5). The second region is the visco-inertial regime, for non-viscous liquids and higher speed than the visco-capillary regime where the inertia becomes important and causes deviations from the proposed correlations for $Ca_\beta > 0.003$. An interesting finding for this regime is that the deviation increases with increasing tube diameter. The third regime is the viscous boundary layer regime which occurs at high velocities where surface tension forces become relatively negligible. The film thickness is then limited by the thickness of the developed viscous boundary layer.

de Ryck [56] extended Bretherton's theory to include weak inertial effects by a regular perturbation method and found good agreement with the results of Taylor [81] and Aussillous and Quéré [68] for moderate Reynolds numbers ($Re_\beta < 1000$).

Comparing the ranges of parameters in Appendix A that are going to be investigated in this work and the results outlined above, it can be concluded that the geometry of bubbles that will be encountered is likely to have spherical caps and a static film. The effect of having Re_β (up to $Re = 35$) on any calculated film thickness should be small and the bubble geometry is unlikely to significantly deviate

from spherical caps, the length of the transition regions between the static film and the caps are likely to be short so that the bubble shape should not deviate much from that of a cylinder with spherical caps.

The work of Edvinsson and Irandoust [76] was repeated (Appendix B) to quantify the effect on the bubble velocity and film development of a short bubble length. Two bubbles of length $L_b = 1.1$ and $L_b = 8$ were considered. For the range of parameters given in Appendix A, the bubble length was seen to have little effect on the bubble velocity for $Ca < 10^{-3}$ and the Re values considered. The shorter bubble length, however, was found to have the velocity increased by 5% at $Ca = 10^{-2}$ for a $Re = 306$.

The effect is expected to increase for larger Ca and Re and may play a role in instabilities of a non periodic flow structure if the different bubbles formed include some of lengths that do not allow a constant film to form.

3.3.3 Flow patterns in the liquid slug

Taylor [81] gave qualitative sketches of three possible streamline patterns in the liquid slugs ahead of the gas bubble (Fig. 3.3). At high Ca_β, for $m > 0.5$, a complete bypass flow pattern was envisaged (Fig. 3.3(a)). With decreasing Ca_β, $m < 0.5$, two possible patterns were sketched, one featuring a stagnation ring around the bubble cap and a single stagnation point at the bubble cap tip (Fig. 3.3(b)). The second showed a stagnation point inside the liquid slug and another at the bubble tip (Fig. 3.3(c)).

Cox [64] showed experimentally the existence of patterns (a) and (b). The numerical analysis of Martinez and Udell [73] and Westborg and Hassager [74] also reveal the two flow fields (a) and (b). Martinez and Udell found $Ca_\beta = 0.7$ corresponds to $m = 0.5$. Edvinsson and Irandoust [76] only report pattern (b) because of the small values of Ca_β they studied.

In their numerical study of the front meniscus of the bubble Giavedoni and Saita [77] observed the three patterns (a)-(c) confirming Taylor's speculations. For $Re_\beta = 0$ and at high Ca_β they noted only a single stagnation point at the bubble tip (pattern (a)). As Ca_β is reduced, there is a transition where vortices started to appear at $Ca_\beta = 0.69$ as described by pattern (c). The point where the stagnation ring develops was identified at $Ca_\beta = 0.60$ so that pattern (c) was observed only in a narrow range $0.6 < Ca_\beta < 0.69$. This limited range may therefore explain why it hadn't previously been observed experimentally. At the back of the Taylor bubble, with increasing Ca_β the contracting stagnation streamlines enclosing the

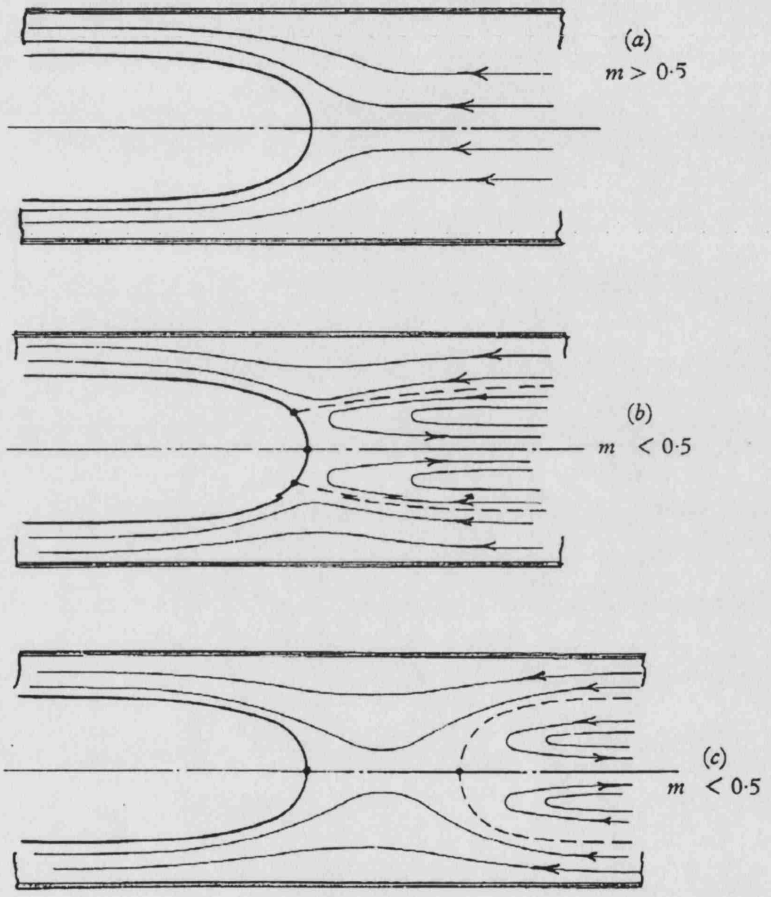

Fig. 3.3: Patterns of streamlines in front of long bubbles for a frame of reference moving with the bubble [81]. The quantity m is defined as $\frac{U_b - U_{ls}}{U_b}$.

vortex break into different regions at $0.6 < Ca_\beta < 0.69$, a wake and recirculating flow separated by a stagnation point (Fig. 3.4) [78]. Heil [80] reported variation of the flow field ahead of the bubble cap with $Re_\beta \neq 0$. The streamlines of pattern (b), drawn open away from the bubble cap in Fig. 3.3(b), change to form a closed vortex at around $Re_\beta = 20$ for $Ca_\beta = 0.05$. The size of the closed vortex increases with increasing Re_β. Heil suggested a "cat's eye" pattern of vortices which decay rapidly with distance from the bubble tip (Fig. 3.5).

Thulasidas et al. [83] using particle image velocimetry (PIV) studied the flow patterns between two Taylor bubbles for ($10^{-4} \leq Ca_\beta < 0.8$ and $10^{-4} < Re_\beta < 2$). They report pattern (a) for $Ca_\beta > 0.47$ and (b) for $Ca_\beta \leq 0.15$. With pattern (b) a single toroidal vortex was seen throughout the liquid slug. The value of Ca_β at which pattern (b) is observed disagrees with the findings by Giavedoni and Saita [77] which would suggest pattern (b) for the whole range studied by Thulasidas et al.. For $L_s > 1.5$ they observed straight parallel streamlines indicating the flow had become a Poiseuille flow while for $L_s < 1$ this was not the case. For parabolic flow, they calculated the centre of the toroidal vortex $\bar{r}^0$ and the radial position of the stagnation streamline $\bar{r}^1$. Pattern (a) would be observed when $\psi = 2$ (equation 3.17) corresponding to $m = 0.5$.

$$\bar{r}^0 = \frac{\sqrt{2-\psi}}{2\sqrt{2}} \tag{3.19}$$

$$\bar{r}^1 = \frac{\sqrt{2-\psi}}{2} \tag{3.20}$$

Thulasidas et al. [83] did not report any similar patterns to those of Heil [80] probably because of the small range of Re_β examined. It is also possible that the interactions of the flow fields of the enclosing caps cause a change to the experimentally observed fields as compared to the semi-infinite analysis. The effects of contaminants are also possible.

Comparing the ranges of parameters in Appendix A of the current work, and the results outlined above, it can be concluded that the flow patterns likely to be encountered in all these cases are of the form of pattern (b) with possibly some effects of inertia Re_β ($Re_\beta = 35$) on the flow field in the slug.

3.3.4 Presence and effect of surface active agents

The discrepancies found between Bretherton's theory and experimental results especially at the lower limit of Ca where it was supposed to be most valid has been

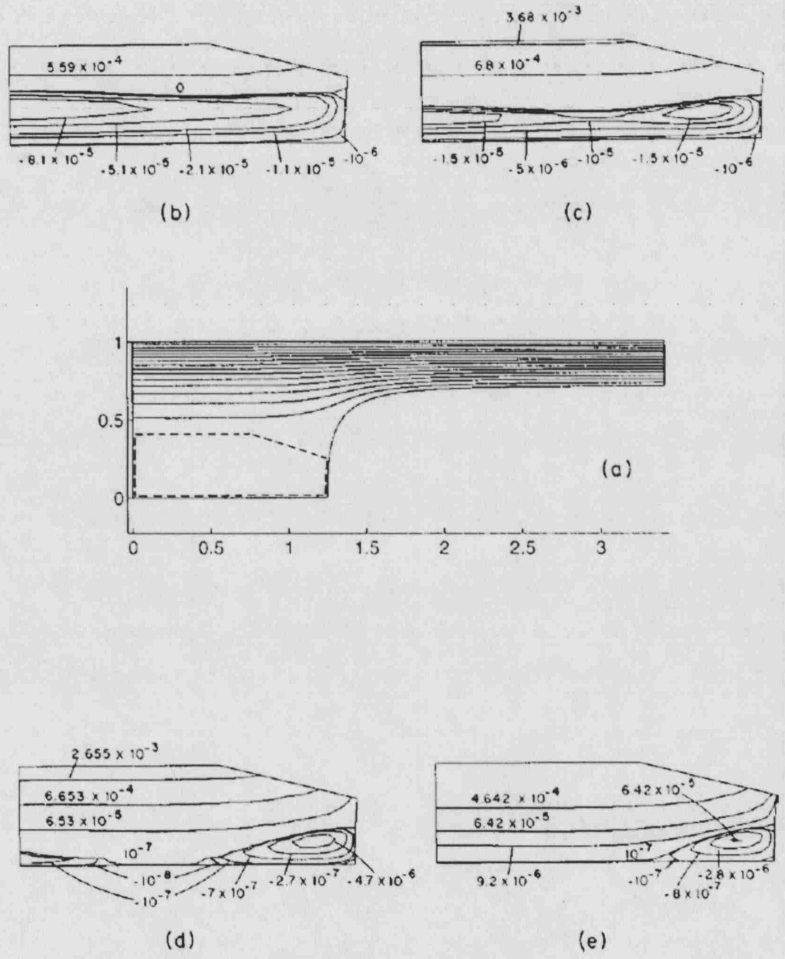

Fig. 3.4: Streamlines pertaining to both external and internal flow regions for a frame of reference moving with the bubble. (i) External flow region; (a) $Ca = 0.65$, $Re = 0$. (ii) Internal flow region; (b) $Ca = 0.60$, $Re = 0$; (c) $Ca = 0.65$, $Re = 0$; (d) $Ca = 0.685$, $Re = 0$; (e) $Ca = 0.70$, $Re = 0$. Diagram from Giavadoni and Saita [78].

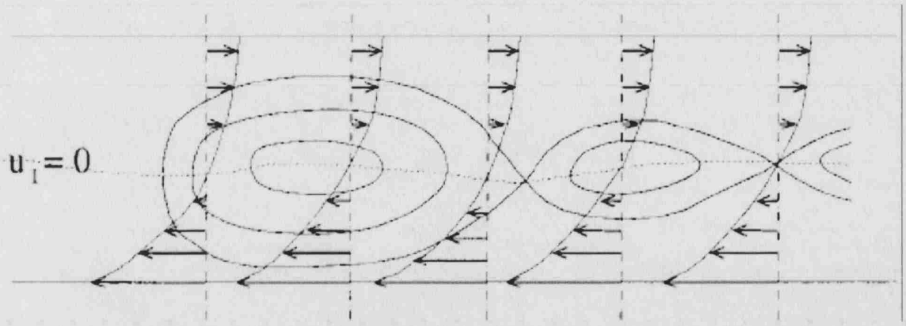

Fig. 3.5: A sketch of the "cat's eye" pattern of vortices ahead of the bubble tip. The dotted line indicates the line along which u_1, the axial component of the velocity field $\mathbf{u}$ is zero and connects the stagnation points between the vortices. Diagram from Heil [80].

attributed by various researchers to the impurities adsorbed on the gas-liquid interface that might act as surface active agents [40, 84, 65]. To correctly assess the surfactant effects on hydrodynamics, their distribution and associated local surface tension at the interface needs to be computed. The additional equations 2.17, 2.18 and 2.20 as well as first order expressions for the rates of adsorption and desorption make the problem very complex to solve. A number of dimensionless numbers arising from non-dimensionalisation of the Marangoni equations are given in Table 3.6. Unfortunately, these numbers cannot be determined experimentally for trace amounts of (usually unknown) contaminants. However, the sensitivity of film thickness, pressure drop across the bubble and the field ahead of the bubble to these parameters can be determined. It is difficult to document the interplays of the many different parameters, so only the effects associated with the film thickness and the flow field which would occur for low surfactant concentration and at low Ca that are relevant to this work will be noted here.

Ginley and Radke [85] assumed that the concentration of a contaminant in the liquid phase was uniform, and that the adsorption/desorption process controlled the local concentrations on the interface. Under these conditions, they obtained a thinner film compared to the surfactant free case.

Ratulowski and Chang [86] applied an asymptotic analysis to both the hydrodynamics and the mass transport valid for $Ca \to 0$ and for very low concentrations of surfactant. They constructed a model where the diffusive-adsorption model are important. For very low bubble velocities the film thickness increases by a maximum factor of $4^{2/3}$ compared to the surfactant free case when the surfactant transport in the film is limited by mass transfer from the bulk phase ahead of the bubble. Park

Bulk Peclet number	$Pe = \frac{U_b d}{D_\beta}$	Relates convection to bulk diffusion rates
Surface Peclet number	$Pe_s = \frac{U_b d}{D_s}$	Relates convection to surface diffusion rates
Elasticity number	$El = \frac{RT\Gamma_{sat}}{\gamma_0}$	Ability of surfactant to modify the surface tension
Adsorption Stanton number	$St_a = \frac{k^a d}{U_b}$	Relates adsorption to surface convection rates
Desorption Stanton number	$St_d = \frac{k^d d}{U_b}$	Relates desorption to surface convection rates
Adsorption depth	$\lambda = \frac{\Gamma_{sat}}{c_0 d}$	Depth of fluid required to bring Γ to Γ_{sat}

Tab. 3.6: Additional Dimensionless groups appearing from the equation modelling the Marangoni effects

[87] found that the increase was dependent on having a bubble larger than a critical length in agreement with the experimental findings of Schwartz et al.[84].

Stebe and Barthès-Biesel [88] carried out another asymptotic analysis of the problem valid when the concentration of surfactant in the liquid phase is very large such that adsorption and desorption govern the local concentration for $Ca_\beta \rightarrow 0$. Their film values were in between those predicted by Ratulowski and Chang and those obtained from the analysis of Bretherton.

Gadiali and Gaver [25] using a finite element method for $0.015 \leq Ca \leq 10$ numerically investigated how a soluble surfactant influences the fluid dynamics in a viscous liquid. Their equations take into account the non-linear effects of high surfactant concentrations. Severino et. al. [27] performed a similar numerical analysis on the 2D version of Taylor flow for $10^{-4} \leq Ca \leq 1$. Both works reported increased film thickness resulting from the surfactants. The *relative* magnitude of change compared to the surfactant free case was largest for small Ca because the films are smallest in that region, while the effect increases with increasing surfactant concentration. Qualitatively, surface tension gradients increase with increasing convection and decrease with phenomena which counter surfactant concentration gradients such as increased Pe_s and decrease in the adsorption/ increase in desorption rates. Pe affects the rate of transfer between the bulk and surface and as such can make the adsorption/desorption rates more or less effective. For a given El, the magnitude of the film thickness change depends on Ca, however, Severino et. al. reported a value of Ca below which the change in film thickness no longer changes. On the other hand, the system becomes insensitive to El at large Ca.

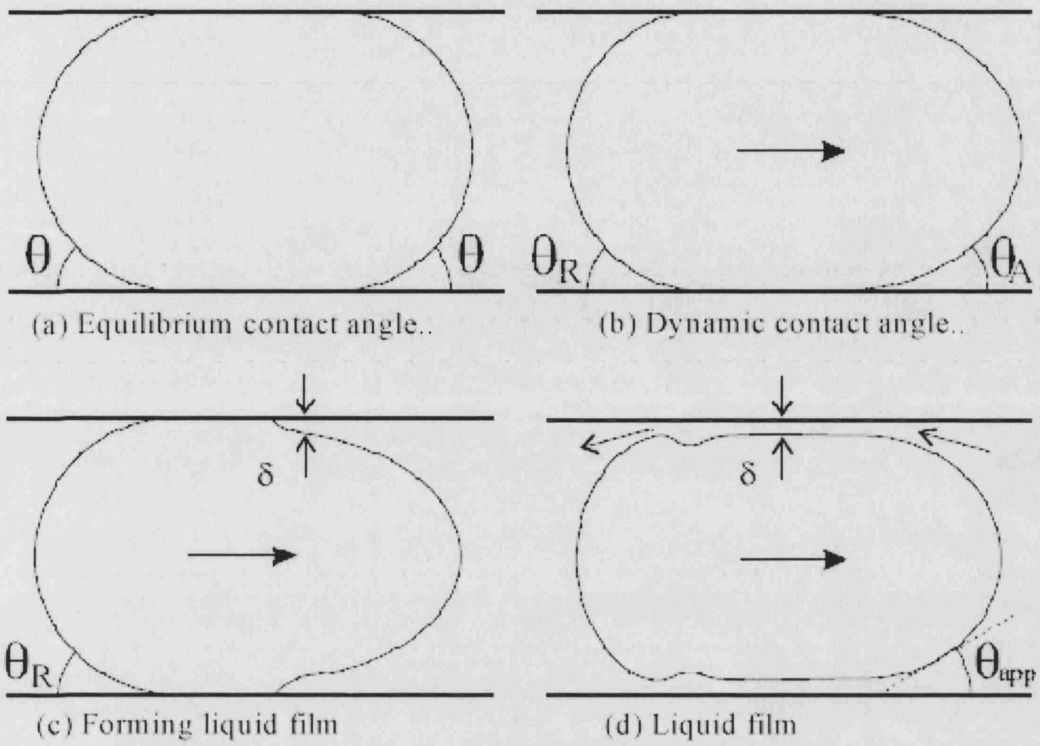

Fig. 3.6: Schematic progress in the wetting behaviour of bubbles at increasing capillary numbers [90].

Extrapolating the results from the plane case to that of the tube, the flow field for low Ca and low El does not differ significantly from the case of the surfactant free system. The surfactants are concentrated towards the tip of the bubble cap by the convection. Increasing El first causes the stagnation ring to narrow towards the symmetry line and eventually to coincide with the stagnation point on the symmetry line [27]. This causes the velocity along the bubble interface to become unidirectional from the tip to the film so that all the surfactant will be convected towards the film. Further increases in El cause the stagnation point to move along the symmetry line away from the bubble. With increasing El the surface of the bubble behaves like the surface of a rigid body, and a region of low velocity is present. The vortex is pushed away from the surface into the core.

3.3.5 *Existence of a film surrounding the Taylor bubbles*

A static bubble in a capillary will have a finite non-zero equilibrium contact angle θ with the wall and no film will be present. If the bubble moves with sufficiently low speed, then the bubbles will form an advancing and a receding dynamic contact

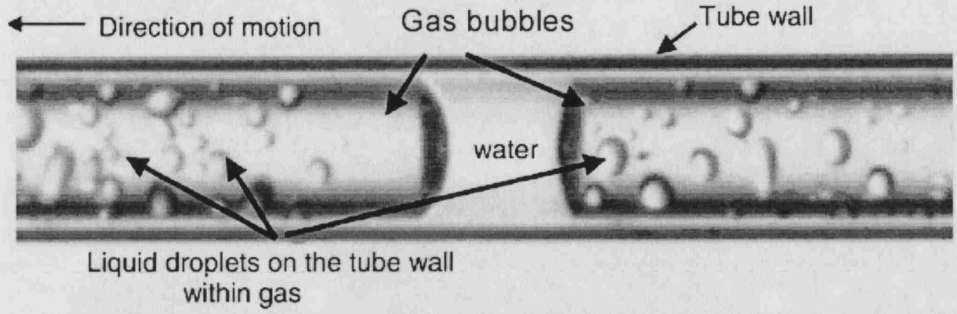

Fig. 3.7: Presence of droplets in steam-water flow through a 100 μm quartz capillary on the walls in the gas bubble was taken as evidence for the lack of liquid film [91].

angles θ_A and θ_B at the front and back respectively with the wall (Fig. 3.6). With increased speed, the viscous forces start to become important and a liquid film starts to form. Further increase in speed will create a wetting liquid film around the bubble. In this last configuration there will still be an apparent contact angle θ_{app} as the film is generally very thin. The overwhelming experimental evidence suggests the presence of a liquid film. Most of these results have come from studies with wetting liquids in tubes of size $0.5 - 3$ mm (Table 3.4 and 3.5). The difference between the bubble and average slug speed is necessarily by the presence of the film. Geng et. al.[89] identified from the oscillatory movement of the Taylor bubble caps in 1 mm glass tubes (typical when a contact lines is present) the absence of a liquid film. This movement may have resulted from oscillatory flow that was studied, or may be a transitory stage before the liquid film develops. Serizawa et. al. [91] report cases for 100 μm quartz tubes where the film does not seem to appear (Fig. 3.7). Although, to the author's knowledge no other sources report lack of film in Taylor flow, there are however numerous works, in the context of coating films, on the stability of liquid films and mechanisms of its instability. Schultze et al. [92] experimentally identified two mechanisms that destabilised liquid films, one based on growing fluctuation waves favoured with wetting surfaces, and the second based on nucleation inside the film favoured when non wetting surfaces are present. They suggest a critical film thickness δ_{crit} and a film lifetime which depend on the nature of the interactions between the liquid and the wall and the homogeneity of the solid surface. It's not unlikely that with decreasing tube size a film thickness is reached which is smaller than δ_{crit} when the film ruptures. The order of δ_{crit} reported was ~ 50 nm).

4. ON TAYLOR BUBBLE FORMATION AND ITS MODELLING

Nomenclature

d	Tube diameter	m
D	Cubic equation determinant	
d_{B0}	Diameter of spherical bubble remaining at nozzle after breakup	m
d_n	Nozzle diameter	m
l	Axial length from the wall contact point to nozzle	m
L	Length of liquid separating formed and forming bubbles	m
L_0	Length of liquid separating formed and forming bubbles at breakup	m
p	Pressure	$\mathrm{N/m^2}$
Q	Volumetric flow rate	$\mathrm{m^3/s}$
r	Radial coordinate	m
S	Arclength	m
t_s	Time for a spherical bubble to form and touch the walls	s
t_t	Time for a Taylor bubble to form and break from a spherical bubble	s
T	Total time for bubble formation	s
u	Average cross sectional velocity	m/s
u_0	Gas velocity at the inlet	m/s
U	Superficial velocity	m/s
V_s	Volume of spherical bubble touching the walls	$\mathrm{m^3/s}$
V_i	Volume of liquid behind spherical bubble when it first touching the walls	$\mathrm{m^3/s}$

$V_{\max}$	Maximum volume of liquid behind a Taylor bubble before it breaks	m^3/s
We_g	Weber number $\frac{\rho_g u_{g0}^2 d}{\gamma}$	
z	Axial coordinate	m
Greek symbols		
α	Angle with horizontal the tangent to the meniscus makes	
γ	Interfacial tension	N/m
λ	Arclength from wall contact point to nozzle	m
ρ	Density	kg/m^3
θ	Apparent or real contact angle of a formed bubble	
θ_1	Apparent or real contact angle of a forming bubble	
Subscripts		
g	Gas phase	
gs	Gas superficial	
l	Liquid phase	
ls	Liquid superficial	

4.1 Introduction

Taylor flow is one of the dominant two-phase flow patterns in channels with dimensions in the micron region. It consists of elongated bubbles with equivalent diameter usually many times that of the channel diameter, separated by liquid slugs. The bubbles adopt a characteristic capsular shape. They completely fill the channel cross section and only a thin liquid film separates them from the channel wall. Because of the presence of bubbles in front and at the back of the slugs, the flow field in the liquid is modified compared to single-phase flow and toroidal vortices are formed [93]. As a result Taylor flow offers many advantages as compared to single-phase laminar flow[94]. In particular:

1. The separation of the bulk liquid with the bubbles significantly reduces axial mixing in the liquid [95, 96]. The film surrounding the bubbles is the only means of communication between two successive slugs and in the majority of cases its thickness is only a fraction of a percentage of the tube diameter.

2. The recirculation within the liquid slugs improves heat and mass transfer from liquid to wall and interfacial mass transfer from gas to liquid [97].

With intensifying research on miniaturisation of chemical engineering unit operations, it becomes important to investigate how the benefits of Taylor flow combine with the advantages offered by operating in microchannels.

It has been found that during Taylor flow, gas-liquid and axial mass transfer is strongly correlated to the liquid slug length [95, 97]. In addition, pressure drop is also dependent on the number of bubbles in the channel as well as on the length of wall perimeter wetted by the liquid slugs [98]. It is important therefore to be able to predict bubble and slug lengths under different fluid properties, channel design and operational parameters. Although the bubble to slug length ratio can be found from the inlet gas and liquid flowrates [99], their absolute values will depend on the dynamics of the two-phase contacting at the inlet. Yet despite its importance, to the best of the authors knowledge, there is no systematic investigation on Taylor bubble formation in small channels.

Existing literature covers larger systems/vessels and mainly small, non-Taylor bubbles (with bubble diameter smaller than the channel diameter). Bubbles are typically produced by injecting gas into a liquid through a small orifice from which they break, usually through the influence of buoyancy. Studies were originally driven by applications such as bubble columns and fermentation vessels. In early literature, bubble formation from an orifice in an open (unconfined) liquid medium under gravity was considered [100].

As a bubble is formed, the pressure within the bubble changes due to changing pressure head, depending on the height of the liquid above the bubble, and due to the change in its diameter ($\Delta p = 4\gamma/d_b$ for spherical bubbles) which is the more dominant pressure in small tubes. If the gas is supplied at constant pressure then the gas flow rate changes with time due to changing bubble pressure. If there is a sufficiently large pressure drop, or one is introduced, between the gas reservoir and the orifice, the capillary pressure can become insignificant in comparison and the gas flow rate can be taken as constant. Two limiting cases of gas introduction can therefore be identified, constant pressure and constant flow rate. For intermediate cases, the volume of the gas between the reservoir and the orifice, referred to as the chamber volume, needs to be considered. Mechanistic models are usually proposed for bubble formation, based on photographic observations. For low to intermediate gas flow rates two models have been suggested for bubble growth and detachment, namely single-stage and multiple-stage (for a review see Clift et. al. [101]). In the

single-stage model, bubbles originating at the orifice are assumed to grow smoothly until detachment when buoyancy exceeds the attaching forces. In a multiple-stage model it is assumed that there is a basic change in the growth mechanism at one or more points in the process of formation. Typically, it is assumed that the bubbles reside on the orifice during the first stage; the second stage begins with the bubble "lift-off" and formation of a neck connecting the bubble to the orifice. At higher gas flow rates, bubble pairing has been observed at the orifice, where the forming bubble coalesce with the one formed just before. For still higher gas flow rates jetting occurs with drops forming by jet breakup.

Increased power demands in spacecraft necessitates high rates of cooling and led to the study of thermally efficient two-phase flow systems under reduced gravity conditions. Bubble formation and detachment will affect in this case the distribution of the dispersed phase and the heat transfer rate. Under microgravity conditions in spacecraft, other forces usually less significant than buoyancy become important and may be used to control the bubble breakage instead. Pamperin and Rath [102] demonstrated that the inertia of the gas injected into a liquid containing tank, may cause the bubbles to detach under reduced gravity conditions. Kamotani and coworkers studied the effect of imposing a flow around the injection orifice to cause the bubble to detach. In these studies the breakage has been simulated using a multiple-stage model for cross-flow [103, 104] and co-flow [105] nozzle arrangements. For higher flow rates in a co-flow arrangement, Oğuz and Zeng [106] found that the forming bubble becomes elongated while remaining coaxial in the tube and bubbles are shed from the tip of the attached bubble, in a way similar to jetting behaviour.

Even though the studies of Bhunia et al. [105] and Kim et al.[103] were limited to non-Taylor bubbles, their models are useful as they identify conditions where Taylor rather than non-Taylor bubbles are formed. Using their models, if the forming bubble diameter reaches 98% of the tube diameter without detachment, the bubble is assumed to develop into a Taylor bubble.The two models, however, cannot give any further information as to the size of the formed Taylor bubbles. Bhunia et al.[105] studied the formation of spherical bubbles from a coaxial inlet arrangement similar to that described in this work but for larger tube diameters. A force balance on the bubble was used to identify when detaching forces overcome the attaching surface tension force anchoring the bubble to the nozzle. Subsequent necking takes place and the bubble was formed when that neck breaks. When the detaching forces were insufficient for the bubble to break before necking starts, Taylor bubbles were observed. For small channels surface tension forces dominate and Taylor bubbles

are more likely to form.

In this work the mechanisms of Taylor bubble formation are studied experimentally in small cylindrical channels with a coaxial gas-liquid inlet arrangement, using air and either water or octane as the liquid phase. A simple model based on neck stability considerations is developed for the prediction of the Taylor bubble size for the most common of the observed mechanisms. The period of the bubble formation from these models is compared to corresponding experimental values.

4.2 Experimental Setup

The experiments on Taylor flow formation in microchannels were carried out in the set up shown in Fig. 4.1. The liquids were introduced into the test section using a (0 – 6 mL/min) pump (milliGat, Global FIA, Inc). The air flow rate was supplied from a gas cylinder and was regulated with a mass flow controller (EL-FLOW F-110C, Bronkhorst). Rigid plastic tubing was used for the fluidic connections in order to reduce any effects caused by flexible tube expansion. A large pressure drop just before the gas inlet was introduced by a tube clamp to limit any pressure fluctuations from disturbing the flow in the test section. Two liquids with different surface tension were chosen, n-octane (Fluka n^o 74823, purum > 95%, GC) with properties $\gamma = 21.49\,\mathrm{mN/m}$, $\rho = 703\,\mathrm{kg/m^3}$ and $\mu = 10^{-3}\,\mathrm{Pa\ s}$ and deionised water with properties $\gamma = 72.26\,\mathrm{mN/m}$, $\rho = 1000\,\mathrm{kg/m^3}$ and $\mu = 5.2 \times 10^{-4}\,\mathrm{Pa\ s}$. Zero grade air (BOC) ($\rho = 1.19\,\mathrm{kg/m^3}$) was used for the gas phase.

The test section was a 30 cm long, 1 mm precision bore glass capillary in vertical configuration and is shown in Fig. 4.2. The liquid entered the capillary through a side tube joining the capillary at 90°, while the gas was introduced via a stainless steel nozzle concentric to the test channel. Two nozzles 10 cm long were used (Hamilton, USA) with 0.64 mm OD and 0.34 mm ID and with 0.21 mm OD and 0.11 mm ID, respectively. They were held in place with a small PTFE holder and wax which also served as a sealant. The nozzles extended 4 cm above the liquid inlet to ensure developed flow of the liquid at the point where it reaches the nozzle tip and contacts the gas.

At the end of the test section a disengagement chamber was attached to help the flow of Taylor bubbles in the test channel to become more regular. It was found that when the test tube exit was open to the atmosphere, each time a Taylor bubble reached the exit it burst and generated a pressure fluctuation that would not only affect the movement of the other Taylor bubbles in the tube but also the

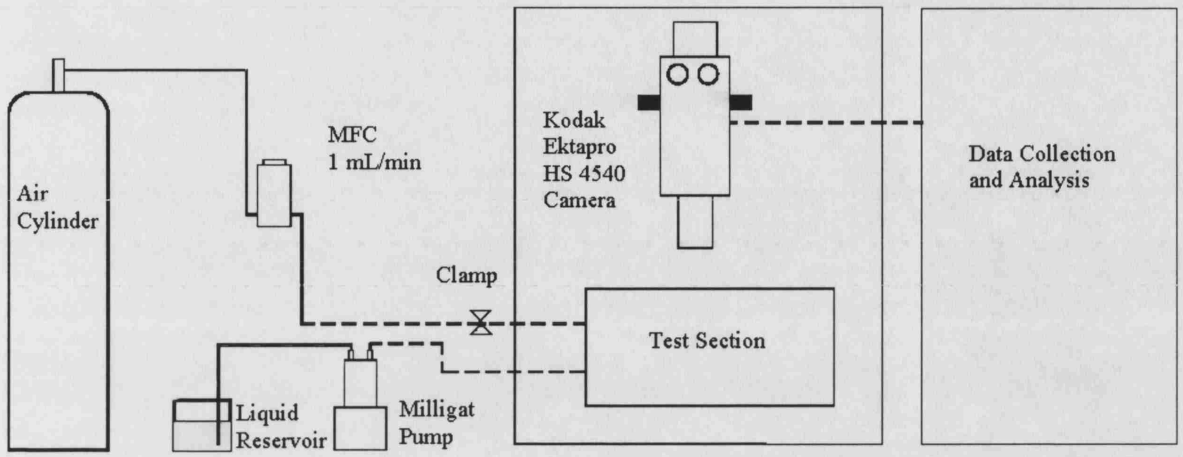

Fig. 4.1: Schematic view of the apparatus for study of Taylor bubble formation in liquid.

bubble formation at the inlet. As the pressure fluctuation caused by the bubble burst is due to the pressure difference between the inside and outside of the bubble caused by surface tension, the magnitude of these fluctuations was much larger for water because of its larger surface tension. Immersing the capillary end into a liquid reservoir reduced the pressure fluctuations but did not remove them completely as there was still a sudden change in bubble curvature radius from that in the tube equal to tube diameter to that in the disengagement chamber where the bubble became spherical. There was a gradual enlargement of the capillary ID at the exit, due to the chamber attachment procedure and this reduced further the sudden pressure fluctuations. For the cases where very long Taylor bubbles of volume larger than the volume of the expansion section were formed, however, the pressure fluctuations could not be eliminated.

For the observation of the Taylor bubble formation at the inlet of each test section a high-speed camera Kodak Ektapro HS 4540 was used, which can record images up to $4,500$ frames per second with full resolution of 256×256, with a $40\times$ lens. Recording speeds of either 250 fps or 125 fps for the slower flow rates were found to be sufficient. The duration of the bubble formation could be found from the number of frames taken. For each experimental condition 20 or more bubbles were analysed and the times necessary to form bubbles were averaged.

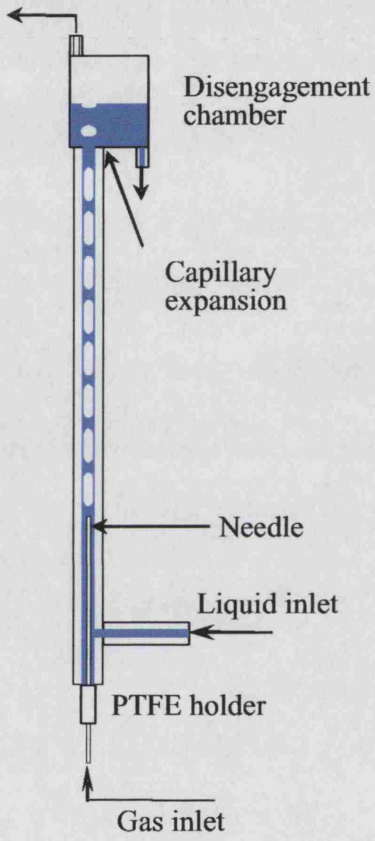

Fig. 4.2: Test section schematic showing the vertical co-flow capillary arrangement.

4.3 Results

For each nozzle size and each liquid, the liquid flow rate was varied from $0.06 - 1.2$ mL/ min and the gas flow rate was varied from $0.07 - 1.6$ mL/ min. These correspond to superficial velocities $0.001 - 0.025$ m/ s for the liquid and $0.002 - 0.04$ m/ s for the gas . Taylor bubble formation followed two steps (a Taylor bubble is considered "formed" when there would be no further modification to its length within the test section):

1. Bubble formation at the nozzle; the formed bubbles were either Taylor or non-Taylor (with their diameter less than the tube diameter).

2. Bubble size modification after its formation by coalescence or pairing inside the test channel after the inlet.

It should be mentioned that having the tube and the nozzle precisely concentric could not be achieved with this apparatus. This however has revealed other possible mechanisms of Taylor bubble formation which might not have occurred in perfect axi-symmetric conditions.

4.3.1 Mechanisms of bubble formation

The following mechanisms were observed:

Mechanism 1 (Fig. 4.3) was characterized by the formation of a gas chamber ahead of the nozzle, with the gas in contact with the tube walls in one or more areas. Bubbles broke at the tip of this gas chamber. The gas in this case covered the entire top surface of the needle up to its outer diameter. The rate of bubble formation once this mechanism was initiated was stable and the bubble movement was very smooth with no pressure fluctuations associated with the bubble breakup at the inlet. However, the initiation of such a mechanism was difficult, and with changing flowrates, the size of the gas chamber changed, or even disappeared completely at high liquid flow rates.

The time periods required for the Taylor bubble formation at any fixed gas and liquid flow rates varied from extremely regular, with an error of less than 1/250 s, for conditions leading to the formation of the smallest bubbles, to fluctuating for conditions leading to large bubbles (see Fig. 4.4). The large discrepancies in the latter case resulted from the effects of long bubbles exiting into the liquid-gas disengagement chamber. In general, for mechanism 1 time periods decreased with increasing liquid and gas flow rates with the curves becoming flatter at high flow rates (Fig. 4.5). However there were points in the trends where there seems to be a sudden

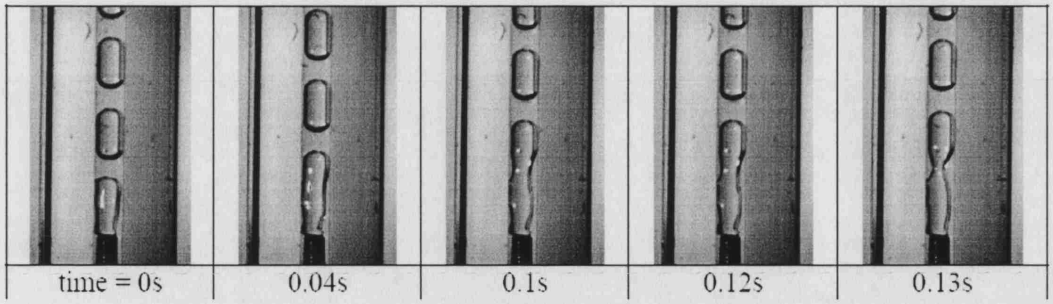

Fig. 4.3: Mechanism 1 for Taylor bubble formation in water for a 0.34 mm ID nozzle. Liquid superficial velocity, $U_{LS} = 0.0076$ m/s, gas superficial velocity, $U_{GS} = 0.0190$ m/s.

jump or fall in the period, in disagreement with the general trends. These variations arose from changes in gas chamber size and were not reproducible. This mechanism was seen for the large nozzle and water as the test fluid.

Mechanism 2 (see Fig. 4.6) occurred at the same range of flow rates as mechanism 1 and was most dramatic at low gas flow rates. The mechanism observed seemed to depend on the initial conditions in the tube. If the gas was introduced into the dry tube before introducing the liquid, mechanism 1 was sometimes observed, however the reverse always resulted in mechanism 2. In mechanism 2, at the beginning of bubble formation, the gas formed a meniscus at the nozzle tip while the pressure built up behind the meniscus. When the pressure reached a critical value, the gas broke through and very rapidly formed a bubble. At low liquid flow rates, this initial fast growth phase did not always terminate with bubble detachment from the nozzle, but the bubble would continue to grow and to form a neck at the nozzle. Eventually the bubble would detach when this neck destabilised and broke. The necking and subsequent breakage are similar qualitatively to what was usually seen in mechanism 3. Interestingly, the volume of the bubble formed did not seem to be affected by the liquid flow rate, at low to moderate liquid flow rates. Instead, an increase in the liquid flow rate simply increased the separation between the formed bubbles. As liquid flow rate was increased, instead of one Taylor bubble forming, a number of shorter Taylor bubbles formed in the abrupt gas burst with total volume approximately the same as the initial single bubble at lower liquid flowrates. The number of these bubbles increased with increasing liquid flow. Clearly this mechanism is not a constant flow rate mechanism and due to compressibility effects it is not a constant pressure mechanism either. Generally, mechanism 2 generated much larger bubbles for the same gas and liquid flow rates

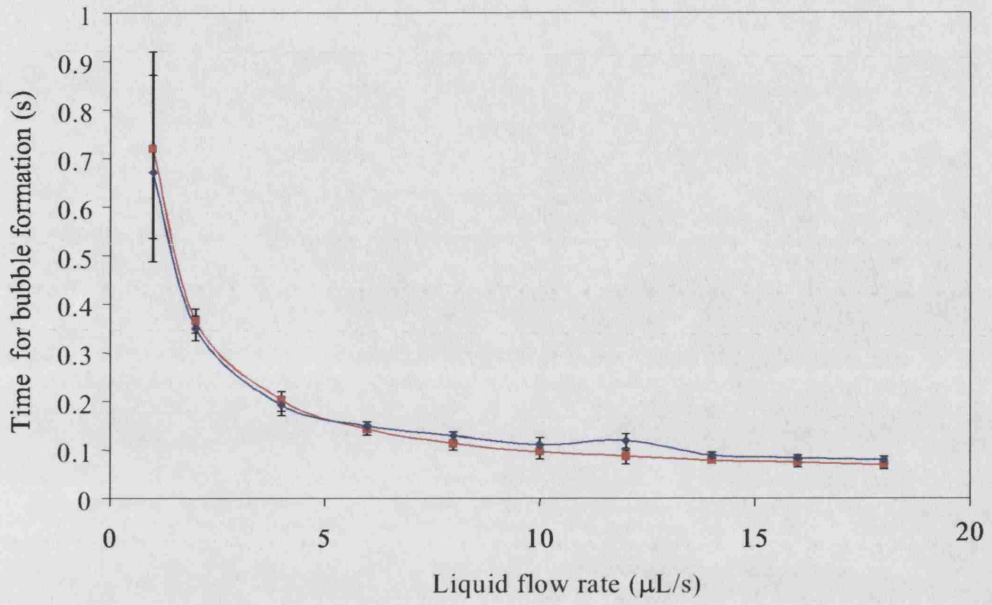

Fig. 4.4: Two sets of experiments showing the range of obtained periods in mechanism 1 for air flow rate of 0.88mL/ min into water and 0.34 m ID nozzle. Error is largest for largest periods.

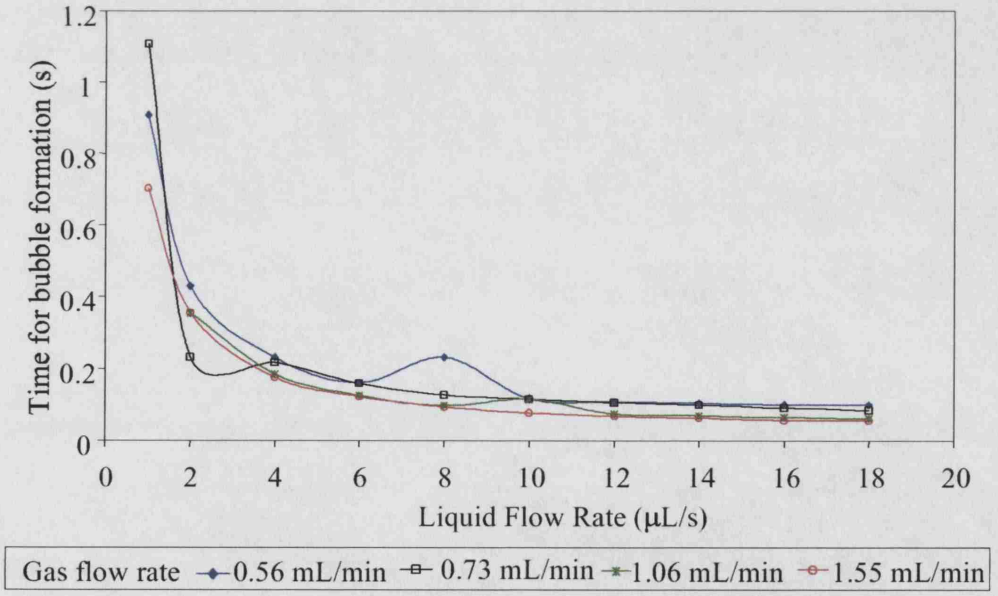

Fig. 4.5: Periods of bubble formation with mechanism 1 for air flow into water using a 0.34 mm ID nozzle.

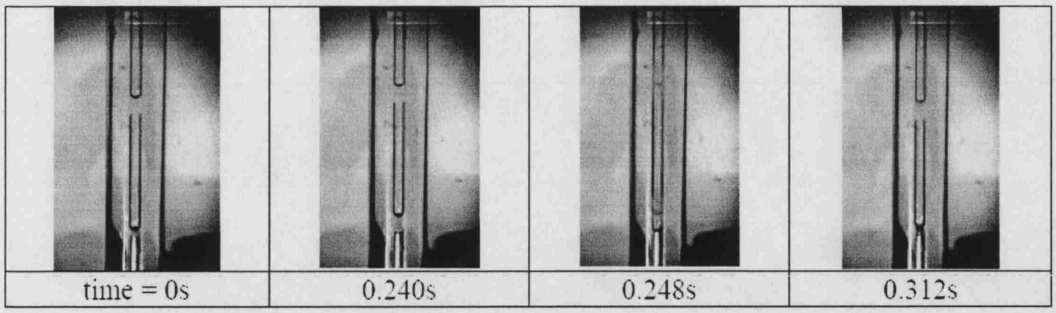

Fig. 4.6: Mechanism 2 for Taylor bubble formation in water for a 0.34 mm ID nozzle. There is no observed gas flow rate till 0.248s. A rapid *burst* of gas forms most of the bubble at 0.248s. The bubble continues to grow at a much slower rate and detaches from the nozzle at around 0.312s. Liquid superficial velocity, U_{LS} = 0.000632 m/s, gas superficial velocity, U_{GS} = 0.00511 m/s.

compared to mechanism 1. The movement of bubbles appeared to pulsate every time a bubble formed while the bubble volume depended mainly on the volume of gas pressurised upstream of the nozzle tip. No periods of formation were collected for this mechanism.

Mechanism 3, as seen in Figs. 4.7- 4.9 in octane was similar to the non-Taylor bubble formation mechanism described in the literature [105]. During the first stage the bubble resided on the nozzle while in the second stage the bubble "lifts-off" and a neck was formed at the nozzle. For large tubes or low liquid surface tension, the detachment forces became larger than the attaching surface tension forces at the inlet earlier and breakup of the neck occurred when the bubbles were still small and spherical (Fig. 4.7). For small tubes, large nozzles (compare Figs. 4.7 and 4.8) or large surface tension (compare Figs. 4.7 and 4.9), the attaching forces stabilised the bubble long enough for it to grow and become a Taylor bubble. Liquid then built up behind the bubble and the shape of the back of the bubble was modified to resemble a neck. Subsequently the neck broke and the bubble detached.

Similar to mechanism 1, the time periods necessary for Taylor bubble formation were either very regular, with an error of less than 1/250 s, when small bubbles were formed, or very irregular when large bubbles were formed caused by the pressure fluctuations as the bubbles entered into the liquid-gas disengagement chamber (Figs. 4.10 and 4.11). Results from octane and 0.11 mm ID nozzle are not reported because the bubbles formed were either small, non-Taylor or their sizes changed further in the test section after detachment due to pairing and/or coalescence (Fig. 4.25).

The measured times for bubble formation with mechanism 3 showed regular

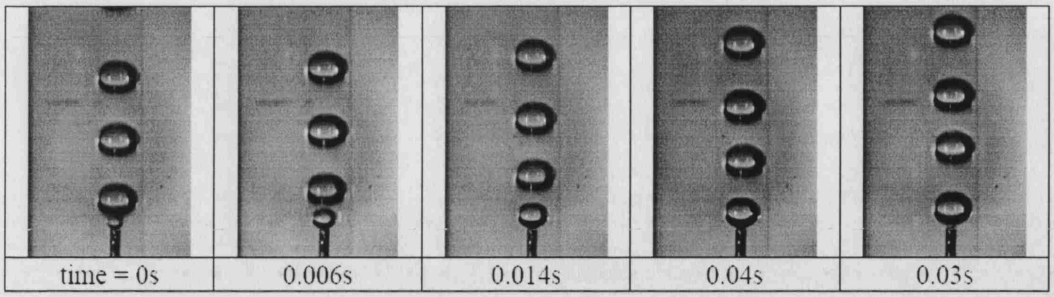

Fig. 4.7: Mechanism 3 causes the initial formation of non-Taylor bubble in octane for a 0.11 mm ID nozzle. Liquid superficial velocity, $U_{LS} = 0.0178$ m/s, gas superficial velocity, $U_{GS} = 0.0120$ m/s.

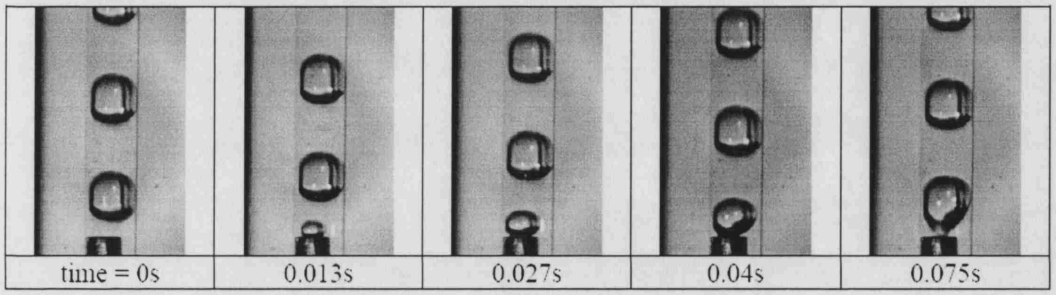

Fig. 4.8: Mechanism 3 of Taylor bubble formation in octane for a 0.34 mm ID nozzle. Liquid superficial velocity, $U_{LS} = 0.0178$ m/s, gas superficial velocity, $U_{GS} = 0.0120$m/s

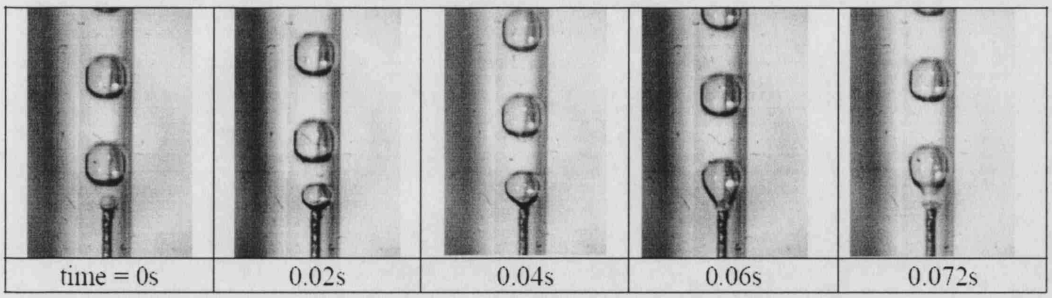

Fig. 4.9: Mechanism 3 of Taylor bubble formation in water for a 0.11 mm ID nozzle. Liquid superficial velocity, $U_{LS} = 0.0178$ m/s, gas superficial velocity, $U_{GS} = 0.0120$m/s

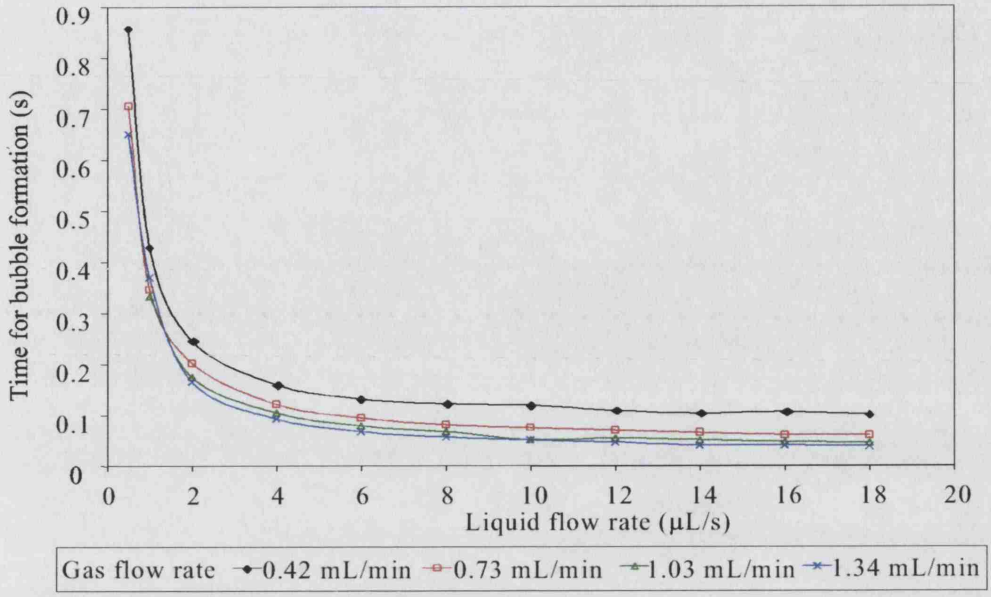

Fig. 4.10: Periods of bubble formation with mechanism 3 for air flow into water using a 0.11 mm ID nozzle.

trends of decreasing periods with increasing liquid flow rate and gas flow rates.

4.3.2 Model for bubble formation by mechanism 3

4.3.2.1 Stages of bubble formation

The steps by which a Taylor bubble is formed by mechanism 3 are illustrated in Fig. 4.12. A near spherical bubble grows from the tip of the nozzle to fill the entire channel cross section without necking (Figs. 4.12 (a) and 4.12(b)). When it touches the wall, either the continuity of the bubble interface is broken to form two contact lines at the wall, or the continuity of the liquid phase is preserved and a thin liquid film is formed separating the bubble from the wall. In the first case the contact angles are real, in the second they are apparent. Apparent contact angles depend on the local hydrodynamics of the flow near the wall [107]. In both cases, once the bubble reaches the wall, all subsequent liquid flow will accumulate behind it (Fig. 4.12 (c)). This is obvious when the bubble touches the wall, but would also be valid when a film forms between the bubble and the wall as the liquid flow in the film is negligibly small for the cases encountered here (e.g. see Figs. 4.8 and 4.9).

For constant gas and liquid flow rates two time parameters need to be identified whose sum adds up to the total time of bubble formation. The time necessary for

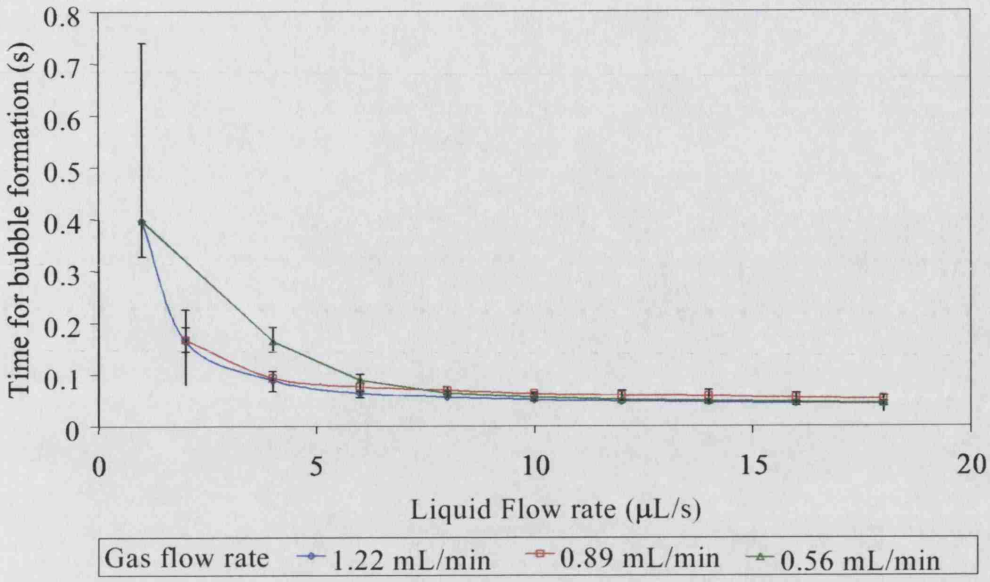

Fig. 4.11: Periods of bubble formation with mechanism 3 for air flow rate into octane using a 0.34 mm ID nozzle.

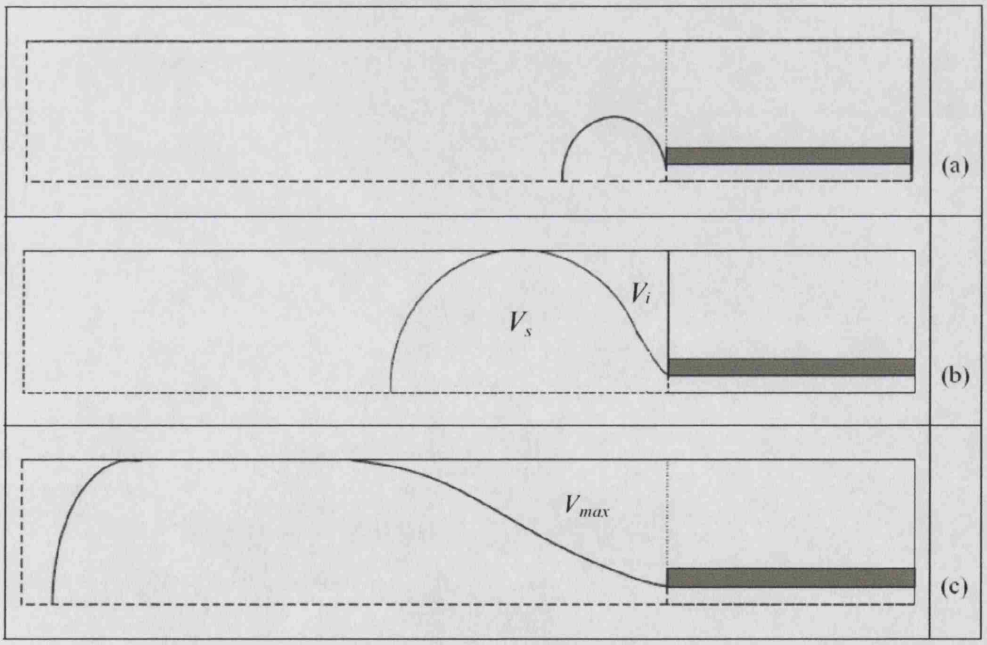

Fig. 4.12: The different stages in the Taylor bubble formation by mechanism 3. (a) Formation of a "small" spherical bubble. (b) The spherical bubble touches the wall and becomes a Taylor bubble. (c) The point at which the neck behind the Taylor bubble becomes unstable, leading to detachment from the nozzle.

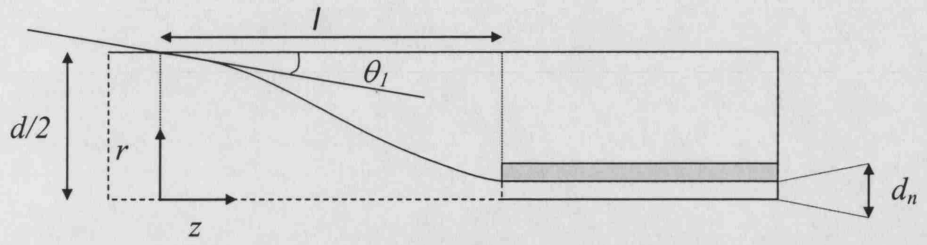

Fig. 4.13: A snapshot in the formation of a Taylor bubble. At the walls θ_1 is the real or apparent contact angle.

the approximately spherical bubble to reach the wall, t_s, and the time between the bubble reaching the wall and detaching from the nozzle, t_t. t_s is easily calculated from equation 4.1 if bubbles are assumed spherical. This is a good approximation when compared to the experimental observations (Figs. 4.7 and 4.8). Higher flow rates may result in significant deviations from this assumption due to forces other than surface tension becoming important [105].

$$t_s = \frac{V_s}{Q_g} = \frac{\pi d^3}{6Q_g} \tag{4.1}$$

t_t can be found from equation 4.2 where $V_{\max}$ is the maximum volume of liquid behind the Taylor bubble (attained at the point of detachment) and V_i is the initial liquid volume when the bubble touches the wall. $V_{\max}$ is related to the stability of the interfacial profile at the back of the forming bubble.

$$t_t = \frac{V_{\max} - V_i}{Q_l} = \frac{V_{\max} - \frac{\pi d^3}{24}}{Q_l} \tag{4.2}$$

4.3.2.2 Profile and stability of the meniscus at the back of the forming Taylor bubble

A snapshot of the bubble formation is given in Fig. 4.13. The assumptions of the model are:

1. The liquid flow rate is small such that velocity does not contribute to the pressure on the meniscus (quasi-static system).
2. The gas is assumed to be inviscid and incompressible.
3. The radial pressure gradients in the gas are negligible.

4. The real or apparent contact angle remains constant.

5. The bubble forming eventually becomes a Taylor bubble (This can be tested using the force balance method of Bhunia et al. [105] if 'lift-off' does not occur before the bubble touches the wall).

The average gas velocity changes with changing cross section according to the continuity equation:

$$u = u_{g0}\frac{d_n^2}{4r^2} \tag{4.3}$$

where u_{g0} is the known velocity of the gas through the nozzle.

The pressure p_g in the gas phase varies according to the Bernoulli equation:

$$p_g = p_{g0} + \frac{1}{2}\rho_g u_{g0}^2\left(1 - \frac{d_n^4}{16r^4}\right) \tag{4.4}$$

To obtain the interface profile at the back of the bubble the Young-Laplace equation is used.

$$p_g - p_l = p_{g0} + \frac{1}{2}\rho_g u_{g0}^2\left(1 - \frac{d_n^4}{16r^4}\right) - p_l = \gamma\left[\frac{1}{r\left[1+\left(\frac{dr}{dz}\right)^2\right]^{1/2}} - \frac{\frac{d^2r}{dz^2}}{\left[1+\left(\frac{dr}{dz}\right)^2\right]^{3/2}}\right] \tag{4.5}$$

This can be non-dimensionalised using d as characteristic length and γ/d as characteristic pressure as follows:

$$\bar{p}_{g0} + \frac{We_g}{2}\left(1 - \frac{\bar{d}_n^4}{16\bar{r}^4}\right) - \bar{p}_l = \left[\frac{1}{\bar{r}\left[1+\left(\frac{d\bar{r}}{d\bar{z}}\right)^2\right]^{1/2}} - \frac{\frac{d^2\bar{r}}{d\bar{z}^2}}{\left[1+\left(\frac{d\bar{r}}{d\bar{z}}\right)^2\right]^{3/2}}\right] \tag{4.6}$$

Parameterisation of equation 4.6 using the arc length $\bar{S}$ and angle α of the interface with the horizontal gives:

$$\frac{d\bar{r}}{d\bar{S}} = \sin\alpha \tag{4.7}$$

$$\frac{d\bar{z}}{d\bar{S}} = \cos\alpha \tag{4.8}$$

$$-\frac{d\alpha}{d\bar{S}} = \Delta\bar{P} + \frac{We_g}{2}\left(1 - \frac{\bar{d}_n^4}{16\bar{r}^4}\right) - \frac{\cos\alpha}{\bar{r}} \tag{4.9}$$

The dimensionless numbers arising from the Laplace equation and the boundary conditions are:

Gas Weber number $We_g = \frac{\rho_g u_{g0}^2 d}{\gamma}$

Ratio of diameters $\bar{d}_n = d_n/d$

Pressure difference $\Delta\bar{P} = \bar{p}_{g0} - \bar{p}_l = \frac{d}{\gamma}(p_{g0} - p_l)$

To solve the set of equations 4.7-4.9 two procedures can be followed based on the known end values ($r = \frac{d_n}{2}$ at the nozzle and $r = \frac{d}{2}$ at the point where the interface touches the wall) and the real/apparent contact angle at the wall. The solution can start from the nozzle by guessing a contact angle at the nozzle tip (a controlled variable) then calculating from the solution the contact angle at the wall and iteratively adjusting the guessed angle until the real/apparent contact angle at the wall is obtained. Alternatively the solution can start at the wall with the given wall contact angle and proceed to calculate the interface profile until the nozzle radius is reached. The second method was chosen because of its convenience.

The dimensionless initial conditions are:

$$\bar{r}(0) = 1/2 \tag{4.10}$$

$$\bar{z}(0) = 0 \tag{4.11}$$

$$\alpha(0) = -\theta_1 \tag{4.12}$$

The set of equations 4.7-4.9 was solved using a 5-6 order Runge-Kutta method in Mathematica 5.1, Wolfram Research Inc. for a given $\Delta\bar{P}, We_g$ and θ_1 and a sufficiently long meniscus arc length. The points at which the $\bar{r}(\bar{S}) = \bar{d}_n/2$ such that the apparent angle between the meniscus and the nozzle tip α is always within a range of allowable apparent angles (Fig. 4.14), would be valid solutions. The only profiles disallowed are those which cut the nozzle wall (profile (d)). Profile (a) differs from (b) in that it has a minimum value smaller than $\bar{d}_n/2$. Although this profile is allowed it was not experimentally observed. The arc length at that point

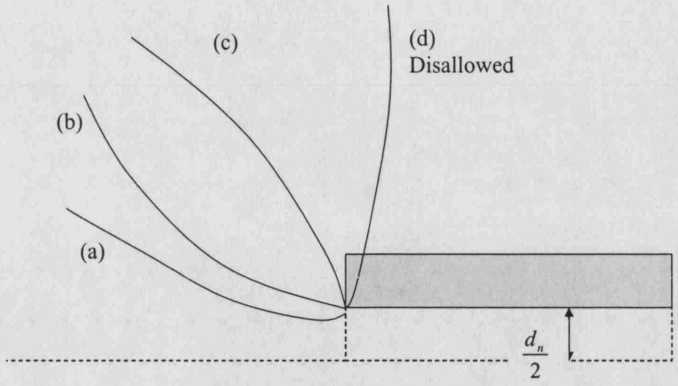

Fig. 4.14: Schematic of allowable angles when investigating the range of allowable profiles. Profile (a) where the interface dips below the nozzle radius before rising (b) with upward concavity (c) with downward concavity. Arrangement (d) shows an angle and interface which are not physically possible.

was obtained from the numerical solution ($\bar{S} = \bar{\lambda}$) and the distance along the wall from the nozzle is $\bar{z}(\bar{\lambda}) = \bar{l}$, (Fig. 4.13). If $\bar{r}(\bar{S}) \neq \bar{d}_n/2$ at any value of $\bar{S}$, or the angle at the nozzle exceeds the physically possible angles, then for the given set of parameters, the problem was regarded as having no solution. It is assumed that by moving from a set of parameters which give a valid solution, or solutions, to those with no solution, some instability occurs and the bubble detaches. The point at which this change took place was found for given We_g and θ_1 by trial of $\Delta\bar{P}$ values until two are found which bracket the instability point, then iteratively shrinking that bracket to that point. It should be noted that in reality $\alpha(\bar{\lambda})$ would be dependent on the value of the real contact angle with the material and the local surface geometry of the nozzle tip. As an example, if the nozzle tip is smooth and tapered and the receding contact angle is θ_2, the values of $\alpha(\bar{\lambda})$ would be limited to a range between $\theta_2 - 90° < \alpha(\bar{\lambda}) < \theta_2$, (see Fig. 4.15). Since the nozzle tip geometry is not usually known the criteria of Fig. 4.15 is not used in the simulations.

For a given profile, calculating the volume of liquid behind the bubble up to the nozzle tip is given by equation:

$$\bar{V}_l = \int_{\bar{z}=0}^{\bar{z}=\bar{l}} \pi(\frac{1}{4} - \bar{r}^2)\, d\bar{z} = \int_{\bar{S}=0}^{\bar{S}=l} \pi(\frac{1}{4} - \bar{r}^2)\cos\alpha\, d\bar{S} \tag{4.13}$$

The maximum value of $\bar{V}_l$ is labelled as $\bar{V}_{\max}$ obtained as $\Delta\bar{P}$ is varied. The time of bubble formation can then be easily calculated from the sum of times of equations 4.1 and 4.2.

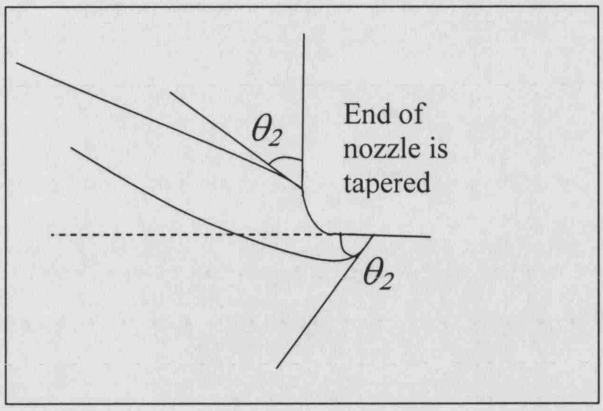

Fig. 4.15: For a smooth tapered nozzle, only apparent contact angles between $\theta_2 - 90° < \alpha < \theta_2$ should be observed.

	Water	Octane
$\bar{d}_n$	0.11	0.34
θ_1	0°	0°
We	$9.09 \times 10^{-3} - 1.13 \times 10^{-1}$	$3.35 \times 10^{-4} - 4.15 \times 10^{-3}$

Tab. 4.1: Parameter values for the cases where Mechanism 3 was observed

4.3.3 Comparison of model predictions and experimental results

The range of the parameters in the two sets of experimental data where mechanism 3 appeared are given in Table. 4.1. It is clear that the resulting values of We are small, and the term associated with We in equation 4.6 may be neglected. In fact the values of $\bar{V}_{\max}$ calculated varied by less than 6% for the whole range of We. This result is interesting because it shows We and hence surface tension γ have limited influence on the Taylor bubble size formed by this mechanism. Of course, if γ is sufficiently small, the bubble might not remain attached to the nozzle long enough to become a Taylor bubble [105].

Nevertheless, the full set of equations 4.7-4.9 is solved and the results predicted by the theory are compared to those obtained experimentally in Figs. 4.16. and 4.17. The trends are adequately captured by the model, however, increased discrepancy between experimental and theoretical results is observed with decreasing liquid and gas flow rates.

Before accounting for the discrepancies, the sum of expressions 4.1 and 4.2 can be rearranged as follows:

$$\frac{Q_l}{Q_g} = \frac{1}{V_s}\left(Q_l\, T\right) - \frac{V_{\max} - V_i}{V_s} \tag{4.14}$$

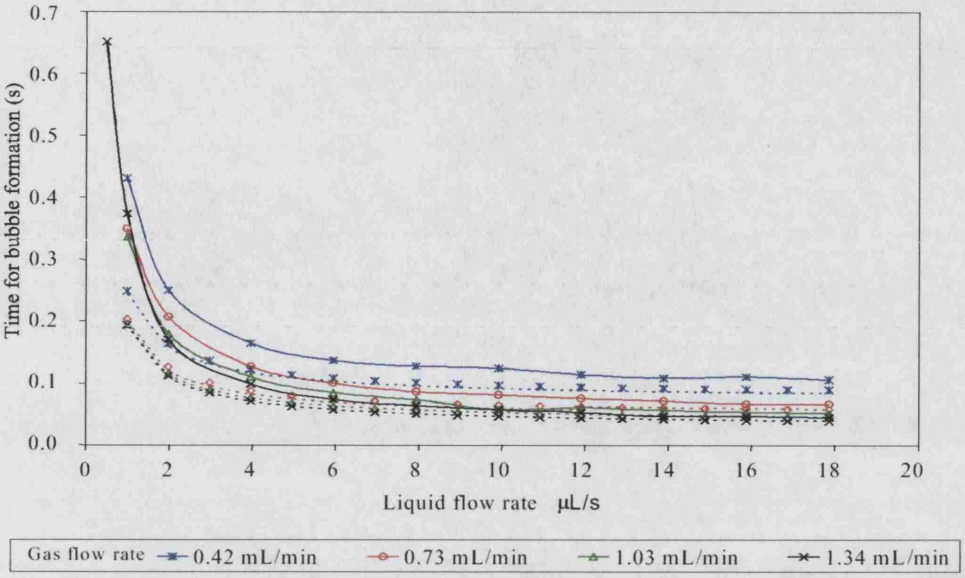

Fig. 4.16: Comparison of obtained periods from experiments and theory for different flow rates of air and water, 0.11 mm ID nozzle. Solid lines: Experimental. Dashed lines: theoretical.

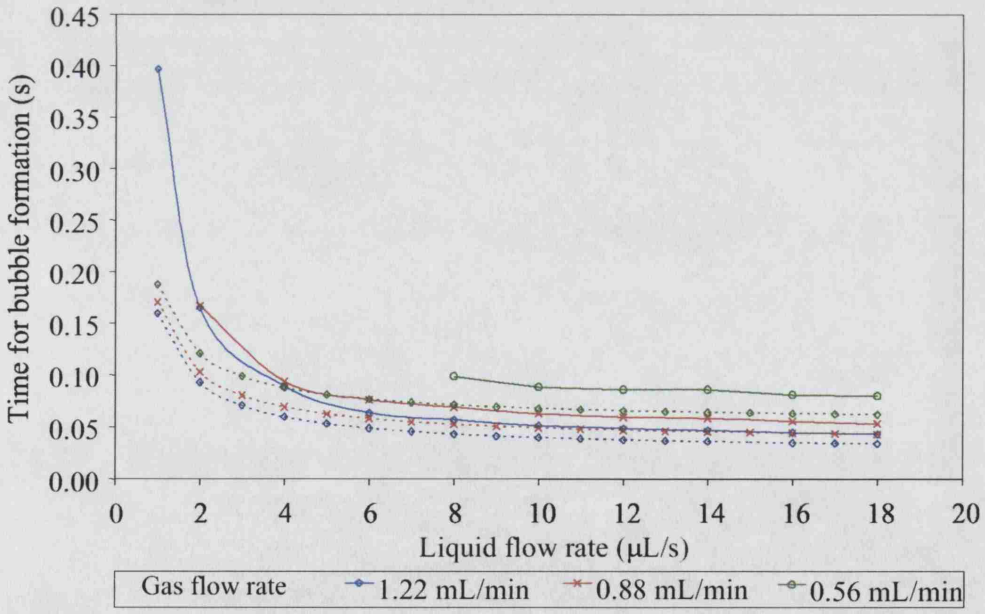

Fig. 4.17: Comparison of obtained periods from experiments and theory for different flow rates of air and octane, 0.34 mm ID nozzle. Solid lines: Experimental. Dashed lines: theoretical.

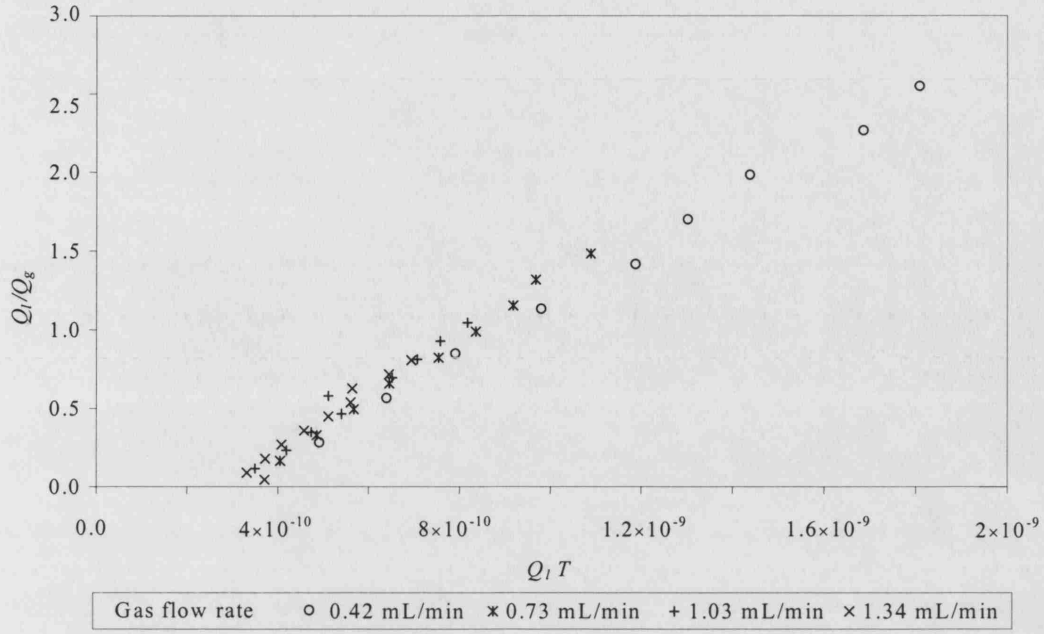

Fig. 4.18: Plot of $\frac{Q_l}{Q_g}$ vs $Q_l T$, for 0.11 mm ID nozzle and air-water system.

Gas flow rate	0.42 mL/min	0.73 mL/min	1.03 mL/min	1.34 mL/min
$\bar{V}_s^{\text{exp}}$	0.592	0.515	0.511	0.476
$\bar{V}_{\text{max}}^{\text{exp}} - \bar{V}_i^{\text{exp}}$	0.309	0.317	0.284	0.297
$\bar{V}_{\text{max}} - \bar{V}_i$	0.170	0.156	0.159	0.165

Tab. 4.2: Experimental and theoretical volumes for the air-water case and ID 0.11mm nozzle

where:

$$T = t_s + t_t \tag{4.15}$$

Plotting all the experimental data in air-water for nozzle size 0.11 mm in terms of $\frac{Q_l}{Q_g}$ versus $Q_l T$ allows V_s and $V_{\text{max}}^{\text{exp}} - V_i^{\text{exp}}$ to be calculated (Fig. 4.18). These values are made dimensionless by dividing by d^3 and tabulated in Table 4.2.

It can be seen that $\bar{V}_s^{\text{exp}}$ increased with decreasing gas flow rate but nevertheless was close to the value of 0.524 obtained if a sphere is assumed to form initially (within 11%). Similarly, the volume of the liquid from the moment the bubble touches the wall until the Taylor bubble breaks ($\bar{V}_{\text{max}} - \bar{V}_i$) also showed an increasing trend with decreasing gas flow rate. These values are however consistently under-predicted by the model (by about 51%).

Similar conclusions can be drawn from the results for the air-octane system with

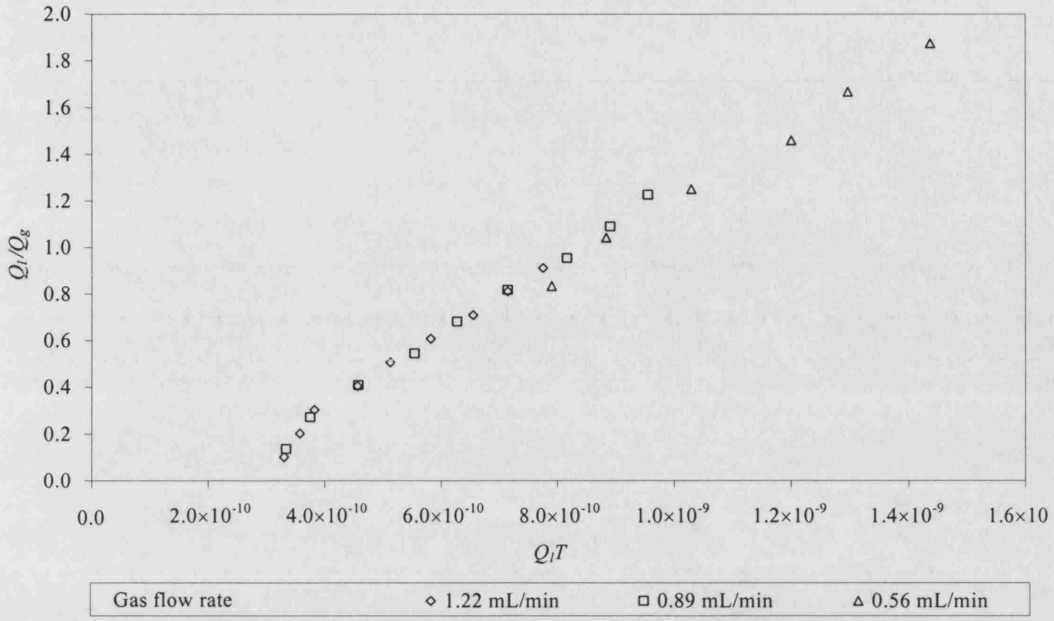

Fig. 4.19: A plot of $\frac{Q_l}{Q_g}$ vs Q_lT , for 0.34 mm ID nozzle and air-octane system.

Gas flow rate	0.56 mL/min	0.89 mL/min	1.22 mL/min
$\bar{V}_s^{\text{exp}}$	0.641	0.603	0.588
$\bar{V}_{\text{max}}^{\text{exp}} - \bar{V}_i^{\text{exp}}$	0.239	0.225	0.232
$\bar{V}_{\text{max}} - \bar{V}_i$	0.133	0.135	0.133

Tab. 4.3: Experimental and theoretical volumes for the air-octane case and ID 0.34mm nozzle

nozzle size 0.34 mm experiments, shown in Fig. 4.19 and Table. 4.3. The differences in this case between model and experiments are of the same order as in the air-water system (18% difference for $\bar{V}_s$ and 44% in $\bar{V}_{\text{max}} - \bar{V}_i$).

It can be concluded that there is some error in assuming the initial, pre-Taylor bubble to be a perfect sphere. In fact the larger experimental volume implies that the bubbles were slightly elongated and the error was larger for the larger nozzle (Table. 4.3). The deviation may be partly related to the non-concentric arrangement of the nozzle in the tube. In addition, there may have been stabilisation effects in the second stage of Taylor bubble formation associated with the neglected inertial and viscous forces or with the non-concentric arrangement of the nozzle in the tube which lead to larger bubbles being formed experimentally than predicted by the simple model proposed here.

Experimental values of $\left(\bar{V}_{\text{max}}^{\text{exp}} - \bar{V}_i^{\text{exp}}\right)$ show little variation ($< 6\%$ from average)

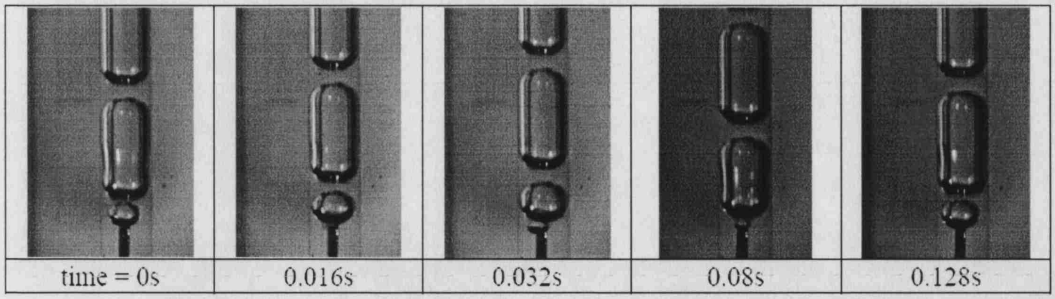

Fig. 4.20: Base pairing causing the formation of a Taylor bubble from a Taylor bubble in octane for a 0.11 mm ID nozzle. Liquid superficial velocity $U_{LS} = 0.0051$ m/s, gas superficial velocity $U_{GS} = 0.019$ m/s.

with gas flow rates in both of Tables 4.3 and 4.2 consistent with the earlier discussion of We. A similar conclusion can be drawn from the relatively good correlation to a straight line of the points in Figures 4.18 and 4.19 for each of the gas flow rates as to the limited effect of liquid flow rates on the values of $\left(\bar{V}_{\max}^{\exp} - \bar{V}_i^{\exp}\right)$. The effect of changing the nozzle on the other hand from 0.11 mm to 0.34 mm changed $\left(\bar{V}_{\max}^{\exp} - \bar{V}_i^{\exp}\right)$ by 40%. Formation times by mechanism 3 are therefore mostly functions of nozzle sizes and flow rates.

4.3.4 Bubble size modification

4.3.4.1 Bubble Pairing

Bubble pairing is a common phenomenon at high flowrates [101], where a new bubble before it can break away from the nozzle coalesces with the bubble formed just before it which would quickly neck and detach (Fig. 4.20). Due to the slow movement of Taylor bubbles, the phenomenon appeared at much lower flow rates than would be observed in unconfined liquid with non-Taylor bubbles. This would repeat for the next bubble forming at the nozzle until enough liquid had accumulated behind the large bubble such that no further pairing could take place.

An idealised schematic of pairing between a Taylor bubble and a forming bubble for coaxial inlets is given in Fig. 4.21. After the neck breaks up and the Taylor bubble forms, the volume of the neck is distributed between the formed bubble and the nozzle (depending on the location along the neck at which the breakage occurs). The volume left attached to the nozzle forms a small spherical bubble with diameter d_{B0}.

Experimental observations (Fig. 4.20) show no gas volume to be left behind at

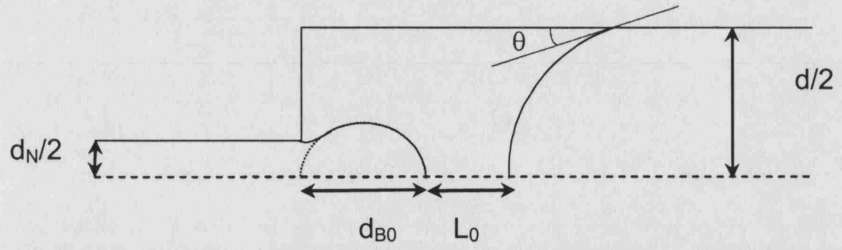

Fig. 4.21: Schematic of a formed Taylor bubble and the volume of gas formed by the collapse of the neck still attached to the nozzle.

the nozzle, ($d_{B0} \sim 0$). The profile of the formed bubble is taken as spherical with a radius of curvature determined from the (apparent or actual) contact angle θ (Fig. 4.21).

With constant volumetric flow rates of gas Q_g and liquid Q_l the diameter d_B of the forming bubble with time t is given by:

$$d_B = \sqrt[3]{\frac{6}{\pi} Q_g t + d_{B0}^3} \tag{4.16}$$

The initial distance separating the formed bubble from the nozzle is determined as $d_{B0} + L_0$. The distance separating the formed bubble from the nozzle at time t is given by:

$$L = (d_{B0} + L_0) + \frac{4\,(Q_g + Q_l)}{\pi d^2} t \tag{4.17}$$

Pairing occurs when the diameter, d_B of the forming bubble, and the separation L become equal i.e.

$$\frac{6}{\pi} Q_g t + d_{B0}^3 = \left((d_{B0} + L_0) + \frac{4\,(Q_g + Q_l)}{\pi d^2} t \right)^3 \tag{4.18}$$

The above equation must have real roots for t that also satisfy the condition:

$$0 < t < \frac{\pi\,(d^3 - d_{B0}^3)}{6 Q_g} \tag{4.19}$$

The upper limit in expression 4.19 is a physical limit, as the bubble diameter cannot exceed that of the tube. When it does reach that size, expression 4.16 is no longer valid.

As the existence of a valid solution for t from equation 4.18 is a necessary con-

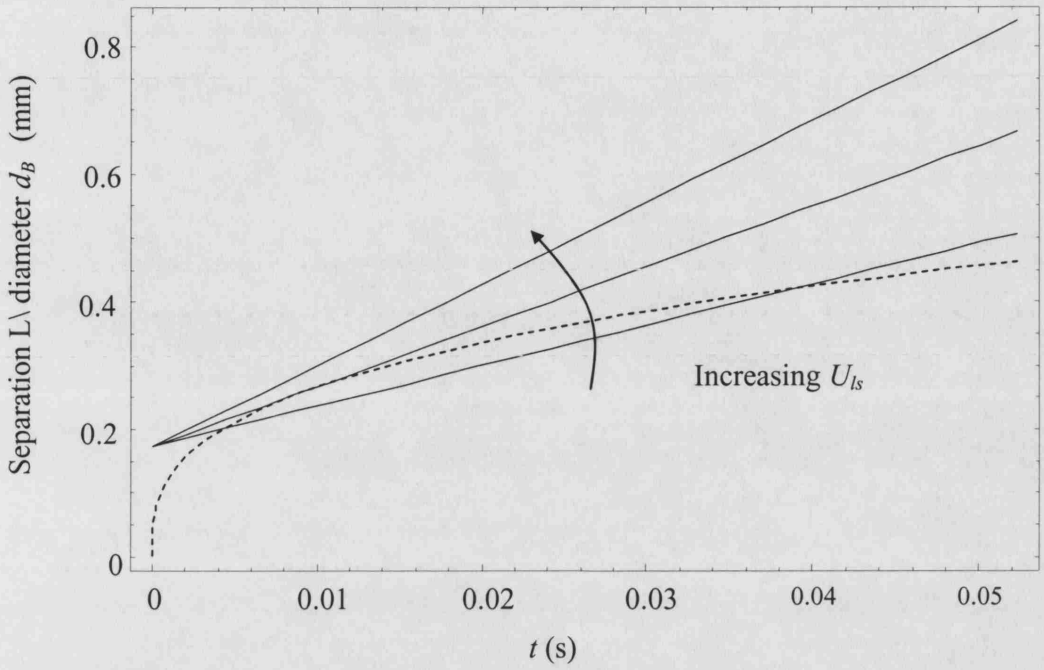

Fig. 4.22: The change of separation L (solid line) and forming bubble diameter d_B (dashed line) with time.

dition for pairing to occur it is worth investigating the properties of equation 4.18 which guarantee the existence of this solution. For flow rate combinations which form Taylor bubbles, and for a given gas flowrate, there is always a liquid flow rate at which pairing occurs. In Fig. 4.22, the LHS (solid) and the RHS (dashed) of equation 4.18 are plotted for various U_{ls} values. Clearly when these curves cross or touch, pairing occurs. Increasing the liquid flow (provided that Taylor bubbles still form), eventually causes pairing to stop, see Fig. 4.22. The condition for not having a solution t is: $D > 0$, where D is the discriminant of the cubic equation 4.18 (Appendix C). The stability boundary of the pairing mechanism is given by $D = 0$.

The quantities d_{B0} and L_0 need to be supplied and are usually difficult to predict. If the volume of liquid before the bubble breaks $V_{\max}$ is known, then mass conservation necessitates that equation 4.20 be satisfied.

$$V_{\max} = \underbrace{\frac{\pi d^2}{4}(L_0 + d_{B0} + \frac{d}{2}(\sec\theta - \tan\theta))}_{\text{Volume of cylinder from nozzle to contact point}} - \underbrace{\frac{\pi d^3 (2+\sin\theta)(1-\sin\theta)^2}{24\cos^3\theta}}_{\text{Volume of bubble cap}} - \underbrace{\frac{\pi d_{B0}^3}{6}}_{\text{Initial Sphere volume}} \tag{4.20}$$

If d_{B0} is set to zero, and the $V_{\max}$ from the model developed for bubble formation in section 4.3.2.1 is used L_0 can then be predicted from equation 4.21:

$$L_0 = \frac{4}{\pi d^2}\left(V_{\max} + \frac{\pi d^3 (2+\sin\theta)(1-\sin\theta)^2}{24\cos^3\theta}\right) - \frac{d}{2}(\sec\theta - \tan\theta) \tag{4.21}$$

The value of θ depends on the capillary number Ca [107]. For $d_{B0} = 0$, expression $D = 0$ gives:

$$Q_l = \frac{1 - \frac{9}{2}\left(\frac{L_0^2}{d^2}\right)}{\frac{9}{2}\left(\frac{L_0^2}{d^2}\right)} Q_g \tag{4.22}$$

This equation can be used to obtain boundaries between pairing/non-pairing Taylor flow (section 4.3.5).

4.3.4.2 Bubble Coalescence

Depending on the flow conditions, small non-Taylor bubbles can be formed, which may pair near the inlet to Taylor (as seen previously) or non-Taylor bubbles (smaller than tube diameter). The non-Taylor bubbles can undergo further modification away from the inlet by coalescing with other bubbles. Coalescence of bubbles within the test channel was nearly always seen for the small nozzle and high liquid flow rates which resulted in small non-Taylor bubbles that do not pair. In such a sequence most bubbles had very similar velocities. Occasionally a bubble formed which had a higher rise speed than the preceding one. At a point along the channel, these two bubbles coalesced to form a Taylor bubble (Fig. 4.23). A Taylor bubble is much slower than the non-Taylor bubbles so that subsequent non-Taylor bubbles caught-up and coalesced with the Taylor bubble causing it to grow further. The process continued until another pair of non-Taylor bubbles coalesced upstream of the Taylor bubble. All remaining non-Taylor bubbles in between subsequently coalesced with the Taylor bubble downstream (if the channel length was sufficient). The final distribution of Taylor bubble sizes was observed to be determined by the frequency of coalescence of two non-Taylor bubbles.

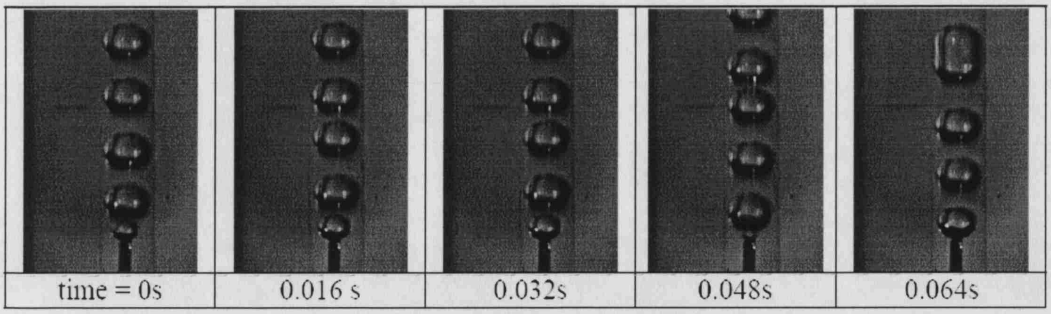

Fig. 4.23: Non-Taylor bubble coalescence causing the formation of a Taylor bubble in octane for a 0.11 mm ID nozzle. Liquid superficial velocity $U_{LS} = 0.0204$ m/s, gas superficial velocity $U_{GS} = 0.019$ m/s.

Distributions of sizes for these cases were not investigated in the current work because the channel length was not always sufficient for all the non-Taylor bubbles to coalesce. However, from qualitative observations it can be concluded that the range of final Taylor bubble sizes increased with increasing flow rates. It would be wise to avoid the conditions that favour this mechanisms if regular Taylor bubbles are required.

Bubble coalescence was most probably caused by the dependence of bubble velocity on the bubble size. It appears that even small variations in size affect the velocity with the smaller bubbles having higher velocities than larger bubbles possibly due to reduction of the wall drag. The reason why a slightly different bubble is randomly formed could be due to minor flow or pressure fluctuations.

4.3.5 Maps of Taylor bubble formation/modification by pairing or coalescence

The gas and liquid superficial velocities for which the different Taylor bubble formation mechanisms appeared can be seen in Fig. 4.24 for the air-octane system and the large size nozzle (ID 0.34 mm). In the majority of cases Taylor bubbles formed at the nozzle without any further modification downstream. However, for low U_{ls}, pairing at the inlet occurred. Equations 4.20-4.22 can be used to find the limiting conditions for bubble pairing to occur. L_0 was calculated from equation 4.21 (with $\theta \approx \frac{\pi}{4}$) as was estimated from the photos. Equation 4.22 then becomes:

$$U_{ls} = 7.30\, U_{gs} \tag{4.23}$$

According to the above equation bubble pairing should occur for the entire range of flow rates studied, which clearly was not the case (compare equation 4.23 with the

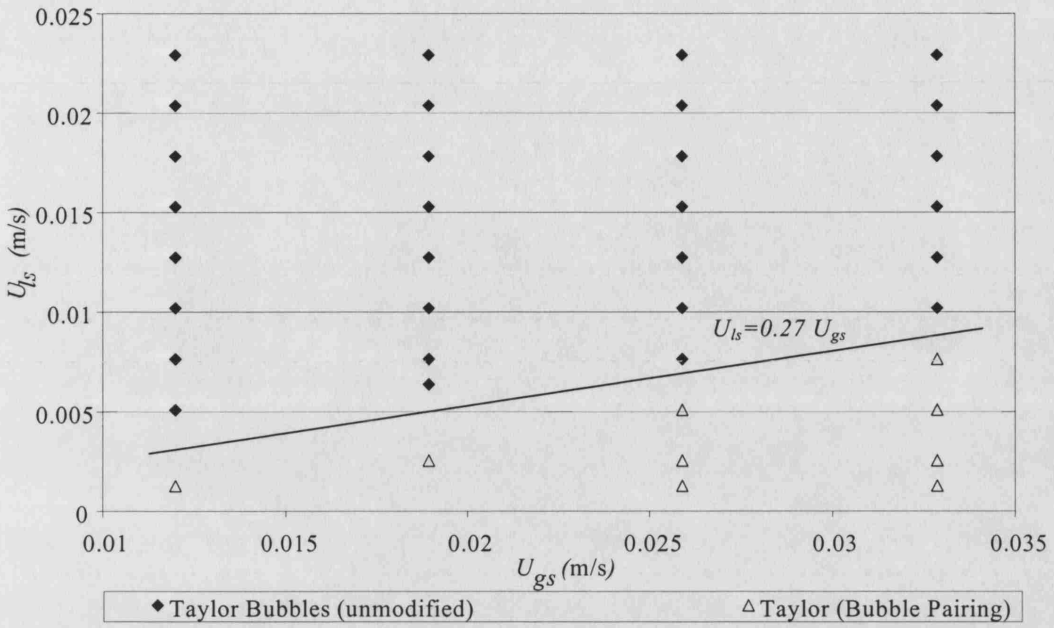

Fig. 4.24: Map of bubbles formed in octane for a 0.34 mm ID nozzle.

experimental slope in Fig. 4.24). Investigating the experimental results carefully revealed that:

1. On bubble detachment from the nozzle, the gas meniscus disappeared into the nozzle. A length of time passed before the interface emerged again which caused L_0 to be larger than would be predicted by equation 4.21.

2. The non-concentric arrangement of the nozzle increased the initial length L_0 which the forming bubble diameter needed to match before the pairing occurred.

Equation 4.22 can be modified to account for nozzle eccentricity from the tube axis and can still be used if an expression for L_0 can be found which accounts for liquid entering the nozzle. In its current form it may be useful as a 'worst case' analysis method.

A similar map of Taylor bubble formation mechanisms is shown in Fig. 4.25 for air octane with the small gas nozzle (ID 0.11 mm). In the majority of cases all initial bubbles are non-Taylor and become Taylor either by pairing or coalescence or even a combination of the two cases (see Fig. 4.26 for an example of combined pairing and coalescence).

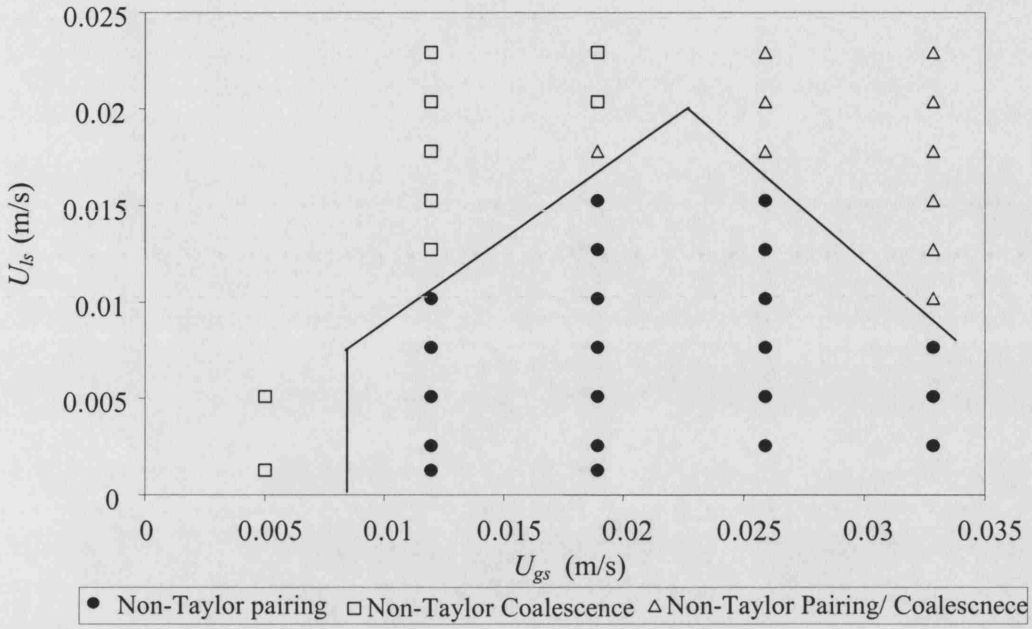

Fig. 4.25: Map of bubbles formed in octane for a 0.11 *mm* ID nozzle.

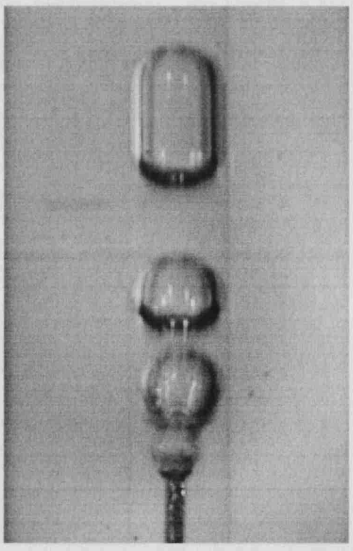

Fig. 4.26: Non-Taylor bubble pairing followed by coalescence causing the formation of a Taylor bubble in octane for a 0.11 mm ID nozzle. Liquid superficial velocity $U_{LS} = 0.0204$ m/s Gas superficial velocity $U_{GS} = 0.0259$ m/s.

Maps for air-water system are not presented because for the larger nozzle the mechanism of formation alternated between mechanism 1 and mechanism 2 for the same gas and liquid flow rates while for the small nozzle, Taylor bubbles were always formed by mechanism 3 without further modification.

4.4 Conclusions

Taylor bubble formation in capillary tubes has been studied theoretically and experimentally in a co-flow gas-liquid contacting arrangement for two liquids with different properties. The following can be concluded:

1. Three different mechanisms of bubble formation were observed. With careful design of the capillary outlet uniform bubble sizes were produced in the majority of cases.

2. Mechanism 3 in which the bubble necked and broke, led to the formation of Taylor or non-Taylor bubbles and was found to be prevalent for most conditions studied.

3. Taylor bubbles formed with mechanism 3 were found to have periods that depend mainly on gas and liquid flowrates and were almost independent of the surface tension. A concentric bubble formation arrangement can therefore be used to generate bubbles of a specific volume irrespective of the liquid used.

4. The simple model proposed for Taylor bubble lengths formed by mechanism 3 was found to agree with the experimental trends satisfactorily apart from low liquid and gas flow rates where long bubbles on exiting the tube influence the bubble formation at the inlet. The model can be further improved by taking into account the shape of the bubble at the nozzle before it reaches the capillary wall and by including viscous and inertial phenomena as well as further investigating the nature of the contact with the wall.

5. Bubble pairing and coalescence were present in some cases and considerably modified the sizes of the already formed bubbles. For cases where coalescence was present, a wide distribution of bubble sizes was obtained.

6. A simple bubble pairing model was proposed for predicting pairing for concentric tube nozzle arrangements. The model over-predicted the range of liquid flowrates at which pairing was observed experimentally. The model can be

modified by taking into account any deviations from the concentric inlet arrangement inherent in the setup as well as the exact initial position of the meniscus after the neck breakage. The model in its current form may however be used as a 'worst case' predictor of bubble pairing.

5. AXIAL MASS TRANSFER IN TAYLOR FLOW THROUGH MICROCHANNEL CAPILLARIES

Nomenclature

A_s	Area separating the vortex and film regions in slug	m^2
A_f	Cross sectional area of film	m^2
c	Tracer concentration	kg/m^3
C	$\mathcal{L}(c)$, Laplace transform of c	
Ca	Capillary number $\frac{\mu U_b}{\gamma}$	
d	Microchannel diameter	m
D	Diffusivity of tracer species	m^2/s
$E(t)$	Unit cell residence time distribution (RTD) curve	s^{-1}
$E(\bar{t})$	Non-dimensionalised $E(t)$	
$E_{CSTR-PFR}(\bar{t})$	CSTR-PFR model RTD curve	
$E_{2Region}(\bar{t})$	Two region model RTD curve	
$E(\bar{s})$	$\mathcal{L}(E(\bar{t}))$, Laplace transform of $E(\bar{t})$	
$F(\bar{t})$	Density function	
$F(\bar{s})$	$\mathcal{L}(F(\bar{t}))$, Laplace transform of $F(\bar{t})$	
Fr	Froude number $\frac{U_b^2}{g\,d}$	
g	Acceleration due to gravity	m/s^2
J_0, J_1	Acceleration due to gravity	
k_l	Mass transfer coefficient between film and vortex	$m^{-2}\,s^{-1}$
$\mathcal{L}$	Laplace transform operator	
l_b	Taylor bubble length	m
l_{cell}	Unit cell length, $l_{cell} = l_b + l_s$	m
$l_{reactor}$	Reactor length	m
l_s	Liquid slug length	m
L_b	Dimensionless Taylor bubble length $\frac{l_b}{d}$	

$L_{reactor}$	Non-dimensionalised $l_{reactor}$, $\frac{l_{reactor}}{d}$	
L_s	Dimensionless liquid slug $\frac{l_s}{d}$	
$\mathbf{n}_b$	Interface unit normal vector	
$\mathbf{n}_t$	Interface unit tangent vector	
$\mathbf{N}$	Tracer flux	$\mathrm{kg\,m^{-2}\,s^{-1}}$
p	Pressure	$\mathrm{N/m^2}$
Pe	Bulk Peclet number $\frac{U_b d}{D}$	
r_0	Radial position of vortex centre	m
r_1	Radial position of streamline separating vortex and film regions in slug	m
Re	Reynolds number $\frac{\rho U_b d}{\mu}$	
s	Variable of Laplace domain	
Sp	Cubic spline polynomial	
Sh	Sherwood number $\frac{k_L d}{D}$	
t	Time	s
t_{cell}	Time for a unit cell to move a length l_{cell}, $\frac{l_{cell}}{U_b}$	s
$t_{reactor}$	Time for a unit cell to pass through reactor, $\frac{l_{reactor}}{U_b}$	s
t_s	$CSTR$ time constant	s
$\mathbf{u}$	Velocity field	m/s
u_z, u_r	Radial and axial velocity components	m/s
V	Volume of slug	$\mathrm{m^3}$
V_1	Volume of slug film region	$\mathrm{m^3}$
V_2	Volume of slug vortex region	$\mathrm{m^3}$
Z_{1n}	n^{th} zero of Bessel function of the first kind of order one	

Greek symbols

α, β, ε, ϕ	Coefficients of spline polynomial	
γ	Interfacial tension	N/m
δ	Thickness of film surrounding bubble	m
μ	Viscosity	$\mathrm{N\,s\,m^{-2}}$
μ^n	n^{th} moment	
ρ	Density	$\mathrm{kg/m^3}$
σ	Standard deviation of RTD	s
ψ	velocity ratio of bubble to average slug velocity	

τ_{cycle}	Vortex cycle time	s
Superscripts		
n	Unit cell number	
$\bar{x}$	Barred symbols are non-dimensionalised	
Subscripts		
0	Initial value at $t = 0$	
av	Average slug value	
i	Inlet value	
o	Outlet value	

5.1 Introduction

Taylor flow is one of the dominant gas-liquid flow patterns in microscale diameter channels. It consists of elongated gas bubbles of equivalent diameter larger than the channel diameter separated by liquid slugs. The bubbles adopt a characteristic capsular shape. They completely fill the channel cross section and are only separated from the wall by a thin film of liquid. Because of the presence of bubbles in front and at the back of the slugs, the flow field in the liquid is modified compared to single phase flow, and toroidal vortices are formed [83].

Compared to single-phase laminar flow, Taylor flow offers many advantages [108]. Because the bulk liquid is separated by the gas bubbles, axial mixing between the liquid slugs is significantly reduced. The film surrounding the bubbles is the only means of communication between two successive slugs and in the majority of cases its thickness is only a fraction of a percentage of the tube diameter. Also within the slugs the recirculation of the liquid improves radial mass transfer, i.e. from liquid to wall and from gas to liquid [109, 97, 110].

The combination of good radial mass transfer and low axial mass transfer in the liquid makes Taylor flow suitable for two-phase applications that involve mass transfer (fluid-fluid or wall-fluid) or single phase liquid applications which suffer from large back-mixing. Good characterisation of the mass transfer attributes of Taylor flow is key to design and optimisation of such applications.

The efficiency of many devices like tubular reactors, tubes with absorbing wall for liquid chromatography and tubular dialysers can be improved by operating them in Taylor flow rather than in single phase [111]. Much work on Taylor flow has been devoted to the investigation and characterisation of the monolith froth reactor (MFR) where the two fluid phases are introduced into the reactor as froth flow and pass

through the catalyst coated channels in Taylor flow pattern [112][98]. The residence time of the liquid in the reactor is related to the conversion and selectivity of such systems. An application which benefited from the low axial mixing properties in Taylor flow is automated analysers [113]. The throughput in these devices should be such that the different samples in the feed line are kept separate. An envisaged extension of the applications of Taylor flow is in high throughput screening as a means of introducing sequentially different reactants/samples within a microchannel reactor/analyser. The enhanced heat and mass transfer rates possible in microchannels would enable a kinetically controlled operating regime to be established that allows the calculation of reaction kinetics. For such application it is important to be able to predict the extent of axial mixing as a function of the hydrodynamics of the two-phase flow.

This chapter aims to develop a method for accurately calculating the residence time distribution in a Taylor flow tubular system. Using this method benchmark cases covering a large range of parameter variations are investigated. The results obtained are also compared to the predictions of previously developed models that were based on simplified assumptions of the flow field in the liquid phase.

5.2 Theory and Literature Review

During Taylor flow in microchannels, strong interfacial forces as well as the contacting at the inlet and separation at the outlet of the two phases may cause pulsation of the flow or a distribution of bubble and slug sizes[114]. The liquid film surrounding the bubbles may appear or disappear depending on the wall surface and liquid properties as well as on the operating conditions [114, 115]. In this paper Taylor flow is assumed to be regular (non-pulsating) and periodic (no variation in bubble or slug sizes) in agreement with the wider body of literature on this flow pattern in small tubes[1]. In addition, there is negligible flow in the liquid film surrounding the bubbles and the geometry of the bubble is axi-symmetric.

In periodic Taylor flow, a single period consists of a bubble and a slug, or a slug and two half bubbles, usually referred to as a *unit cell.* The unit cell moves with the velocity of the bubble, which is faster than the average liquid velocity in the slug because of the presence of the stagnant liquid film separating the bubble from the

[1] The description of small implies the dominance of surface tension over gravity forces. Various criteria can be found in literature to indicate when this happens. The criterion used here is $\frac{\rho g d^2}{\gamma} \lesssim 3.37$ based on the work by Bretherton [40].

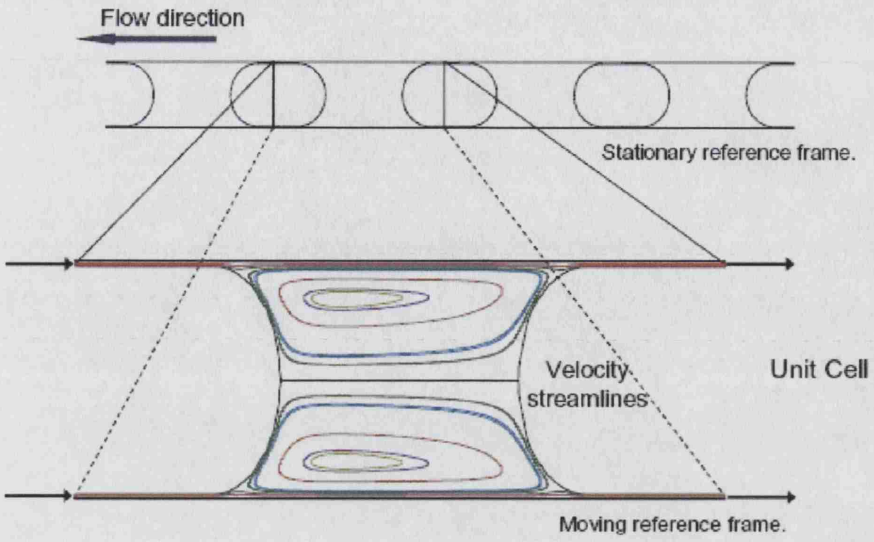

Fig. 5.1: The moving unit cells through a reactor channel appear when viewed with a frame of reference moving with the velocity of the bubbles appears as a small vessel with two inlets and two outlets. The flow patterns inside are typical patterns for the operating conditions in microreactor channels for chemical engineering applications.

wall. A moving unit cell, seen from a frame of reference moving with the bubble resembles a reactor with one inlet and one outlets (Fig. 5.1).

Following the pulsed tracer experimental methodology for determining the residence time distribution curve, a tracer is conceptually introduced at time zero into a Taylor flow reactor of length $l_{reactor}$ such that it fills (and is only confined to) a single unit cell (see Fig. 5.2(a)). The amount of tracer material introduced into the channel is calculated from the product of the tracer concentration and the liquid slug volume. As the tracer cell moves through the reactor some tracer is communicated upstream through the film into the next cell that enters the reactor. When the whole of cell 2 is in the reactor the time passed is $t_{cell} = l_{cell}/U_b$, (see Fig. 5.2(b)). The process continues as more cells enter the reactor and each cell experiences at its inlet the tracer that the downstream cell deposits behind. When cell 1 completely exits the reactor, its residence time in the reactor is $t_{reactor} = l_{reactor}/U_b$, see Fig. 5.2(c). The concentration of the exiting slug is averaged and noted as the reactor outlet concentration for time interval $t_{reactor} - t_{cell} \leq t \leq t_{reactor}$. The amount of tracer material output can be calculated from the product of the slug volume and its concentration.

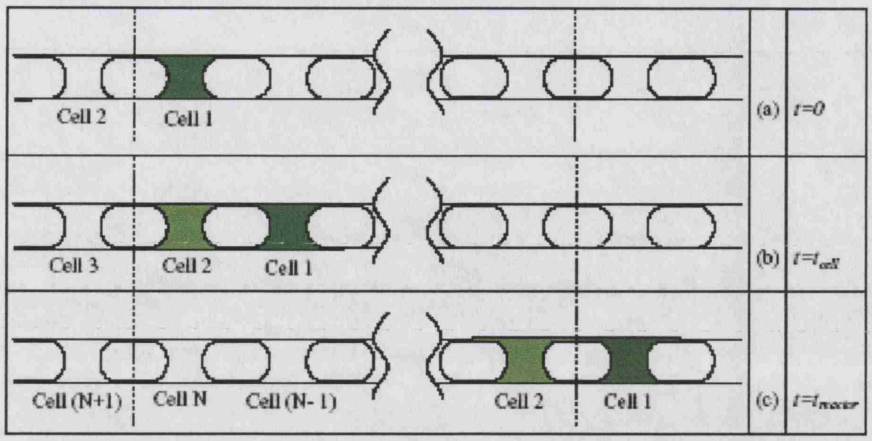

Fig. 5.2: Method of acquiring the residence time distribution curve. The boundaries of the reactor are denoted by the dashed vertical lines.

Determining the output and internal concentration of a unit cell for a given time varying tracer input is the next step. Thiers et. al. [116] assumed perfect mixing in the slugs obtaining a tank-in-series model. Other authors [96] have restricted the assumption of perfect mixing to low Peclet numbers ($Pe < 500$) and used a CSTR-PFR in series model to predict the response of the unit cell. They further showed that for very low Peclet numbers, forward axial mixing as well as back axial mixing occurs and introduced a variation of the CSTR-PFR model which can account for that. Such models in general allow an analytic expression for exiting reactor concentrations to be obtained.

In more sophisticated models, the region of the slug can be divided into two separate regions; a closed vortex region where the recirculation occurs, and an enclosing open thin liquid annulus region (Fig. 5.1). This division is the basis of two-region models. Pedersen and Hovarth [117] proposed a two-region model where the two regions are assumed to be well mixed and a mass transfer coefficient is used to account for mass transfer between the regions. They obtained this parameter from studies of slug to wall mass transfer coefficients [118]. Average mass transfer coefficients can also be found in other sources [97, 110, 98, 119]. Thulasidas et. al. [112] assumed the two regions of the liquid slug to be well mixed in the axial direction and exchange mass only by diffusion in the radial direction. A one dimensional transient diffusion equation is then used to account for the mass transfer. Starting with an initial concentration in the annulus region and in the core circulation region, the

Dimensionless Number	Definition
Re	$\frac{\rho U_b d}{\mu}$
Ca	$\frac{\mu U_b}{\gamma}$
L_s	$\frac{l_s}{d}$
L_b	$\frac{l_b}{d}$
Fr	$\frac{U_b^2}{gd}$

Tab. 5.1: Dimensionless numbers governing the hydrodynamics of Taylor flow

equation is solved for a time equivalent to that of a single circulation cycle, then the concentrations of the two regions are averaged. This average core concentration is then used as an initial condition for the next solution, while the average concentration in the annulus region is the output response of the unit cell for the duration of the solved time. Kreutzer [98] developed a "continuous multi-zone model" version of the two-region model of Pedersen and Hovarth [117] with the discrete unit cell approximated by a differential element.

Convolution methods are then used to obtain from the residence time distribution in a single cell, the residence time distribution of the whole Taylor flow channel. Comparisons of the resulting reactor residence time distribution curves with experimental ones have been used to validate the single cell models. One of the aims of this work is to provide accurate residence time distribution data of unit cells against which previous models can be directly compared.

5.3 Unit cell analysis

To totally account for the hydrodynamics during gas-liquid Taylor flow, bubble shapes and velocity, film thickness and flow field in the liquid slugs need to be known. If surface active agents are neglected, the governing dimensionless parameters derived from the Navier-Stokes equations for a gas-liquid Taylor flow are given in Table 5.1.

The influence of these parameters are discussed in detail in chapter 3. In general the effect of increasing Ca is always to increase the thickness of the liquid film surrounding the bubbles. The flow pattern inside long slugs soon attains a parabolic profile away from the bubble caps for sufficiently long L_s. For $Ca < 10^{-3}$, the shapes of the bubble caps can be assumed spherical and the meniscus reaches terminal film

Ca	δ/d	$Re_{\min}$	$Re_{\max}$	$Pe_{\min}$	$Pe_{\max}$
10^{-3}	6.36×10^{-3}	4.95×10^{-5}	3.09×10^{2}	3.70	1.78×10^{6}
10^{-4}	1.41×10^{-3}	4.95×10^{-5}	3.09×10^{1}	3.70	1.78×10^{5}
10^{-5}	3.06×10^{-4}	4.95×10^{-5}	3.09	3.70	1.78×10^{4}
10^{-6}	6.60×10^{-5}	4.95×10^{-5}	3.09×10^{-1}	3.70	1.78×10^{3}

Tab. 5.2: Range of dimensionless numbers for typical reaction engineering applications

thickness quickly so that the body of the bubble can be approximated by a cylinder. The increase in Re causes an increase in the distance from the bubbles where a parabolic profile in the slug is attained. Re has limited affect on the shape of the bubble and film thickness for $Ca < 10^{-3}$. While the bubble length L_b has been shown to affect the terminal velocity of the bubble when it is smaller than a certain minimum length which depends on Re and Ca, it is only for the cases where $Ca > 10^{-3}$ that these are significant. In practice L_b needs to be made sufficiently large ($L_b \gtrsim 1.2$) for a constant film thickness to be reached.

The dominance of surface forces in small diameter channels brings to prominence the effect of contaminant surface active agents (chapter 3). Their presence usually results in a larger film thickness than predicted by theory and modifications to the flow field. The characterisation of such effects requires the introduction of many more parameters (surfactant interface adsorption/desorption rates, and interface diffusivity) which vary from system to system and are mostly inestimable and difficult to measure. Instead of trying to justify the relationship of $\bar{\delta}$ to Ca, the film thickness $\bar{\delta}$ is reported instead of Ca as a parameter (correlation of Tables 3.4 and 3.5 are nevertheless used for order of magnitude estimation). The change in the flow field with trace contaminant surfactant depends on the El number and the actual contaminant concentration. To facilitate the analysis, it is assumed that the concentrations of the contaminants are such that the effects on the flow field are negligibly small.

Although the different dimensionless parameters are independent, once a specific system is selected all the physical constants are fixed and the parameters are linked by the tube diameter and the bubble velocity. Considering the properties of many common solvents and a range of $1 \times 10^{-6} \leq Ca \leq 1 \times 10^{-3}$ (deduced from tube lengths, diameters and reaction residence times which could be encountered in microreactor engineering applications), the ranges of other dimensionless numbers were constructed (Table 5.2). The limits on Peclet number were deduced for diffusivities $5 \times 10^{-11} \leq D_{AB} \leq 1 \times 10^{-8}$ obtained from the tabulated diffusivity values of many materials in water. The lower limit corresponds to diffusivities of large molecules.

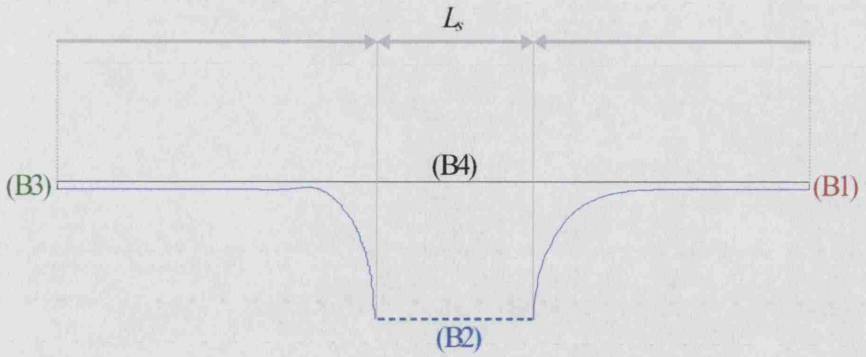

Fig. 5.3: Geometry and boundaries of the computational domain.

5.3.1 Problem formulation and solution

For the range $10^{-6} \leq Ca \leq 10^{-3}$ bubbles are well approximated by a cylinder with spherical cap ends. Film thickness range was estimated from correlations in terms of Ca [76]. As explained in the previous section the results for $Ca \leq 10^{-3}$ will be reported in terms of film thickness rather than Ca. Slug lengths were taken as $\{\frac{1}{4}, 1, 4\}$ tube diameters, such lengths are based on previous experimental work [114]. The upper limit did not exceed 4 diameters because the mass transfer performance of Taylor reactors worsens with increased lengths [96][119]. Liquid films surrounding bubbles are generally thin and well mixed radially. In general they can be approximated as plug flow reactors (PFR) whose only effect is to delay the signal output of a step pulse input. The effect of increasing bubble length would be a shift to the right in the time axis of the residence time distribution curve. As a result only a bubble length of 1.1 diameters was used in all simulations.

The flow field in the liquid slug between two consecutive bubbles (see for example Fig. 5.1) is calculated by solving the Navier-Stokes equations 5.1 for that geometry (shown in Fig. 5.3).The characteristic dimensions used in the non-dimensionalisation of the equations and boundary conditions are given in Table (5.3).

$$Re\ \bar{\mathbf{u}} \cdot \bar{\nabla}\bar{\mathbf{u}} = -\bar{\nabla}\bar{p} + \bar{\nabla}^2 \cdot \bar{\mathbf{u}} \tag{5.1}$$

The boundary conditions are given in Table 5.4. To solve equation 5.1, a commercial finite element software package, Femlab® by Comsol is used. Standard 2nd order elements were used for the velocity fields and 1st order elements for the

Velocity	U_b, terminal velocity of the bubble
Length	d, tube diameter
Time	d/U_b
Concentration	c_i, constant inlet concentration

Tab. 5.3: Characteristic dimensions

(B1)	Inlet	$\bar{u}_z = -1,\ \bar{u}_r = 0$
(B2)	Slip or symmetry	$\mathbf{n}_b \cdot \bar{\mathbf{u}} = 0,\ \frac{\partial \bar{\mathbf{u}}}{\partial n} = 0$
(B3)	Straight-out condition	$\mathbf{n}_t \cdot \bar{\mathbf{u}} = 0\ ,\ \bar{p} = 0$
(B4)	Wall	$\bar{u}_z = -1,\ \bar{u}_r = 0$

Tab. 5.4: Boundary conditions when solving for hydrodynamics

pressure field. The total number of elements varied between 2851 and 11270 with larger concentration of elements near the bubble caps and at the boundary between the liquid film and the vortex region.

The convection-diffusion equation 5.2 with boundary conditions given by Table 5.5 was then solved with Femlab, using a similar computational domain as that used for the hydrodynamics (see Fig. 5.3). The calculated velocity field was interpolated to obtain the velocity term in the equation. The initial conditions of the tracer in the computational domain is constant concentration of $\bar{c} = 0$. The output concentration at boundary (B3) at regular time steps was averaged over the cross section.

$$\frac{\partial \bar{c}}{\partial \bar{t}} + \bar{\mathbf{u}} \cdot \bar{\nabla} \bar{c} - \left(\frac{1}{Pe}\right) \bar{\nabla}^2 \bar{c} = 0 \tag{5.2}$$

Third order elements were used for the concentration of the tracer. Their number varied from 5620 to 15431. The numerics of the simulation limited the values of Peclet number which could be used. Beyond Pe of the order of 10^5 significant overshooting (concentration in excess of the maximum concentration of 1) and undershooting (negative concentrations) develop around areas of high concentration gradients (specifically in the region of the stream line separating the film and the circulating area).While these can be treated using various shock capturing techniques [121] they introduce artificial diffusion and for that reason were not used.

(B1)	$\bar{c}_i = 1$
(B2)	$\mathbf{N} \cdot \mathbf{n}_b = 0$
(B3)	$\mathbf{N} \cdot \mathbf{n}_b =$ Convective Flux
(B4)	$\mathbf{N} \cdot \mathbf{n}_b = 0$

Tab. 5.5: Boundary conditions for the convection diffusion equation

Therefore the upper limit considered was $Pe = 10^5$, and even for that limit some shock effects are observed during the early stages of the simulation which did not disappear with local grid refinements. The overshoot/undershoot in concentration was localised and of a value less than ± 0.08 which disappears as the concentration gradients reduced with time.

The solution of hydrodynamics and convection-diffusion equations was carried out using an Athlon 1.6GHz processor with 1Gb RAM. The hydrodynamic solution is easily obtained in $\sim$ 8 minutes of CPU time. The concentration at the output of the reactor for the time-dependent solution of the convection-diffusion equation was evaluated in up to ten stages. Initially output concentrations were stored at time steps $\Delta\bar{t} = 0.1$ then the storage steps were increased in size at different stages, $\Delta\bar{t} = 100$ was the maximum time step size used to resolve the long tail of the distribution for some systems. The CPU time required for the initial stage was longest (maximum ~8 h for the highest Pe) but dropped to $\sim$ 7 min. for the other stages.

5.3.2 Residence time distribution in a unit cell

The concentration at the outlet of a unit cell in response to a step input gives the density function $F(\bar{t})$. This output is calculated for all time steps and an interpolation using natural cubic splines of this data corresponds to the continuous function $F(\bar{t})$. The equation of the natural cubic spline function coefficient for a set of numerical data can be written as:

$$\begin{aligned} Sp(\bar{t}) &= \alpha_1 + \beta_1(\bar{t}-\bar{t}_1) + \varepsilon_1(\bar{t}-\bar{t}_1)^2 + \phi_1(\bar{t}-\bar{t}_1)^3 && \text{for } \bar{t}_1 \le \bar{t} \le \bar{t}_2 \\ &= \alpha_2 + \beta_2(\bar{t}-\bar{t}_2) + \varepsilon_2(\bar{t}-\bar{t}_2)^2 + \phi_2(\bar{t}-\bar{t}_2)^3 && \text{for } \bar{t}_2 \le \bar{t} \le \bar{t}_3 \\ &\vdots \\ &= \alpha_{n-1} + \beta_{n-1}(\bar{t}-\bar{t}_{n-1}) + \varepsilon_{n-1}(\bar{t}-\bar{t}_{n-1})^2 + \phi_{n-1}(\bar{t}-\bar{t}_{n-1})^3 && \text{for } \bar{t}_{n-1} \le \bar{t} \le \bar{t}_n \end{aligned} \tag{5.3}$$

The spline coefficients were calculated using an adaptation of the method by Burden et. al. [122] in Mathematica® [123]. Splines were used in the interpolation because they have continuous first and second derivatives. The derivative of $\bar{F}(\bar{t})$ with respect to time gives the residence time distribution curve $\bar{E}(\bar{t})$. The process of differentiating the data introduces spurious errors specifically around areas where there is a sharp change in the gradient of $\bar{F}(\bar{t})$ and not enough sampling points.

With that in mind the curves obtained for the residence time distributions $\bar{E}(\bar{t})$ still produced useful information.

Once the residence time distribution curves are obtained, their moments are calculated up to the third one to characterise them. Whilst moments are also easily to calculate to any order from the residence time distribution function, to avoids introducing errors from the differentiation in obtaining $\bar{E}(\bar{t})$, equation 5.4 is used instead.

$$\bar{\mu}^{(n)} = n \int_0^\infty \bar{t}^{n-1} \left[1 - F(\bar{t})\right] d\bar{t} \tag{5.4}$$

$$\bar{\sigma}^2 = \bar{\mu}^{(2)} - \bar{t}^2 \tag{5.5}$$

These moments are of little practical use beyond the third moment while larger errors in their calculation are introduced with increasing moment order[124]. The models used to describe the behaviour of the unit cell in literature, usually have at most a single adjustable parameter which accounts for the incomplete knowledge of the mixing process in the liquid slug. This parameter is determined for unit cells by comparing the model predictions against experimental data for the whole reactor and picking a value for parameter so that the model best matches the data in some sense. In this work the models by others for a single unit cell are fitted to the numerical data obtained from the simulations. Two steps are necessary: first assess/obtain the fitting parameter and then compare the quality of the fit with the original numerical data.

Two possible procedures are available for fitting and comparing the quality of the fit, as discussed by Nauman and Buffham[124]. In the method of moments, the n parameters are fitted to satisfy the first n moments and the quality is assessed by considering the value of the $n+1$ moment[2]. The second method, is to use a fitting algorithm where the parameters of a model are fitted so as to minimise the square of the difference between the data and the model (equation 5.6). In this chapter the second method is used as it was found difficult to make a qualitative judgement of the quality of the fit based on the values of moments. Nevertheless, the values of the moments are also reported because they can easily be used to estimate parameters

[2] The moments μ_0 and μ_1 should be satisfied by any model which conserves mass irrespective of the fitting parameters. μ_0 should have a value of 1, while μ_1 should correspond to the space time of the vessel analysed. Therefore the μ_2 would be used for fitting the data and μ_3 used for judging the fit. The space time is simply the volume of the vessel divided by the volumetric flow rate and for a closed-closed vessel is always equal to the first moment of the vessel [124].

(in comparison to the fitting methods where a set of numerical data is needed). A comment is appropriate here on the way the square error is defined, see equation 5.6. The use of this integral with interpolated density function $F(t)$ rather than the usual numerical non linear regression routines is to avoid the errors introduced by the highly non-uniform distribution of sampled points which put a large emphasis on the early part of the curve where the number of sample points is most dense.

$$\text{square error} = \int_0^\infty \left(F_{model}\left(\bar{t}\right) - F(\bar{t})\right)^2 d\bar{t} \tag{5.6}$$

5.3.3 Calculating the residence time distribution of a reactor

Using simple conservation of mass arguments, the average concentration $\bar{c}_{av}$ inside a slug in dimensionless form can be given by equation 5.7:

$$\frac{d\bar{c}_{av}(\bar{t})}{d\bar{t}} = \frac{A\ d}{V}\left(\bar{c}_i(\bar{t}) - \bar{c}_o(\bar{t})\right) \tag{5.7}$$

where $\bar{c}_i$ and $\bar{c}_o$ are the dimensionless inflow and outflow concentrations respectively.

The Laplace-Transform of the above expression is:

$$\bar{s}\ \bar{C}_{av}(\bar{s}) - \bar{c}_{av}(0) = \frac{A\ d}{V}\left(\bar{C}_i(\bar{s}) - \bar{C}_o(\bar{s})\right) \tag{5.8}$$

A slug of zero initial concentration $\bar{c}_{av}(0) = 0$ experiencing an input $\bar{C}_i(\bar{s})$ gives an output $\bar{C}_o(\bar{s}) = \bar{E}(\bar{s})\bar{C}_i(\bar{s})$, where $\bar{E}(\bar{s})$ is the Laplace Transform of the residence time distribution function of a single unit cell. This can be substituted in equation 5.8 to give:

$$\bar{C}_{av}(\bar{s}) = \frac{A\ d}{V}\frac{\bar{C}_i(\bar{s})\left(1 - E(\bar{s})\right)}{\bar{s}} \tag{5.9}$$

The first slug needs to be considered differently because it has unit concentration and experiences a 0 input concentration. It can be shown that the output of the first slug is given by $\bar{C}_o^1 = \left(\frac{1-E(\bar{s})}{\bar{s}}\right)$ and from equation 5.8 $\bar{C}_{av}^1(\bar{s}) = \frac{1}{\bar{s}} - \frac{A\ d}{V}\left(\frac{1-E(\bar{s})}{\bar{s}}\right)$. The subsequent slugs average concentration and output are given in Table 5.6.

Once $E(\bar{t})$ is known, the problem becomes that of obtaining $E(\bar{s})$ from expressions of $E(\bar{t})$ and of calculating, usually numerically, the inverse Laplace transform for expressions of $\bar{C}_{av}^n(\bar{s})$ at the appropriate reactor space time to obtain the reactor residence time distribution. The Laplace transform of the residence time distribu-

Slug output		Slug concentration	
$\bar{C}_o^1(\bar{s})$	$\left(\frac{1-E(\bar{s})}{\bar{s}}\right)$	$\bar{C}_{av}^1(\bar{s})$	$\frac{1}{\bar{s}} - \frac{A\ d}{V}\left(\frac{1-E(\bar{s})}{\bar{s}^2}\right)$
$\bar{C}_o^2(\bar{s})$	$E(\bar{s})\left(\frac{1-E(\bar{s})}{\bar{s}}\right)$	$\bar{C}_{av}^2(\bar{s})$	$\frac{A\ d}{V}\left(\frac{1-E(\bar{s})}{\bar{s}}\right)^2$
$\bar{C}_o^3(\bar{s})$	$E^2(\bar{s})\left(\frac{1-E(\bar{s})}{\bar{s}}\right)$	$\bar{C}_{av}^3(\bar{s})$	$\frac{A\ d}{V}\left(\frac{1-E(\bar{s})}{\bar{s}}\right)^2 \bar{E}(\bar{s})$
$\bar{C}_o^n(\bar{s})$	$E^{n-1}(\bar{s})\left(\frac{1-E(\bar{s})}{\bar{s}}\right)$	$\bar{C}_{av}^n(\bar{s})$	$\frac{A\ d}{V}\bar{E}^{n-2}(\bar{s})\left(\frac{1-E(\bar{s})}{\bar{s}}\right)^2$

Tab. 5.6: The Laplace Transforms of the output film and average concentration of the slug n

tion curve would need to be calculated from the Laplace transform of the density function.

$$E(\bar{s}) = \bar{s}F(\bar{s}) + F(0) \tag{5.10}$$

To obtain $F(\bar{s})$ the transforms of the spline functions used in the interpolation are needed. For any polynomial of spline interpolating the data in $(\bar{t}_{n-1} \leq \bar{t} \leq \bar{t}_n)$, the Laplace transform is:

$$\begin{aligned}
&\int_{\bar{t}_{n-1}}^{\bar{t}_n} \left[\alpha_{n-1} + \beta_{n-1}(\bar{t} - \bar{t}_{n-1}) + \varepsilon_{n-1}(\bar{t} - \bar{t}_{n-1})^2 + \phi_{n-1}(\bar{t} - \bar{t}_{n-1})^3\right] e^{-\bar{s}\bar{t}} d\bar{t} \\
&= \left[\frac{e^{-\bar{s}\bar{t}_{n-1}} - e^{-\bar{s}\bar{t}_n}}{\bar{s}}\right]\alpha_{n-1} + \left[\frac{\left(e^{-\bar{s}\bar{t}_{n-1}} - e^{-\bar{s}\bar{t}_n}\right)}{\bar{s}^2} - \frac{(\bar{t}_n - \bar{t}_{n-1})\, e^{-\bar{s}\bar{t}_n}}{\bar{s}}\right]\beta_{n-1} \\
&\quad + \left[\frac{2\left(e^{-\bar{s}\bar{t}_{n-1}} - e^{-\bar{s}\bar{t}_n}\right)}{\bar{s}^3} - \frac{2e^{-\bar{s}\bar{t}_n}(\bar{t}_n - \bar{t}_{n-1})}{\bar{s}^2} - \frac{e^{-\bar{s}\bar{t}_n}(\bar{t}_n - \bar{t}_{n-1})^2}{\bar{s}}\right]\varepsilon_{n-1} \\
&+ \left[\frac{6\left(e^{-\bar{s}\bar{t}_{n-1}} - e^{-\bar{s}\bar{t}_n}\right)}{\bar{s}^4} - \frac{6e^{-\bar{s}\bar{t}_n}(\bar{t}_n - \bar{t}_{n-1})}{\bar{s}^3} - \frac{3e^{-\bar{s}\bar{t}_n}(\bar{t}_n - \bar{t}_{n-1})^2}{\bar{s}^2} - \frac{e^{-\bar{s}\bar{t}_n}(\bar{t}_n - \bar{t}_{n-1})^3}{\bar{s}}\right]\phi_{n-1}
\end{aligned}$$

The Laplace transform of the interpolated function $F(\bar{t})$, with N data points is given by:

Function	time for evaluation
$\mathcal{L}^{-1}\bar{C}^1_{av}(s)$	$L_{reactor}$
$\mathcal{L}^{-1}\bar{C}^2_{av}(s)$	$L_{reactor} + (L_b + L_s)$
:	:
$\mathcal{L}^{-1}\bar{C}^n_{av}(s)$	$L_{reactor} + (L_b + L_s)$

Tab. 5.7: Time of evaluation of inverse Laplace Transform

$$\mathcal{L}\left(F(t)\right) = \sum_{n=1}^{N} \left[\frac{e^{-\bar{s}\bar{t}_{n-1}} - e^{-\bar{s}\bar{t}_n}}{\bar{s}}\right] \alpha_{n-1} + \left[\frac{\left(e^{-\bar{s}\bar{t}_{n-1}} - e^{-\bar{s}\bar{t}_n}\right)}{\bar{s}^2} - \frac{\left(\bar{t}_n - \bar{t}_{n-1}\right) e^{-\bar{s}\bar{t}_n}}{\bar{s}}\right] \beta_{n-1} + \left[\frac{2\left(e^{-\bar{s}\bar{t}_{n-1}} - e^{-\bar{s}\bar{t}_n}\right)}{\bar{s}^3} - \frac{2e^{-\bar{s}\bar{t}_n}\left(\bar{t}_n - \bar{t}_{n-1}\right)}{\bar{s}^2} - \frac{e^{-\bar{s}\bar{t}_n}\left(\bar{t}_n - \bar{t}_{n-1}\right)^2}{\bar{s}}\right] \varepsilon_{n-1} + \left[\frac{6\left(e^{-\bar{s}\bar{t}_{n-1}} - e^{-\bar{s}\bar{t}_n}\right)}{\bar{s}^4} - \frac{6e^{-\bar{s}t_n}\left(\bar{t}_n - \bar{t}_{n-1}\right)}{\bar{s}^3} - \frac{3e^{-\bar{s}\bar{t}_n}\left(\bar{t}_n - \bar{t}_{n-1}\right)^2}{\bar{s}^2} - \frac{e^{-\bar{s}\bar{t}_n}\left(\bar{t}_n - \bar{t}_{n-1}\right)^3}{\bar{s}}\right] \phi_{n-1} \tag{5.11}$$

From equation 5.10 the expression for $E(\bar{s})$ needed for the different concentrations of the different slugs (Table 5.6) can be calculated.

To obtain the output concentrations of the reactor, inversion of the Laplace transform of the average concentration needs to be performed. Numerical inversion is ideal for this type of problem as the concentrations that need to be evaluated are those of the slugs at the exit of the reactor. There are various known algorithms for this inversion and the one used in this work is an adaptation of Gaver functionals with Wynn's rho acceleration algorithm [125] as implemented in Mathematica® [126].

The concentration output of each unit cell exiting the reactor is obtained from evaluating the inverse Laplace transform of functions in Table 5.6 at dimensionless times given by Table 5.7. From the speed of each unit cell and its length as well as the length of the reactor, the concentration at different times can be plotted and converted to a reactor residence time distribution curve $E_{reactor}(\bar{t})$ when normalised.

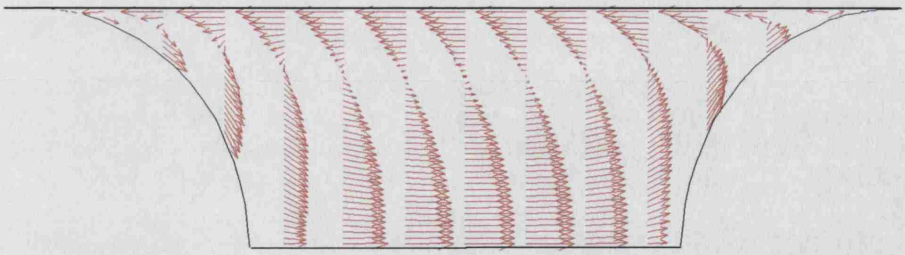

Fig. 5.4: The flow inside the liquid slug plotted as obtained from the solved hydrodynamics. It shows the development of parabolic flow away from the bubble caps. The conditions are ($Ca = 10^{-5}$, $Re = 4.5 \times 10^{-5}$, $L_s = 1, L_b = 1.1$).

5.4 Results and discussion

5.4.1 Hydrodynamics

The hydrodynamic solution shows the typical recirculation patterns in the liquid slug in Taylor flow[83] (Fig. 5.4). As expected longer distance from the bubbles was found for the establishment of parabolic flow to be required with increasing Re (chapter 3).

5.4.1.1 Effect of the different dimensionless numbers

The moments of the residence time distribution curves for the different cases studied are summarised in Table 5.8. The first moment is used as a further check for the quality of the numerical solution. This value should match the value of the space time of the unit cell calculated simply from expression 5.12. It can be seen that all runs with $Pe = 10$ have a considerably lower value of the first mean than the space time of the unit cell. This is attributed to the break down of the assumption that convection dominates mass transfer at the boundaries necessary in residence time distribution analysis. Boundary (B1) is not a naturally conservative boundary and diffusion at the boundary accounts for these results.

$$\text{Dimensionless space time} = \frac{V}{A_f d} = \frac{R(2(R-\delta)+L_s) - \frac{4}{3}(R-\delta)^3}{2R\left(R^2-(R-\delta)^2\right)} + L_b \quad (5.12)$$

δ=3.06 x 10^{-2}	Re	$4.5x10^{-5}$					3
	Pe	100000	10000	1000	100	10	100000
Ls	V/Q	469.0					
	$\bar{\mu}(x10^{-2})$	4.69	4.67	4.68	4.68	2.54	4.69
	$\bar{\mu}^2(x10^{-5})$	6.86	4.52	4.34	4.33	1.28	6.87
	$\bar{\sigma}^2(x10^{-5})$	4.66	2.33	2.15	2.14	0.63	4.67
0.25	$\bar{\mu}^3(x10^{-7})$	162	64	59	59	10	163
	V/Q	1071					
	$\bar{\mu}(x10^{-2})$	10.7	10.6	10.6	9.94	2.59	10.7
	$\bar{\mu}^2(x10^{-5})$	35.4	23.0	22.2	19.4	1.31	35.4
	$\bar{\sigma}^2(x10^{-5})$	24.0	11.7	10.9	9.51	0.644	24.0
1.00	$\bar{\mu}^3(x10^{-8})$	183	71.7	66.9	55.6	0.984	183
	V/Q	3480					
	$\bar{\mu}(x10^{-3})$	3.46	3.47	3.47	3.22	0.87	3.5
	$\bar{\mu}^2(x10^{-5})$	291	244	240	203	15	293
	$\bar{\sigma}^2(x10^{-5})$	171	123	120	100	7.14	173
4.00	$\bar{\mu}^3(x10^{-9})$	360	255	246	187	3.68	368

(a)

δ=1.0 x 10^{-3}	Re	$4.5x10^{-5}$					30
	Pe	100000	10000	1000	100	10	100000
Ls	V/Q	1.46E+02					
	$\bar{\mu}(x10^{-2})$	1.46	1.46	1.46	1.46	0.928	1.46
	$\bar{\mu}^2(x10^{-4})$	12.0	4.89	4.19	4.19	1.69	12.0
	$\bar{\sigma}^2(x10^{-4})$	9.91	2.76	2.07	2.05	0.83	9.91
0.25	$\bar{\mu}^3(x10^{-7})$	18.6	2.49	1.77	1.79	0.463	18.5
	V/Q	333					
	$\bar{\mu}(x10^{-2})$	3.32	3.33	3.33	3.33	2.08	3.33
	$\bar{\mu}^2(x10^{-5})$	6.22	2.52	2.22	2.19	0.856	6.19
	$\bar{\sigma}^2(x10^{-5})$	5.12	1.41	1.11	1.08	0.42	5.09
1.00	$\bar{\mu}^3(x10^{-7})$	205	28.4	21.9	21.4	5.23	203
	V/Q	1083					
	$\bar{\mu}(x10^{-2})$	10.8	10.8	10.8	10.7	7.06	10.8
	$\bar{\mu}^2(x10^{-5})$	40.4	24.5	23.3	22.9	9.64	40.7
	$\bar{\sigma}^2(x10^{-5})$	28.7	12.8	11.6	11.3	4.67	28.97
4.00	$\bar{\mu}^3(x10^{-8})$	239	82.2	74.6	72.7	19.7	239

(b)

δ=1.0 x 10^{-2}	Re	$4.5x10^{-5}$					300
	Pe	100000	10000	1000	100	10	100000
Ls	V/Q	15					
	$\bar{\mu}(x10^{-1})$	1.40	1.56	1.56	1.56	1.35	1.40
	$\bar{\mu}^2(x10^{-3})$	9.85	1.37	0.513	0.434	0.325	9.85
	$\bar{\sigma}^2(x10^{-3})$	9.65	1.12	0.269	0.192	0.144	9.65
0.25	$\bar{\mu}^3(x10^{-5})$	147	2.39	0.293	0.200	0.116	147
	V/Q	34					
	$\bar{\mu}(x10^{-1})$	3.28	3.48	3.45	3.45	3.05	3.28
	$\bar{\mu}^2(x10^{-3})$	48.5	6.60	2.53	2.24	1.69	48.5
	$\bar{\sigma}^2(x10^{-3})$	47.5	5.40	1.34	1.05	0.764	47.6
1.00	$\bar{\mu}^3(x10^{-5})$	1487	27.0	2.93	2.33	1.42	1487
	V/Q	110					
	$\bar{\mu}(x10^{-2})$	1.07	1.10	1.10	1.10	1.01	1.1
	$\bar{\mu}^2(x10^{-4})$	21.8	3.89	2.45	2.25	1.71	22.7
	$\bar{\sigma}^2(x10^{-4})$	20.7	2.67	1.24	1.03	0.685	21.5
4.00	$\bar{\mu}^3(x10^{-6})$	824	22.1	8.20	6.88	4.24	909

(c)

Tab. 5.8: Table of moments comparing the numerical results with other literature model predictions

5.4.1.2 General features of the RTD/spacial variance curves

Two distinct types of unit cell concentration patterns are observed which depend on the Peclet number value. For high Peclet numbers $\{1000, 10000, 100000\}$ the pattern roughly resembles the hydrodynamic flow lines in the liquid. A typical concentration distribution in the slug and corresponding density function $F(t)$ of the output are given in Fig. 5.5. Typical features of these curves are:

1. An initial delay, corresponding to the time for the film to travel across the unit cell.

2. A rapid rise in output concentration as the film exits the unit cell.

3. A slower rise in concentration with a number of plateaus. The length of each plateau corresponds to the time of a single circulation of the vortex in the slug. During this stage the concentration of the outer parts of the vortex increases rapidly to the film concentration. The inner parts of the vortex remain virtually tracer free.

4. A very slow exponential increase to the final unit concentration value. This is a typical behaviour of the diffusion dominated process by which the tracer concentration in the inner part of the vortex slowly builds up.

The discrete points of the $\bar{F}(\bar{t})$ curves can be fitted using splines (section 5.3.2) and differentiated to accurately obtain $\bar{E}(\bar{t})$ which reveals some of the features more clearly (Fig. 5.6). The plateaus in the $\bar{F}(\bar{t})$ curve correspond to residence times with zero/very low probability for an entering solute to remain in the system. The peaks in the $\bar{E}(\bar{t})$ curve correspond to the sharp rises in $\bar{F}(\bar{t})$ and represent the most probable residence times with the area of each peak determining the magnitude of the corresponding probabilities. The peaks do not drop by a fixed factor. Residence time distribution curves such as those shown in Fig. 5.6 are typical of systems with very strong internal circulation.

The second concentration behavioural pattern appears in the cases of low Peclet numbers $\{10, 100\}$ and is exemplified by Fig. 5.7. Typical features of these curves are:

1. An initial delay, corresponding to the time for the film to travel across the unit cell. There is no distinct film region observed from the concentration diagrams.

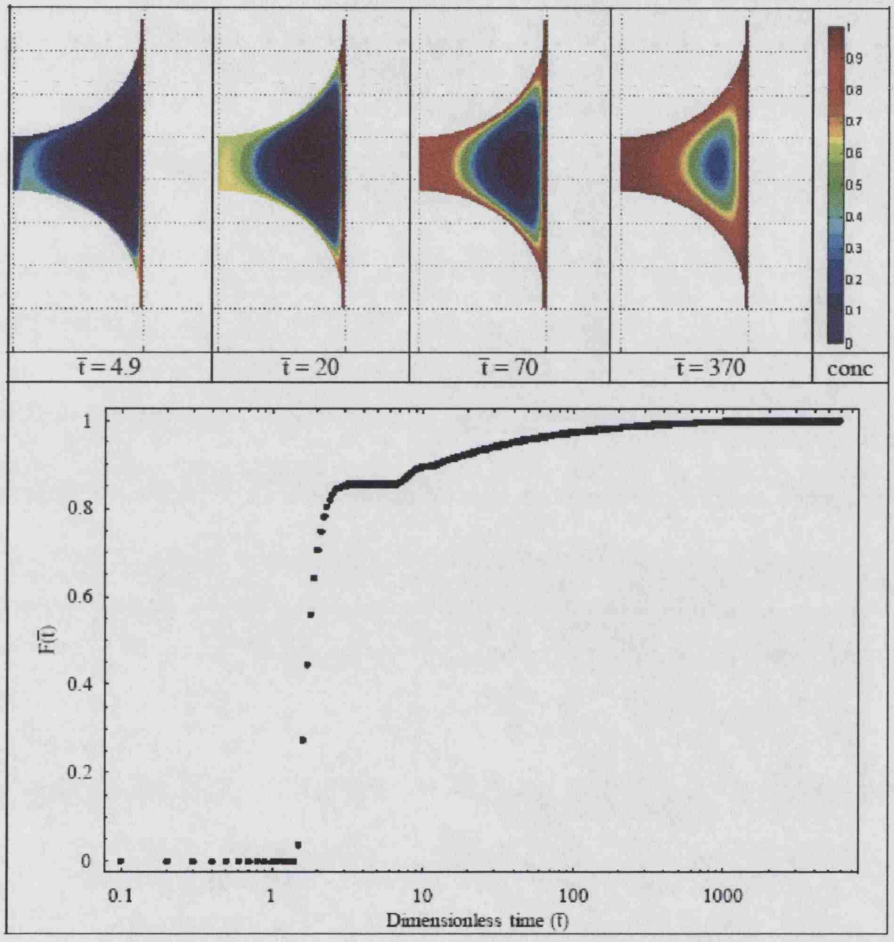

Fig. 5.5: Variation with time of slug concentration profile and density function for high *Pe*.

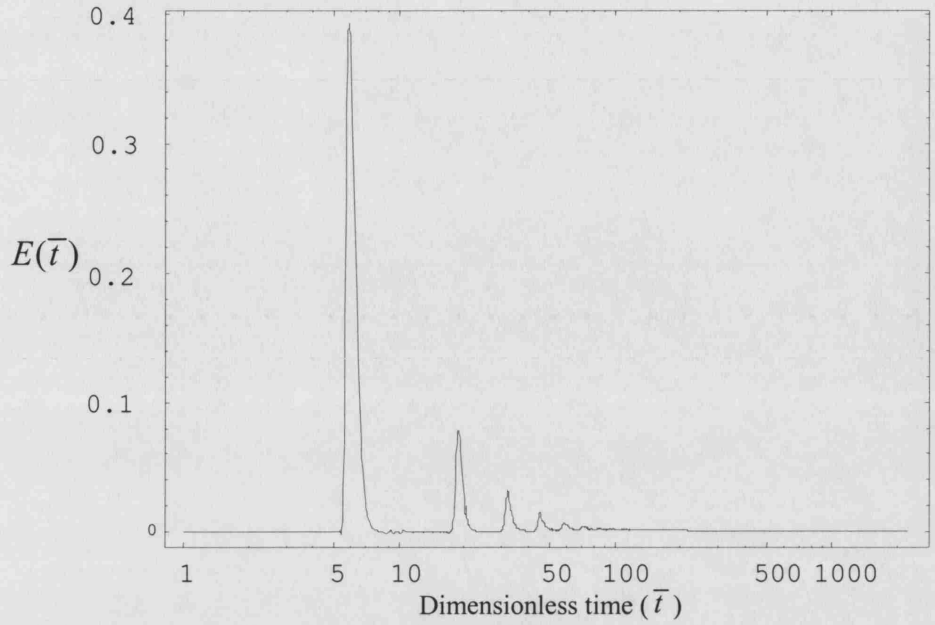

Fig. 5.6: Residence time distribution for a unit cell with parameters: $Ca = 10^{-3}$, $Pe = 10000$, $L_s = 4$, $Re = 4.5 \times 10^{-5}$.

2. The concentration in the unit cell rises rapidly to the final unit concentration value because of strong diffusivity. The region inside the slug is well mixed and the exit concentration behaviour will be shown to be reasonably approximated by an ideal mixer (section 5.4.1.3.1).

The residence time distribution curves of such systems were again obtained by interpolation and differentiation and typically show no peaks corresponding to recirculation times (Fig. 5.8).

5.4.1.2.1 Effect of Re To investigate the effect of Re, a $\bar{\delta} = 10^{-2}$ corresponding to $Ca \sim 10^{-3}$ was chosen as this gives the largest Re range (Table 5.2).In addition the highest Pe for that range was used $Pe = 10^5$, where convection effects are most significant. The graphs, shown in Fig. 5.9 for highest and lowest Re, show a good match between the two curves and it is therefore concluded that the Reynolds number has minimal effect on the residence time distribution for the range of parameters studied. This result allows the influence of Re to be decoupled from the more significant effect of change in film thickness with Re which occurs at larger Ca numbers, $Ca > 10^{-3}$.

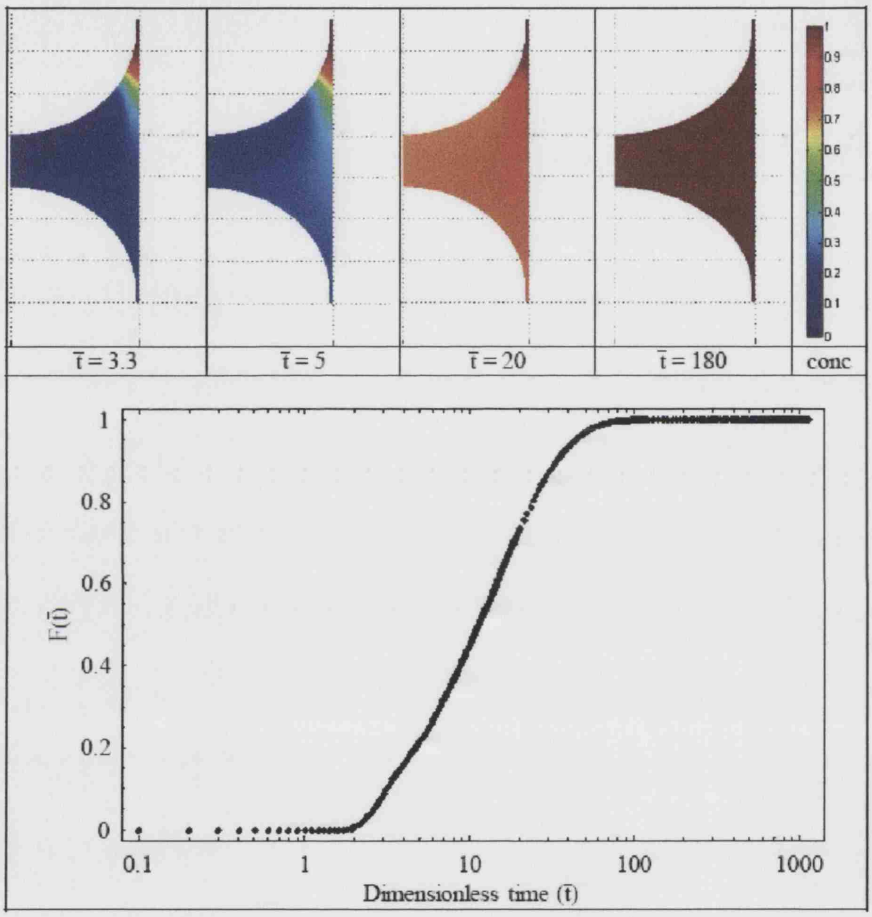

Fig. 5.7: Variation with time of slug concentration profile and density function for low Pe.

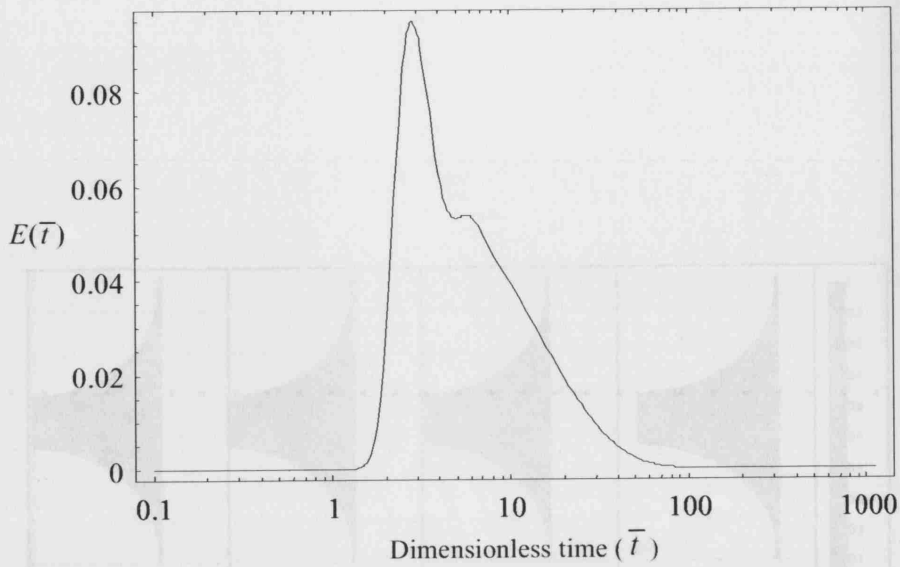

Fig. 5.8: Residence time distribution for a unit cell with parameters: $Ca = 10^{-3}$, $Pe = 100$, $L_s = 0.25$, $Re = 4.5 \times 10^{-5}$.

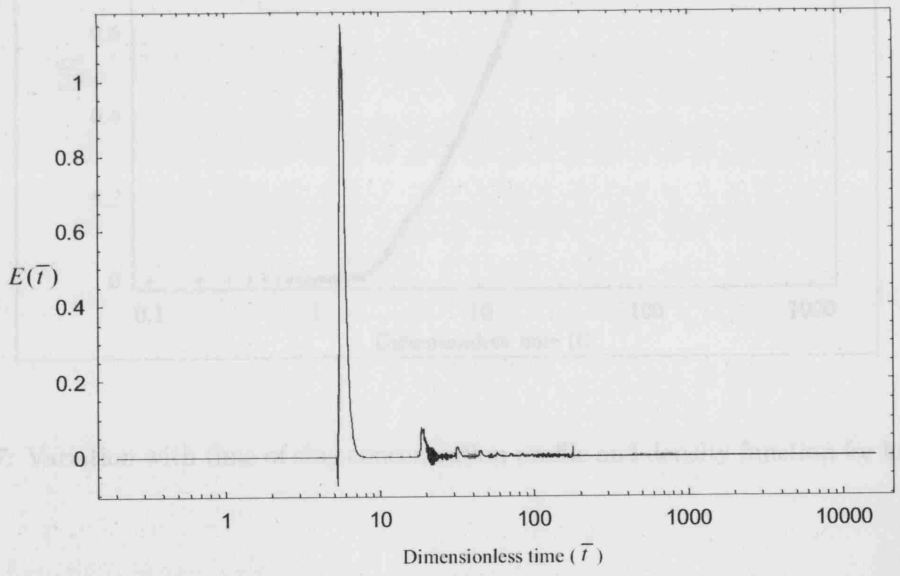

Fig. 5.9: Reynold numbers {Black: $Re = 4.5 \times 10^{-5}$, Red: $Re = 300$} have negligible effects on RTD curve ($\bar{\delta} = 10^{-3}$, $Pe = 10^{-5}$, $L_s = 4$)

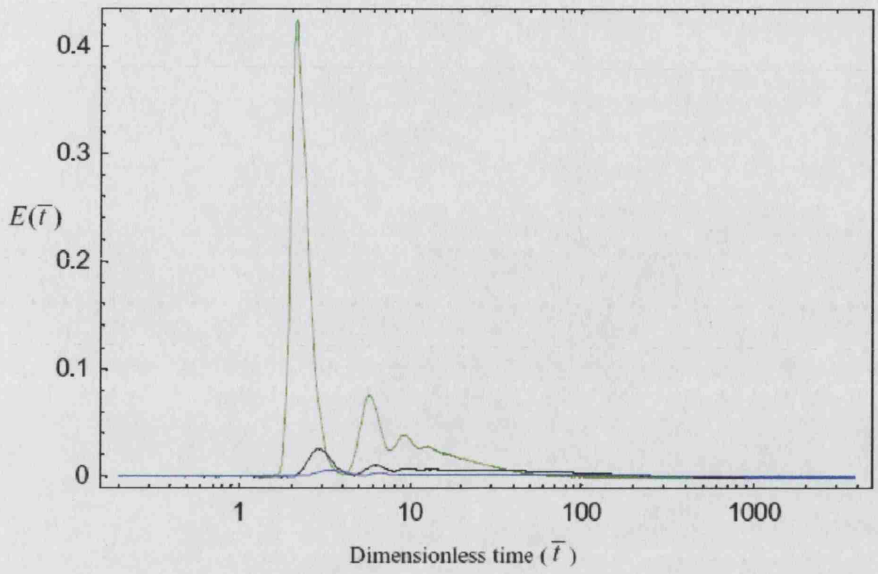

Fig. 5.10: With decreasing $\bar{\delta}$, the peaks of the curve become smaller and less noticeable. $Ls = 0.25$, $Pe = 1000$ {Green: $\bar{\delta} = 10^{-2}$, Black: $\bar{\delta} = 10^{-3}$, Blue: $\bar{\delta} = 3.06 \times 10^{-4}$}

5.4.1.2.2 Effect of film thickness $\bar{\delta}$ With increasing film thickness, the peaks of the $E(\bar{t})$ curve become larger and more distinct, (Fig. 5.10). When the film is thinner it loses more (by percentage) of its tracer content by diffusion to the recirculating vortex as it moves through the slug, which implies that more of the contents mix with the vortex. This effect is also expected to increase with increasing slug length as the length available for diffusion increases.

5.4.1.2.3 Effect of Pe The effect of changing the Peclet number is demonstrated in Fig. 5.11. With decreasing Peclet number diffusive effects dominate and in the $E(\bar{t})$ curve the peaks are shorter and broader. For $Pe = 100$ the peaks are no longer distinguishable.

5.4.1.2.4 Effect of Ls Increasing the slug length increases accordingly the delay before the response in the outlet appears as the concentration has to travel through a longer film. The separation between the peaks on the RTD curve also increases as the resulting circulation time within a slug increases. The increased film length also means that there is a longer distance for diffusion to occur and hence a larger proportion of the material carried in the film is transferred to the vortex region. This results in a decrease in the size of the peaks (Fig. 5.12).

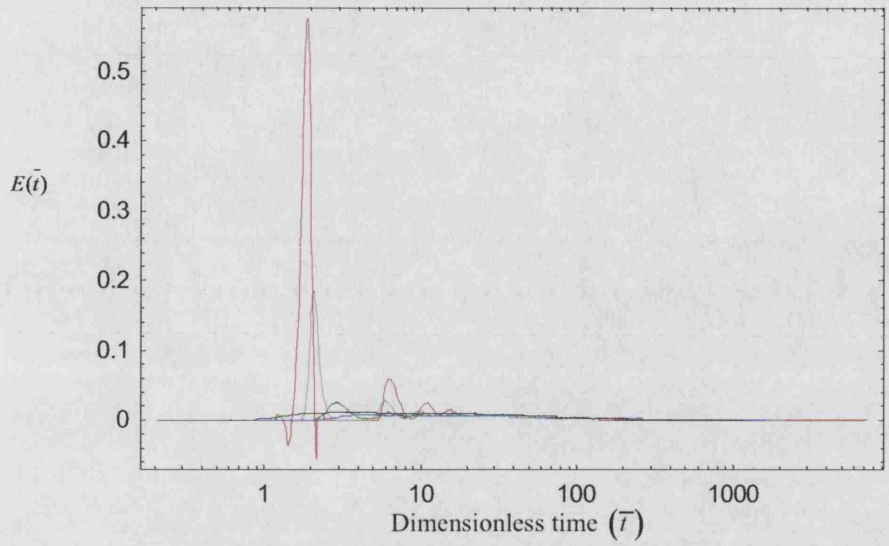

Fig. 5.11: The effects of varying the Peclet number on the shape of the RTD curve $L_s = 0.25$, $\bar{\delta} = 10^{-3}$, $Re = 4.5 \times 10^{-5}$. {Red: $Pe = 10^5$, Grey: $Pe = 10^4$, Green: $Pe = 10^3$, Blue: $Pe = 10^2$, Black: $Pe = 10$. The undershoots ($E(\bar{t}) < 0$) in the curve of $Pe = 10^5$are osscillations which arise from interpolation of near zero numerical values with polynomials and should be ignored.

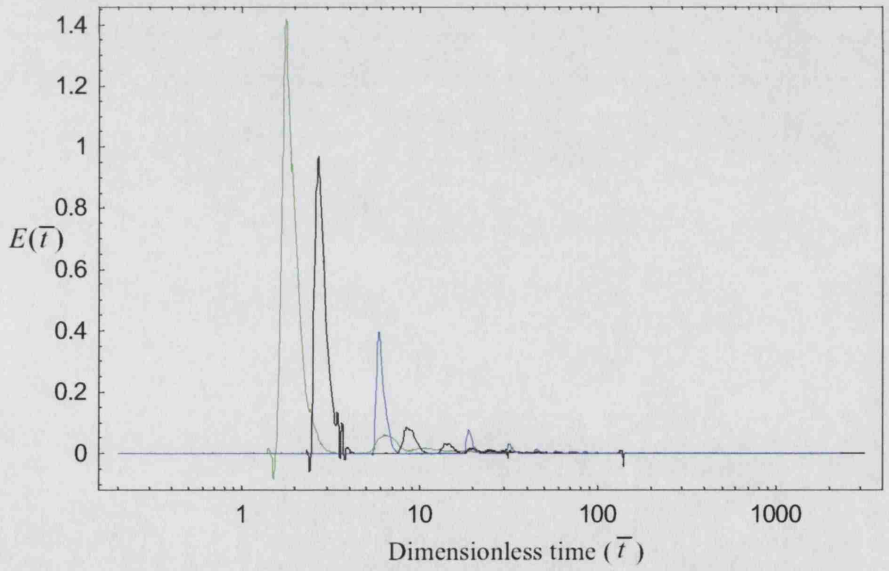

Fig. 5.12: The effects of varying the Peclet number on the shape of the RTD curve $Pe = 10^4$, $\bar{\delta} = 10^{-3}$, $Re = 4.5 \times 10^{-5}$. {Green: $L_s = 0.25$, Black: $L_s = 1$, Blue: $L_s = 4$}

5.4.1.3 Comparison to other existing models

Residence time distribution curves and their moments produced by existing models are compared with the results of the current simulation in this section. The film surrounding the bubbles results in a simple shift of the obtained RTD curve to the left by a time equivalent to the time constant $(L_b - 1.1)$ corresponding to the simple delay the bubble introduces.

5.4.1.3.1 CSTR-PFR combination The residence time curve of a CSTR-PFR unit where the mixing in the slug is assumed to resembles of a CSTR and the film surrounding the bubble behaves like a PFR [96]:

$$E_{CSTR-PFR}(\bar{t}) = \begin{cases} \frac{e^{\frac{L_b - \bar{t}}{\bar{t}_s}}}{\bar{t}_s} & t \geq L_b \\ 0 & t < L_b \end{cases} \tag{5.13}$$

The first three moments are calculated as follows:

$$\bar{\mu}^1 = \bar{t}_s + L_b \tag{5.14}$$

$$\bar{\mu}^2 = L_b^2 + 2L_b\bar{t}_s + 2\bar{t}_s^2 \tag{5.15}$$

$$\bar{\mu}^3 = L_b^3 + 3L_b^2\bar{t}_s + 6L_b\bar{t}_s + 6\bar{t}_s^3 \tag{5.16}$$

where $\bar{t}_s$ is the space time of the slug which can be calculated from the slug geometry:

$$\bar{t}_s = \frac{V_{slug}}{A_f d} = \frac{R^2(2(R-\delta) + L_s) - \frac{4}{3}(R-\delta)^3}{2R\left(R^2 - (R-\delta)^2\right)}$$

This model has no fitting parameters and can thus be easily used. Qualitatively however, it is quite clear that the single exponential decay in the residence time distribution is not going to be able to account for the multi-peak behaviour observed in the residence time distribution curves of high Peclet numbers. Although it contains terms relating to film thickness and slug length, the Peclet number does not feature and the difference between high and low Peclet number cases cannot be resolved. An example where this model is a good representation of the numerical results is shown in Fig. 5.13, noting the logarithmic scales and despite the initial discrepancies. From Table 5.10 it can be observed that the CSTR-PFR moments are furthest

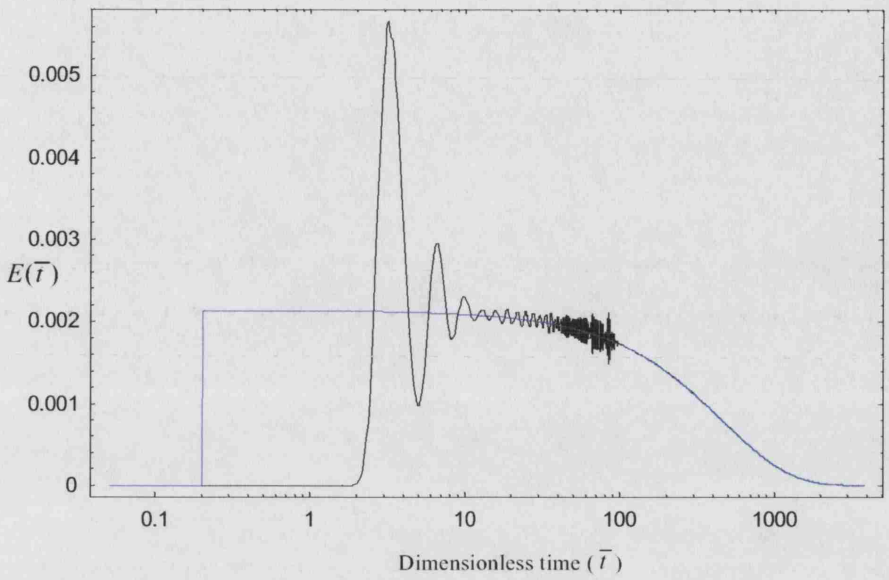

Fig. 5.13: The behaviour of different models {Black: Numerical Simulation, Blue: CSTR-PFR} for the case of $\{\bar{\delta} = 3.06 \times 10^{-4}\ \ Pe = 1000,\ Re = 4.5 \times 10^{-5},\ L_s = 0.25,\ L_b = 1.1\}$. The reader should note the logarithmic time scale used and observe that the discrepancies are mainly for the early parts of the curve.

from the simulation results compared to the other models at ($Pe = 10^5$). It can be concluded therefore, that the CSTR-PFR model is not a good representation of the unit cell at high Pe but a good representation at low Pe. For $Pe < 10$ the unit cell model, because of diffusion through the inlet, does not behave as a closed vessel and cannot be used to judge the results. The decrease in the film thickness also seems to improve results in better matches with the numerical results, this may be due to the improved mixing by diffusion between the incoming liquid and the slug improved by the thin film.

5.4.1.3.2 Two-region model The output concentration of this model is found to be (derived in Appendix D):

$$E_{2Region}(\bar{t}) = \begin{cases} -\dfrac{e^{-\frac{1}{2}(\zeta+\alpha+\beta+\gamma)(\bar{t}-L_b)}(-\zeta-\alpha+\beta+\gamma)(\zeta+\alpha+\beta+\gamma))}{4\zeta} \\ -\dfrac{e^{\left[\zeta-\frac{1}{2}(\zeta+\alpha+\beta+\gamma)\right](\bar{t}-L_b)}(\zeta-\alpha+\beta+\gamma)\left[\zeta-\frac{1}{2}(\zeta+\alpha+\beta+\gamma)\right]}{2\zeta} & t \geq L_b \\ 0 & t < L_b \end{cases} \tag{5.17}$$

The first three moments of the two-region model can be easily calculated as:

$$\bar{\mu}^1 = \frac{(\beta+\gamma)}{\alpha\gamma} + L_b \tag{5.18}$$

$$\bar{\mu}^2 = \frac{2\beta(\alpha+\beta) + 2(2+L_b\alpha)\beta\gamma + (2+L_b\alpha(2+L_b\alpha))\gamma^2}{\alpha^2\gamma^2} \tag{5.19}$$

$$\bar{\mu}^3 = \frac{6\beta(\alpha+\beta)^2 + 6\beta(3\beta+\alpha(2+L_b(\alpha+\beta)))\gamma}{\alpha^3\gamma^3} \tag{5.20}$$

$$+\frac{3(6+L_b\alpha(4+L_b\alpha))\beta\gamma^2 + (6+L_b\alpha(6+L_b\alpha(3+L_b\alpha)))\gamma^3}{\alpha^3\gamma^3} \tag{5.21}$$

where

$$\alpha = \frac{A_f d}{V_1} \tag{5.22}$$

$$\beta = \frac{Sh}{Pe}\frac{A_s d}{V_1} \tag{5.23}$$

$$\gamma = \frac{Sh}{Pe}\frac{A_s d}{V_2} \tag{5.24}$$

While it is difficult to calculate the exact volumes of the film and the vortex region, V_1 and V_2 respectively, and transfer area between them, A_s, without identifying the streamline separating the two regions. They can be however estimated reasonably well though using expressions 5.25-5.27 (see also Appendix D for more detailed comments).

$$V_1 = \pi R^2 (Ls + 2(R-\delta)) \left(\frac{R^2}{(R-\delta)^2} - 1\right) \tag{5.25}$$

$$V_2 = \left[\pi R^2 (Ls + 2(R-\delta)) - \frac{4}{3}\pi (R-\delta)^3\right] - V_1 \tag{5.26}$$

$$A_s = 2\pi (R-\delta)(Ls + 2(R-\delta)) \tag{5.27}$$

This model has a single fitting parameter, the Sherwood number $Sh = \frac{k_L d}{D}$, and includes in its formulation all the dimensionless parameters affecting the behaviour of the slug. Published values for Sh are usually obtained from experiments on liquid to wall mass transfer [97, 110, 98, 118, 119]. Rather than relying on such values however, the model results were fitted to the curves in this work using Sh

Sh								
$\delta = 3.04 \times 10^{-4}$			$\delta = 1 \times 10^{-3}$			$\delta = 1 \times 10^{-2}$		
Ls \ Pe	10000	100000	Ls \ Pe	10000	100000	Ls \ Pe	10000	100000
0.25	60	66	0.25	65	86	0.25	55	63
1.00	37	37	1.00	39	47	1.00	41	41
4.00	39	31	4.00	40	35	4.00	39	33

Tab. 5.9: Table of fitted Sherwood numbers

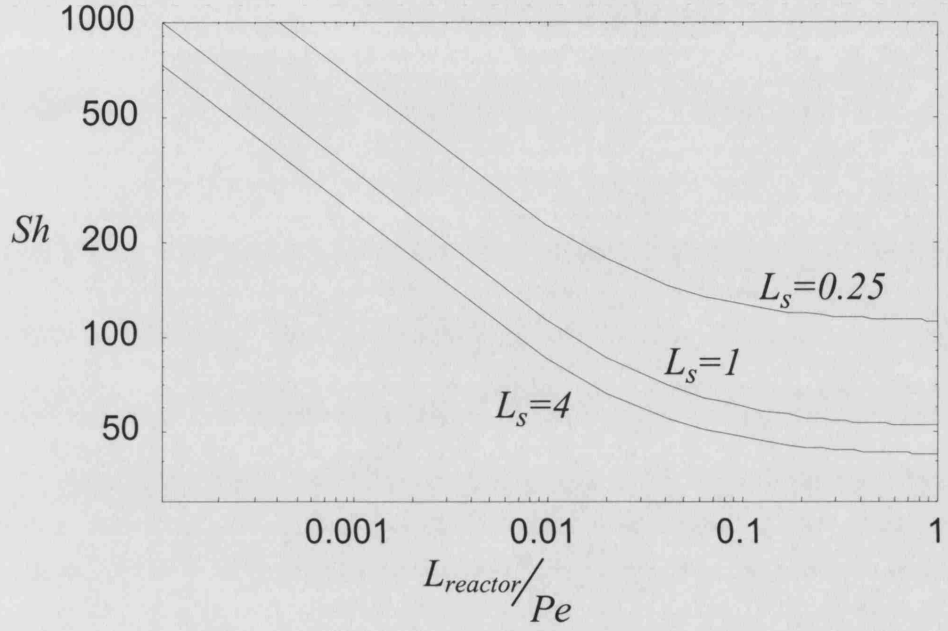

Fig. 5.14: The variation of Sh with $L_{reactor}$, Pe, and L_s based on the correlation by Kreutzer [98].

as the fitting parameter. The method of least square error was used to fit Sh and then the 2nd and 3rd moments were compared. Typical curve shapes obtained at high Peclet numbers are shown in Fig. 5.15 and fitted Sh numbers can be found in Table 5.9.

These values were found to be of the order of those obtained by the correlations published by Kreutzer [98] and Gruber et al. [119]. The values of Sh were found to be smaller by less than a factor of two from what Kreutzer's correlation predicts and by up to a factor of 4 smaller than the correlation of Gruber et al. . It should be noted that Grubers correlation is a fit over a very larger range of slug length values ($1 \leq L_s \leq 600$). The values considered here are very much towards the lower end of that range which may explain the larger discrepancies.

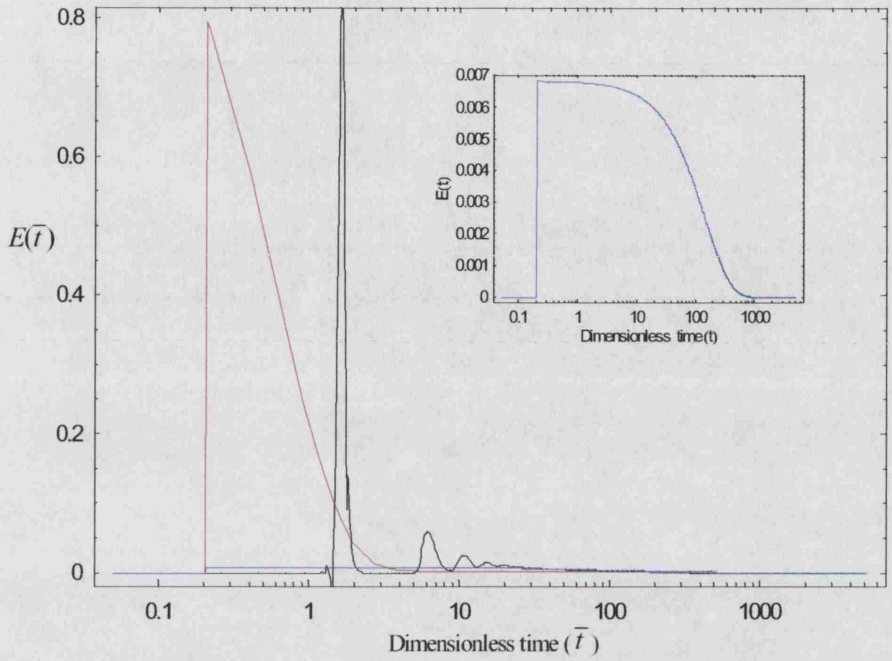

Fig. 5.15: The behaviour of different models {Black: Numerical Simulation, Red: Two Region, Blue: CSTR-PFR} for the case of $\{\bar{\delta} = 10^{-3}, Re = 4.5 \times 10^{-5}, L_s = 0.25, L_b = 1.1\}$. The best fitting Sherwood number for the two region model was found to be $Sh = 87$. The reader should note the logarithmic time scale used which causes the area under the different curves to appear disproportionate.

The correlation of Kreutzer relates the Sh to the ratio $\frac{L_{reactor}}{Pe}$ and L_s. For the cases analysed here $0.2 < \frac{L_{reactor}}{Pe} \leq 2$ which places them at the end where Sh is insensitive to small changes in the ratio (Fig. 5.14) which can also be seen in Table 5.9. The trend of increasing Sh with decreasing L_s is not satisfied when going from the lengths of 1 to 4. The differences may not be due to to wrong estimation of Sh using either of the above correlations but may result from the poor representation of the unit cell by the two-region model.

Qualitatively it is not surprising that the exponential sum expression which results from the two-region model cannot account for the shapes of residence time curves obtained for high Peclet numbers. It is also not surprising for $Pe > 1000$ the first three moments match those of the numerical model better than those of the CSTR-PFR model (Table 5.10).

Interestingly, at Peclet numbers $Pe \leq 1000$ an optimum Sh could not be found, but the fitting was improved when Sh is increased to very large values improved the

fitting. The residual error plateaued to a constant value and was then insensitive to further increases in Sh. These Sh values considered are about 2 or more orders of magnitude larger than those predicted from correlations of [98]. The limit at large Sh for the two-region model is the CSTR-PFR model from which it can be clearly concluded that the two-region model offers no advantage over the CSTR-PFR one for $Pe \leq 1000$.

5.4.1.3.3 The model of Thulasidas et. al. In contrast to the above models, the model by Thulasidas et. al. [112] takes into account the cyclic nature of the output which results from a combination of dominating axial convection and slow radial diffusion. Certain points of the model development are repeated here to provide insight into the output given by the model.

The model assumes a constant output concentration from the unit cell for the duration of a cycle (the time for a complete rotation of a vortex in the slug). To explain how this assumption arises consider that the concentration is determined from the interaction of the film with the vortex which lasts for the entire cycle. During that cycle the vortex region interacts with a length of the film approximately double the slug length. The vortex material which interacts with the film in the first half cycle moves near to the centerline of the tube in the second half cycle and is assumed not to interact with the other part of the vortex (now interacting with the film). This results in the film experiencing the same condition as it moves through the unit cell for the duration of one cycle which results in a constant output.

Neglecting the velocity gradients in the liquid slug and assuming constant initial concentrations in the slug and the film, a unidirectional diffusion equation along the cross section is solved for time equal to one half cycle. The concentrations in the film and the co-flowing part of the vortex are averaged. The averaged concentration of the film at the end of the half cycle is the output concentration for the duration of the cycle whilst that of the top half vortex is the average concentration of the vortex after a complete cycle. The model is then repeated starting with the averaged concentration of the vortex and the 'new' inflow concentration of the film which is the output of the upstream unit cell.

The averaged concentrations obtained from the model, with the typographical errors in the expressions corrected from the original [112], was non-dimensionalised and is given for the film in equation 5.28 and for the vortex region of the slug in equation 5.29:

$$\bar{c}_{fav} = 1 + 4\left[\bar{c}_{10} - \bar{c}_{20}\right]\bar{r}_1^2 + \sum_{n=1}^{\infty} e^{-\frac{\lambda_n^2 \bar{t}}{Pe}} \left[\frac{-4\left[\bar{c}_{10} - \bar{c}_{20}\right]\bar{r}_1^2 J_1^2\left(\lambda_n \bar{r}_1\right)}{(0.5)^2\left(0.5^2 - \bar{r}_1^2\right)\lambda_n^2 J_0^2\left(0.5\lambda_n\right)}\right] \tag{5.28}$$

$$\bar{c}_{vav} = 1 + 4\left[\bar{c}_{10} - \bar{c}_{20}\right]\bar{r}_1 + \sum_{n=1}^{\infty} e^{-\frac{\lambda_n^2 \bar{t}}{Pe}} \left[\frac{16\left[\bar{c}_{10} - \bar{c}_{20}\right]\bar{r}_1 J_1\left(\lambda_n \bar{r}_1\right)\left[\bar{r}_1 J_1\left(\lambda_n \bar{r}_1\right) - \bar{r}_0 J_1\left(\lambda_n \bar{r}_0\right)\right]}{\left(\bar{r}_1 - \bar{r}_0\right)\lambda_n^2 J_0^2\left(0.5\lambda_n\right)}\right] \tag{5.29}$$

where

$$\bar{r}_1 = \sqrt{2 - \psi} \tag{5.30}$$

$$\bar{r}_0 = \frac{\sqrt{2 - \psi}}{\sqrt{2}} \tag{5.31}$$

and the eigenvalues are given in terms of the zeros of the Bessel function of the first order:

$$\lambda_n = 2\ Z_{1n} \tag{5.32}$$

The average film concentration is evaluated using equation 5.28 after a time equal to *half* a cycle time of the vortex with initial concentrations $\bar{c}_{10}$, the initial average vortex concentration, and $\bar{c}_{20} = 1$, the initial film concentration at the beginning of each cycle always taken as 1 for the step tracer input. This value is used as the output for the total cycle time. Similarly the average vortex concentration is evaluated using equation 5.29. The procedure is repeated using the previous averaged vortex concentration for a new $\bar{c}_{10}$ and the constant value of 1 for $\bar{c}_{20}$. The cycle time can be calculated from expression 5.33 which has been modified from the expression given by Thulasidas et. al. to account for the liquid volume around the bubble caps.

$$\bar{\tau}_{cycle} = \frac{2 + 6\ L_s + 4\bar{\delta}\left(3 + 4\bar{\delta}\left(2\bar{\delta} - 3\right)\right)}{3(1 + 8(\bar{\delta} - 1)\bar{\delta})} \tag{5.33}$$

The density function $F(\bar{t})$ obtained by the Thulasidas et. al. model is a series of plateaus, such as those seen with the current model at high Pe (Fig. 5.5). The

corresponding residence time distribution $E(\bar{t})$ from Thulasidas' model is a series of ideal pulses at times corresponding to the vortex circulation times which have an area equal to the calculated change in concentration between the different plateaus in the density function curve.

$$E(\bar{t}) = \sum_{i=1}^{\infty} A_i \, \delta_{dirac}(\bar{t} - L_b - i \times \bar{\tau}_{cycle}) \tag{5.34}$$

The model of Thulasidas et. al. was implemented using the first one hundred terms of the series and the moments are given in Table 5.10. It can be seen that it performs worst at the extremes of high and low Peclet numbers. The way the model is formulated is not conservative, so material which crosses the centre of the vortex is neglected in the averaging. This explains why the difference between the moments of the Thulasidas et. al. model and those of the numerical calculations are worst at low Pe. In addition the first moments do not match even at high Pe. This is attributed to the wrong estimation of the cycle time. $\bar{\tau}_{cycle}$ is the only parameter where the slug length features; from expression 5.33, a longer cycle time translates to a longer slug and hence corresponds to larger space times. Sensitivity analysis on $\bar{\tau}_{cycle}$ showed a small change of the variable to have a significant effect on the the first moment. If the original uncorrected expression of the cycle time by Thulasidas et. al. is used instead of equation 5.33, the performance is much worse. Also the first moments of the Thulasidas et. al. model are closer to the numerical ones with increasing slug length as the regions near the caps, neglected in the Thulasidas model, have lower contribution to the circulation time as compared to the rest of the unit cell. An iterative procedure can be suggested where $\bar{\tau}_{cycle}$ is adjusted until the first mean matches the space time of the unit cell or alternatively is fitted to match the peaks in the numerical data. Doing so will however change the nature from a zero parameter to a single parameter one and will not be attempted. Order of magnitude analysis of the generated moments, using the cycle time given by expression 5.33, shows a worsening performance when changing from $Pe = 10^4$ to $Pe = 10^5$ which may be attributed to the averaging of concentration carried out at the end of each half cycle time.

5.4.1.4 Reactor RTD diagrams

5.4.1.4.1 Comparison with other experimental results To demonstrate how the results obtained from the model developed here are used to calculate the reactor

$\bar{\delta}$=3.06 x 10^{-4}		Numerical	CSTR-PFR	Two-Region	Thulasidas *et. al.*	Numerical	Two-Region	Thulasidas et al	Numerical	Two-Region	Thulasidas *et. al.*	Numerical	Two-Region	Thulasidas *et. al*
Ls	Pe	100000				10000			1000			100		
	$\bar{\mu}$(x10^{-2})	4.69	4.69	4.69	5.12	4.67	4.68	5.12	4.68		5.12	4.68		5.98
	$\bar{\mu}^2$(x10^{-5})	6.86	4.40	6.07	5.19	4.52	4.51	5.30	4.34		5.22	4.33		7.09
	$\bar{\sigma}^2$(x10^{-5})	4.66	2.20	3.87	2.57	2.33	2.32	2.68	2.15		2.60	2.14		3.51
0.25	$\bar{\mu}^3$(x10^{-8})	16.2	6.19	11.8	9.75	6.42	6.38	8.23	5.94		8.01	5.93		12.5
	$\bar{\mu}$(x10^{-2})	10.7	10.7	10.7	11.2	10.6	10.6	11.2	10.6		11.2	9.94		16.0
	$\bar{\mu}^2$(x10^{-5})	35.4	22.9	32.3	25.2	23.0	22.9	25.0	22.2		24.9	19.4		50.6
	$\bar{\sigma}^2$(x10^{-5})	24.0	11.5	20.9	12.7	11.7	11.7	12.5	10.9		12.4	9.51		25.1
1.00	$\bar{\mu}^3$(x10^{-8})	183	73.7	145.6	95.1	71.7	71.4	82.4	66.9		81.8	55.6		237.8
	$\bar{\mu}$(x10^{-2})	34.6	34.8	34.7	35.4	34.7	34.8	35.4	34.7		39.2	32.2		64.6
	$\bar{\mu}^2$(x10^{-5})	291	241	286	255	244	242	250	240		305	203		766
	$\bar{\sigma}^2$(x10^{-5})	171	120	165	130	123	122	125	120		152	100		349
4.00	$\bar{\mu}^3$(x10^{-8})	360	248	345	281	255	251	270	246		358	187		358
$\bar{\delta}$=1.0 x 10^{-3}		Numerical	CSTR-PFR	Two-Region	Thulasidas *et. al.*	Numerical	Two-Region	Thulasidas et al	Numerical	Two-Region	Thulasidas *et. al.*	Numerical	Two-Region	Thulasidas *et. al*
Ls	Pe	100000				10000			1000			100		
	$\bar{\mu}$(x10^{-2})	1.46	1.47	1.46	1.59	1.46	1.47	1.59	1.46		1.59	1.46		1.86
	$\bar{\mu}^2$(x10^{-5})	1.20	0.43	0.82	0.57	0.49	0.48	0.52	0.42		0.51	0.42		0.69
	$\bar{\sigma}^2$(x10^{-4})	9.91	2.14	6.08	3.21	2.76	2.67	2.67	2.07		2.57	2.05		3.41
0.25	$\bar{\mu}^3$(x10^{-7})	18.59	1.88	6.92	4.17	2.49	2.38	2.87	1.77		2.43	1.79		3.90
	$\bar{\mu}$(x10^{-2})	3.32	3.34	3.34	3.47	3.33	3.34	3.47	3.33		3.48	3.33		4.96
	$\bar{\mu}^2$(x10^{-5})	6.22	2.23	4.59	2.51	2.52	2.49	2.49	2.22		2.43	2.19		4.87
	$\bar{\sigma}^2$(x10^{-5})	5.12	1.12	3.48	1.31	1.41	1.38	1.29	1.11		1.21	1.08		2.41
1.00	$\bar{\mu}^3$(x10^{-8})	20.5	2.24	9.49	3.65	2.84	2.75	2.74	2.19		2.66	2.14		7.02
	$\bar{\mu}$(x10^{-2})	10.8	10.8	10.8	11.0	10.8	10.8	11.0	10.8		12.17	10.7		12.2
	$\bar{\mu}^2$(x10^{-5})	40.4	23.5	36.8	24.0	24.5	24.6	24.5	23.3		29.50	22.9		29.2
	$\bar{\sigma}^2$(x10^{-5})	28.7	11.8	25.0	11.9	12.8	12.8	12.4	11.6		14.69	11.3		14.3
4.00	$\bar{\mu}^3$(x10^{-8})	239	76.6	186.9	99.1	82.2	82.5	83.4	74.6		108	72.7		111
$\bar{\delta}$=1.0 x 10^{-2}		Numerical	CSTR-PFR	Two-Region	Thulasidas *et. al.*	Numerical	Two-Region	Thulasidas et al	Numerical	Two-Region	Thulasidas *et. al.*	Numerical	Two-Region	Thulasidas *et. al*
Ls	Pe	100000				10000			1000			100		
	$\bar{\mu}$(x10^{-1})	1.40	1.53	1.48	1.69	1.56	1.55	1.69	1.56		1.70	1.56		2.02
	$\bar{\mu}^2$(x10^{-3})	9.75	0.470	5.82	3.47	1.37	1.08	1.14	0.513		0.622	0.434		0.739
	$\bar{\sigma}^2$(x10^{-3})	9.55	0.235	5.60	3.18	1.12	0.843	0.853	0.269		0.332	0.192		0.331
0.25	$\bar{\mu}^3$(x10^{-5})	141	0.222	35.6	14.7	2.39	1.17	1.56	0.293		0.458	0.200		0.542
	$\bar{\mu}$(x10^{-1})	3.28	3.42	3.30	3.64	3.48	3.43	3.66	3.45		3.69	3.45		7.21
	$\bar{\mu}^2$(x10^{-3})	48.5	2.35	28.8	10.8	6.60	5.00	3.96	2.53		2.67	2.24		9.67
	$\bar{\sigma}^2$(x10^{-3})	47.5	1.18	27.7	9.48	5.40	3.83	2.62	1.34		1.31	1.05		4.47
1.00	$\bar{\mu}^3$(x10^{-5})	1487	2.49	383	65.8	27.0	11.1	8.69	2.93		3.89	2.33		23.6
	$\bar{\mu}$(x10^{-1})	10.7	11.0	10.8	11.5	11.0	11.0	11.5	11.0		12.9	11.0		21.6
	$\bar{\mu}^2$(x10^{-4})	21.8	2.42	16.2	6.58	3.89	3.58	2.44	2.45		2.21	2.25		8.45
	$\bar{\sigma}^2$(x10^{-4})	20.7	1.21	15.0	5.26	2.67	2.37	1.10	1.24		0.55	1.03		3.78
4.00	$\bar{\mu}^3$(x10^{-6})	824	8.00	371	62.5	22.1	17.6	15.5	8.2		13.7	6.9		64.1

Tab. 5.10: Table of moments as calculated from the numerical results

Ca	2.84×10^{-4}
$\bar{\delta}$	2.89×10^{-3}
Pe	19048
L_s	4.15
L_b	13
$L_{reactor}$	285

Tab. 5.11: Conditions for example case

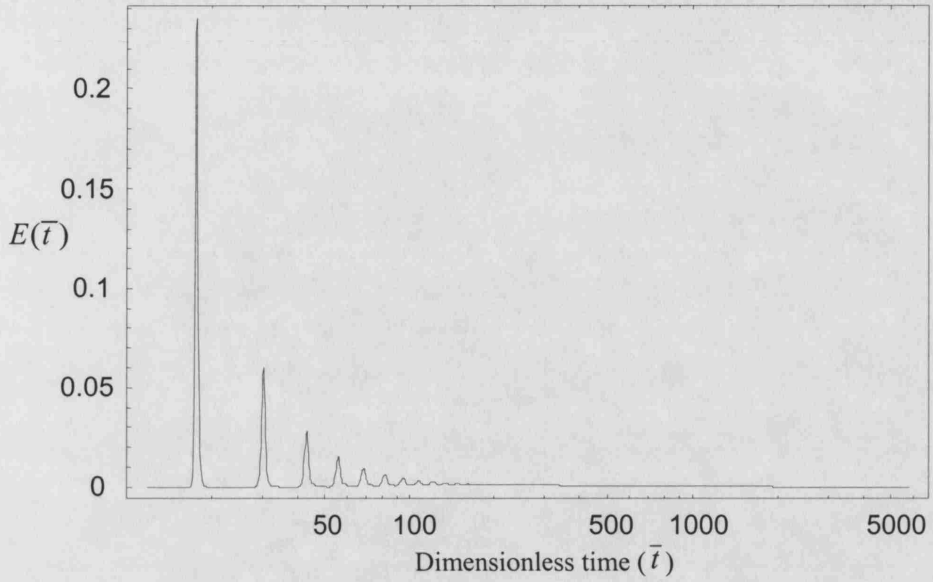

Fig. 5.16: Residence time curve in a unit cell for $\bar{\delta} = 2.89 \times 10^{-3}$, $Pe = 19048$, $\bar{L}_s = 4.15$, which match the match the experimental condition by Thulasidas et. al. [112]

residence time distribution a specific example is used based on the experiments of Thulasidas et. al. [112]. The conditions for that case are given in Table 5.11. For these conditions, the residence time distribution curve of a unit cell is given in Fig. 5.16 and is typical of high Pe (section 5.4.1.2).

The concentration output of each unit cell exiting the reactor is obtained from evaluating the inverse Laplace transform of the functions in Table 5.6 at dimensionless times given at Table 5.7 and the results are presented as a barchart in Fig. 5.17. The figure shows the initial cell exiting the reactor still has the majority of the tracer inside it with subsequent cells containing less and less material. From the velocity of each unit cell and its length as well as the length of the reactor, the concentration at different times can be plotted and converted to the reactor residence time distribution curve $E_{reactor}(\bar{t})$ when normalised (Fig. 5.18). Given the experimental input signal $c_i(t)$and the $E_{reactor}(t)$ curve, the dimensional version of

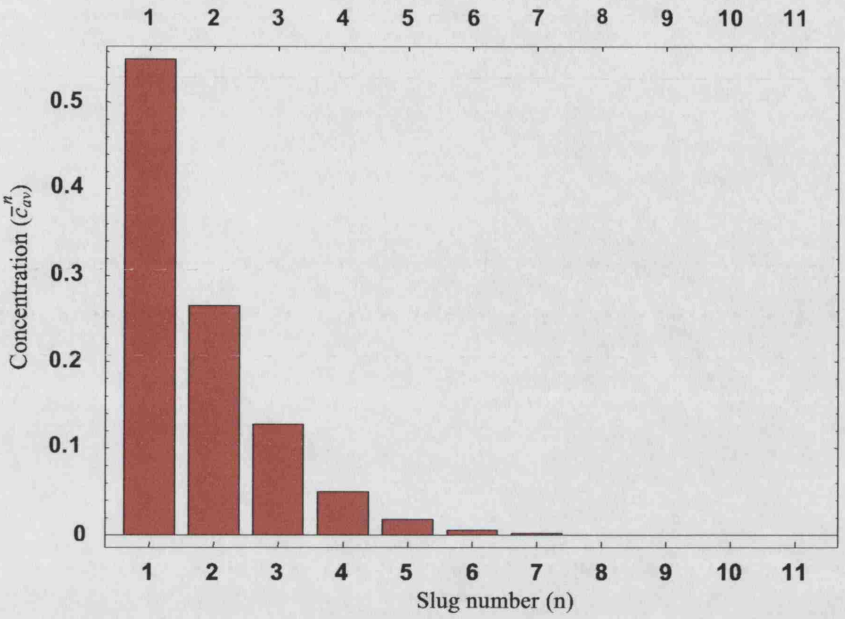

Fig. 5.17: Concentration in the exiting slugs for $\bar{\delta} = 2.89 \times 10^{-3}$, $Pe = 19048$, $L_s = 4.15$, $L_{reactor} = 285$

$E_{reactor}(\bar{t})$, a convolution integral of the two curves allow the calculation of the reactor output curve (Fig. 5.19). The results match the experimental results very well, it should be noted however that the model of Thulasidas et. al. [112] also matched their results despite being the worst performer amongst the models considered here. The model proposed by Kreutzer [98] also gives a reasonable match to the results, although not as good. The reason for all models matching the results is probably the relative short length of the reactor considered. The distinction between all the models should become more apparent with increasing reactor length.

5.5 Conclusions

A model has been developed for the prediction of axial mixing in Taylor flow which does not assume any prior mixing structure in a unit cell. The analysis of the unit cell used in this work was then used to evaluate the accuracy of literature models.

For $Pe > 1000$

1. The CSTR-PFR model is the least accurate of the models considered.

2. The fitted two-region model gives better evaluation than the CSTR-PFR

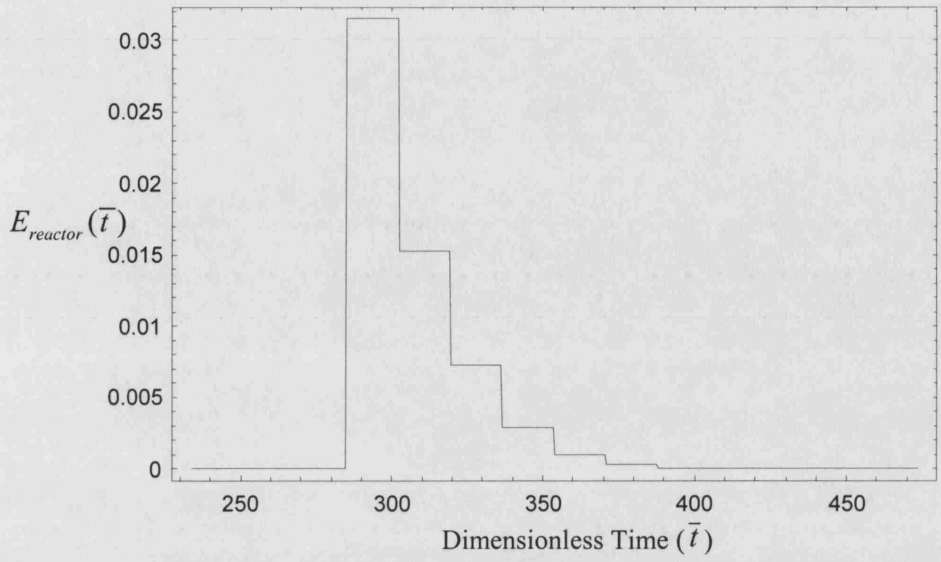

Fig. 5.18: Residence time distribution curve of the reactor for $\bar{\delta} = 0.000284$, $Pe = 19048$, $L_s = 4.15$, $L_{reactor} = 285$.

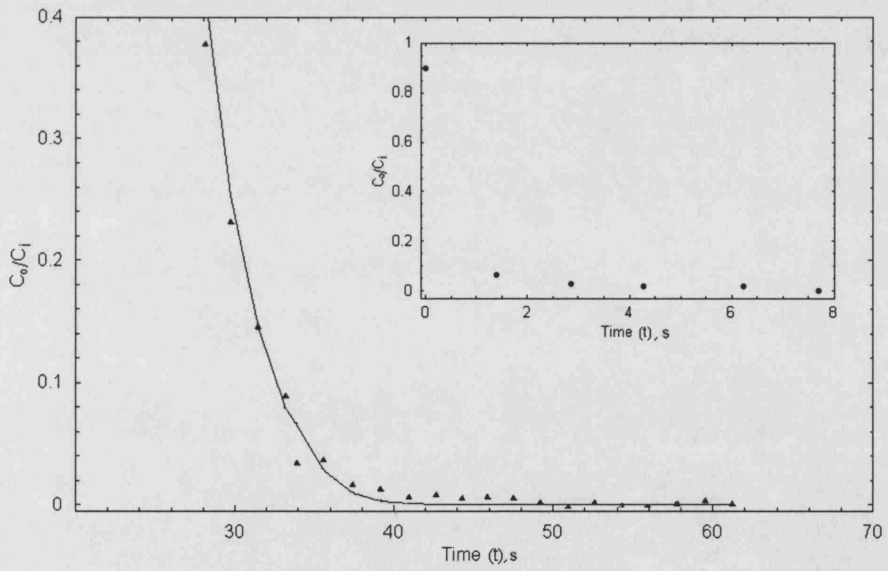

Fig. 5.19: Experimental (points) and theoretical (line) output of a single circular Taylor flow capillary reactor vs time for $\bar{\delta} = 2.89 \times 10^{-3}$, $Pe = 19048$, $L_s = 4.15$, $L_{reactor} = 285$. The top right hand corner insert shows the input tracer signal into the capillary as measured experimentally from Thulasidas et. al. [112].

model. However, the values of Sh found from the fitting are different by up to a factor of 4 from values found in literature correlations and do not show the correct L_s trends.

3. The method of Thulasidas et. al.[112] has shown some agreement with predicted values, however, the method can be further improved by introducing an iterative procedure to calculate the cycle time such that the first moment of the distribution matches the space time of the unit cell.

For $Pe \leq 1000$, based on moments calculated

1. Of the three methods considered, the CSTR-PFR model gives the best description of the unit cell.

2. A fitted two-region model gives $Sh \rightarrow \infty$ converging to that of the CSTR-PFR when fitted.

3. The method proposed by Thulasidas et. al. [112] gives the least accurate predictions.

The unit cell analysis were further used, by means of a convolution method, to calculate the residence time distribution of the unit cell. The results were found to be in agreement with experimental data obtained by Thulasidas et. al. [112] for Pe = 19048.

6. SAMPLE PULSE BROADENING IN TAYLOR FLOW MICROCHANNELS FOR SCREENING APPLICATIONS

Nomenclature

C_i	Inlet concentration	$\mathrm{kg/m^3}$
C_o	Outlet concentration	$\mathrm{kg/m^3}$
Ca	Capillary number $\frac{\mu U_b}{\gamma}$	
d	Microchannel diameter	m
D	Diffusivity of tracer species	$\mathrm{m^2/s}$
$E_{reactor}(t)$	Unit cell residence time distribution (RTD) curve	$\mathrm{s^{-1}}$
$E_{reactor}(\bar{t})$	Non-dimensionalised $E(t)$	
g	Acceleration due to gravity	$\mathrm{m/s^2}$
l_b	Taylor bubble length	m
$l_{reactor}$	Reactor length	m
l_s	Liquid slug length	m
L_b	Dimensionless Taylor bubble length $\frac{l_b}{d}$	
$L_{reactor}$	Non dimensionalised $l_{reactor}$, $\frac{l_{reactor}}{d}$	
L_s	Dimensionless liquid slug $\frac{l_s}{d}$	
n	Exiting slug number	
Pe	Bulk Peclet number $\frac{U_b d}{D}$	
t	Time	s
t_{cell}	Time for a unit cell to move a length l_{cell}, $\frac{l_{cell}}{U_b}$	s
$t_{reactor}$	Time for a unit cell to pass through reactor, $\frac{l_{reactor}}{U_b}$	s
U_b	Bubble velocity	m/s

Greek symbols

γ	Interfacial tension	N/m
δ	Thickness of film surrounding bubble	m
μ	Viscocity	$\mathrm{N\,s\,m^{-2}}$
ρ	Density	$\mathrm{kg/m^3}$

Superscripts

$\bar{x}$	Barred symbols are non-dimensionalised

6.1 Introduction

Residence time of the liquid in the reactor is usually studied in the context of conversion and selectivity [127]. An envisaged application of Taylor flow is to the field of combinatorial chemistry where segmentation can be utilized for introducing sequentially different reactants/samples within a microchannel reactor [128, 129]. Residence time data can be used to show how samples spread in the reactor and consequently provide guidelines regarding the frequency of sample injection. In chapter 5, a method for calculation of the residence time distribution (RTD) of a Taylor flow reactor has been developed. This chapter aims to demonstrate the use of that method for evaluating the effects of flow and diffusion characteristics on sample pulse broadening in a Taylor flow microreactor.

6.2 Theory and Literature Review

The Taylor flow envisaged in this chapter is non-pulsating and periodic (no variation in bubble or slug sizes) in agreement with the wider body of literature on Taylor flow in small tubes. In addition, it is assumed that there is negligible flow in the liquid film surrounding the bubbles and the geometry of the bubble is axi-symmetric, (correct for $Ca \leq 10^{-3}$).

In the study of Taylor flow, a bubble and a slug, or a slug and two half bubbles, are referred to as a unit cell. The unit cell moves with the velocity of the bubble, which is faster than the average liquid velocity in the slug because of the presence of the stagnant liquid film separating the bubble from the wall. A moving unit cell, seen from a frame of reference moving with the bubble resembles a reactor with an inlet and an outlet (Fig. 6.1).

In order to obtain the RTD of the reactor, one needs to calculate the RTD of a moving unit cell. This is described in chapter 5. The unit cell behavior is governed by the variables listed in Table 6.1. It is worth repeating that for $Ca \leq 10^{-3}$ the film thickness δ is only a function of Ca and the relationship is monotonic and increasing.

Convolution methods are then used to obtain the RTD of the whole reactor from the RTD of a single unit cell as described in section 5.3.3.

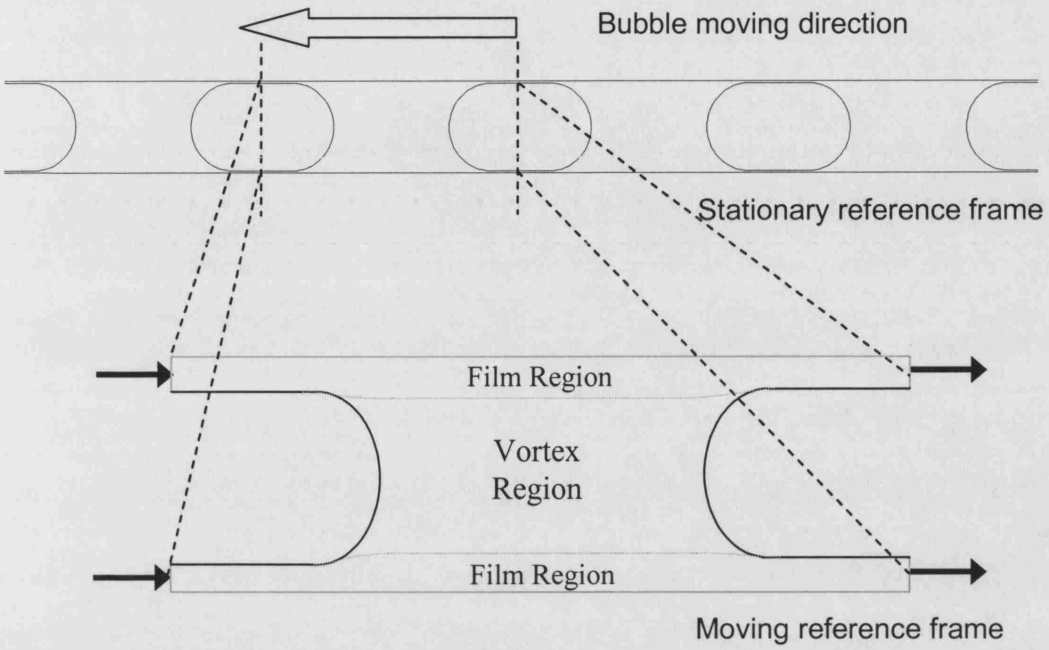

Fig. 6.1: Schematic of a moving unit cell. The film region and vortex regions are highlighted.

Dimensionless Number	Definition
Pe	$\frac{U_b d}{D}$
Ca or $\bar{\delta}$	$\frac{\mu U_b}{\gamma}$ or $\frac{\delta}{d}$
L_s	$\frac{l_s}{d}$
L_b	$\frac{l_b}{d}$
$L_{reactor}$	$\frac{l_{reactor}}{d}$

Tab. 6.1: Dimensionless numbers governing the residence time distribution of the unit cell.

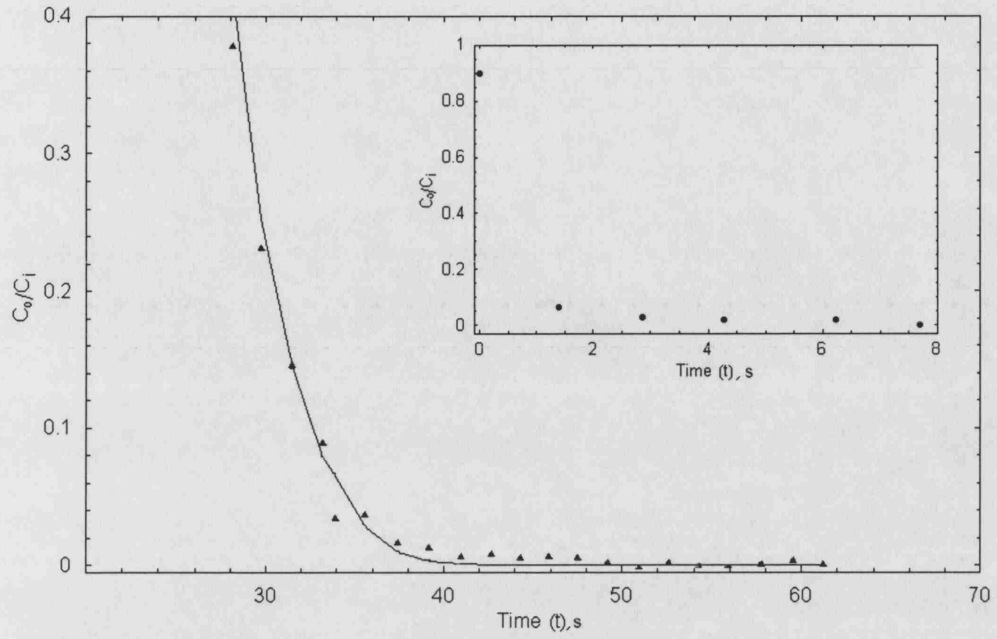

Fig. 6.2: Compared experimental and theoretical output of single circular capillary vs time. Top right hand corner insert shows the input tracer signal into the capillary as measured experimentally.

6.3 Results and discussion

A demonstration of how the slug averaged concentration at the exit of the reactor is obtained has been demonstrated in chapter 5 for a specific example with conditions similar to those of Thulasidas et. al. [112]. After determining the RTD $E_{reactor}(t)$, the output concentration for a given input concentration $C_i(t)$ of Thulasidas et. al. [112] was calculated using a convolution integration of $C_i(t)$ and $E_{reactor}(t)$. As can be seen in Fig. 6.2 the methodology provides good agreement with experimental data. The reactor RTD is sufficient to characterise its behaviour for any (arbitrary) input concentration profile.

Fig. 6.3 shows the average slug concentration as each one exits the reactor as depicted in Fig. 5.2(c). For $Pe = 10^5$, the first cell still contains the highest amount of tracer. The rest of the tracer is distributed to 35 downstream cells, so that a maximum concentration is observed in cell 6. For $Pe = 10^4$ and 10^3 the first cell has lost most of the tracer with the maximum tracer concentration now observed in cell 7. The tracer spreading is minimal for the lowest Pe number. The change in the spread is lower between $Pe = 10^4$ and 10^3 than between 10^5 and 10^4. Interestingly this can correspond to high tracer diffusivity (if everything else remains constant)

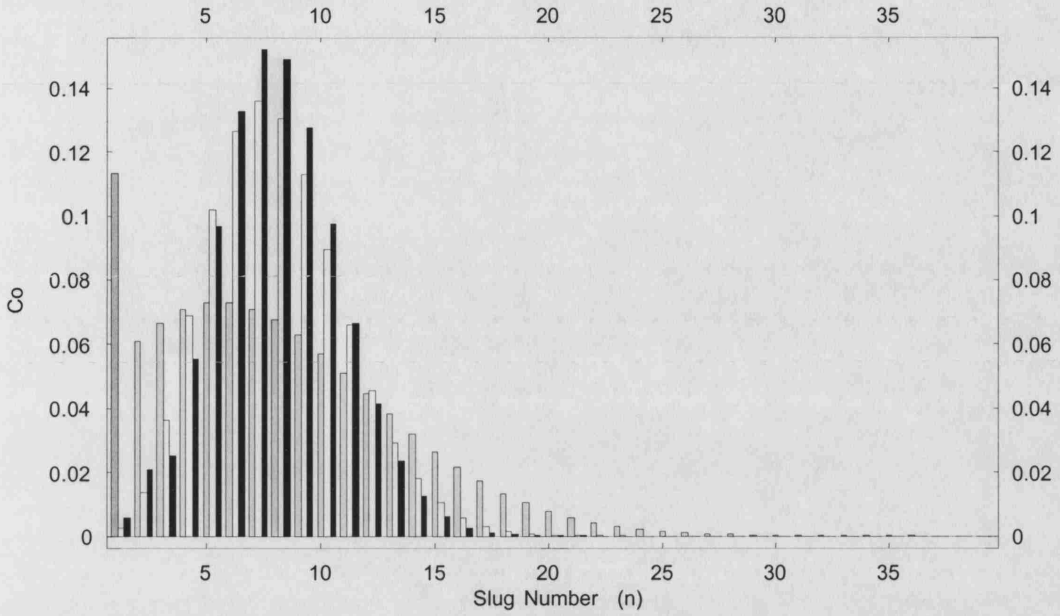

Fig. 6.3: Effect of Pe on the concentration of exiting slugs for an input concentration $C_i = 1$ in cell 1. $\bar{\delta} = 10^{-3}$, $L_s = 0.25$, $L_{reactor} = 1000$. $Pe = 100000$ (Grey), $Pe = 10000$ (white), $Pe = 1000$ (Black).

or to smaller diameter (if L_s, L_b and $L_{reactor}$ are scaled accordingly). This behavior can be explained if one considers the flow streamlines in the unit cell which break down the slug into two distinct regions as shown in Fig.6.1: film and vortex regions. Mass transfer taking place between them is only by diffusion. Material with low diffusivity has difficulty transferring into the film. Also, when transferred into the film, it does not diffuse easily into the vortex regions of the immediately subsequent slugs and is convected further downstream resulting in an increased spread.

The effect of slug length variation is demonstrated in Fig 6.4. In both cases for $Pe = 10^5$, Fig. 6.4(a) and for $Pe = 10^3$, Fig. 6.4(b), the spreading of tracer into subsequent unit cells seems to increase with decreasing slug length. However, the spread is much reduced for the case of $Pe = 10^3$, consistent with the findings of Fig. 6.3. The effect of slug length can be explained by noting that the volume of the slug determines the speed of average slug concentration response to incoming tracer. As a result only a few large slugs are sufficient to fully contain the whole tracer amount, see Fig. 6.4(b). Since large Pe would correspond to low residence times, the above results indicate that the slug length needs to be carefully considered for screening applications where different residence times are required.

When transforming the exiting slug concentration profiles, Figs. (6.3,6.4) to

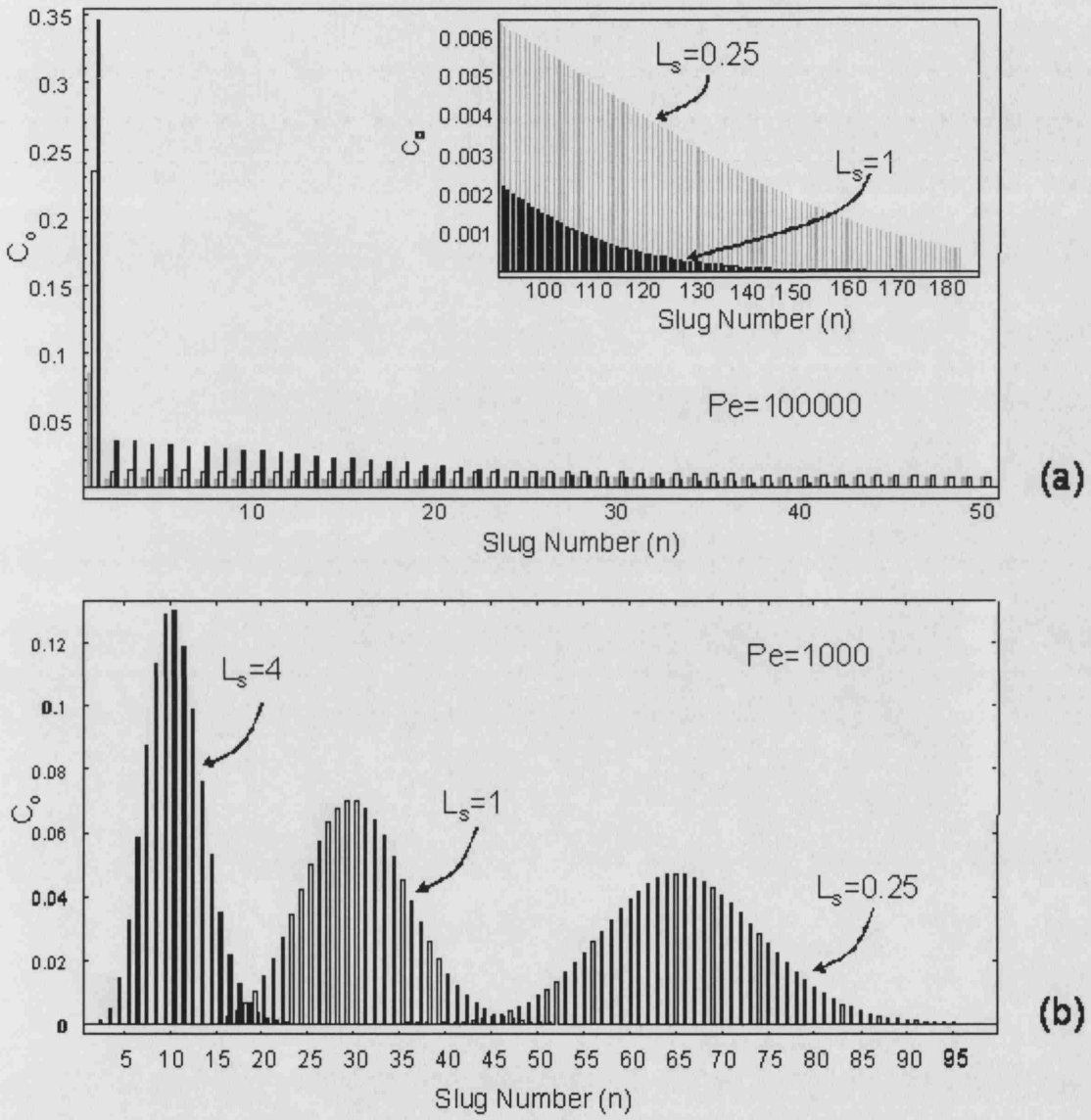

Fig. 6.4: Effect of slug length on concentration of exiting slugs for an input concentration $C_i = 1$ in cell 1. $\bar{\delta} = 10^{-2}$, $L_{reactor} = 1000$. $L_s = 0.25$ (Grey), $L_s = 1$(white) , $L_s = 4$ (Black). (a) $Pe = 10^5$, (b) $Pe = 10^3$.

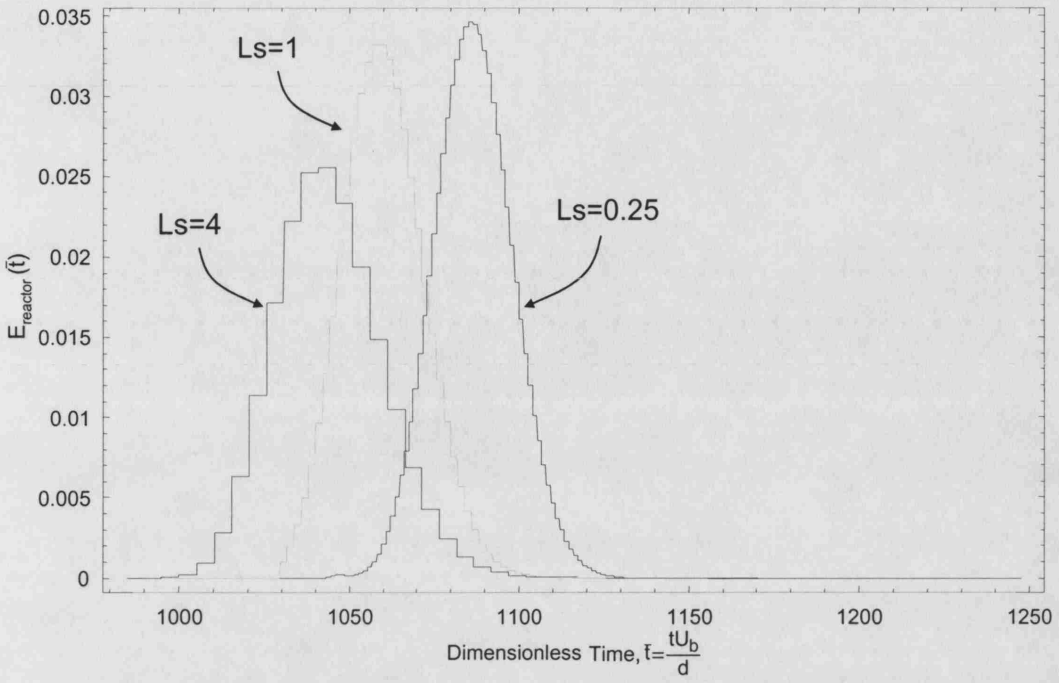

Fig. 6.5: Effect of slug length on residence time distribution curves. $\bar{\delta} = 10^{-3}$, $Pe = 10^3$, $L_{reactor} = 1000$, $L_b = 1.1$.

RTD, one needs to consider that the exit time of slug will depend on the slug length and slug number (an $L_s = 4$ slug requires $16\times$ longer time to exit than an $L_s = 0.25$ slug). In Fig 6.5 the reactor residence time distribution, $E_{reactor}(t)$, is presented for the exiting slug concentration profiles corresponding to Fig 6.4(b). In this representation, the spread of the pulse (in terms of time) is lower for the smallest slugs in contrast with the behavior of pulse spreading in terms of the slug number. It is worth noting that bubble length has been kept constant, resulting in dimensionless liquid residence times of (1086, 1060, 1044) for $L_s = 0.25, 1$ and 4 respectively. The slug length can be increased by increasing the liquid flowrate. However, this will also result in a reduction of bubble length. A way to change the slug length while keeping constant the bubble length would be to change the inlet geometry in addition to the liquid flowrate. Even though such an approach would be difficult to implement in practice, in Fig. 6.5 the bubble length was kept constant for illustration purposes.

The decrease in film thickness, caused by a decrease of the capillary number results in a reduction in the distribution of the tracer (compare Fig. 6.6 with Fig. 6.4(b)). This is due to the fact that the film is the only means of communication between the different slugs. Hence thinner films inhibit tracer exchange between

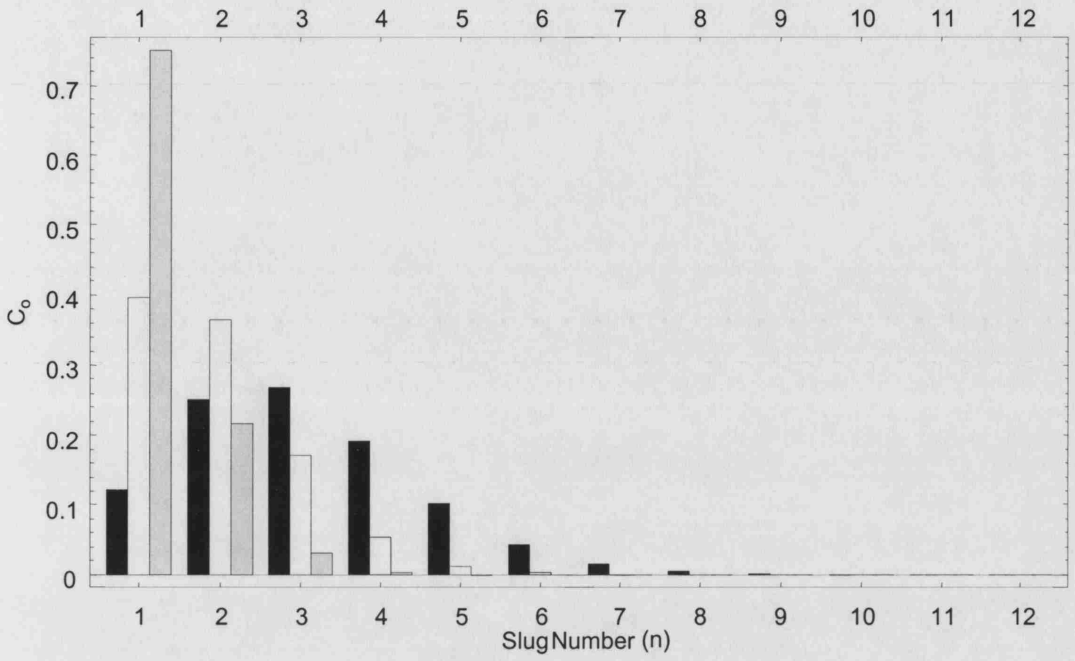

Fig. 6.6: Effect of slug length on concentration of exiting slugs. $\bar{\delta} = 3 \times 10^{-4}, Pe = 10^3$, $L_{reactor} = 1000$. $L_s = 0.25$ (Grey), $L_s = 1$(white) , $L_s = 4$ (Black).

slugs. A decrease in Capillary number is only affected (for the same gas-liquid system) by a decrease in the velocity, which also decreases the Peclet number. It can then be concluded that operation with smaller bubble velocity results in narrower RTD due to thinner liquid film and efficient mass transfer between the film and vortex regions.

6.3.1 Case Study

An example is presented in this section to illustrate the application of the above procedure for the characterisation of a Taylor flow system with operational and design parameters given in Table 6.2 and unit cell residence time ˜12 min which is typical for screening applications [130]. Two possible arrangements are considered for a reactor channel which has a 1 mm diameter. In set 1, a 20 cm long channel with large slug and bubble length is used, while in set 2, a 2 m channel with small slug and bubble length is employed. The increase of slug and bubble length with decreasing flow rates is consistent with experimental observations [114]. An initial concentration 1 kg/ m^3 was used for cell 1. The unit cell residence time in both cases is kept the same by keeping the ratio (L_s/L_b) (or equivalently the ratio of the liquid to gas flowrate) constant, and altering appropriately the gas and liquid flowrates

	Set 1	Set 2
$l_{reactor}$	20 cm	2 m
U_b	10^{-4} m/s	10^{-3} m/s
D	5×10^{-10} m^2/s	5×10^{-10} m^2/s
L_s	4	0.25
L_b	17.6	1.1
Ca	10^{-5}	10^{-4}
δ	3×10^{-4}	1×10^{-3}
Pe	100	1000

Tab. 6.2: Values of parameters used in the case study.

and reactor length.

The RTD for the two sets is given in Fig. 6.7. It can be seen that the residence times are longer than 12 min, because 12 min is the residence time of a unit cell, based on the bubble velocity. Set 2 shows a slightly longer mean, which results from the fact that larger Ca causes thicker films to form and the ratio of bubble to average liquid velocity is higher [76]. Choosing a cutoff concentration of 10^{-4} kg/ m^3 shows the spread to cover 27 short slugs for set 2 whilst that for set 1 covers 3 long slugs. These results show that the tracer spreading is reduced by decreasing slug length despite of increasing Peclet number and film thickness. The tracer RTD curve also helps to define the frequency of injections in screening applications where each tracer pulse would correspond to a catalyst injection. The maximum injection frequency would be 19 samples/ h for set 1 and 120 samples/ h for set 2. Pennemann et. al.[131] have used a glass tube with hexagonal (foamy) flow. For a 12 min residence time the maximum injection frequency would be approximately 30 samples/h. Admittedly, a significant dispersion for that system occurred in the hardware upstream of the main channel. Other factors, depending on the application, such as the sample volume or mixing within the slugs need also to be carefully considered before selecting appropriate values of operating and design parameters.

6.4 Conclusions

The effect of different parameters on the residence time distribution of a tracer injected in a Taylor flow microreactor were investigated. It was found that increase in the Peclet number, the capillary number or slug length resulted in larger tracer spreading. The mass transfer between the film region and the vortex region of the unit cell plays a major role in explaining the observed behavior. Appropriate design and operation of a Taylor flow reactor can achieve high injection frequencies in

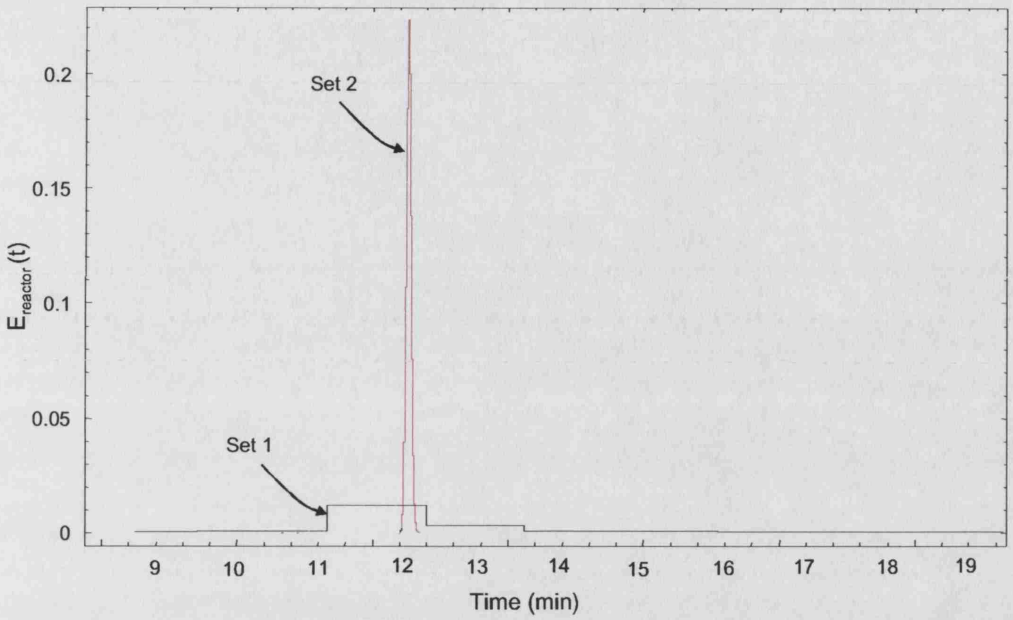

Fig. 6.7: Residence time distribution curves for the parameter sets investigated in the case study.

screening applications.

7. AXIAL MIXING DURING TAYLOR FLOW IN MICROCHANNELS AT LOW PECLET NUMBERS

Nomenclature

A	Cross sectional area of film	m^2
c	Tracer concentration	$\mathrm{kg/m}^3$
Ca	Capillary number $\frac{\mu U_b}{\gamma}$	
d	Microchannel diameter	m
D	Diffusivity of tracer species	m^2/s
D_e	Dispersion coefficient of tracer species	m^2/s
$E(t)$	Unit cell residence time distribution (RTD) curve	s^{-1}
Fr	Froude number $\frac{U_b^2}{g\ d}$	
g	Acceleration due to gravity	$\mathrm{m/s}^2$
k	Tracer cell number	
l_b	Taylor bubble length	m
l_{cell}	Unit cell length, $l_{cell} = l_b + l_s$	m
$l_{reactor}$	Reactor length	m
l_s	Liquid slug length	m
L_b	Dimensionless Taylor bubble length $\frac{l_b}{d}$	
$L_{reactor}$	Non dimensionalised $l_{reactor}$, $\frac{l_{reactor}}{d}$	
L_s	Dimensionless liquid slug $\frac{l_s}{d}$	
N	Total number of cells in model	
$\mathbf{N}$	Tracer flux	$\mathrm{kg\,m^{-2}\,s^{-1}}$
N_A	Number of cells ahead of tracer cell	
p	Pressure	$\mathrm{N/m}^2$
Pe	Bulk Peclet number $\frac{U_b d}{D}$	
Re	Reynolds number $\frac{\rho U_b d}{\mu}$	
t	Time	s
t_m	mean of reactor RTD	s
$\mathbf{u}$	Velocity field	m/s

u	One dimensional velocity field	m/s
U_b	Bubble velocity	m/s
V	Volume of slug	m^3
VDN	Vessel dispersion number $\frac{D_e}{U_b L_{reactor}}$	
x	Axial coordinate	m
Greek symbols		
γ	Interfacial tension	N/m
δ	Thickness of film surrounding bubble	m
μ	Viscocity	$N s m^{-2}$
ρ	Density	kg/m^3
σ	Standard deviation of RTD	s
τ_p	Residence time for PFR	s
τ_s	Residence time for CSTR	s
Superscripts		
$+$	left end of the liquid slug	
$-$	right end of the liquid slug	
$\bar{x}$	Barred symbols are non-dimensionalised	
Subscripts		
0	Initial value at $t = 0$	

7.1 Introduction

The results from the model described in Chapter 5 show the first moment for all cases with $Pe = 10$ to have a considerably lower value than the space time of the unit cell. This is attributed to the break down of the assumption that convection dominates mass transfer at the boundaries. Another model which can account for diffusive effects at the boundaries becomes necessary [132]. At the same time modeling of numerous upstream unit cells is too computationally expensive to carry out.

As an alternative to solving for the velocity and concentration fields, a simple homogeneous region is assumed in the liquid slug. This description has been demonstrated in section 5.4.1.3.1 to give the best behaviour of all the known models for low Pelet values and has been employed by Thiers et. al. [116] in their tank-in-series model of the flow. Their method, however, does not account for diffusion. This work is aimed at modifying such a model to account for the mass transfer by diffusion in the liquid film surrounding the bubbles. The applicability of the model is also assessed for a range of system parameters.

Dimensionless Number	Definition
Re	$\frac{\rho U_b d}{\mu}$
Ca	$\frac{\mu U_b}{\gamma}$
L_s	$\frac{l_s}{d}$
L_b	$\frac{l_b}{d}$
Fr	$\frac{U_b^2}{gd}$

Tab. 7.1: Dimensionless numbers governing the hydrodynamics of Taylor flow

7.2 Model development

The parameters that are expected to affect axial mixing are listed in Table. 7.1. The thickness of the liquid films that surround gas bubbles δ and the gas slip ratio $\frac{U_b}{U_{ls}}$ are functions of Re, Fr and Ca. The influence of the two numbers Re and Fr decreases with decreasing Ca values and for $Ca < 10^{-3}$ the film thickness can be correlated only to Ca, see Tables. 3.4 and 3.5. The length of the bubbles, determines the length of the liquid films, and the length of the liquid slugs affects recirculation and mass transfer within these slugs.

The current study assumes non-pulsating and periodic (no variation in bubble or slug sizes) in agreement with the wider body of literature on Taylor flow in small tubes and uses a unit cell analysis based on a single slug and two half bubbles (Fig. 7.1).

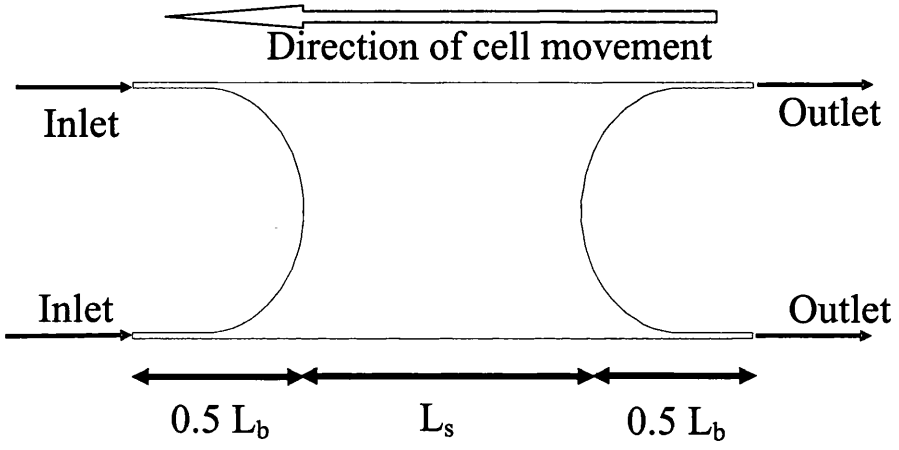

Fig. 7.1: Schematic of a unit cell with two half bubbles and one liquid slug. The length of the bubble is L_b. The length of the slug is L_s.

To study axial mixing a pulse of tracer is added as a unit cell of concentration c_0 in the microchannel at time $t = 0$. The concentrations of the slugs exiting the reactor give the residence time distribution curve. All other unit cells ahead and behind the tracer cell have initially 0 concentration. As the tracer unit cell moves in the reactor some tracer is transferred from it to the neighbouring cells through the liquid film. In a moving frame of reference with the same velocity as the initial tracer cell, each unit cell resembles a vessel with an inlet and an outlet,see (Fig. 7.1).

The convection-diffusion equation can be written in dimensionless form for a unit cell as follows:

$$\frac{\partial \bar{c}}{\partial \bar{t}} + \bar{\mathbf{u}} \cdot \bar{\nabla} \bar{c} - \left(\frac{1}{Pe}\right) \bar{\nabla}^2 \bar{c} = 0 \tag{7.1}$$

where all terms have been appropriately non-dimensionalised.

To solve equation 7.1 the flow field $\bar{\mathbf{u}}$ in the convection term needs to be known. With decreasing Peclet number, the diffusion term in the equation starts to gain importance. As was seen in Chapter 5, the increased importance of diffusion coupled with recirculation means that concentration within the slugs becomes uniform very quickly, (Fig. 7.2) . The increased importance of diffusion however, can also result in a flux of the tracer from both ends of the unit cell. To account for this, the cells both in front and at the back of the tracer injection cell need to be taken into account. Each of the surrounding cells will also have a tracer concentration that will be linked via the film to the cells surrounding it and so on. It is therefore important to include in the modelling a sufficient number of cells on both sides of the initial tracer cell so that the end cells on either side have negligible tracer concentrations and there is no mass transfer between them and their neighbours. At the boundaries of the first and last cells, solute flux can then be neglected. It is also assumed that the film surrounding the bubbles has uniform velocity (in a frame of reference moving with the bubble) and is well mixed radially. As a result the film can be adequately modelled using a unidirectional convection-diffusion equation. A schematic diagram of the elements used in the model is shown in Fig. 7.3.

The following characteristic parameters are used to non-dimensionalise equation 7.1.

Characteristic time	$\frac{d}{U_b}$
Characteristic length	d
Characteristic velocity	U_b

The characteristic time is related to convection which will still dominate even at increased diffusion contribution.

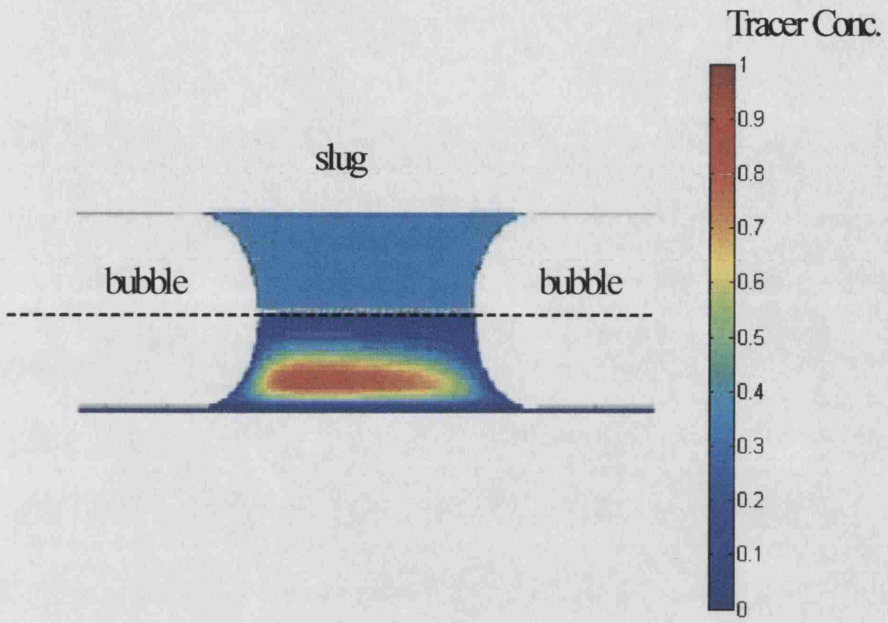

Fig. 7.2: Tracer concentration in a liquid slug with initial unit concentration after it passed through a 10 cm reactor filled with tracer free liquid. Top: Pe=990, Bottom: Pe=64800.

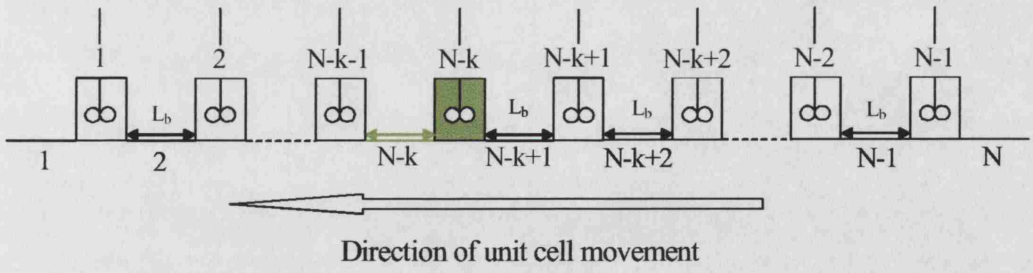

Fig. 7.3: A schematic diagram of the elements of the model. The tracer is initially introduced in a single unit cell at position k with k-1 cells behind and N-k+1 cells in front.

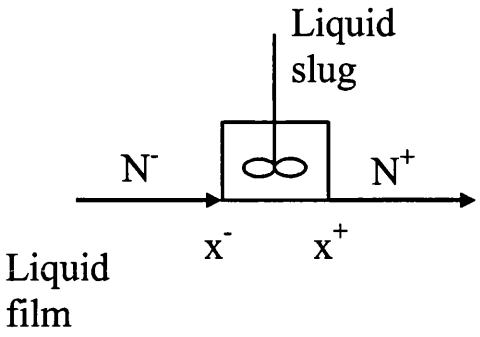

Fig. 7.4: A diagram depicting the mass balance on a single slug. The volume of the liquid slug is V and the tracer flux into the volume is through a film of cross sectional area A.

For the analysis of axial mixing with a step or pulse change, the following transform is applied:

$$\bar{c} = \frac{c}{c_0}$$

where c_0 is the tracer concentration in the tracer unit cell at time t_0.

For any film k the resulting equation can be stated as:

$$\left\{ \frac{\partial \bar{c}}{\partial \bar{t}} + \left(\frac{\partial \bar{c}}{\partial \bar{x}} \right) - \frac{1}{Pe} \frac{\partial^2 \bar{c}}{\partial \bar{x}^2} \right\}_k = 0 \tag{7.2}$$

For a mixed slug region k of volume V and a film having a cross sectional area A (see Fig. 7.4), a mass balance yields:

$$\left\{ V \frac{\partial c}{\partial t} + A \left(\mathrm{N}^- - \mathrm{N}^+ \right) \right\}_k = 0 \tag{7.3}$$

where N^- and N^+ refer to the fluxes downstream and upstream of the slug respectively, those can be found from

$$\mathrm{N}^- = \left\{ (uc) - D \frac{\partial c}{\partial x} \right\}_{x^-} \tag{7.4}$$

$$\mathrm{N}^+ = \left\{ (uc) - D \frac{\partial c}{\partial x} \right\}_{x^+} \tag{7.5}$$

Points x^- and x^+ refer to the positions at the left and right ends of the liquid slug.

Equations 7.3 - 7.5 can be non-dimensionalised to give:

$$\left\{\frac{\bar{V}}{\bar{A}}\frac{\partial \bar{c}}{\partial \bar{t}} + \left(\bar{\mathrm{N}}^{-} - \bar{\mathrm{N}}^{+}\right)\right\}_{k} = 0 \tag{7.6}$$

$$\bar{\mathrm{N}}^{-} = \left\{(\bar{c}) - \frac{1}{Pe}\frac{\partial \bar{c}}{\partial \bar{x}}\right\}_{\bar{x}-} \tag{7.7}$$

$$\bar{\mathrm{N}}^{+} = \left\{(\bar{c}) - \frac{1}{Pe}\frac{\partial \bar{c}}{\partial \bar{x}}\right\}_{\bar{x}+} \tag{7.8}$$

A set of N equations of the form of equation 7.2 and $(N-1)$ equations of the form of equation 7.6 connecting them is obtained. If the number of cells ahead and behind the tracer cell is large, then the concentrations at the end cells should be low such that the boundaries imposed would be either the Neumann boundary conditions

$$\left\{\bar{\mathrm{N}}^{-}\right\}_{k=0} = \left\{(\bar{c}) - \frac{1}{Pe}\frac{\partial \bar{c}}{\partial \bar{x}}\right\}_{\bar{x}-} = 0 \tag{7.9}$$

$$\left\{\bar{\mathrm{N}}^{+}\right\}_{k=N-1} = \left\{(\bar{c}) - \frac{1}{Pe}\frac{\partial \bar{c}}{\partial \bar{x}}\right\}_{\bar{x}+} = 0 \tag{7.10}$$

or the Dirichlet boundary conditions

$$(\bar{c})_{k=0,\bar{x}-} = 0 \tag{7.11}$$

$$(\bar{c})_{k=N-1,\bar{x}+} = 0 \tag{7.12}$$

The model given by equations 7.2-7.12 can only be solved numerically. However, for large Pe an analytical expression can be obtained. The asymptotic limit of expression 7.2 as the Peclet number value becomes large is given by equation 7.13. This is the governing equation of a Plug Flow Reactor (PFR). Furthermore, each slug can be considered as a Continuous Stirred Tank Reactor (CSTR). Each unit cell appears then as a combination of PFR-CSTR in series. The tracer flux is governed purely by convection in the film and only cells upstream of the initial tracer cell will be affected.

$$\frac{\partial \bar{c}}{\partial \bar{t}} + \left(\frac{\partial \bar{c}}{\partial \bar{x}}\right) = 0 \tag{7.13}$$

The residence time distribution of a PFR-CSTR series is given by [132].

$$E(t) = 0 \qquad (t < \tau_p) \tag{7.14}$$

$$E(t) = \frac{e^{-\frac{t-\tau_p}{\tau_s}}}{\tau_s} \qquad (t \geq \tau_p) \tag{7.15}$$

For a cell at the inlet of the reactor with unit concentration that encounters clear liquid at its inlet as it moves, the concentration in the slug is given by equation 7.16:

$$\bar{c}(t) = 1 + \left(e^{-\frac{t-\tau_p}{\tau_s}} - 1\right) h(t) \tag{7.16}$$

where $h(t)$ is the Heaviside unit step function.

Subsequent cell n can be shown to have a slug concentration given by equation 7.17

$$\bar{c}^n(t) = \frac{e^{\frac{t-(n+1)\tau_p}{\tau_s}} h\left(t-(n+1)\tau_p\right)\left(\frac{t-(n+1)\tau_p}{\tau_s}\right)^n}{\Gamma(n+1)} + \frac{\left[\Gamma(n) - \Gamma\left(n, \frac{t-n\tau_p}{\tau_s}\right)\right] h\left(t-n\tau_p\right)}{\Gamma(n)} - \frac{\left[\Gamma(n) - \Gamma\left(n, \frac{t-(n+1)\tau_p}{\tau_s}\right)\right] h\left(t-(n+1)\tau_p\right)}{\Gamma(n)} \tag{7.17}$$

where Γ is the Gamma function.

From the unit cell velocity and the geometry, the two parameters τ_p and τ_s can be calculated:

$$\tau_p = \frac{l_b}{U_b} \tag{7.18}$$

$$\tau_s = \frac{\bar{V}/\bar{A}}{U_b} \tag{7.19}$$

7.2.1 Numerical solution of the low Peclet number model

A finite volume method is used to discretise the set of equations 7.2 and 7.6 and the Dirichlet boundary conditions 7.11 and 7.12. The solution algorithm uses the exponential spatial discretisation scheme and an implicit time discretisation method. Details of the solution method can be found in Patankar [133]. The liquid slug appears as a finite volume cell of volume equivalent to the liquid slug volume. For the first and last films in the series of cells, the left and right hand boundary conditions

can be either zero flux Neumann or zero concentration Dirichlet boundary conditions. The solution of the system is independent of which is used provided enough cells on both sides of the tracer cell have been specified. The Dirichlet boundary condition was chosen because it is not conservative i.e. there will appear a loss of tracer mass from the system if the number of cells ahead or after the tracer cells are insufficient. A mass balance at the end of the simulation serves as a check for the number of cells chosen. The tridiagonal system of algebraic equations is solved at each time step to obtain concentration profiles in the film and slugs. The simulations start with the tracer cell just inside the reactor.

The concentration of the tracer at the channel outlet determines the simulation time. The dimensionless time at which the first unit cell exits is $L_{reactor} - (N_A)L_{cell}$. At each time step, the unit cell exiting and its concentration at the reactor outlet are recorded. The simulations stop when a cell with concentration smaller than a tolerance concentration ($\bar{c} < 10^{-6}$) leaves the reactor.

A matlab code was written implementing the method outlined above. The correct implementation of the numerical method was verified in a number of ways. The solution of the convection-diffusion equation 7.2 for a single film using this method compared well with an analytical solution [134] for the specific initial and boundary conditions used. In addition, the numerical prediction of the model when the value of the Peclet number was set to an arbitrary large value agreed well with the prediction of the analytical solution given by expression 7.17. The CPU time never exceeded one hour for the largest system when executed on an AMD Athlon 1.6GHz processor.

7.3 Results

The model is applied to a circular channel reactor with $1m$ length and $300\mu m$ diameter, which corresponds to $L_{reactor} = 3333$. An example is given below for a tracer diffusivity typical of a liquid-liquid system, ethanol and air physical properties, combination of bubble and liquid slug lengths and a residence time in reactor ($\sim$ 7.8 min) such that $Pe = 500$, $Ca = 1 \times 10^{-4}$, $L_b = 1.10$, $L_s = 1$. For this Ca the film thickness is equal to $\bar{\delta} = 0.00249$ [65]. Assuming the geometry of a bubble corresponds to a cylinder with spherical caps, the ratio $\frac{\bar{V}}{\bar{A}}$ is calculated to be 122.6. For the simulation the initial tracer cell is placed with 5 cells ahead and 50 cells behind.

The system is solved and the outlet concentrations are given in Fig. 7.5. The

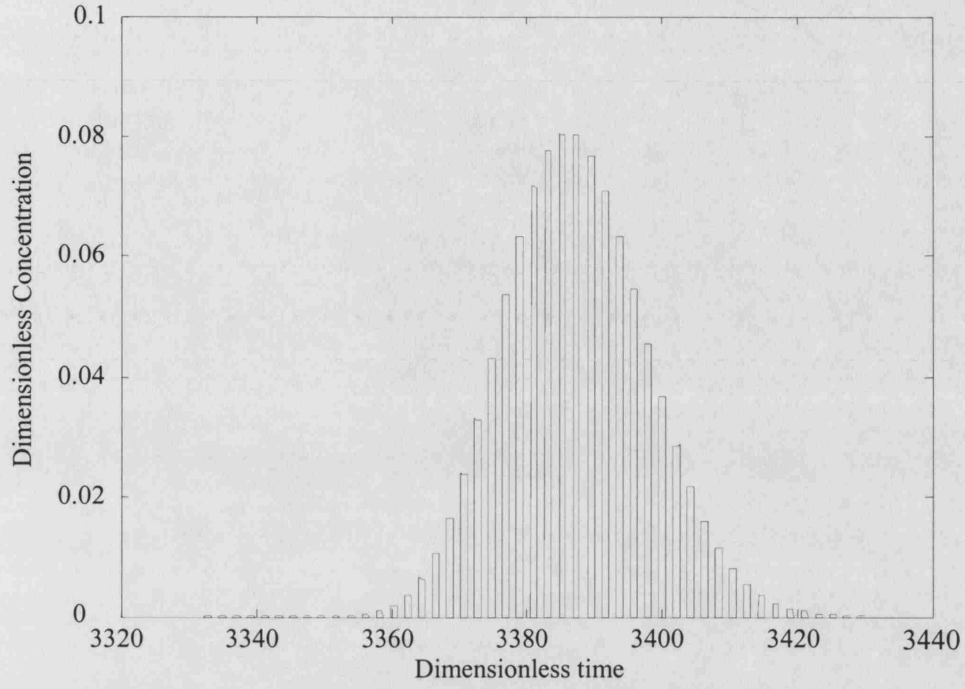

Fig. 7.5: Concentration of tracer in the liquid slugs exiting the reactor channel. Each peak corresponds to the concentration in an exiting slug. The spacing between the peaks is determined by the length of the liquid film surrounding the bubbles.

residence time distribution curve is obtained by normalising the concentration-time graph.

The mean and standard deviation of the distribution can be used to calculate the vessel dispersion number (VDN) using equation 7.20 [132] :

$$\frac{\sigma^2}{t_m^2} = 2\,(VDN) + 8\,(VDN)^2 \tag{7.20}$$

where t_m and σ are the mean and standard deviation of the distribution given in Fig. 7.5. The vessel dispersion number is the non-dimensionalised dispersion coefficient in the dispersion model [132]. In the above example $VDN = 4.92 \times 10^{-6}$.

The effect on the vessel dispersion number of the three non-dimensional numbers, Ca, L_s and L_b that define the geometric characteristics in a Taylor flow system can be seen in Figs. 7.6 and 7.7. Both figures show very low VDN values, confirming that axial mass transfer in a liquid is significantly reduced with Taylor flow to near PFR level. For comparison, the vessel dispersion number for laminar flow of liquids in tubes is at least 3 orders of magnitude larger [132]. An increase in VDN, and

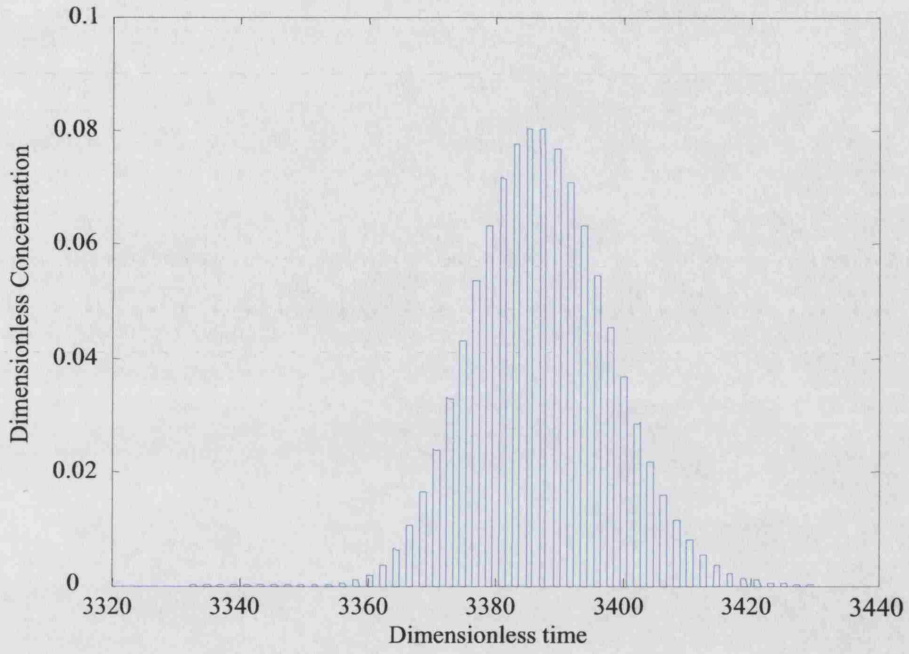

Fig. 7.5: Concentration of tracer in the liquid slugs exiting the reactor channel. Each peak corresponds to the concentration in an exiting slug. The spacing between the peaks is determined by the length of the liquid film surrounding the bubbles.

residence time distribution curve is obtained by normalising the concentration-time graph.

The mean and standard deviation of the distribution can be used to calculate the vessel dispersion number (VDN) using equation 7.20 [132] :

$$\frac{\sigma^2}{t_m^2} = 2\,(VDN) + 8\,(VDN)^2 \tag{7.20}$$

where t_m and σ are the mean and standard deviation of the distribution given in Fig. 7.5. The vessel dispersion number is the non-dimensionalised dispersion coefficient in the dispersion model [132]. In the above example $VDN = 4.92 \times 10^{-6}$.

The effect on the vessel dispersion number of the three non-dimensional numbers, Ca, L_s and L_b that define the geometric characteristics in a Taylor flow system can be seen in Figs. 7.6 and 7.7. Both figures show very low VDN values, confirming that axial mass transfer in a liquid is significantly reduced with Taylor flow to near PFR level. For comparison, the vessel dispersion number for laminar flow of liquids in tubes is at least 3 orders of magnitude larger [132]. An increase in VDN, and

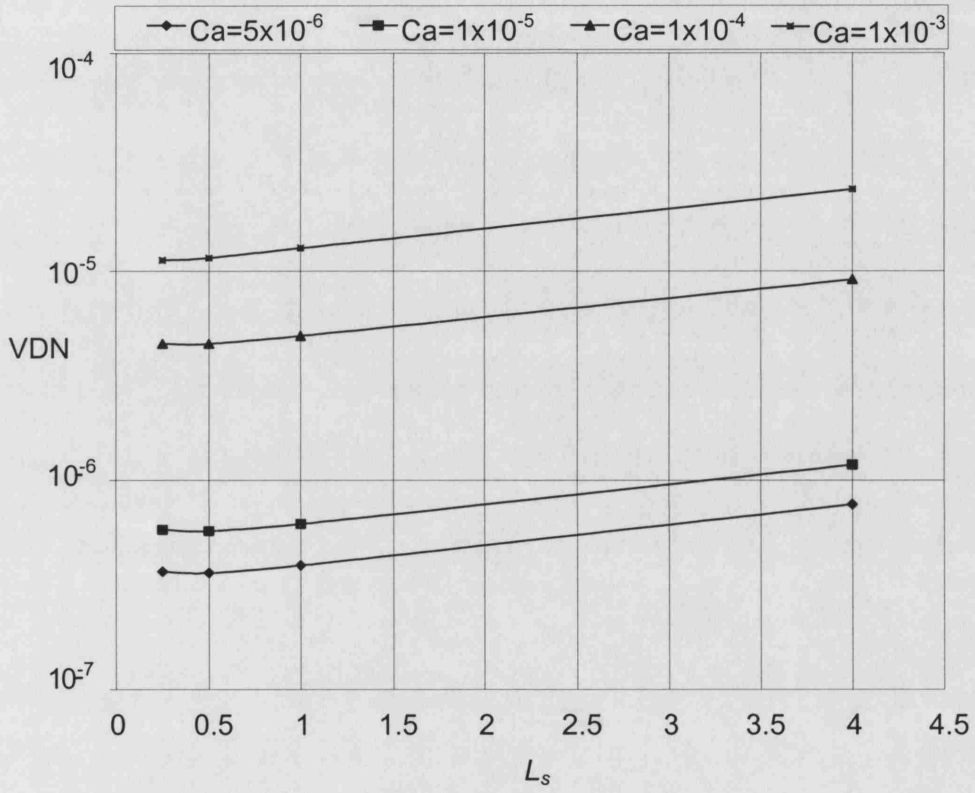

Fig. 7.6: Variation of the vessel disperion number with L_s and Ca for a bubble length of $L_b = 1.1$.

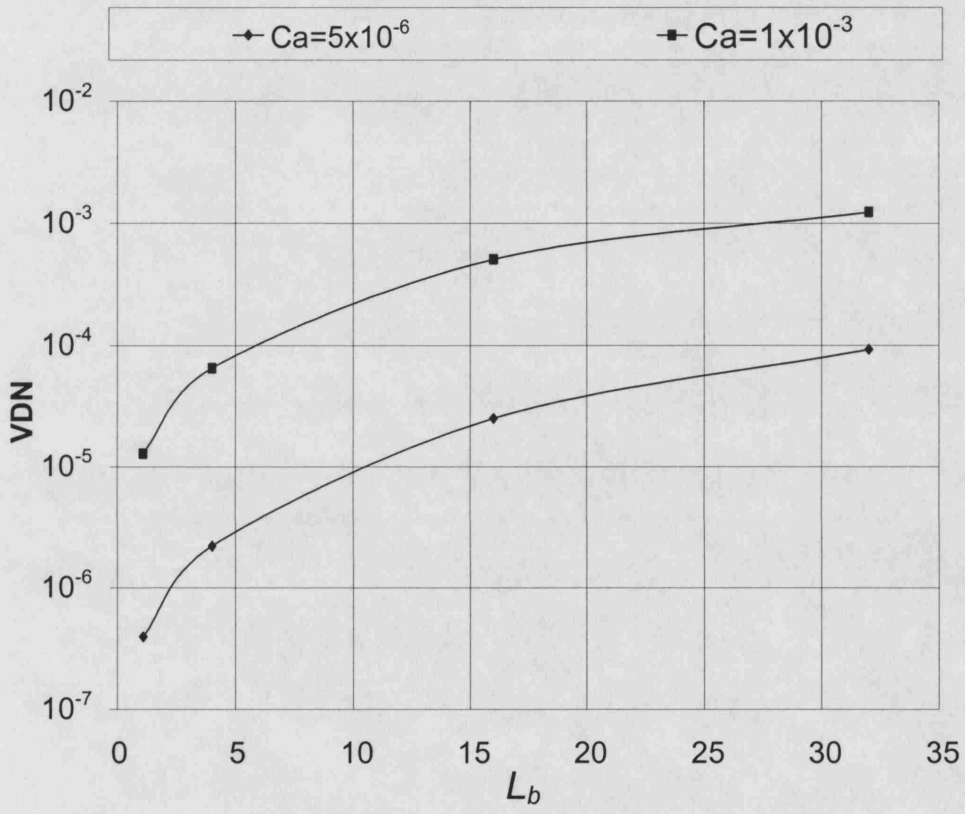

Fig. 7.7: Variation of the vessel dispersion number with bubble length L_b and Ca for slug length of $L_s = 1.0$.

hence axial mixing, with increasing Ca can also be seen. This is to be expected as increased Ca results in thicker liquid films that would favour communication between slugs. It can also be seen that VDN generally increases with L_s and L_b. It should be noted that a change in L_b does not affect the concentration of the exiting slugs. The increase in the spacing between the different slugs caused by the increased bubble length affects the mean and standard deviation of the residence time distribution as predicted by equation 7.20 and hence VDN. For reduced VDN in a Taylor flow system with mass transfer, short bubble and slug lengths should be formed at the inlet. Comparison of the results from the numerical technique to the analytical solution given by equation 7.17 showed about 2% difference in predictions for $Pe = 10$. Decreasing the Peclet number below 10 to a value of 2 showed a much more significant difference in the predictions of the two models. The analytical solution (equation 7.17) can therefore be used for Pe larger than 10.

The simple numerical model described above is suitable for low Peclet numbers where diffusion and convection are sufficiently large for mixing to ensure uniform concentration in the slug. To find the upper limit of the Peclet number up to which this simple model can be used, results were compared with the detailed numerical simulations of Chapter 5, which incorporate the flow field inside each unit cell. These showed that the present model may be used for Pe up to 1000, based on unit cell comparisons. It is worth noting that the curves in Figs 7.6 and 7.7 are independent of the Peclet number for $10 < Pe < 1000$.

It should be remembered that with increasing slug length, the behaviour of the unit slug deviates more and more from being a well mixed region (Table 5.10) and the time needed for the material to convect and diffuse from one end of the slug to the other would become significant. It should also noted that the Pe lower limit can only be determined experimentally, or with significant computational effort if all the slugs are rigorously modelled

7.4 Conclusions

A numerical model has been developed for axial mixing in microchannel Taylor flow. The model assumes uniform concentration in the liquid slugs and uses a uniform velocity and concentration in the film surrounding the bubbles. The model can either be solved numerically, or for $Pe > 10$, simplified to yield an analytical solution.

The model was found to be suitable for ranges $Ca < 10^{-3}$, $Pe < 1000$. Axial mixing was in general very low. Trends show increasing vessel dispersion number

(increasing axial mixing) with increasing capillary number and slug and bubble lengths. In addition, for $10 < Pe < 1000$ a simple analytical expression was also able to predict axial mixing with small deviations from the numerical model.

8. REACTION REGIMES IN TAYLOR FLOW REACTORS

Nomenclature

a	Mass transfer area/volume	$\mathrm{m}^2/\mathrm{m}^3$
c	Concentration of dissolving gas	kg/m^3
c_0'	Surface equilibrium concentration	kg/m^3
Ca	Capillary number $\frac{\mu U_b}{\gamma}$	
d	Microchannel diameter	m
D	Diffusivity of tracer species	m^2/s
Fo	Fourier number $\frac{1}{Pe}\frac{(L_b-1)}{\delta^2}$	
Fr	Froude number $\frac{U_b^2}{g\ d}$	
Ha_n^f	Film Hatta number for reaction of order n	$\frac{d^2}{D^i}k_n c_0'^{n-1}$
Ha_n^S	Slug Hatta number for reaction of order n	$\frac{\delta^2}{D^i}k_n c_0'^{n-1}$
k	Mass transfer coefficient	$\mathrm{m}^{-2}\,\mathrm{s}^{-1}$
k^0	Mass transfer coefficient for reaction free systems	$\mathrm{m}^{-2}\,\mathrm{s}^{-1}$
k_n	Order n reaction rate constant	$\mathrm{m}^{-2}\,\mathrm{s}^{-1}$
l_b	Taylor bubble length	m
l_s	Liquid slug length	m
L_b	Dimensionless Taylor bubble length $\frac{l_b}{d}$	
L_s	Dimensionless liquid slug $\frac{l_s}{d}$	
$\mathbf{N}$	Gas solute flux into the liquid	$\mathrm{kg}\,\mathrm{m}^{-2}\,\mathrm{s}^{-1}$
p	Pressure	N/m^2
Pe	Bulk Peclet number $\frac{U_b d}{D}$	
Q_{film}	Volumetric flow rate in liquid film	m^3/s
Q_l	Liquid volumetric flow rate in reactor	m^3/s
Re	Reynolds number $\frac{\rho U_b d}{\mu}$	
r	Reaction rate expression	$\mathrm{kg}\ \mathrm{m}^{-3}\,\mathrm{s}^{-1}$
R	Tube radius	m
Sh	Sherwood number $\frac{kd}{D}$	
Sh_t	Transient Sherwood number $\frac{kd}{D}$	

t	Time	s
t^r	Reaction characteristic time	s
t^d, t^D	Diffusion characteristic time	s
t^c	Convection characteristic time	s
t^{res}	Reactor residence characteristic time	s
$\mathbf{u}$	Velocity field	m/s
V	Volume of slug	m^3
x	Radial axis in film	m
z	Axial axis in film	m
Greek Symbols		
γ	Interfacial tension	N/m
δ	Thickness of film surrounding bubble	m
ε	Gas holdup	
μ	Viscosity	$N s m^{-2}$
ρ	Density	kg/m^3
$d\sigma$	Surface area element	m^2
Superscripts		
n	Reaction order	
$\bar{x}$	Barred symbols are non-dimensionalised	
Subscripts		
0	Initial value at $t = 0$	
av	average slug value	
ov	Overall value	
gs	Bubble to slug	
gf	Bubble to film	
in	Inlet value	
o	Outlet value	

8.1 Introduction

As a consequence of the small scales in microreactors the thin fluid layers improve mass and heat transfer rates. The small volumes involved makes microreactors suitable for reaction kinetics determination. With two-phase reactions, depending on the flow pattern differences of contact area between phases and mass transfer rates result. These determine whether a system is under kinetic control so that reaction kinetics can be extracted.

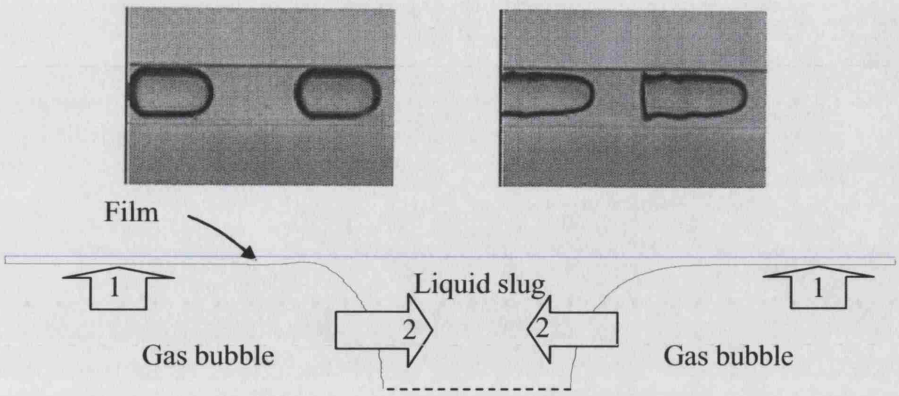

Fig. 8.1: Mass transfer from a Taylor flow unit cell. Black arrows: (1) gas to liquid mass transfer occuring into the liquid film from the bubble, (2) gas to liquid mass transfer occuring into the liquid slug from the bubble caps.

One of the dominant flow patterns during gas-liquid flow in microsystems is Taylor flow. In this pattern long gas bubbles adopt a characteristic capsular shape and completely fill the channel cross section with only a thin liquid film separating them from the wall. The presence of bubbles in front and at the back of the slugs modifies the flow field in the liquid compared to single phase flow, and toroidal vortices are formed [83]. The large exchange area in the film and the mixing in the slug make it suitable as a flow pattern for kinetic studies. In addition, axial mixing between the liquid slugs is significantly reduced as a result of the segmentation of the liquid phase by the gas bubbles and the gas-liquid and liquid to wall mass transfer is improved by the presence of vortices in the liquid slugs [143, 97, 110].

The first aim of this work is to identify the conditions under which a Taylor flow microreactor operates in the kinetics regime for a gas-liquid reaction. A second aim is to identify, for a given reaction and flow conditions, which actual regime is dominant in different parts of the flow. This is a prerequisite to understanding the reactor behaviour if it is to be used for production rather than analysis.

8.2 Literature Review

8.2.1 Theory

Generally, liquid phase reaction where one of the reactants is supplied from the gas phase proceeds by the following steps:

1. Diffusion of reactants from the gas phase to the gas-liquid interface.

2. Diffusion of the reactants from the interface towards the bulk of the liquid phase.

3. Chemical reaction within the liquid phase.

4. Diffusion of the reactants initially present within the liquid phase and reaction products within the liquid phase due to the concentration gradients created by the chemical reaction.

To obtain kinetics from a Taylor flow reactor (and any gas-liquid reactor) it is necessary that all steps have characteristic times shorter than the reaction time so that reaction (step 3) is the slowest step in the sequence.

The study of gas-liquid mass transfer and reaction in Taylor flow is complicated by the fact that there exist two regions in the liquid phase, film and slug, with very different associated interface areas and diffusion lengths and consequently reaction rate ranges in which they are in the kinetics limit (Fig. 8.1). Different gas-liquid mass transfer coefficients would need to be used for the film (k_{gf}) and the slug (k_{gs}) to separately account for different reaction regimes in these two regions.

It will be assumed that no concentration gradients exist in the gas phase. This will be true if the gas bubbles contain pure reactant gas, otherwise, for gas mixtures, the large diffusivities of gases ensure the homogeneity of the bubble composition. The limiting mass transfer resistance is always in the liquid phase and step 1 need not be considered further.

neither of step 2 or 3 can be eliminated except under limiting conditions which depends on the relative dominance of the kinetic or mass transfer rates as well as the interfacial area per unit volume (a) through which the transfer occurs. Before mathematically stating these limits it is worth characterising these rates using a reaction time t^r and a mass transfer time t^D.

The characteristic reaction time is:

$$t^r = \frac{c}{r} \tag{8.1}$$

where r is the reaction rate and c is the actual concentration of the reactant considered, assuming irreversible reactions. The physical meaning of the reaction time is the amount of time required by the reaction to proceed to an appreciable extent.

The diffusion time of the gas in a flow depends on its diffusivity D in the liquid and the liquid hydrodynamics. It is usually defined differently depending on the hydrodynamic model adopted. Two models exist in the literature for the estimation

of diffusion time, namely the film theory [135, 136] and penetration theory [137, 138]. The penetration theory model has two main formulations (Higbie's constant or Danckwerts' exponential distribution of surface renewal time). Experimentally it has been found that k^0 has a $D^{1/2} - D^{1/3}$ dependency which is more in agreement with the penetration theory $k^0 \propto D^{1/2}$ than with the film theory (linear dependency) [139].

Using penetration theory diffusion times for the slug t^D_{gs} and the film t^D_{gf} can be defined as [139]:

$$t^D_{gf} = \frac{D}{\left(k^0_{gf}\right)^2} \tag{8.2}$$

$$t^D_{gs} = \frac{D}{\left(k^0_{gs}\right)^2} \tag{8.3}$$

where k^0_{gf} and k^0_{gs} are the gas-liquid mass transfer coefficients for the two regions which result only from physical adsorption. The diffusion time depends on the hydrodynamic conditions and represents the time actually available for the unsteady diffusion process within the surface elements, while the reaction time depends only on the the kinetics of the reaction considered, and it is not the time available for the reaction but the time required by it.

When yield is being calculated, a third characteristic time should be considered, namely the time which is actually available for the reaction. That is obviously the total residence time in the reactor, t^{res}.

$$t^{res} = \frac{(1-\varepsilon_g)\,V}{Q_l} \tag{8.4}$$

where ε_g is the gas hold-up, V is the reactor volume and Q_l is the liquid volumetric flow rate.

Astarita [139] gives practical experimental criteria to identify when an entire reactor is operating in the kinetics regime: The two limiting conditions which need to be satisfied throughout are given by conditions 8.5, and 8.6:

$$t^D \ll t^r \tag{8.5}$$

$$r(c_0) \ll k^0_{ov} a_{ov} V c'_0 \tag{8.6}$$

where c_0' is the equilibrium concentration of diffusing species at the interface $k_{ov}^0 a_{ov}$ is the product of the overall mass transfer coefficient and total interfacial area per unit volume and V is the holdup. For a system where equations 8.5, and 8.6 are both satisfied throughout, the concentration throughout is very nearly c_0'. It has been established that the absorption rate of the gas into the liquid has characteristics:

1. Independent of interface area, aV,
2. Dependent on the liquid hold-up, V
3. Independent of k_L^0
4. Proportional to r.
5. Influenced by the overall driving force c_0' only.

The characteristics 1-5 need to be tested before the correct kinetics are said to be obtained from experimental data for an unknown reaction rate. However, one can determine beforehand the upper limit of the reaction rates that a reactor of a given size and flow structure can be used to measure. One only needs to ensure that k_{ov}^0 (or better still k_{gs} and k_{gf} individually in Taylor flow) always satisfy expressions 8.5 and 8.6 throughout the flow for the reaction to be limiting and for step 2 to be negligible.

Experimentally the mass transfer of gaseous oxygen into water, ethanol and ethylene glycol was studied by Irandoust et al. [143] in a Taylor flow reactor. The steady state convection diffusion equation was solved to calculate k_{gf}^0 for the film, assuming that convection predominated with a steady falling film velocity profile in the axial direction and molecular diffusion the only means of mass transfer in the radial direction. While for calculating k_{gl}^0 a correlation from Clift et al. [140] for mass transfer from solid spheres was used. The overall gas-liquid mass transfer coefficient was the sum of the two contributions as shown in equation 8.7.

$$\left(k_{ov}^0 a_{ov}\right)_{calc} = k_{gf}^0 a_{gf} + k_{gs}^0 a_{gs} \tag{8.7}$$

$$\left(k_{ov}^0 a_{ov}\right)_{calc} = 0.686 \left(k_{ov}^0 a_{ov}\right)_{\exp} \tag{8.8}$$

The authors suggested a correction factor of 0.686 (equation 8.8) to correct for the model assumption of perfect mixing of the liquid film surrounding the bubble with the subsequent liquid slug. The remaining scatter between the model and the

experimental data was attributed to impurities which affect the thickness of the liquid film surrounding the bubbles. Applying a numerical method to an air-water system with and without reaction on the wall, Irandoust et. al. [143] concluded that the mass transfer contributions came equally from the liquid film and the liquid slug. This contradicts intuition that a fast reaction on the wall would increase the mass transfer contribution of the film because of usually larger area associated with the film. It should also be noted the correlation of Clift et al. [140] is for a single spherical bubble and cannot be adapted for a finite slug lengths except when limited diffusion takes place in the slugs so that they may be approximated as infinite.

Berčič and Pintar [97] tested experimentally the correlations of Irandoust et al. [143] and investigated the effect of capillary diameter, unit cell length and gas hold-up on the measured $k_{ov}a_{ov}$ using methane as the transferred species. The results were correlated by equation 8.9:

$$k^0_{ov}a_{ov} = \frac{0.111U_b^{1.19}}{(l_s)^{0.57}} \tag{8.9}$$

The mass transfer coefficient measured was found to be smaller than that predicted by Irandoust et al. [109]. No explanation was given by Berčič and Pintar [97] for this difference but careful analysis of their experiments shows that they have used very long liquid slugs in experiments, probably beyond the range examined by Irandoust et al. [143]. A key finding of their experiments is that the mass transfer coefficient of the bubble is independent of bubble length and depends only on the slug length in contradiction to the conclusions of Irandoust et al. [109]. A possible reason for this independence is that the liquid in the film quickly saturates within a short distance from coming into contact with the bubble surface so that the remaining length does not contribute to mass transfer. This is particularly true for long bubbles used by Berčič and Pintar [97].

Berčič [110] generalised expression (8.9) for other gases as follows:

$$\left(k^0_{ov}a_{ov}\right)_i = \left(k^0_{ov}a_{ov}\right)_{Me}\left(\frac{D}{D^{Me}}\right)^{0.66} \tag{8.10}$$

where D^{Me} is the diffusivity of methane in the water.

Kreutzer[98], in his work on monoliths with reaction at the wall, developed a simple model for mass transfer in a unit cell. For the liquid film surrounding the bubble a simple linear concentration gradient was assumed which is zero at the wall and equal to the saturation concentration at the surface of the bubble. For the mass transfer from the bubble caps Higbie's penetration theory [137] was used (equation

8.3). The diffusion time was calculated to be $t_{gl}^{D} \sim \frac{8U_b}{\pi d}$ giving an expression for the flux N_{gs}:

$$N_{gs} = k_{gl}^{0} a_{gl} \left(c_0' - c_{slug}\right) \sim 2 \cdot 2\sqrt{\frac{8U_{ls}D}{\pi d}} \frac{1}{2} \pi d^2 \left(c_0' - c_{slug}\right) \tag{8.11}$$

where N_{gl} is the gas to liquid flux from the bubble caps, c_0' is the saturation concentration at the interface and c_{slug} is the slug average concentration. Differences were found between the model predictions and results from numerical calculations of the transfer from a unit cell at high Peclet number (Pe) values. Kreutzer [98] attributed this discrepancy to concentration gradients in the liquid slug where, because of low diffusivity, the high concentration near the bubbles is not transferred fast enough to the core of the circulating vortex.

Kreutzer's results are not applicable to the current study where only reactions in the bulk liquid phase are considered.

van Baten and Krishna [141] calculated the transfer coefficient from the gas bubble caps into the liquid slugs using penetration theory. Using a constant contact time $t_{gl}^{D} \sim \frac{8U_b}{\pi^2 d}$ (equation 8.3) they obtained:

$$k_{ls}^{0} = \sqrt{2\frac{DU_b}{\pi^2 d}} \tag{8.12}$$

$$a_{ls} = \frac{4}{l_b + l_s} \tag{8.13}$$

The contribution from the liquid film was found from Sherwood et. al. [142] as[1]:

$$k_{lf}^{0} = \frac{Q_{film}}{\pi d(l_b - 2R_b)} \ln\left(\frac{1}{\Delta}\right) \tag{8.14}$$

where Q_{film} is the volumetric flow of the liquid film down the channel walls and Δ is given as an infinite series:

$$\begin{aligned} \Delta \;=\; & 0.7857 \exp\left(-5.121 Fo\right) + 0.1001 \exp\left(-39.21 Fo\right) \\ & +0.0360 \exp\left(-105.6 Fo\right) + 0.0181 \exp\left(-204.7 Fo\right) \\ & +..., \end{aligned} \tag{8.15}$$

The Fourier number is defined as

[1] Based on an analytical solution of the convection diffusion equation for a steady falling film.

$$Fo \equiv \frac{D^i}{t_{film}\delta^2} \tag{8.16}$$

and t_{film} is the residence time of the liquid in the film calculable from the average flow velocity. van Baten and Krishna [141] suggest that it is more convenient to approximate equation 8.14 based on two limits as follows:

$$k_{gf} = 2\sqrt{\frac{D}{\pi t_{film}}}\frac{\ln\left(\frac{1}{\Delta}\right)}{(1-\Delta)}; \quad Fo < 0.1 \tag{8.17}$$

$$k_{gf} = 3.41\frac{D}{\delta}; \quad Fo > 1 \tag{8.18}$$

For long film contact times with $Fo > 0.8$ and $\Delta \rightarrow 0$, the liquid film approaches saturation and its contribution to the overall mass transfer will be decreased. All conditions investigated by van Baten and Krishna were for $Fo < 0.1$.

The liquid film area was given by:

$$a_{film} = 4\frac{(l_b - 2R_b)}{d}\frac{1}{l_b + l_s} \tag{8.19}$$

The overall mass transfer coefficient was found from:

$$k_{ov}a_{ov} = k_{gf}a_{gf} + k_{gs}a_{gs} \tag{8.20}$$

Computational fluid dynamics simulations by van Baten and Krishna [141] seemed to confirm the validity of their simple model. Their analysis covered Pe in the range of $(2.25 \times 10^5 < Pe < 1.65 \times 10^6)$ and $Ca > 10^{-3}$. The two variables have a higher range than was considered in the present work (Appendix A).

8.3 Problem formulation and solution

8.3.1 Unit cell hydrodynamics

To totally account for the hydrodynamics during gas-liquid Taylor flow, bubble shapes and velocity, film thickness and flow field in the liquid slugs need to be known. If surface active agents are neglected, the governing dimensionless parameters derived from the Navier-Stokes equations for a gas-liquid Taylor flow are given in Table 8.1.

The influence of these parameters is discussed in detail in chapter 3. In general

Dimensionless Number	Definition
Re	$\frac{\rho U_b d}{\mu}$
Ca	$\frac{\mu U_b}{\gamma}$
L_s	$\frac{l_s}{d}$
L_b	$\frac{l_b}{d}$
Fr	$\frac{U_b^2}{gd}$

Tab. 8.1: Dimensionless numbers governing the hydrodynamics of Taylor flow

the effect of increasing Ca is always to increase the thickness of the liquid film surrounding the bubbles. The flow pattern inside long slugs soon attains a parabolic profile away from the bubble caps for sufficiently long L_s. For $Ca < 10^{-3}$, the shapes of the bubble caps can be assumed spherical and the meniscus reaches terminal film thickness quickly so that the body of the bubble can be approximated by a cylinder. The increase in Re causes an increase in the distance from the bubbles where a parabolic profile in the slug is attained. Re has limited affect on the shape of the bubble and film thickness for $Ca < 10^{-3}$. The bubble length L_b has been shown to affect the terminal velocity of the bubble when it is smaller than a certain minimum length which depends on Re and Ca.

In a vertical arrangement Fr influences the amount of liquid flowing in the falling film surrounding the bubbles. Increasing Fr increases bubble velocity. In general the effects of Pe, Fr and L_b can be neglected for $Ca \leq 10^{-3}$. For these Ca, bubbles can be taken as cylindrical with spherical caps. L_b also needs to be made sufficiently large ($L_b \gtrsim 1.2$) for a constant film thickness to be reached.

The dominance of surface forces in small diameter channels brings to prominence the effect of contaminant surface active agents (chapter 3). Their presence usually results in a larger film thickness than predicted by theory and modifications to the flow field. The characterisation of such effects requires the introduction of many more parameters (surfactant interface adsorption/desorption rates, and interface diffusivity) which vary from system to system and are difficult to estimate or measure. Instead of trying to obtain a relationship between $\bar{\delta}$ and Ca, the film thickness $\bar{\delta}$ is reported instead of Ca as a parameter (correlations in Tables 3.4 and 3.5 are nevertheless used for order of magnitude estimation). The change in the flow field with trace contaminant surfactant depends on the effect of the contaminant concentration on the local surface tension actual contaminant concentration. Without

Dimensionless Number	Definition
Pe	$\frac{U_b d}{D}$
Ha_n	$\left(\frac{d^2}{D} k_n c_0'^{n-1}\right)$

Tab. 8.2: Dimensionless numbers governing the diffusion and reaction of Taylor flow

Ca	δ/d	$Re_{\min}$	$Re_{\max}$	$Pe_{\min}$	$Pe_{\max}$
10^{-3}	6.36×10^{-3}	4.95×10^{-5}	3.09×10^{2}	3.70	1.78×10^{6}
10^{-4}	1.41×10^{-3}	4.95×10^{-5}	3.09×10^{1}	3.70	1.78×10^{5}
10^{-5}	3.06×10^{-4}	4.95×10^{-5}	3.09	3.70	1.78×10^{4}
10^{-6}	6.60×10^{-5}	4.95×10^{-5}	3.09×10^{-1}	3.70	1.78×10^{3}

Tab. 8.3: Range of dimensionless numbers for typical reaction engineering applications

further data, and to facilitate the analysis, it is also assumed that the concentrations of the contaminants are such that the effects on the flow field are negligibly small.

8.3.2 Mass transfer and reaction

To study mass transfer and reaction in the Taylor flow system a single reaction rate equation dependent only on the gas component concentration will be considered. It will be assumed that the liquid reactant/liquid confined reactants are in excess such that the concentrations of these components remain constant. The low solubility of most gases in the liquids means that this assumption is correct in most practical cases. In addition, large solubility gases would couple the gas-liquid mass transfer to the hydrodynamics in ways which can not be dealt with using the methodologies of this work so that the analysis is necessarily restricted to low solubility gases.

When considering mass transfer and reaction another two dimensionless parameters appear Pe and Ha_n (see Table 8.2 for their definition).

Although the different dimensionless parameters in Tables 8.1 and 8.2 are independent, once a specific reactant and a reaction are selected all the physical constants are fixed and the parameters are linked by the tube diameter and the bubble velocity. Considering the properties of many common solvents and a range of $1 \times 10^{-6} \leq Ca \leq 1 \times 10^{-3}$ (see Appendix A), the ranges of the other dimensionless numbers were found (Table (8.3)).

No specific range for Ha_n was investigated because of the wide variety of reaction that could take place, instead Ha_n was used as a parameter to investigate the different prevailing regimes in the unit cell.

Previous studies on axial mass transfer (chapter 5) indicated that Re has negli-

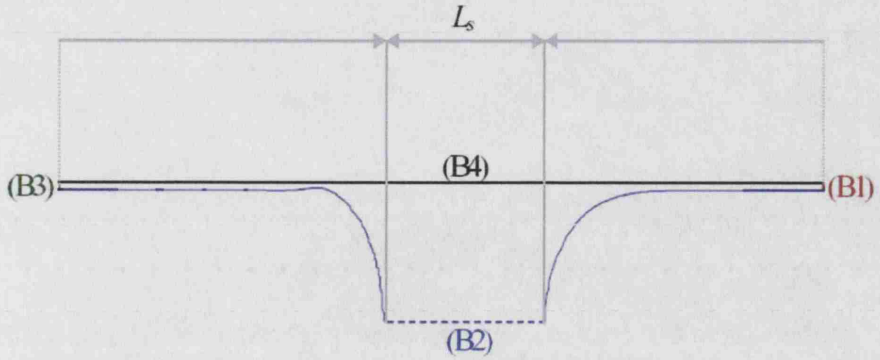

Fig. 8.2: Geometry and Boundaries of the computational domain for the unit cell hydrodynamics.

gible effect even for conditions where hydrodynamics was expected to play a larger role.

8.3.2.1 Simulation set up and analysis

The diffusion distances in the film, given by the film thickness δ (where usually $\frac{\delta}{d} < 1/100$) are very short compared to those in the slug (given by the slug length l_s or slug diameter d). It can be argued that to guarantee the kinetics regime, it is sufficient to ascertain its existence in the slugs. For this reason only limiting cases will be considered for the liquid film while the different regimes in the slugs will be investigated in detail.

As before for the analysis of reaction regimes in a Taylor flow system a unit cell consisting of a liquid slug between two half gas bubbles will be considered.

Representative slug lengths were taken as $\left\{\frac{1}{4}, 1, 4\right\}$ tube diameters are based on typical experimental findings [114]. Longer slug lengths would result in worse mass transfer behaviour (lower gas-wall mass transfer [98] and higher axial mixing as was seen in chapters 5 and 7. The lower limit $d/4$ was taken because shorter lengths may lead to bubble coalescence or other flow patterns developing such as ring flow (see chapter 2).

The liquid film will be treated separately in the next sections. To reduce the size of the computational domain in the simulations and to ensure minimal entrance effects, only a film of length of 0.1 diameters, i.e. $L_b = 1.1$ is considered.

The flow field in the liquid slug between two consecutive bubbles is calculated

Velocity	U_b terminal velocity of the bubble
Length	d tube diameter
Time	d/U_b
Concentration	c_{in} : constant inlet concentration

Tab. 8.4: Characteristic dimensions

(B1)	Inlet	$\bar{u}_z = -1,\ \bar{u}_r = 0$
(B2)	Slip or symmetry	$\mathbf{n}_b \cdot \bar{\mathbf{u}} = 0,\ \frac{\partial \bar{\mathbf{u}}}{\partial n} = 0$
(B3)	Straight-out condition	$\mathbf{n}_t \cdot \bar{\mathbf{u}} = 0\ ,\ \bar{p} = 0$
(B4)	Wall	$\bar{u}_z = -1,\ \bar{u}_r = 0$

Tab. 8.5: Boundary conditions when solving for hydrodynamics

by solving the Navier-Stokes equation (8.21) for that geometry (Fig. 8.2). The characteristic dimensions used in the non-dimensionalisation of the equations are given in Table 8.4, and the boundary conditions are given in Table 8.5.

$$Re\ \bar{\mathbf{u}} \cdot \bar{\nabla}\bar{\mathbf{u}} = -\bar{\nabla}\bar{p} + \bar{\nabla}^2 \cdot \bar{\mathbf{u}} \tag{8.21}$$

To solve equation 8.21, a commercial finite element software, Femlab [121] is used. Standard 2nd order elements were used for the velocity fields and 1st order elements for the pressure field. The total number of elements varied between 2851 and 11270 with larger concentration near the bubble caps and at the boundary between the liquid film and the vortex region in the slug. An Athlon 1.6 GHz processor with 1 Gb RAM was used. The hydrodynamic solution is easily obtained in $\sim$ 8 minutes of CPU time.

8.3.3 Model for reaction and mass transfer in the liquid film

Neglecting surface tension gradients in the film and their effects on film thickness as well as gravity effects results in a uniform velocity field in the film. This is equivalent to zero velocity in the absolute frame and is a good approximation of reality. The no-slip condition assumed at the wall and the small film thickness necessarily cause any gravity or surface tension gradient flows to be insignificant.

With the velocity unidirectional in the liquid film the convection-diffusion equation in the thin liquid film is given by:

$$\frac{\partial c}{\partial t} + \left(U_b \frac{\partial \bar{c}}{\partial z}\right) = D^i \left(\frac{1}{r}\frac{\partial c}{\partial r} + \frac{\partial^2 c}{\partial r^2} + \frac{\partial^2 c}{\partial z^2}\right) - r \tag{8.22}$$

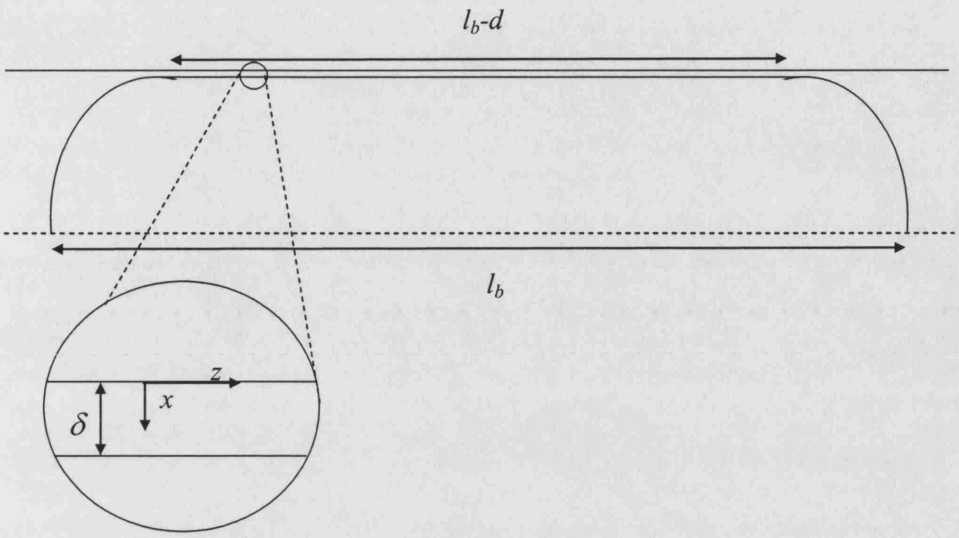

Fig. 8.3: Schematic of the film region showing the coordinate system used and the characteristic lengths.

which can be changed using a linear transformation, $r = R(1 - x/R) : dr = -dx$ to an equation of the form (Fig. 8.3):

$$\frac{\partial c}{\partial t} + \left(U_b \frac{\partial c}{\partial z}\right) = D^i \left(\frac{-1}{R(1-x/R)} \frac{\partial c}{\partial x} + \frac{\partial^2 c}{\partial x^2} + \frac{\partial^2 c}{\partial z^2}\right) - r \tag{8.23}$$

For small x, by neglecting the terms of order higher than 1 in the expansion of $\frac{1}{(1-x)}$, equation 8.23 can be rewritten :

$$\frac{\partial c}{\partial t} + \left(U_b \frac{\partial c}{\partial z}\right) = D^i \left(\frac{-2}{d} \frac{\partial c}{\partial x} + \frac{\partial^2 c}{\partial x^2} + \frac{\partial^2 c}{\partial z^2}\right) - r \tag{8.24}$$

The characteristic times can be, the reaction, the convective, or the diffusive times:

$$\begin{array}{ll} t^r & \frac{c_0'}{r(c_0')} \\ t^c & (l_b - d)/U_b \\ t^d & \delta^2/D^i \end{array}$$

The characteristic distances are:

$$\begin{array}{ll} d_z & l_b - d \\ d_x & \delta \end{array}$$

Non-dimensionalisation with the diffusion time is used as the characteristic time[2]

[2] Note that for the slug convection time $\hat{t} = d/U_b$, was used instead.

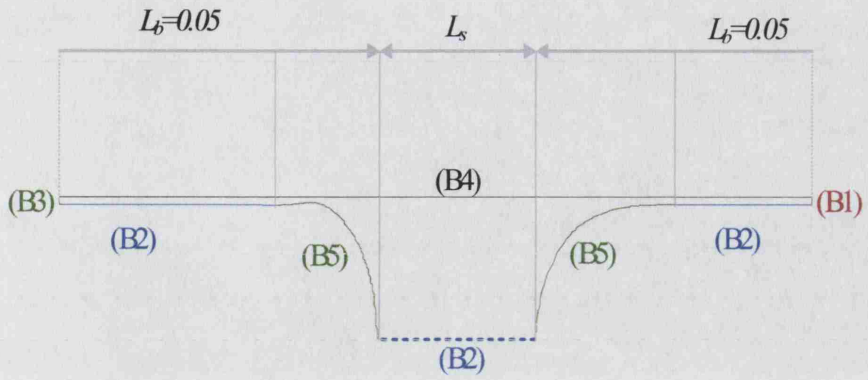

Fig. 8.4: Geometry and Boundaries of the computational domain for the convection-diffusion-reaction in the unit cell.

results in equation 8.25:

$$\frac{\partial \bar{c}}{\partial \bar{t}} + \left(\underbrace{\left(\frac{dU_b}{D^i}\right)}_{Pe} \frac{\delta}{l_b - d} \frac{\delta}{d} \frac{\partial \bar{c}}{\partial \bar{z}} \right) = \left(\left(\frac{-2\delta}{d}\right) \frac{\partial \bar{c}}{\partial \bar{x}} + \frac{\partial^2 \bar{c}}{\partial \bar{x}^2} + \left(\frac{\delta}{l_b - d}\right)^2 \frac{\partial^2 \bar{c}}{\partial \bar{z}^2} \right) - \frac{\delta^2}{D^i} \frac{r}{c_0'} \tag{8.25}$$

which in terms of the different characterisitic times is equivalent to:

$$\frac{\partial \bar{c}}{\partial \bar{t}} + \left(\frac{t^d}{t^c} \frac{\partial \bar{c}}{\partial \bar{z}} \right) = \left(\left(\frac{-2\delta}{d}\right) \frac{\partial \bar{c}}{\partial \bar{x}} + \frac{\partial^2 \bar{c}}{\partial \bar{x}^2} + \left(\frac{\delta}{l_b - d}\right)^2 \frac{\partial^2 \bar{c}}{\partial \bar{z}^2} \right) - \frac{t^d}{\left(\frac{c_0'}{r}\right)} \tag{8.26}$$

and the reaction time appear indirectly:

$$\left(\frac{c_0'}{r(c)}\right) \geq \left(\frac{c_0'}{r(c_0')}\right) = t^r \tag{8.27}$$

8.3.4 Model for reaction and mass transfer in the liquid slug

The transient convection-diffusion-reaction equation for the given domain is:

$$\frac{\partial \bar{c}}{\partial \hat{t}} + \bar{\mathbf{u}} \cdot \bar{\nabla} \bar{c} - \left(\frac{1}{Pe}\right) \bar{\nabla}^2 \bar{c} + \left(\frac{1}{Pe}\right) \left(\frac{d^2}{D^i} \frac{r}{c_o'}\right) = 0 \tag{8.28}$$

where r is the rate of consumption of the species $\bar{c}$. For steady state it becomes:

(B1)	$\bar{c} = \bar{c}_{in}$
(B2)	$\mathbf{N} \cdot \mathbf{n} = 0$
(B3)	$\mathbf{N} \cdot \mathbf{n}$ =Convective Flux
(B4)	$\mathbf{N} \cdot \mathbf{n} = 0$
(B5)	$\bar{c} = 1$

Tab. 8.6: Boundary conditions for the convection diffusion reaction equation

$$\bar{\mathbf{u}} \cdot \bar{\nabla} \bar{c} = \left(\frac{1}{Pe}\right) \bar{\nabla}^2 \bar{c} - \left(\frac{1}{Pe}\right) \left(\frac{d^2}{D^i} \frac{r}{c_o'}\right) \tag{8.29}$$

The convection-diffusion-reaction equation 8.28 with the boundary conditions given in Table 8.6 was solved with Femlab [121], for a similar computational domain as that used for the hydrodynamics (Fig. 8.4). The calculated velocity field was interpolated to obtain the velocity term in equation 8.28. The initial condition of the tracer in the computational domain is constant concentration either $\bar{c}_{init} = 0$ or $\bar{c}_{init} = 1$ depending on the type of simulation being carried out. The output concentration at boundary (B3) (at regular time steps or at steady state) was averaged over the cross section and stored as were the average concentrations in the active domains.

Third order elements were used for the concentration of the tracer. Their number varied from 5620 to 15431 elements depending on the length of the slug. The numerics of the simulation limited the values of Peclet number which could be used. Beyond Pe of the order of 10^5 significant overshooting (concentration in excess of the maximum concentration of 1) and undershooting (negative concentrations) developed around areas of high concentration gradients (specifically the region of the stream line separating the film and the vortex). It also became difficult to establish the grid independence of the results. While overshooting/undershooting effects can be reduced by using various shock capturing techniques [121] these introduce significant artificial diffusion and for that reason are not implemented here. Therefore the upper limit considered was $Pe \sim 10^5$. It will be shown later that at the upper values of Pe the reaction controlled regime is difficult to achieve in the system.

8.3.4.1 Simulations and methodology for result analysis

Volume averaging of equation 8.28 yields expression 8.30.

$$\frac{1}{\bar{V}_{slug}} \int_{\bar{V}_{slug}} \left[\frac{\partial \bar{c}}{\partial \hat{t}} + \bar{\mathbf{u}} \cdot \bar{\nabla} \bar{c} - \left(\frac{1}{Pe}\right) \bar{\nabla}^2 \bar{c}\, d\bar{V} + \left(\frac{1}{Pe}\right) \left(\frac{d^2}{D^i} \frac{r}{c_o'}\right)\right] dV = 0 \tag{8.30}$$

By applying Gauss's divergence law equation 8.30 becomes equation 8.31.

$$\frac{\partial \bar{c}_{av}}{\partial \hat{t}} + \frac{1}{\bar{V}_{slug}} \underbrace{\oint \bar{\mathbf{u}}\bar{c} \cdot d\bar{\boldsymbol{\sigma}}}_{Convective} - \left(\frac{1}{\bar{V}_{slug}}\right) \underbrace{\oint \frac{\bar{\nabla}\bar{c}}{Pe} \cdot d\bar{\boldsymbol{\sigma}}}_{Diffusive} + \frac{1}{\bar{V}_{slug}} \int_{\bar{V}_{slug}} \left(\frac{1}{Pe}\right) \left(\frac{d^2}{D^i} \frac{r}{c_o'}\right) dV = 0 \tag{8.31}$$

The terms of the surface integrals can be divided into the different regions reflecting the boundary conditions used:

$$\begin{aligned} 0 = \frac{\partial \bar{c}_{av}}{\partial \hat{t}} &+ \frac{1}{\bar{V}_{slug}} \left(\int_{inlet} \left(\bar{\mathbf{u}}\bar{c} - \frac{\bar{\nabla}\bar{c}}{Pe} \right) \cdot d\bar{\boldsymbol{\sigma}} - \int_{exit} \left(\bar{\mathbf{u}}\bar{c} - \frac{\bar{\nabla}\bar{c}}{Pe} \right) \cdot d\bar{\boldsymbol{\sigma}} \right) \\ &- \frac{1}{\bar{V}_{slug}} \left(\int_{bubble} \frac{\bar{\nabla}\bar{c}}{Pe} \cdot d\bar{\boldsymbol{\sigma}} \right) + \frac{1}{\bar{V}_{slug}} \int_{\bar{V}_{slug}} \left(\frac{1}{Pe}\right) \left(\frac{d^2}{D^i} \frac{r}{c_o'}\right) dV \end{aligned} \tag{8.32}$$

The flux from the interface is related to the mass transfer coefficient and the gradient of concentration. In dimensionless form this is given by equation 8.33:

$$\frac{1}{\bar{V}_{slug}} \left(\int_{bubble} \frac{\bar{\nabla}\bar{c}}{Pe} \cdot d\bar{\boldsymbol{\sigma}} \right) = \frac{Sh}{Pe} \bar{a} \left(1 - \bar{c}_{av}\right) \tag{8.33}$$

where the Sherwood number, Sh is:

$$Sh = \frac{k_{lf} d}{D^i} \tag{8.34}$$

and the circular geometry used in the simulations give a value of specific area $\bar{a}$:

$$\bar{a} = \frac{12\left(1 - 2\bar{\delta}\right)^2}{3L_s + 2\bar{\delta}\left(4\bar{\delta}\left(2\bar{\delta} - 3\right) + 3\right) + 1} \tag{8.35}$$

Substitution of equation 8.33 into 8.32 gives:

$$\begin{aligned} \frac{Sh_t}{Pe} \bar{a}\left(1 - \bar{c}_{av}\right) = \frac{\partial \bar{c}_{av}}{\partial \hat{t}} &+ \frac{1}{\bar{V}_{slug}} \left(\int_{inlet} \left(\bar{\mathbf{u}}\bar{c} - \frac{\bar{\nabla}\bar{c}}{Pe} \right) \cdot d\bar{\boldsymbol{\sigma}} - \int_{exit} \left(\bar{\mathbf{u}}\bar{c} - \frac{\bar{\nabla}\bar{c}}{Pe} \right) \cdot d\bar{\boldsymbol{\sigma}} \right) \\ &+ \frac{1}{\bar{V}_{slug}} \int_{\bar{V}_{slug}} \left(\frac{1}{Pe}\right) \left(\frac{d^2}{D} \frac{r}{c_o'}\right) dV \end{aligned} \tag{8.36}$$

If all the terms in the equation are known, the transient Sherwood number Sh_t can then be calculated as follows:

$$Sh_t = Pe\frac{1}{\bar{a}\left(1-\bar{c}_{av}\right)}\frac{\partial \bar{c}_{av}}{\partial \hat{t}} - \left(1-\frac{1}{\left(1-2\bar{\delta}\right)^2}\right)Pe\frac{\left(\bar{N}_{in}-\bar{N}_{out}\right)}{\left(1-\bar{c}_{av}\right)} + \frac{\int_{\bar{V}_{slug}}\left(\frac{d^2}{D}\frac{r}{c_o}\right)dV}{\bar{V}_{slug}\bar{a}\left(1-\bar{c}_{av}\right)} \tag{8.37}$$

where $\bar{N}$ is the average convective and diffusive flux across the inlet and outlet boundaries:

$$\bar{N} = \frac{1}{\bar{A}}\int\left(\bar{\mathbf{u}}\bar{c} - \frac{\bar{\boldsymbol{\nabla}}\bar{c}}{Pe}\right)\cdot d\bar{\sigma} \tag{8.38}$$

Equation (8.37) in dimensional form and without reaction was used by van Batten and Krishna [141] to calculate the mass transfer coefficient. It can easily be seen that the reaction rate increases the Sherwood number Sh_t and hence the mass transfer.

Three different simulations were carried out. Firstly steady state simulations were performed neglecting the reaction rate. That yields the adsorption Sherwood number Sh :

$$Sh = -\left(1-\frac{1}{\left(1-2\bar{\delta}\right)^2}\right)Pe\frac{\left(\bar{N}_{in}-\bar{N}_{out}\right)}{\left(1-\bar{c}_{av}\right)} \tag{8.39}$$

This however does not show how quickly the steady state is reached, which necessitates transient simulations (again neglecting the reaction rate)

$$Sh_t = Pe\frac{1}{\bar{a}\left(1-\bar{c}_{av}\right)}\frac{\partial \bar{c}_{av}}{\partial \hat{t}} - \left(1-\frac{1}{\left(1-2\bar{\delta}\right)^2}\right)Pe\frac{\left(\bar{N}_{in}-\bar{N}_{out}\right)}{\left(1-\bar{c}_{av}\right)} \tag{8.40}$$

In both these simulations $\bar{c}_{in} = 0$ and $\bar{c}_{init} = 0$. Although the inlet concentration $\bar{c}_{in}$ is usually close to 1, a value of 0 is used instead. If $\bar{c}_{in} = 1$ was to be used instead the steady state average slug and the output concentrations would be essentially 1. This would make expression (8.39) indeterminate and would complicate the calculation of the terminal concentration by (8.40). In the third set of simulations, equation 8.29 is solved directly. The average concentration in the slug region is reported for these. If the unit cell concentration $\bar{c}_{av}$ at steady state, meets some criteria (say $\bar{c}_{av} \geq 0.95$) despite the reaction, the slug is said to be in the kinetics regime. Assuming an n^{th} order reaction rate, equation 8.29 becomes:

$$\bar{\mathbf{u}}\cdot\bar{\nabla}\bar{c} = \left(\frac{1}{Pe}\right)\bar{\nabla}^2\bar{c} - \left(\frac{Ha_n^S}{Pe}\right)\bar{c}^n \tag{8.41}$$

where:

$$Ha_n^S = \frac{d^2}{D^i} k_n c_0'^{n-1} \tag{8.42}$$

8.4 Results and Discussion

8.4.1 Reaction and mass transfer in the liquid film

Three possible limiting cases are investigated. The three cases are:

$$\begin{aligned} &(1) \quad t^d \ll t^c \quad t^d \ll t^r \\ &(2) \quad t^d \approx t^c \quad t^d \ll t^r \\ &(3) \quad t^d \ll t^c \quad t^d \approx t^r \end{aligned}$$

A fourth arrangement is also possible ($t^c \ll t^d, t^c \approx t^r$), however, as the problem investigated is that of mass transfer from the bubble to the liquid, it is not a useful limit to consider because it neglects diffusion. Equation 8.25 can be simplified for the three limiting cases. Since $\delta \ll d$ and $\delta \ll (l_b - d)$, the ratios $\frac{\delta}{d}$ and $\frac{\delta}{(l_b-d)}$ are at most of the order of $O(10^{-2})$ (Table 8.3) and the terms with coefficients of only $\frac{\delta}{l_b-d}$ or $\frac{\delta}{d}$ can be eliminated to give equation 8.43.

$$\frac{\partial \bar{c}}{\partial \bar{t}} + \left(\underbrace{\left(\frac{dU_b}{D^i}\right)}_{Pe} \frac{\delta}{l_b - d} \frac{\delta}{d} \frac{\partial \bar{c}}{\partial \bar{z}} \right) = \frac{\partial^2 \bar{c}}{\partial \bar{x}^2} - \frac{\delta^2}{D^i} \frac{r}{c_0'} \tag{8.43}$$

8.4.1.1 Case (1) (slow reaction regime, $t^d \ll t^c$, $t^d \ll t^r$)

In this case the coefficient of $\frac{\partial \bar{c}}{\partial \bar{z}}$ in equation 8.43, needs careful consideration. The Peclet number would vary between ~ 3 and 10^6 meaning that the coefficient of $\frac{\partial \bar{c}}{\partial \bar{z}}$ can be of the order of 1 or larger for the higher Pe values and hence cannot be neglected, which leads to case (2). However for $Pe \lesssim 10^3$ and long thin films the convection term can be neglected.

When the rate of reaction is not important, $t^d \ll t^r$, i.e.:

$$r(c_0) < r(c_0') \ll \frac{D^i c_0'}{\delta^2} \tag{8.44}$$

Equation 8.43 reduces to that of pure diffusional mass transfer:

$$\frac{\partial \bar{c}}{\partial \bar{t}} = \left(\frac{\partial^2 \bar{c}}{\partial \bar{x}^2} \right) \tag{8.45}$$

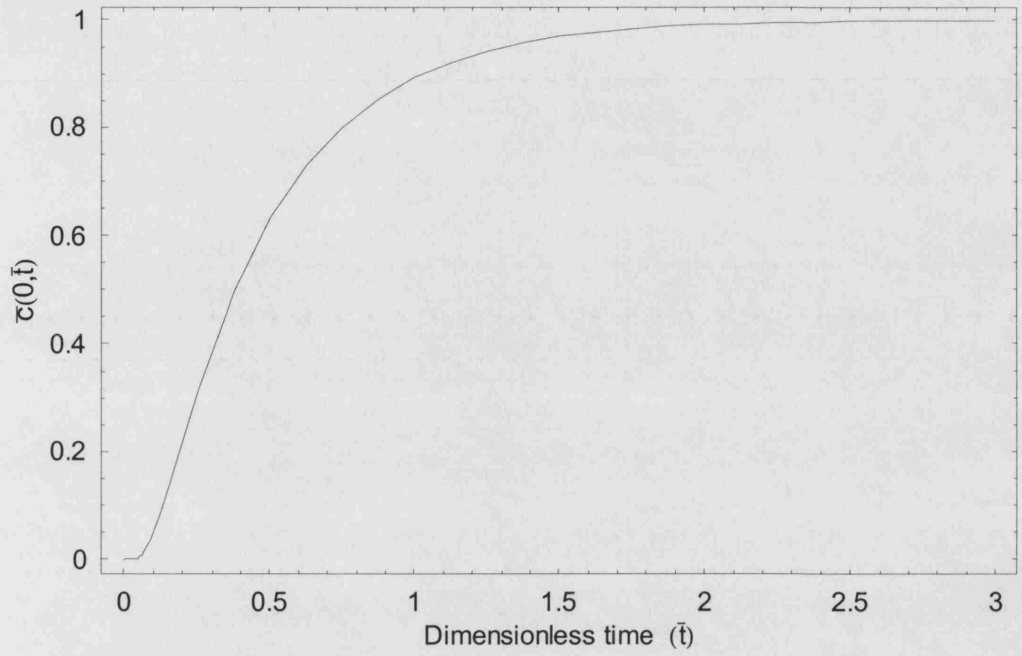

Fig. 8.5: Wall concentration variation with dimensionless time.

with boundary conditions at the bubble surface and wall of:

$$\bar{c}(1,\bar{t}) = 1 \quad \left.\frac{\partial \bar{c}}{\partial \bar{x}}\right)_{(0,\bar{t})} = 0 \tag{8.46}$$

and initial condition:

$$\bar{c}(x,0) = \bar{c}_{in} \tag{8.47}$$

It can be shown using standard solution methods that equation 8.45 has a solution $\bar{c}(\bar{x},\bar{t})$:

$$\bar{c}(\bar{x},\bar{t}) = 1 - (1-\bar{c}_{in}) \sum_{n=0}^{\infty} \frac{4\cos(n\pi)}{(1+2n)\,\pi}\, e^{-\bar{t}\left[\frac{\pi}{2}(1+2n)\right]^2} \cos\left(\frac{\pi}{2}(1+2n)\bar{x}\right) \tag{8.48}$$

A plot of the concentration change at the wall with time is shown is Fig. 8.5. In conclusion the film becomes saturated very quickly ($\bar{t} \approx 2$). As an example, for the thickest film in Table 8.3 ($\bar{\delta} = 6.36 \times 10^{-3}$) and a $1mm$ channel diameter

$$t = \bar{t}\,\frac{\bar{\delta}^2}{D^i}d^2 \sim 2\frac{(6.36\times10^{-3})^2}{10^{-9}}\left(10^{-3}\right)^2 = 8.0\times10^{-2}s$$

For all purposes the transient term in equation 8.43 can therefore be neglected.

8.4.1.2 Case (2) (slow reaction regime $t^d \approx t^c$, $t^d \ll t^r$)

For $t_d \approx t_c$ to be satisfied:

$$\delta^2/D^i \approx O((l_b - d)/U_b) \approx O(l_b/U_b) \tag{8.49}$$

The dimensionless film thickness, $\bar{\delta} = \dfrac{\delta}{d}$, can be estimated from Aussilous and Quère [144]:

$$\bar{\delta} = \frac{0.66Ca^{2/3}}{1+3.33Ca^{2/3}} \approx O\left(\sqrt{\frac{D^i}{U_b d}\frac{l_b-d}{d}}\right) = \sqrt{\frac{L_b-1}{Pe}} \tag{8.50}$$

which is only going to be true for the smallest values of $\sqrt{\frac{L_b-1}{Pe}}$ and the thickest film of interest, see Table 8.3, i.e. for $Pe \sim 10^5$ assuming $L_b \sim O(1)$ otherwise the film will always be saturated.

Equation 8.43 neglecting the reaction term will be:

$$\frac{\partial\bar{c}}{\partial\bar{t}} + \left(\underbrace{\left(\frac{dU_b}{D^i}\right)}_{Pe}\frac{\delta}{l_b-d}\frac{\delta}{d}\frac{\partial\bar{c}}{\partial\bar{z}}\right) = \frac{\partial^2\bar{c}}{\partial\bar{x}^2} \tag{8.51}$$

From case (1), it was shown that the solution approaches the steady state very quickly so:

$$\left(\frac{\partial\bar{c}}{\partial\bar{z}}\right) = Fo\left(\frac{\partial^2\bar{c}}{\partial\bar{x}^2}\right) \tag{8.52}$$

where

$$Fo \equiv \left(\frac{D^i}{dU_b}\right)\left(\frac{l_b-d}{\delta}\right)\left(\frac{d}{\delta}\right) = \frac{1}{Pe}\frac{(L_b-1)}{\bar{\delta}^2} \tag{8.53}$$

The boundary conditions on the bubble surface and the wall are:

$$\bar{c}(1,\bar{z}) = 1 \qquad \left(\frac{\partial\bar{c}}{\partial\bar{x}}\right)_{(0,\bar{z})} = 0 \tag{8.54}$$

The solution at the film exit is given by:

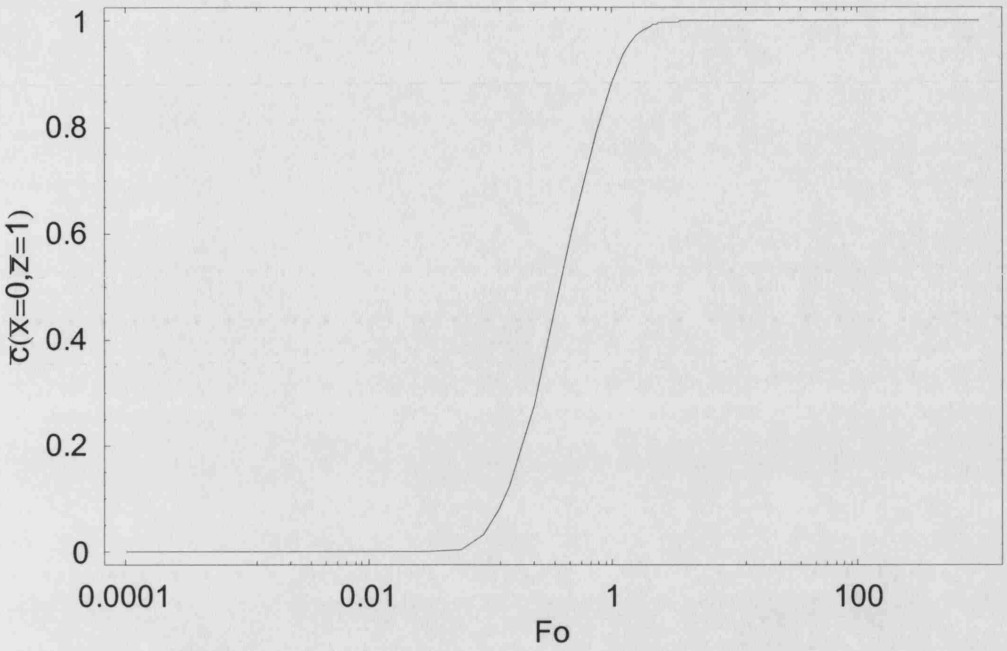

Fig. 8.6: A plot of concentration at the wall at the film exit ($\bar{x} = 0$, $\bar{z} = 1$) as a function of the Fourier number Fo. The diagram shows that deviation from the saturated film occurs for $Fo < 1.31$ (based on $\bar{c}_{in} = 0$, $\bar{c}_{out} = 0.95$)

$$\bar{c}(\bar{x},\bar{z}) = 1 - (1-\bar{c}_{in}) \sum_{n=0}^{\infty} \frac{4\cos(n\pi)}{(1+2n)\,\pi}\, e^{-\bar{z}Fo\left[\frac{\pi}{2}(1+2n)\right]^2} \cos\left(\frac{\pi}{2}(1+2n)\bar{x}\right) \qquad (8.55)$$

The concentration at the film exit at the wall is plotted in Fig. 8.6 where it can be seen that the film leaves *unsaturated* (based on 95% saturation) if $Fo < 1.31$. The above analysis is similar to that by Sherwood et. al. [142] apart from the velocity profile in the film which here is assumed to be constant rather than parabolic.

The average concentration $c_{av} = \int_0^1 \int_0^1 \bar{c}(\bar{x},\bar{z}) d\bar{x} d\bar{z}$ in the film is also plotted in Fig. 8.7 as a function of Fo and it shows that the convective effects can be neglected for $Fo > 6.67$ (based on 95% saturation). Naturally requiring the average concentration is 95% of saturation in the entire volume is a more stringent to requiring it at the wall at the film exit requirement and therefore a higher Fo results. Higher Fo in practice corresponds to longer film , thinner films, higher diffusivity or slower velocity. From the definition of Fo, equation 8.53, such Fourier numbers exist if $Pe < \frac{(L_b-1)}{6.67\times(0.01)^2}$.

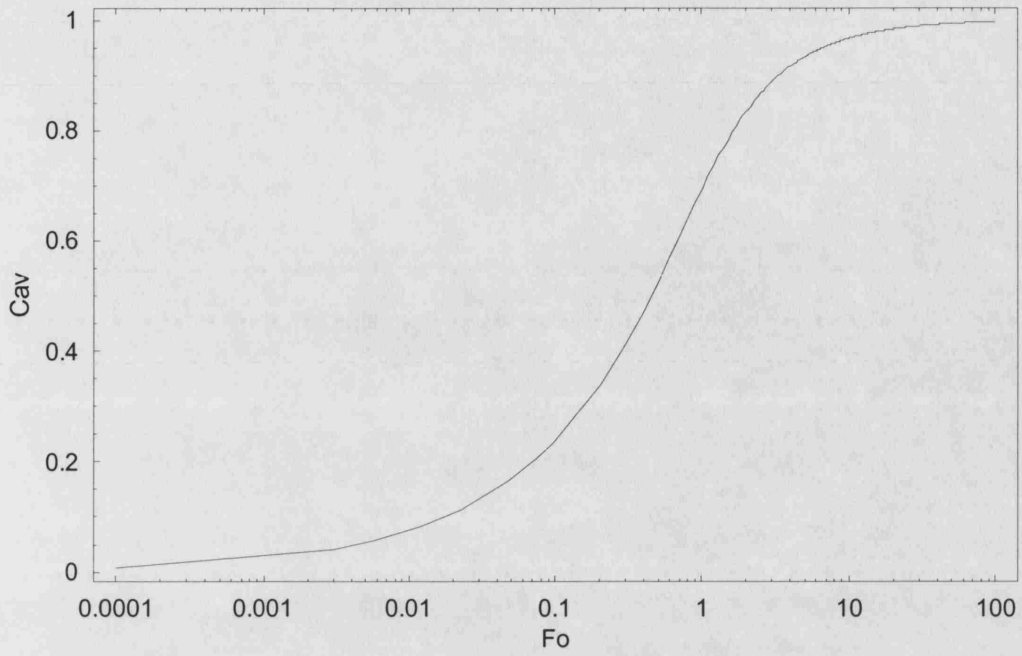

Fig. 8.7: A plot of $\bar{c}_{av}$ in the liquid film. The diagram shows that the deviation from the film saturation occurs for $Fo < 6.67$ (based on $\bar{c}_{in} = 0$, $\bar{c}_{av} = 0.95$).

8.4.1.3 Case (3) (slow to fast reaction transition $t^d \ll t^c$, $t^d \approx t^r$)

The condition $t^d \ll t^c$ is satisfied if condition 8.56 is true:

$$\bar{\delta} \ll \sqrt{\frac{L_b - 1}{Pe}} \tag{8.56}$$

For steady state equation 8.43 becomes:

$$\left(\frac{\partial^2 \bar{c}}{\partial \bar{x}^2}\right) = \frac{\delta^2}{D} \frac{r}{c_0'} \tag{8.57}$$

and the boundary for the wall and the bubble surface are given by:

$$\bar{c}(1) = 1 \quad \left.\frac{\partial \bar{c}}{\partial \bar{x}}\right)_{(\bar{x}=0)} = 0 \tag{8.58}$$

Equation 8.57 can only be solved analytically for zero and first order reactions. For a first order reaction $r = k_1\, c$:

$$\left(\frac{\partial^2 \bar{c}}{\partial \bar{x}^2}\right) = \underbrace{\frac{k_1 \delta^2}{D}}_{Ha_1^f} \bar{c} \tag{8.59}$$

where the constant is the Hatta number:

$$Ha_1^f = \frac{\delta^2}{D} k_1 \tag{8.60}$$

The solution is:

$$\bar{c}(\bar{x}) = \frac{e^{\sqrt{Ha_1^f}(1-\bar{x})} + e^{2x\sqrt{Ha_1^f}+\sqrt{Ha_1^f}(1-\bar{x})}}{1 + e^{2\sqrt{Ha_1^f}}} \tag{8.61}$$

For reactions of any order n the equation becomes [139]:

$$\left(\frac{\partial^2 \bar{c}}{\partial \bar{x}^2}\right) = \underbrace{\left(\frac{\delta^2}{D} k_n c_0'^{n-1}\right)}_{Ha_n^f} \bar{c}^n \tag{8.62}$$

where a new Hatta number Ha_n^f is defined as:

$$Ha_n^f = \frac{\delta^2}{D} k_n c_0'^{n-1} \tag{8.63}$$

The equation is then solved for c as a function of the Ha_n^f and n according to Astarita [139]:

$$\frac{d\bar{c}}{d\bar{x}} = -\sqrt{\frac{2}{n+1} Ha_n^f c(\bar{x})^{n+1} + A} \tag{8.64}$$

When $\bar{x} = 0$, $\frac{d\bar{c}}{d\bar{x}} = 0$, this allows the calculation of A

$$A = -\frac{2}{n+1} Ha_n^f \bar{c}(0)^{n+1}$$

where A is the constant of integration. A second integration gives:

$$\int_{\bar{c}(\bar{x})}^{1} \frac{d\bar{c}}{\sqrt{\frac{2}{n+1} Ha_n^f \left[c(\bar{x})^{n+1} - \bar{c}(0)^{n+1}\right]}} = \bar{x} \tag{8.65}$$

The value of $\bar{c}(0)$ can be numerically calculated from the evaluation of the integral:

$$\int_{\bar{c}(0)}^{1} \frac{d\bar{c}}{\sqrt{\frac{2}{n+1} Ha_n^f \left[\bar{c}(x)^{n+1} - \bar{c}(0)^{n+1}\right]}} = 1 \tag{8.66}$$

or equivalently by iteratively solving the algebraic equation which arises from the evaluation of the integral 8.66:

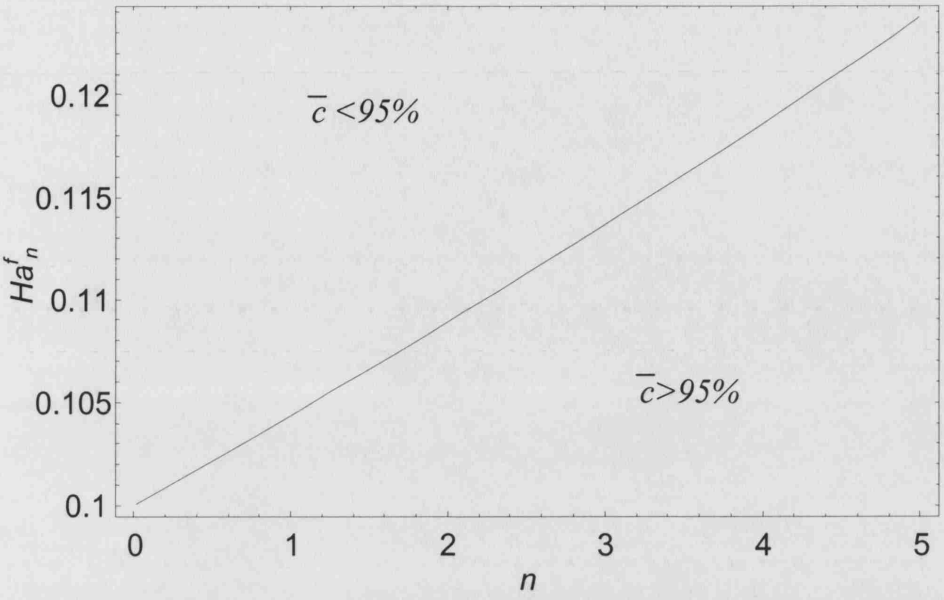

Fig. 8.8: Values for Ha_n^f and n to obtain a $\bar{c}(0) = 0.95$ saturation at the wall.

$$\frac{\bar{c}(0)B_{\bar{c}(0)}\left(\frac{1}{2}-\frac{1}{n+1},\frac{1}{2}\right)-\sqrt{\pi}\Gamma\left(\frac{1}{2}-\frac{1}{n+1}\right)}{\Gamma\left(-\frac{1}{n+1}\right)\sqrt{2\frac{Ha_n^f\ \bar{c}(0)^{n+1}}{n+1}}}=1 \tag{8.67}$$

where B is the Beta function, Γ is the gamma function. $\bar{c}(0)$ can then be numerically calculated. The analysis enables the determination of values of the Ha_n^f and n for which the concentration of the tracer at the wall is near saturated (for example $\bar{c}(0) = 0.95$), see Fig. 8.8.

The solution is guaranteed to exist for $n > 1$ however, for $0 < n < 1$ there are certain combinations of Ha_n^f and n where a solution could not be numerically evaluated. This corresponds to the existence of a depth of penetration of the concentration of $\bar{c}$ from the surface of the bubble, after which there is no presence of $\bar{c}$ in the remaining domain. It may be concluded from Fig. 8.8 that reaction order n has only a small effect on the value of Ha_n^f at which the film operates in the reaction regime. This can be explained by considering the reaction rate expression, $r \propto \bar{c}^n$, which for concentration close to 1 is almost independent of n, but for low concentration it could change significantly with n.

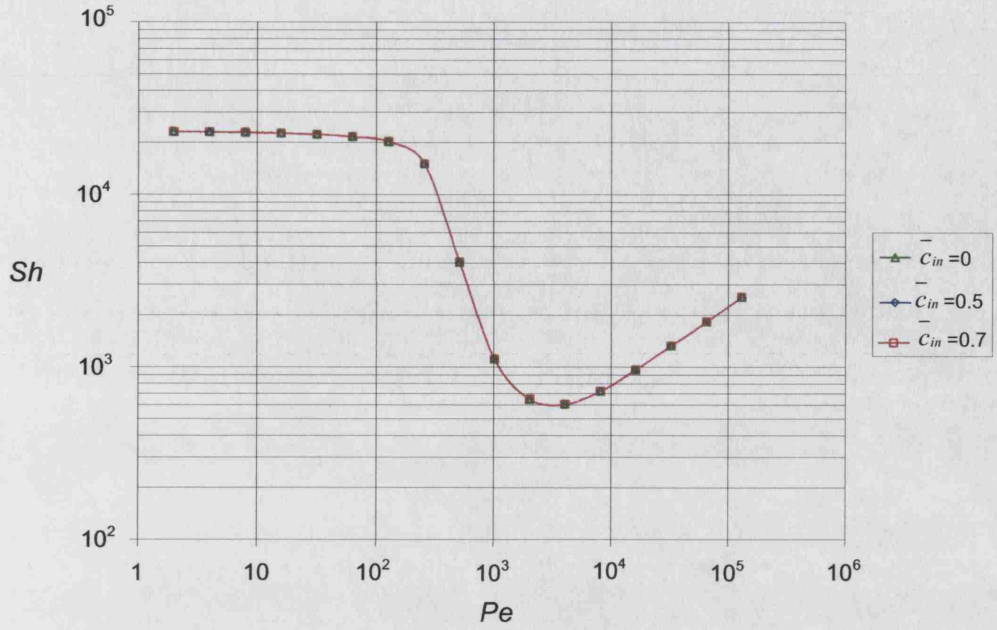

Fig. 8.9: Sh versus *Pe* for different values of $\bar{c}_{in}$.($L_s = 0.25$, $\bar{\delta} = 0.01$)

8.4.2 Reaction and mass transfer in the liquid slug

8.4.2.1 Physical adsorption steady state results

A sensitivity analysis of the effect of the input concentration $\bar{c}_{in}$ on the value of Sh calculated using equation 8.39 is given in Fig. 8.9. The graph shows large steady values of Sh which are insensitive to Pe at low Pe which fall at $Pe \sim 10^2$ by more than an order of magnitude and subsequently starts to increase with increasing Pe. It can be seen that Sh is unaffected by the input concentration which justifies the use of $\bar{c}_{in} = 0$ as the inlet concentration. This invariation can be explained simply for it is always possible to define a dimensionless concentration which incorporates the initial concentration and hence remove it from consideration (with the exception of limiting value $\bar{c}_{in} = 1$ which would give a different solution).

The average concentration in the slug is plotted in Fig. 8.10 as a function of Pe for different film thickness $\bar{\delta}$, and slug length L_s. It can be seen that as convection starts to dominate with increasing Pe, the average concentration decreases to values lower than the saturation concentration. This is more prominent at large film thickness. At $\bar{\delta} = 3.06 \times 10^{-4}$, (not shown in Fig. 8.10) the average concentration at $Pe = 6.6 \times 10^4$ is 0.995. The average steady state concentration is also affected by the slug length. A decrease in L_s results in a larger decrease of $\bar{c}_{av}$ with Pe.

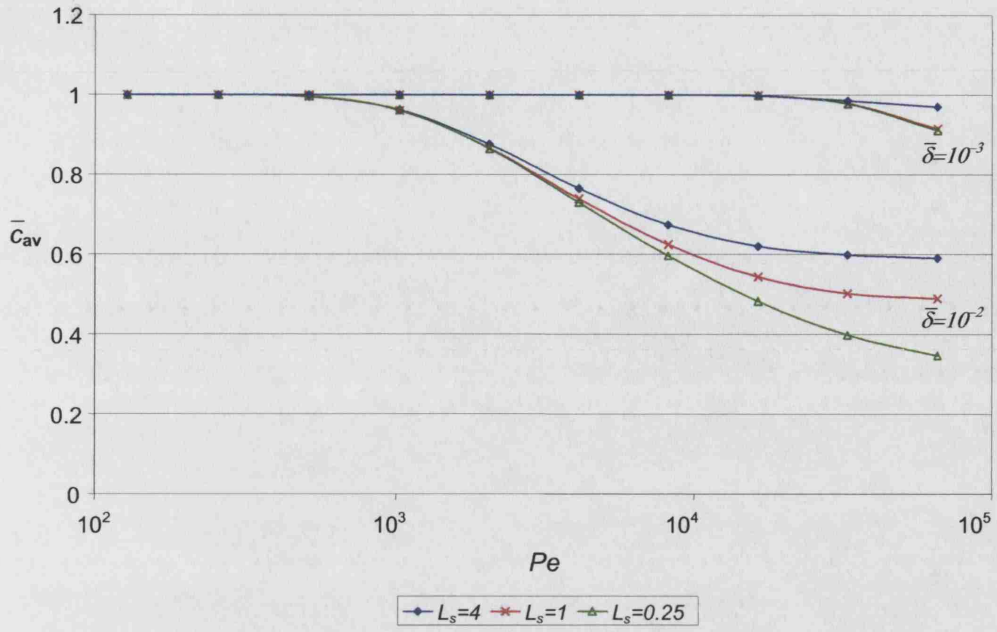

Fig. 8.10: Variation of average slug $\bar{c}_{av}$ concentration with Pe.

An explanation for that is as follows: as the liquid enters into the slug it passes initially through a region similar in dimension to the film and is almost saturated before it continue across the remainder of the slug. As it moves across the slug in a thin liquid film near the walls (Fig. 6.1) it exchanges material with the vortex region of the slug then exits the slug region with whatever material remaining. The liquid film transfers more of its content to the vortex before it exits as the slug becomes longer and as such causes the bubble to have a higher average concentration at steady state. It should be noted that the inlet concentration used in the steady state analysis is $\bar{c}_{in} = 0$ which will not be the case in reality as the liquid leaving the film to enter the slug would be nearly saturated.

The variation of Sh with Pe, from equation 8.39, is plotted in Figs. 8.11 and 8.12 for $\bar{\delta} = 0.01$ and $\bar{\delta} = 0.001$ respectively. In both cases Sh remains initially constant with increasing Pe and then decreases by a few orders of magnitude starting at a value of Pe that depends on the film thickness ($Pe \sim 200$ for $\bar{\delta} = 0.01$ in Fig. 8.11 and $Pe \sim 20000$ for $\bar{\delta} = 0.001$ in Fig. 8.12). For $\bar{\delta} = 3.06 \times 10^{-4}$ (Fig. 8.13) the trend appears to be developing similarly, however, the Pe where this transition starts would be at a higher value than the range investigated in this work. The value of Pe where Sh starts to decrease is almost independent of L_s. For $\bar{\delta} = 0.001$

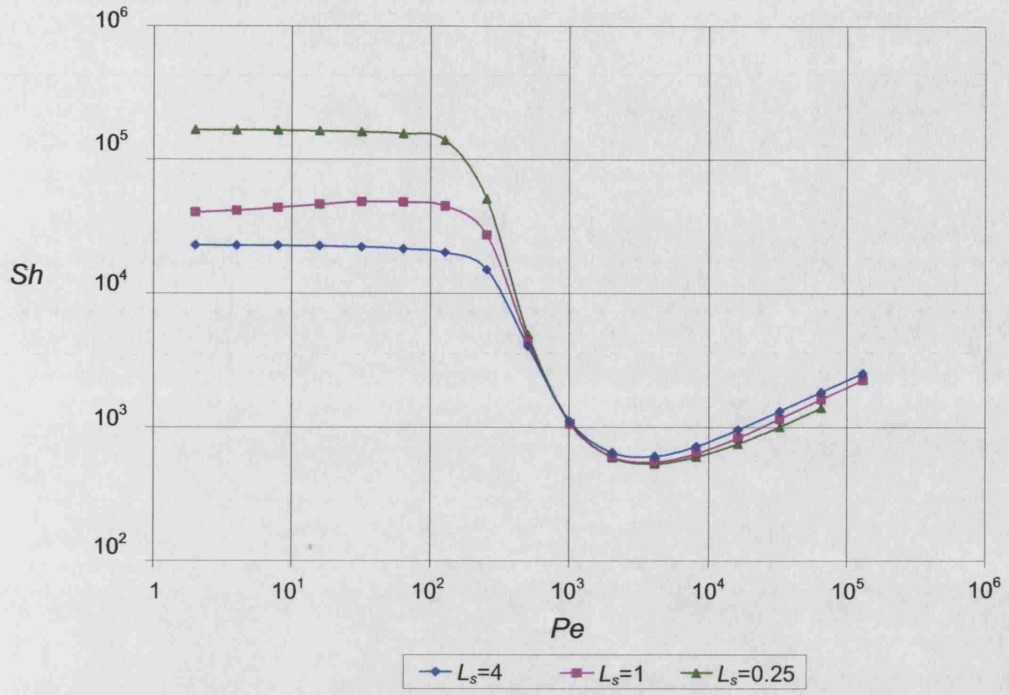

Fig. 8.11: Sh versus *Pe* for $\bar{\delta} = 0.01$.

a minimum value of *Sh* is reached followed by an increase with further increase of *Pe* (Fig. 8.11). This increase shows an order of $0.46 - 0.48$ dependence on *Pe* and is brings to mind the 0.5 dependence which is suggested by the surface renewal theory. This perhaps justifies the use of such penetration theory models for large *Pe* [98, 141]. A similar increase is not seen for $\bar{\delta} = 10^{-3}$ probably because it happens at *Pe* larger than those used in this analysis for the thinnest films (Fig. 8.13), only the start of the *Sh* decrease could be seen for the range of *Pe* used.

Comparing Fig. 8.10 and Figs. 8.11 - 8.13, the *Pe* numbers where the sharp decrease in *Sh* appears are similar to those where the average concentration in the slug becomes uniform and approach the saturation concentration. It can also be seen that at similar *Pe* ($Pe \leq 256$ as seen for Fig. 8.11 and $Pe \leq 1.6 \times 10^4$ for Fig. 8.12) the concentration of the the liquid leaving the slug approaches the saturation concentration $\bar{c}_{av} = 1$. At these conditions the denominator of equation 8.39 used to calculate *Sh* approaches zero leading to very large values of *Sh* from the magnification of any numerical errors in the numerator. The results for low *Pe* should be therefore considered as suspect.

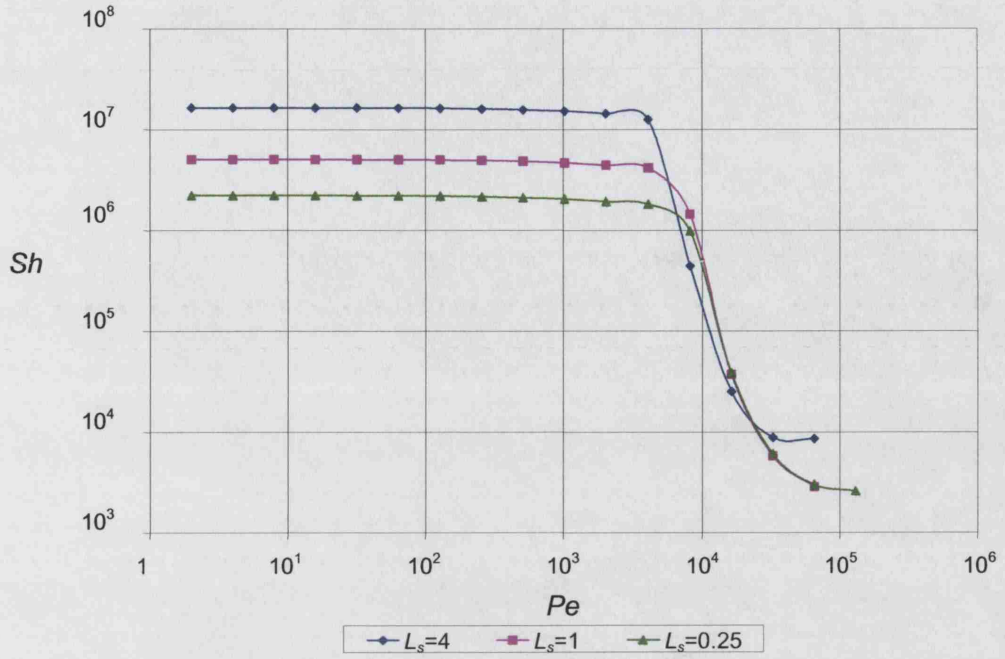

Fig. 8.12: Sh versus *Pe* for $\bar{\delta} = 1 \times 10^{-3}$.

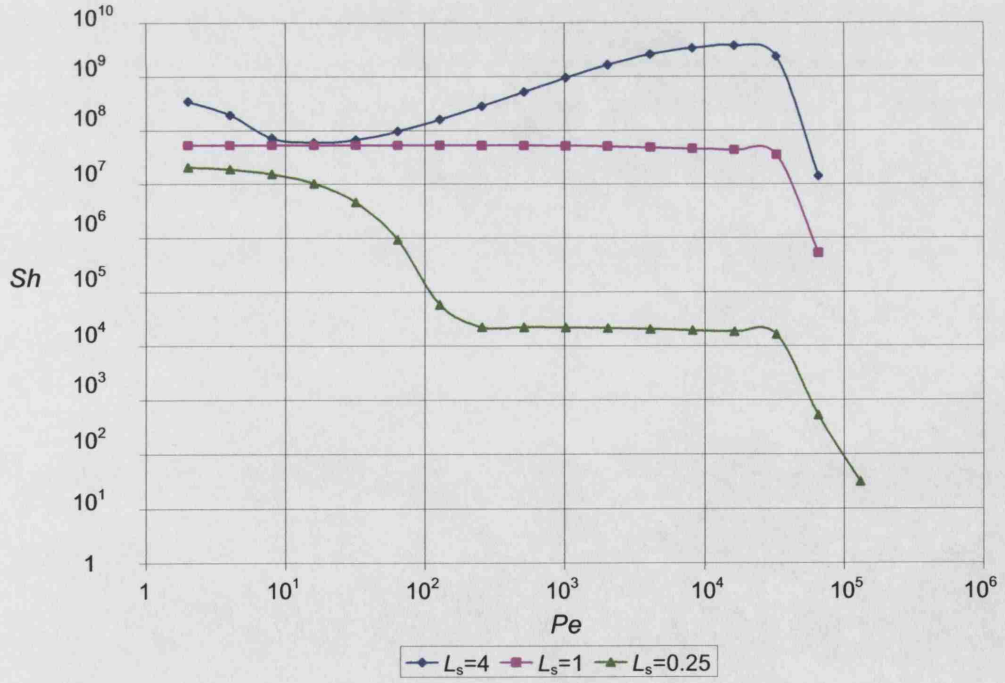

Fig. 8.13: Sh versus *Pe* for $\bar{\delta} = 3.06 \times 10^{-4}$.

8.4.2.2 Transient values analysis of Sh_t

The transient analysis will indicate the time necessary to achieve steady state and the variation of Sh_t during that time (equation 8.40). At low Pe (Fig. 8.14(a)) there is an initial transient drop of Sh_t obscured by a subsequent sharp rise in Sh_t. The saturation concentration is reached in a short time ($\hat{t} \sim 15$ for $Pe = 10^2$, Fig.8.14(a)). In contrast at high Pe (Fig. 8.14(c)) there is no subsequent rise in Sh_t after the initial drop and steady state is reached at $\hat{t} \sim 500$. In all cases average concentration and Sh are in agreement with the results of the previous section when steady state is reached.

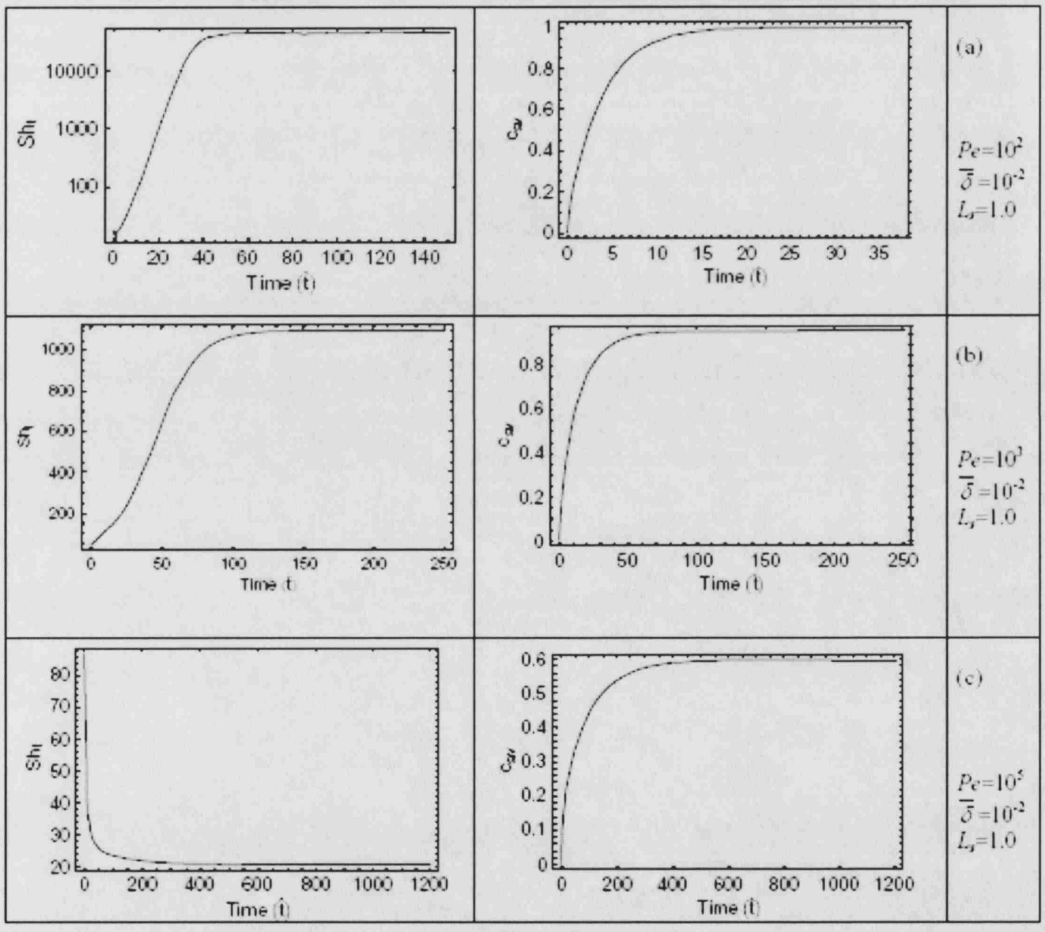

Fig. 8.14: A sample of the results showing the variation of Sh_t and $\bar{c}_{av}$ with time $\bar{t}$.

The time required for the average concentration in the slug $\hat{t}_{\bar{c}_{av}}$ and the outlet concentration $\hat{t}_{\bar{c}_o}$ to reach 0.95 of the saturation concentration are given in Table 8.7. Examining the values of $\hat{t}_{\bar{c}_o}$ reveals that they have values of the order of those necessary for the film to reach steady state. $\hat{t}_{\bar{c}_o}$ is is also much shorter than that

$\bar{\delta}$	L_s	Pe	$\hat{t}_{\bar{c}_o=0.95}$	$\hat{t}_{\bar{c}_{av}=0.95}$
0.01	0.25	100	0.13	3.54
	0.25	1000	3.13	25.1
	0.25	10000	N/A	N/A
0.00031	1.0	100	0.09	11.5
	1.0	1000	0.09	48.1
	1.0	10000	0.09	311
0.01	4.0	100	0.48	43.6
	4.0	1000	29.1	159
	4.0	10000	N/A	N/A
0.01	1.0	100	0.45	10.9
	1.0	1000	7.81	61.8
	1.0	10000	N/A	N/A

Tab. 8.7: The times for achieving 0.95 saturation for output and average concentrations

of the average concentration to reach steady state[3]. For $\bar{\delta} = 0.01$, as an example, $\hat{t}_{\bar{c}_o=0.95} \approx 7.81$ which is of the same order of magnitude as that required for the concentration in the film to reach everywhere the saturation value (Fig. 8.5), which is much shorter time than that of the average concentration. Only for $L_s = 4.0$ and $Pe = 1000$, is $\hat{t}_{\bar{c}_o=0.95}$ much larger. In this case the outlet concentration rises sharply to a value of 0.9 in 6 time units then slowly increases to the value 0.95 as the concentration builds up in the slug. The reason for reaching steady state rapidly at the outlet is that the inlet and outlet regions of the unit cell near the bubble caps have a similar dimensions to that of the film, and therefore behave in a similar way. The length of that small section becomes insufficient to reach saturation concentration with increasing Pe values.

Time $\hat{t}_{\bar{c}_{av}=0.95}$ is seen to increase with increasing L_s and Pe. This is in agreement with the expectations of longer times to reach steady state with larger volumes (larger L_s) and slower mass transfer processes (larger L_s). No results are reported for the cases where the concentration never reaches $\bar{c}_{av} = 0.95$ in the steady state. Values of $\hat{t}_{\bar{c}_{av}=0.95}$ also reveal a different conclusion than would be drawn from the steady state section with respect to mass transfer coefficients. When comparing $\hat{t}_{\bar{c}_{av}=0.95}$ values for different $\bar{\delta}$ in Table 8.7 we conclude that $\bar{\delta}$ has little influence on $\hat{t}_{\bar{c}_{av}=0.95}$ and consequently that the mass transfer in the liquid slug has only a little dependent on the liquid film thickness. This is in contrast to the orders of magnitude change in Sh seen earlier (Figs. 8.11, 8.12 and 8.13).

[3] Conversion between the two dimensionless times: $\hat{t} = \bar{\delta}\ Pe\ \bar{t}$.

8.4.2.3 Reaction rate

Since the values of Sh could not be correctly calculated from the volume averaged steady state simulations, equation 8.29 is solved directly to provide concentration patterns in the liquid slug under reaction conditions. Different regimes were observed from examining the concentration patterns of the dissolved reacting gas. These depended on Pe which represents the rate of convection to rate of diffusion and Ha_n^S represents the rate of reaction to rate of diffusion respectively. Fig. 8.15 illustrates qualitatively the different patterns for a first order reaction $n = 1$. For small Ha_n^S and Pe as would result from fast diffusion and slow reaction systems, there is almost no concentration gradients. The entire slug volume is very near to the saturation concentration of the dissolved gas in the liquid and this necessarily corresponds to the reaction regime [139], required for obtaining the kinetics. As Ha_n^S increases, concentration patterns are observed within the liquid slug indicating the diffusional regime [139]. The patterns change depending on the value of Pe. For the higher Pe ($Pe = 1000$) values, the patterns resemble the flow lines of the vortex within the slug with the region of lowest concentration at the core of the vortex. For low ($Pe = 10$) convection has limited effects Lowest concentration appears furthest away from the bubble surface. For still higher Ha_n^S the fast reaction regime is observed. The concentration distribution is limited to a small depth away from the bubble surface with the majority of the slug volume having very low concentration.

An example of the change in average concentration with Ha_n^S is given in Fig. 8.16. Initially, for low Ha_n^S values, the slug is in the reaction regime. The diffusion rate is significantly larger than the reaction rate so that no effect is observed of increasing the reaction rate until the diffusion and reaction rates are of the same order ($Ha_n^S \sim 10^{-2}$). At this point the concentration starts to drop until it reaches a near zero value in the fast reaction regime. The drop seems to become sharper with decreasing reaction order. The reaction order however, does not significantly affect the value at which the concentration is at 95% of its saturation value. This can be explained by considering the reaction rate expression, $r \propto \bar{c}^n$, which for concentration close to 1 is almost independent of n, but for low concentration it increases with increasing n.

The effect of Pe on the calculated $\bar{c}_{av}$ is seen in Fig. 8.17 which shows that the decrease in average concentration happens at progressively lower Ha_n^S for increasing values of Pe (an order of magnitude decrease in Ha_n^S for every order of magnitude increase in Pe). An increase in the slug length has also the same effect as can be seen in Figs. 8.18 and 8.19. Interestingly, for the two figures, the $Pe = 1000$ plots show

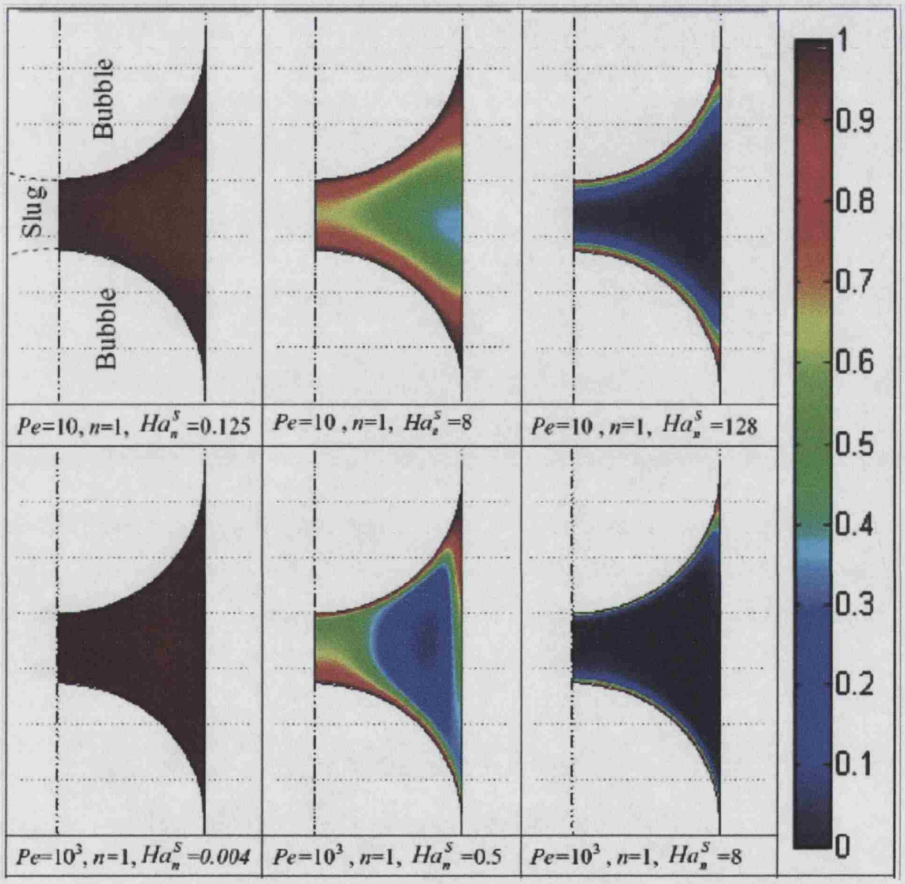

Fig. 8.15: Qualitative effects of the change in Pe and Ha_n^S on the concentration distribution in the liquid slug for a first order reaction. ($\delta = 3 \times 10^{-5}, L_s = 0.5, n = 1$)

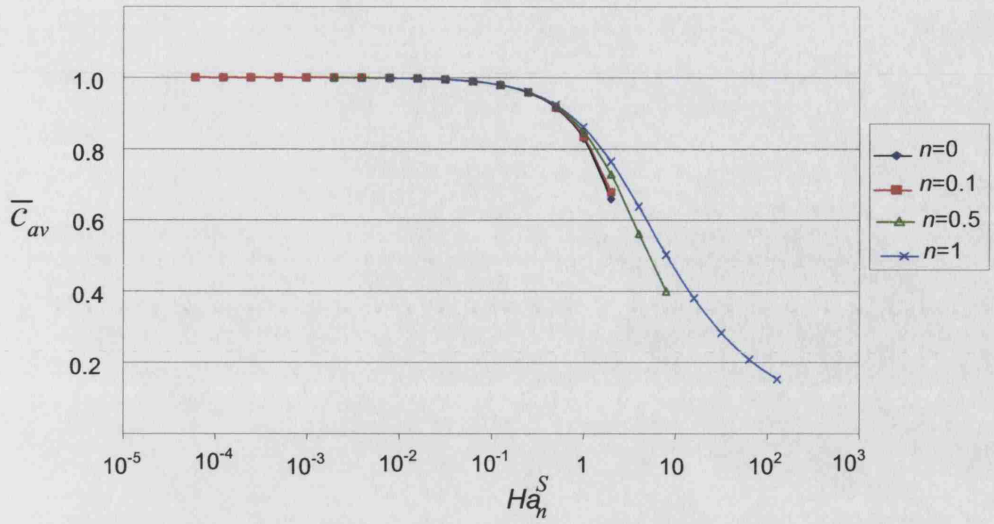

Fig. 8.16: Effect of Ha_n^S on the observed mean concentration $\bar{c}_{av}$ in the liquid slug. ($Pe = 10,\ L_s = 0.5$)

that the limiting concentration that can be obtained is $\bar{c}_{av} \sim 0.96$. This further shifts back the value of the Ha_n^S at which the reaction regime is said to occur and is because the rate of dissolved gas convected becomes equal to the rate of gas diffusing. It should be noted that the chosen inlet concentration $\bar{c}_{in} = 0$, is an unlikely condition as the liquid entering from the region film would be near saturated, however it is fortuitous that the choice of the boundary condition has revealed that effect.

The effect of film thickness on the slug concentration is given in Fig. 8.20. For low Peclet number the effect is negligible in agreement with the analysis of the $\hat{t}_{\bar{c}_{out}}$ and $\hat{t}_{\bar{c}_{av}}$ in the transient analysis. However, at $Pe = 1000$ the higher film thickness results in a decrease in the maximum concentration at low Ha_n^S which as explained before, happens when convection and diffusion rates are equal. When at this Pe the film thickness decreases the quantity of material that can be convected from the slug also decreases bringing the maximum concentration back to almost 1.

As would be expected increasing the slug length would increase the diffusion lengths and reduce the upper Ha_n^S limit at which the reaction limit exists (Fig. 8.21). As slug length can be a controllable design parameter, the aim should be to have the minimum stable slug length possible.

Finally, given the numerical results, it is worth checking the qualitative argument made earlier that it is sufficient to ascertain the existence of the kinetics regime in the slug to ascertain its presence throughout the reactor. Equation 8.68 and the

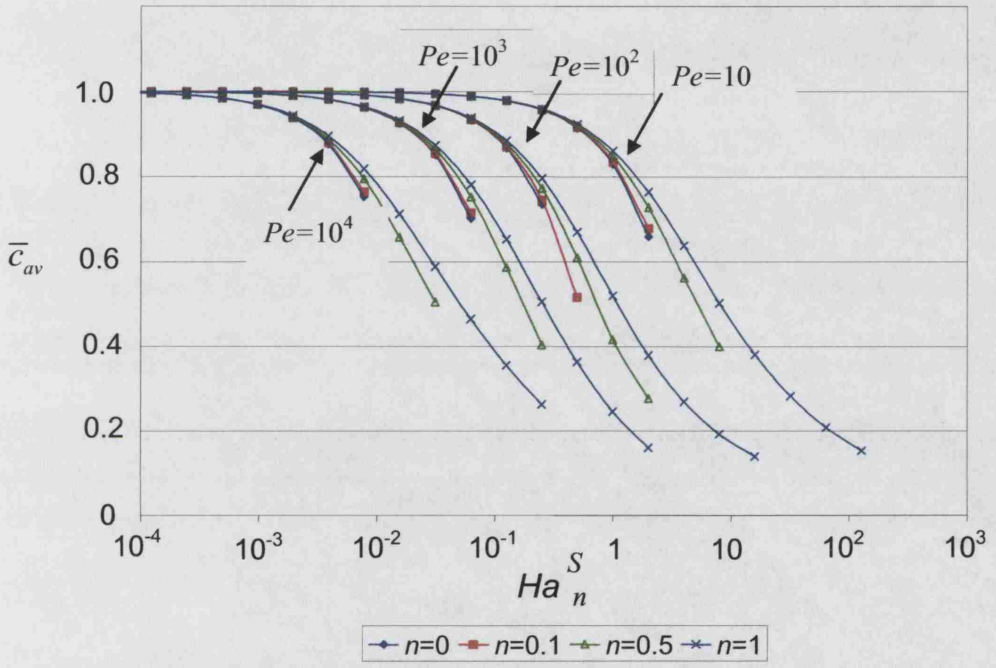

Fig. 8.17: Averaged unit cell concentration as a function of Ha_n^S for various Pe and n.($L_s = 0.25, \bar{\delta} = 0.01$)

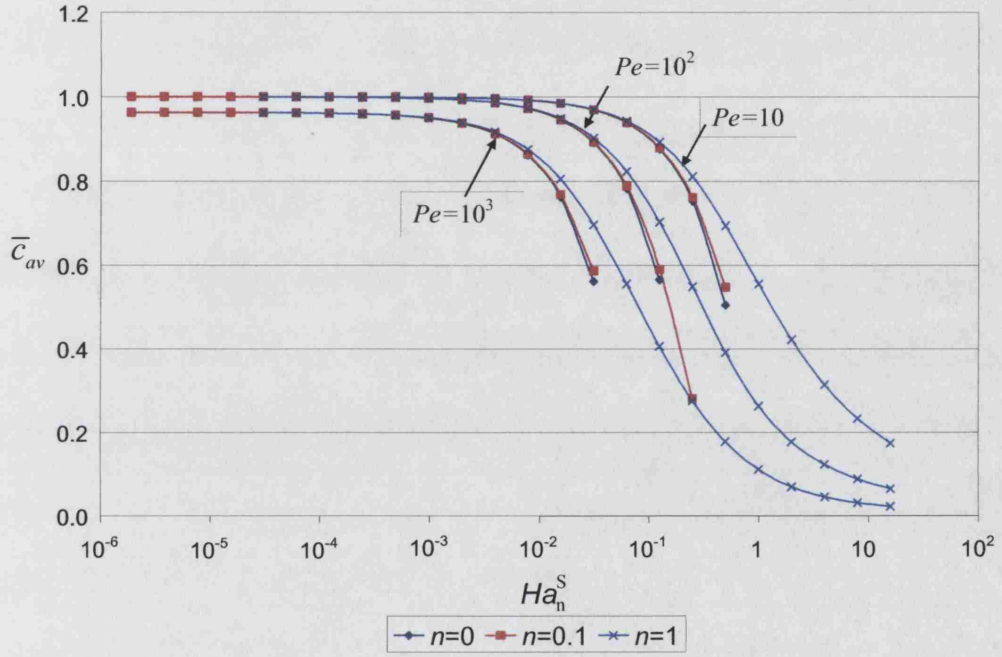

Fig. 8.18: Averaged unit cell concentration as a function of Ha_n^S for various Pe and $n.(L_s = 1.0, \bar{\delta} = 0.01)$

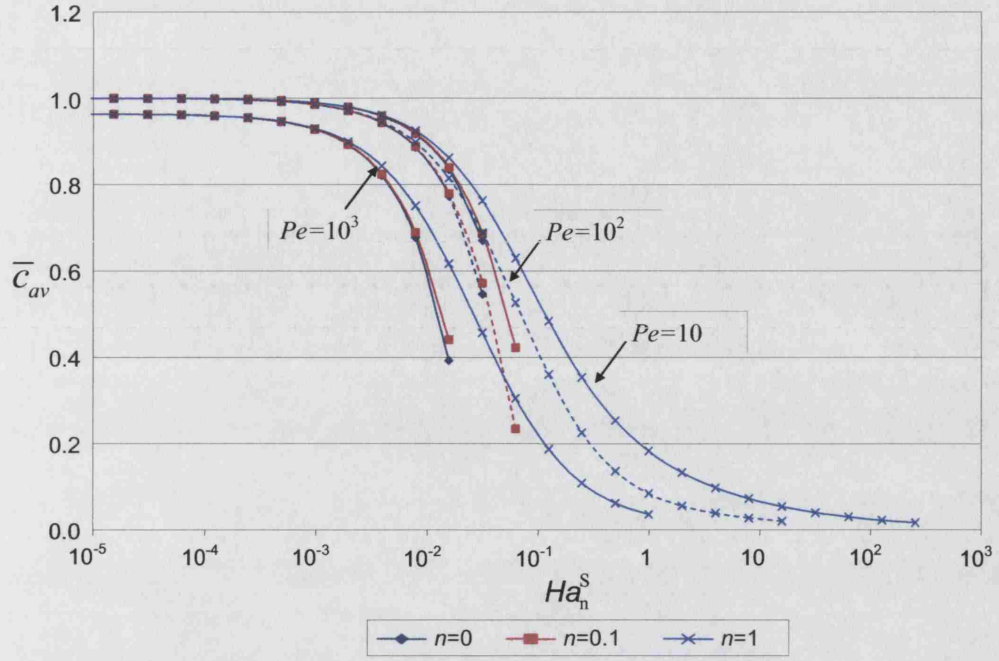

Fig. 8.19: Averaged unit cell concentration as a function of Ha_n^S for various Pe and $n.(L_s = 4..0, \bar{\delta} = 0.01)$

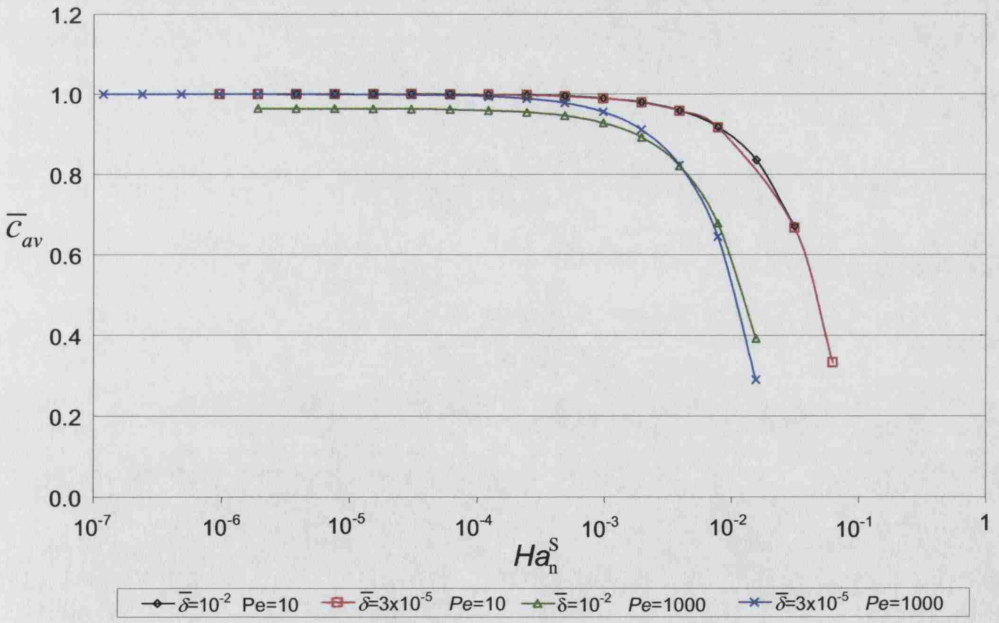

Fig. 8.20: The effect of varying the film thickness on the $\bar{c}_{av}$ vs. Ha_n^S curves.

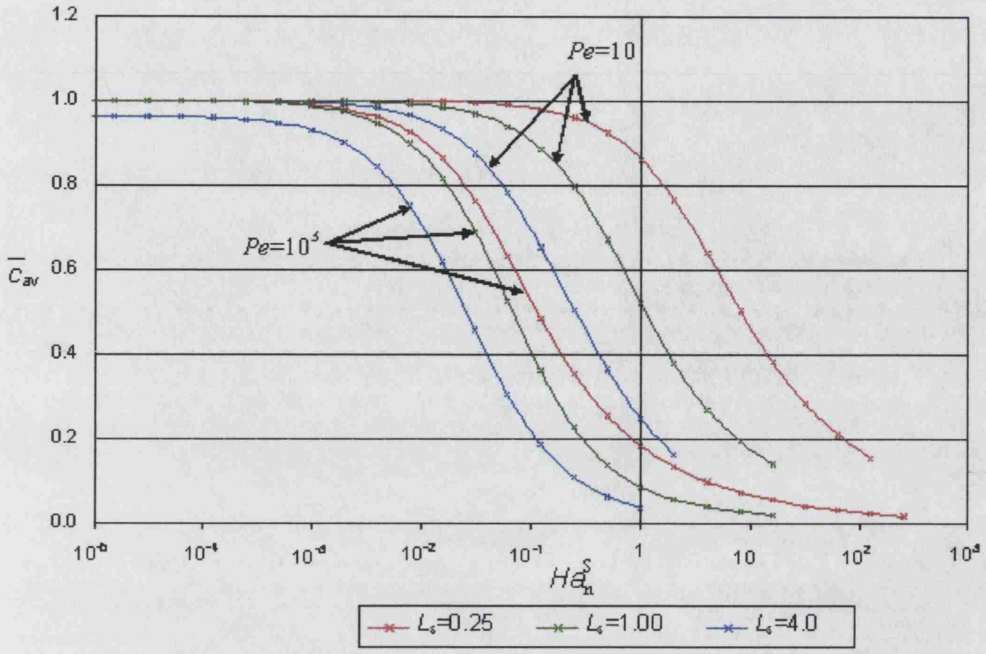

Fig. 8.21: The effect of slug length on the $\bar{c}_{av}$ vs. Ha_n^S curves.

ranges of $\bar{\delta}$ in Table 8.3 ensures Ha_n^S to be orders of magnitude larger for the slug. Comparison of the necessary Ha values for the kinetics regime, Ha_n^f from Fig. 8.8 and Ha_n^S in Figs. 8.16-8.21 verifies the initial statement.

$$\frac{Ha_n^S}{Ha_n^f} = \bar{\delta}^{-2} \tag{8.68}$$

8.5 Conclusions

The solution of the volume averaged steady state convection-diffusion equation without reaction in the liquid slug revealed that the calculated Sh gives wrong estimates of the mass transfer for low Pe. From the solution of the volume averaged transient convection-diffusion and the steady state convection-diffusion-reaction simulations the following trends were seen:

1. Decreasing L_s as well as decreasing Pe extends the reaction regime to larger reaction rates.

2. Increasing L_s as well as increasing Pe extends the necessary time before steady state is reached in the slug, this may be a large percentage of the available

residence time in the reactor, leading to the estimation of incorrect reaction kinetics.

3. The film remains in the reaction regime for much larger Ha_n^S than the slug. This has implication for chemical methods which are usually used to characterise the available gas-liquid interfacial area.

9. CONCLUSIONS AND FUTURE WORK

When assessing the contribution of the work to the to the field of screening and HTE, it is worth restating the requirements set by de Bellefon [2]:

1. Multiphase capabilities: The reactor must allow the contact between the several phases, gas-solid, gas-liquid, gas-liquid-solid and liquid-liquid.
2. No mass and heat transfer limitations. This is to ensure intrinsic kinetics are under evaluation.
3. Ideal hydrodynamics (flow pattern) for easy reactor modelling.
4. Flexible residence (reaction time)
5. Flexible range of operating conditions (pressure,temperature).
6. Sample catalyst inventory from milligrams down to micrograms.
7. Significant throughput testing frequency (>100/day).
8. Easy and inexpensive automation (sampling)

Taylor flow (or any other multiphase flow pattern) satisfies requirement 1 from the list while coupling Taylor flow with a microreactor setup and its associated small scales helps in satisfying requirements 2, 5 and 6 to a certain extent. Requirements 4 and 8 on the other hand are best satisfied by Taylor flow because of its segmented behaviour.

Chapter 2 deals predominantly with requirement 3. It described issues of operating in microscale and associated modelling problems. In addition it investigated the different observable flow patterns at small scale. The possibility of describing the flow as a continuum was found to be valid in microchannels down to an order of $1\mu m$ for gases. The 'no-slip boundary condition' was reasoned to be an appropriate approximation of a boundary condition in the $100\mu m - 1mm$ scales but may not be appropriate at smaller scales with non-wetting liquids. The literature on different flow patterns was collated to show the different dominant patterns seen by many

researchers as well as less common patterns seen by few. The dominance of Taylor flow was demonstrated at the low flow rates relevant for kinetics studies and the effect of surface tension and wetting properties on the flow were also pointed out. A practical conclusion from this chapter is that scales larger than $100\mu m$ and wetting surfaces produce the most reproducible and stable conditions.

Chapter 3 is an extension of chapter 2 which focused on characterising Taylor flow in circular microchannels based on the different flow rates and different liquid properties. For $Ca < 10^{-3}$ gravity and inertial effects were concluded to be small and the bubble caps are hemispherical allowing easy modelling. The film thickness is a function only of the Ca and the flow pattern in the liquid slugs was found to be always recirculating. Although modelling of Taylor flow with surfactants can be found in literature and parametric studies exist for the different parameters present, the assessing of the values of these parameters for trace amounts of unknown contaminants can not be easily to specified. Perhaps the most useful of the results was the the limiting increase of the film thickness because of tracer contaminant to factor of $4^{2/3}$. Similarly, the effect of tracer contaminants on the flow field could not be assessed and were reasoned to be negligible. The effect of contaminants in the flow field have not been experimentally investigated and need to be checked to validate the assumptions of this work. In addition systems which contain reactants or products which are themselves surface active agents (large surfactant concentration) were not investigated and are left for future work.

A limited number of reports of lack of film surrounding the bubbles in capillaries exist and while they can be explained by the possible presence of an instability for film thicknesses of the order of $50nm$, this needs to be investigated further. A suggested approach for experimental investigation in circular channels is by analysing the spread of tracer material using axial mixing analysis of chapter 5.

Chapter 4 covers experimental studies on bubble formation for one of many possible inlet configurations (the coaxial arrangement). This is aimed at requirements 3 (directly) and 6 (as inlet conditions define bubble and slug sizes for given flowrates). Three different mechanisms of formation were identified. Mechanisms 1 and 2 give regular flows however the first is not always producible while the second depends on the apparatus set up and is unpredictable. Mechanism 3 on the other hand is reproducible and can be modelled using a simple model. To avoid the first two mechanisms the gas inlet nozzle must be aligned with the channel axis and significant pressure drop must be introduced before the tip. Smaller nozzles seem less likely to result in mechanism 2 because of the higher pressure drop they introduce

but are also likely to produce small non-Taylor bubbles.

After a Taylor or non-Taylor bubble is formed further modifications may occur to the formed bubble size by coalescence or pairing. Bubble pairing is encouraged by smaller nozzles and flowrates while coalescence is seen only for cases where non-Taylor bubbles form. While pairing is a reproducible effect which does not significantly alter the periodicity of the Taylor flow, coalescence on the other hand produces random distributions of bubble sizes and should be avoided. A simple way of avoiding the occurrence of coalescence is by insuring that the bubbles formed at the nozzle are only Taylor bubbles.

Two simple models have been proposed, the first predicts the size of the Taylor bubbles formed by mechanism 3 while the second attempts to predict the condition for bubble pairing to occur. The bubble formation model captures the experimental trends reasonably well and predicts a strong dependence of Taylor bubbles formed with mechanism 3 on the gas and liquid flow rates and a weak dependence (if at all) on the surface tension of the liquid used. A particular inlet bubble formation arrangement can therefore be used to generate bubbles of a specific volume irrespective of the liquid used. Some mismatch with the experimental results still exists. The difference is caused (at least in part) by the experimental setup where there was no perfect axial alignment of the gas inlet. The experiments also suffered from problems at the outlet at low flow rates where smooth disengagement could not be ensured for long Taylor bubbles. An improved apparatus design which overcomes these problems is necessary and experiments may need to be repeated before more rigorous modelling is undertaken.

A simple geometrical model for pairing was also proposed which predicts pairing for concentric tube nozzle arrangements. The model overpredicted the range of liquid flowrates at which pairing was observed experimentally because of the misalignment of the nozzle with the channel axis and the collapse of the meniscus inside the nozzle after the neck breakage. While alignment can be amended in a new apparatus design, the collapse of the meniscus into the nozzle needs to be investigated further.

A natural continuation of the work (both theoretical and experimental) is through the investigation of non-circular channels and other (non-coaxial) inlet arrangements.

Chapters 5-7 address requirements 4 and 7 directly. In chapter 5, previous modelling methodologies aimed at addressing the axial mixing in Taylor flow were assessed based on comparison of the assumed residence time distribution curves of the unit cells from reactor models to the with the RTD curves calculated numerically

in this work. The performances varied with the value of Pe:

For $Pe > 1000$:

1. The CSTR-PFR model is the least accurate of the models considered.
2. The fitted two-region model matches better the moments found numerically than the CSTR-PFR model however, the values of Sh found from the fitting do not correspond to values calculated from literature correlations.
3. The method of Thulasidas et. al.[112] showed reasonable agreement with the numerically predicted moments.

For $Pe \leq 1000$, based on calculated moments

1. Of the three methods considered, the CSTR-PFR model gives the best description of the unit cell.
2. A fitted two-region model gives $Sh \rightarrow \infty$ converging to that of the CSTR-PFR.
3. The method proposed by Thulasidas et. al. [112] gives the least accurate predictions.

A method for calculating the residence time distribution of a reactor based on the residence time distribution of a unit cell by means of a convolution method was also introduced and gave results which compared very well with experimental data by Thulasidas et. al. [112]. The short length of the reactor used in the experiments however could not allow proper differentiation from other models investigated, which also showed good agreement with the experimental data. More experimentation with axial mixing in long reactors is necessary.

Chapter 6 directly applies the method developed in chapter 5 to determine the frequency of injection of experimental mixtures into a Taylor flow reactor and is directly associated with requirement 7. The effects of different parameters on the residence time distribution of a tracer injected in a Taylor flow microreactor were investigated. It was found that increase in the Peclet number, the capillary number or slug length resulted in larger tracer spreading. The mass transfer between the film region and the vortex region of the unit cell plays a major role in explaining the observed behavior. The chapter demonstrates that the appropriate design and operation of a Taylor flow reactor can achieve high injection frequencies in screening applications.

Chapter 7 reformulates the methodology of chapter 5 to account for the forward diffusion at low Pe by placing the tracer unit cell in between a sufficient number of cells able to contain the forward and backward spread of the tracer for a given reactor length. To reduce the problem to a manageable computation level, the model assumes concentration homogenous liquid slugs. The model can either be solved numerically, or for large Peclet numbers, simplified to yield an analytical solution.

The model was found to be suitable for ranges $Ca < 10^{-3}$, $Pe < 1000$ and $L_s < 4$. Axial mixing was in general very low. Trends show increasing vessel dispersion number (increasing axial mixing) with increasing capillary number and slug and bubble lengths.

Chapter 8 deals with gas-liquid mass transfer of requirement 2 by identifying the necessary flow rates and channel and slug lengths in the reactor which must be achieved to allow operations in the kinetic regime in the liquid. It also begins to address the issue of modelling yield and selectivity in Taylor flow reactors by identifying which reaction regime is dominant in which region in the flow. It should be noted that a sufficient condition for having the kinetic regime in the reactor is having the kinetic regime in the slug.

Time to reach steady state in the slug was reported and showed that increasing L_s as well as increasing Pe extends the necessary time before steady state is reached in the slug which may be a large percentage of the available residence time in the reactor, leading to incorrect reaction kinetics. Limiting conditions were identified in the film and the boundaries of kinetic regime were investigated as a function of Pe, L_s and Ha for the slug. Decreasing L_s as well as decreasing Pe was found to extend the reaction regime to larger reaction rates.

Beyond the screening applications, reactor models able to predict the yield and selectivity of a Taylor flow reactor have been left for future work. Residence time distribution curves of unit cells in chapter 5 already provide the temporal mixing information, the concentration data generated from the simulations can be further used to analyse spatial mixing. Chapter 8 addresses the reaction regimes which need to be accounted for in these models. Issue of scale-out of Taylor flow systems was not directly addressed in this work but remains an active area of research within the reaction engineering group in the department. The findings of chapter 4, however, do provide some essential information on what occurs in each one of the channels, although limited to coaxial configuration.

APPENDIX

A. RANGES OF DIMENSIONLESS NUMBERS

A.1 Hydrodynamic parameter ranges

As a criterion for the residence time in a screening device, the minimum residence time is 1/2 min while the maximum residence time is 45 min. For a reactor length of $1m$, a survey of some of the most commonly used liquids, see table A.1, yields the following values for the dimensionless numbers.

$$9.68 \times 10^{-02} \leq Re_\beta \leq 3.47 \times 10^{+01} \tag{A.1}$$

$$4.16 \times 10^{-06} \leq Ca_\beta \leq 3.29 \times 10^{-03} \tag{A.2}$$

$$Fr_\beta = \left\{ \begin{array}{c} 2.10 \times 10^{-01} \text{ for longer residence Time} \\ 1.89 \times 10^{+01} \text{ for shorter residence Time} \end{array} \right\} \tag{A.3}$$

By taking a ratio of the Reynolds to the Capillary number for all the substances considered, it is possible to define a dimensionless number which does not contain the velocity of the system. Doing so yields the following range of numbers.

$$1072 \leq \frac{\mathrm{Re}}{Ca} \leq 83.3 \times 10^5 \tag{A.4}$$

A.2 Mass transfer studies

Values of the diffusivity are also scarce. Typical values of the diffusivity in liquids are:

$$5 \times 10^{-11} \leq D_{AB} \leq 1 \times 10^{-08} \tag{A.5}$$

of particular note are the following substances:

Liquid	CAS	T (°C)	Density	Surface Tension	Viscosity (298K)
H_2O	7732-18-5	15.6	10^3	7.34×10^{-2}	8.91×10^{-4}
$CH_3(CH_2)_3CH_3$	109-66-0	20	6.30×10^{2}	1.84×10^{-2}	2.24×10^{-4}
$CH_3(CH_2)_4CH_3$	110-54-3	20	6.60×10^{2}	1.89×10^{-2}	2.94×10^{-4}
$CH_3(CH_2)_5CH_4$	142-82-5	20	6.80×10^{2}	1.92×10^{-2}	3.96×10^{-4}
$CH_3(CH_2)_6CH_4$	111-65-9	20	7.00×10^{2}	1.95×10^{-2}	6.14×10^{-4}
CH_2Cl_2	75-09-2	20	1.32×10^{3}	2.80×10^{-2}	4.25×10^{-4}
$CHCl_3$	67-66-3	20	1.48×10^{3}	2.71×10^{-2}	5.42×10^{-4}
CCl_4	56-23-5	20	1.59×10^{3}	2.24×10^{-2}	8.80×10^{-4}
CS_2	75-15-0	20	1.26×10^{3}	3.23×10^{-2}	3.63×10^{-4}
CH_3OH	67-56-1	20	7.90×10^{2}	2.26×10^{-2}	5.53×10^{-4}
CH_3CH_2OH	64-17-5	20	7.90×10^{2}	2.28×10^{-2}	1.06×10^{-3}
$CH_3CH_2CH_2OH$	71-23-8	20	8.00×10^{2}	2.30×10^{-2}	2.27×10^{-3}
C_6H_6	71-43-2	20	8.80×10^{2}	2.89×10^{-2}	6.01×10^{-4}
C_6H_{12}	110-82-7	20	7.80×10^{2}	2.50×10^{-2}	8.95×10^{-4}
$C_6H_5NH_2$	62-53-3	20	1.02×10^{3}	2.83×10^{-2}	3.71×10^{-4}
$C_6H_5CH_3$	108-88-3	20	8.70×10^{2}	2.39×10^{-2}	5.50×10^{-4}
$C_6H_4(CH_3)_2$	95-47-6	20	8.80×10^{2}	2.57×10^{-2}	7.54×10^{-4}
$C_6H_4(CH_3)_2$	108-38-3	20	8.60×10^{2}	2.38×10^{-2}	5.79×10^{-4}
$C_6H_4(CH_3)_2$	106-42-3	20	8.60×10^{2}	2.27×10^{-2}	6.03×10^{-4}
CH_3CO_2H	67-64-1	20	1.05×10^{3}	2.76×10^{-2}	1.16×10^{-3}
CH_3COCH_3	67-64-1	20	7.90×10^{2}	2.37×10^{-2}	3.16×10^{-4}
$C_2H_5OC_2H_5$	60-29-7	20	7.10×10^{2}	1.70×10^{-2}	2.22×10^{-4}
$CH_3Si(CH_3)_2OSi(CH_3)_3$	107-46-0	20	7.90×10^{2}	1.60×10^{-2}	4.95×10^{-4}

Tab. A.1: Properties of liquids considered

Substance A	Substance B	T (K)	$D_{AB}(m^2/s)$
Ethanol	H_2O	298	0.12×10^{-8}
Glucose	H_2O	298	0.69×10^{-9}
Glycerol	H_2O	298	0.94×10^{-9}
Acetone	H_2O	298	0.13×10^{-8}
CO_2	H_2O	298	0.20×10^{-8}
O_2	H_2O	298	0.24×10^{-8}
H_2	H_2O	298	0.63×10^{-8}
N_2	H_2O	298	0.26×10^{-8}

the lower limit of diffusivities arise because of the diffusivities of some substance such as pyrogalol $D_{AB} \sim 10^{-11}$ which have been studied by some of the partners.

This gives a Peclet number range of

$$1.11 \times 10^{+01} \leq Pe \leq 2.00 \times 10^{+05} \tag{A.6}$$

a similar approach of defining a dimensionless number which does not have the velocity values included yields:

$$2.01 \times 10^{+03} \leq \frac{Pe}{Ca} \leq 5.34 \times 10^{+08} \tag{A.7}$$

B. THE EFFECT OF A TAYLOR BUBBLE LENGTH ON THE VELOCITY OF THE BUBBLE

Edvinsson and Irandoust [76] reported that the length of bubble had little or no effect on slip ψas long as the length of the bubble was sufficiently long to reach a constant film thickness. Giavedoni and Saita [77] when analysing the front semi-infinite bubble problem reported larger transition regions before the film reaches a constant value. This appendix repeats the work of Edvinsson and Irandoust [76] to explore the effect of Taylor bubble length on the velocity of the bubble if the length of the bubble was not sufficient for a constant film thickness to develop.

B.1 Theory

Model assumptions

1. The bubbles studied are either single bubbles moving in a long tube or a periodic bubble train with enough separation between the bubbles to achieve a fully developed parabolic profile. As an approximation, the distance necessary for the flow to develop is calculated by analogy with distance, in a circular tube, from an inlet a constant flow needs to develops into a parabolic flow,$\frac{L}{d} = 0.056Re$. Imposing Dirichlet boundary conditions of parabolic velocity may cause errors if the distance is not accounted for, similarly, radial pressure profiles have been shown to occur ahead of the bubble for the larger Re value [80] which would disappear when the parabolic flow develops so constant pressure boundaries are also inaccurate.

2. The channel orientation is horizontal and/or gravity effects are negligible.

3. Flow is axially symmetric and non-swirling.

4. The flow is laminar, consistent with the values of Re used in this study and the known value of Re for transition to turbulent flow in tubes.

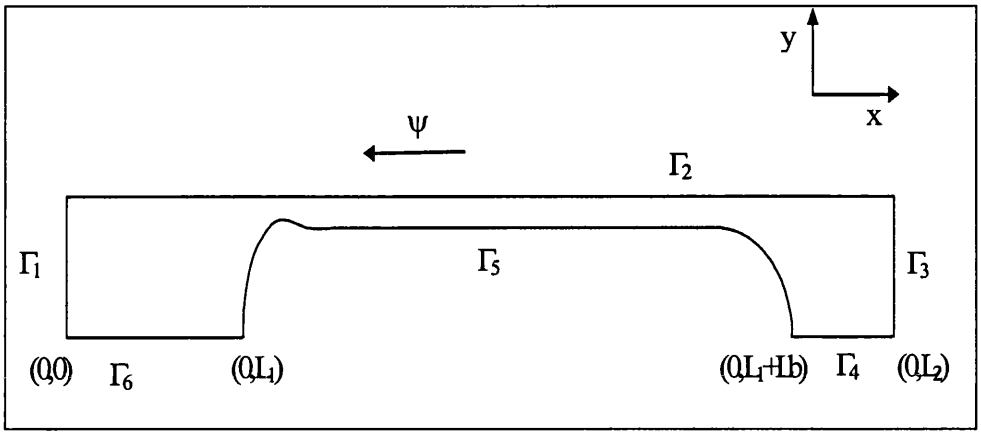

Fig. B.1: Bubble geometry problem and boundary conditions.

5. Constant pressure within a gas bubble. Pressure gradients in the gas can be shown on dimensional grounds to be small (Chapter 3).

6. All fluids, including the gas, are considered Newtonian and incompressible.

7. The physical properties are assumed to be constant with no spatial or time variation. This includes the surface tension where contaminants and surfactants are assumed absent.

Governing Equation

The equations to be solved are the axi-symmetric cylindrical coordinates conservation of mass and momentum equations for the liquid phase coupled with the appropriate boundary conditions for the gas-liquid interface.

$$\frac{1}{\bar{r}}\frac{\partial}{\partial \bar{r}}(\bar{r}\bar{u}_r) + \frac{\partial \bar{u}_z}{\partial \bar{z}} = 0 \tag{B.1}$$

$$\alpha\left(\bar{u}_r\frac{\partial \bar{u}_r}{\partial \bar{r}} + \bar{u}_z\frac{\partial \bar{u}_r}{\partial \bar{z}}\right) = -\frac{\partial \bar{p}'}{\partial \bar{r}} + \gamma\left(\frac{1}{\bar{r}}\frac{\partial}{\partial \bar{r}}\left(\bar{r}\frac{\partial \bar{u}_r}{\partial \bar{r}}\right) - \frac{\bar{u}_r}{\bar{r}^2} + \frac{\partial^2 \bar{u}_r}{\partial \bar{z}^2}\right) \tag{B.2}$$

$$\alpha\left(\bar{u}_{\bar{r}}\frac{\partial u_z}{\partial \bar{r}} + \bar{u}_z\frac{\partial u_z}{\partial \bar{z}}\right) = -\frac{\partial \bar{p}'}{\partial \bar{z}} + \gamma\left(\frac{1}{\bar{r}}\frac{\partial}{\partial \bar{r}}\left(\bar{r}\frac{\partial \bar{u}_z}{\partial \bar{r}}\right) + \frac{\partial^2 \bar{u}_z}{\partial \bar{z}^2}\right) \tag{B.3}$$

The velocity components have been non-dimensionalised with the average liquid velocity in the slug U_{ls} and the diameter d. The coefficients (α, γ) depend on the

Dominant Force	Inertia	Viscous	Surface tension
$\bar{p}'$	$\frac{p}{\rho U_{ls}}$	$\frac{p}{\frac{\mu U_{ls}}{d}}$	$\frac{pd}{\gamma}$
α	1	Re	$ReCa$
γ		$\frac{1}{\mathrm{Re}}$	Ca

Tab. B.1: The various coefficients of the Navier Stokes equations for different dominant forces

non-dimensionalisation of the pressure p which reflects the interplay of surface tension, viscous or inertial forces and can take a number of values as shown in Table B.1. It is mathematically irrelevant which non-dimensionalisation scheme is used for equations B.1-B.3 complete without neglecting terms. Numerically however, it was found that using the surface tension for our non-dimensionalisation scheme is important for $Ca \leq 10^{-4}$ otherwise the solution does not converge. For larger Ca it is inconsequential which scheme we choose as both yield the same results.

Boundary Conditions

The equations are solved with reference to a translating coordinate system. The relative rate of translation is $\psi = \frac{U_b}{U_{LS}} > 0$, see Fig. B.1. The boundary conditions are specified as follows:

For the axial velocity:

$$[\bar{u}_z]_{\Gamma_1} = [\bar{u}_z]_{\Gamma_3} = 2(1 - 4\bar{r}^2) - \psi \tag{B.4}$$

For the radial velocity:

$$[\bar{u}_r]_{\Gamma_1} = [\bar{u}_r]_{\Gamma_3} = 0 \tag{B.5}$$

At the wall:

$$[\bar{u}_r]_{\Gamma_2} = 0 \quad ; \quad [\bar{u}_z]_{\Gamma_2} = -\psi \tag{B.6}$$

Axial symmetry:

$$[\bar{u}_r]_{\Gamma_4} = [\bar{u}_r]_{\Gamma_6} = 0 \quad ; \quad \left[\frac{\partial \bar{u}_r}{\partial \bar{r}}\right]_{\Gamma_4} = \left[\frac{\partial \bar{u}_r}{\partial \bar{r}}\right]_{\Gamma_6} = 0 \tag{B.7}$$

At the gas-liquid interface the kinematic boundary condition:

$$[u_n]_{\Gamma_5} = 0 \tag{B.8}$$

The normal and tangential interfacial stress condition:

$$\left[\frac{\partial \bar{u}_t}{\partial n}\right]_{\Gamma_5} = -\nabla\gamma = 0 \tag{B.9}$$

$$[\bar{p}]_{\Gamma_5} = \frac{\mathbf{2}}{\mathrm{Re}}\frac{\partial \bar{u}_n}{\partial n} + \frac{2}{\mathrm{Re}\,Ca}H = 0 \tag{B.10}$$

where H is the surface curvature.

B.2 Solution method

The solution of equation B.1-B.10 has been carried out using the commercial software FIDAP [145]. The expected solution is of the form given in expression B.11.

$$(\psi, \delta_f) = f_1(\mathrm{Re}, Ca, L_b) \tag{B.11}$$

The approach adopted to obtaining the solution is that that of Edvinsson and Irandoust [76] by solving a transient version of the equations (B.1-B.10) and dropping the requirement that the bubble should remain at the same position. This gives the following non-stationary solution expression B.12 where ψ' is the best estimation of the bubble velocity. The symbol ψ'' is defined as the net drift velocity given in expressionB.13. ψ is determining by starting from an approximation of this velocity, the change in the position of the bubble is then used to determine the drift velocity which enables us, using expression B.13, to calculate a new approximation of ψ. This iterative procedure quickly converges to the right value of ψ which can be evaluated to four of five decimal places.

$$(\psi'', \delta_f) = f_1(\mathrm{Re}, Ca, L_b, \psi') \tag{B.12}$$

$$\psi'' = \psi - \psi' \tag{B.13}$$

Details of how the finite elements are formulated and their solution methodology can be found in the software manuals [145].

$Ca = 10^{-5}$					
Re	ψ		$\bar{p}'$		δ
	$L_b = 1.1$	$L_b = 8.0$	$L_b = 1.1$	$L_b = 8.0$	$L_b = 8.0$
4.95×10^{-5}	1.0010	1.0010	8.67×10^{-3}	8.67×10^{-3}	3.09×10^{-4}
3.09	1.0010	1.0010	9.97×10^{-3}	9.97×10^{-3}	3.10×10^{-4}
$Ca = 10^{-4}$					
Re	ψ		$\bar{p}'$		δ
	$L_b = 1.1$	$L_b = 8.0$	$L_b = 1.1$	$L_b = 8.0$	$L_b = 8.0$
4.95×10^{-5}	1.0051	1.0053	4.05×10^{-2}	4.65×10^{-2}	1.411×10^{-3}
30.9	1.0051	1.0013	4.15×10^{-2}	4.72×10^{-2}	1.413×10^{-3}
$Ca = 10^{-3}$					
Re	ψ		$\bar{p}'$		δ
	$L_b = 1.1$	$L_b = 8.0$	$L_b = 1.1$	$L_b = 8.0$	$L_b = 8.0$
4.95×10^{-5}	1.0203	1.0228	1.82×10^{-1}	1.92×10^{-1}	6.4×10^{-3}
1	1.0203	—	1.82×10^{-1}	—	—
309	1.0207	1.0239	2.70×10^{-1}	2.80×10^{-1}	6.7×10^{-3}
$Ca = 10^{-2}$					
Re	ψ		$\bar{p}'$		δ
	$L_b = 1.1$	$L_b = 8.0$	$L_b = 1.1$	$L_b = 8.0$	$L_b = 8.0$
4.95×10^{-5}	1.1126	1.1195	7.23×10^{-1}	7.59×10^{-1}	2.822×10^{-2}
100	1.0203	1.1171	9.08×10^{-1}	9.25×10^{-1}	2.772×10^{-2}
500	1.0976	1.1309	1.58	1.64	3.062×10^{-2}
1000	1.1181	1.6463	2.27	2.41	3.747×10^{-2}

Tab. B.2: The results of the simulations showing the effect of bubble length on film thickness, pressure and velocity ratioψ

C. PROPERTIES OF CUBIC EQUATION

Starting with equation 4.18:

$$\frac{6}{\pi}Q_g t + d_{B0}^3 = \left((d_{B0} + L_0) + \frac{4\left(Q_g + Q_l\right)}{\pi d^2}t\right)^3 \tag{C.1}$$

The expression can be rearranged to take the form:

$$t^3 + a_1 t^2 + a_2 t + a_3 = 0 \tag{C.2}$$

with:

$$a_1 = \frac{3d^2\left(d_{B0} + L_0\right)\pi}{4\left(Q_g + Q_l\right)} \tag{C.3}$$

$$a_2 = \frac{3d^4\pi^2\left(2\left(Q_g + Q_l\right)\left(d_{B0} + L_0\right)^2 - d^2 Q_g\right)}{32\left(Q_g + Q_l\right)^3} \tag{C.4}$$

$$a_3 = \frac{d^6 L_0\left(3d_{B0}^2 + 3d_{B0}L_0 + L_0^2\right)\pi^3}{64\left(Q_g + Q_l\right)^3} \tag{C.5}$$

Using the properties of cubic equations new variables can be defined:

$$Q = \frac{3a_2 - a_1^2}{9} = \left(-\frac{d^6\pi^2 Q_g}{32\left(Q_g + Q_l\right)^3}\right) \tag{C.6}$$

$$\begin{aligned} R &= \frac{9a_1a_2 - 27a_3 - 2a_1^3}{54} \\ &= \frac{d^6\pi^3}{256\left(Q_g + Q_l\right)^4}\left[2d_{B0}^3\left(Q_g + Q_l\right) - 3d^2\left(d_{B0} + L_0\right)\right] \end{aligned} \tag{C.7}$$

The discriminant of the cubic equation $D = Q^3 + R^2$

1. One root is real and two are complex conjugates if $D > 0$
2. All roots are real and at least two are equal if $D = 0$

3. All roots are real and unequal if $D < 0$

R and Q are always negative and a_1, a_2, a_3 are positive quantities when considering any realisable values of the variables.

Two additional variables may be defined:

$$S = \sqrt[3]{R+\sqrt{D}} \tag{C.8}$$

$$T = \sqrt[3]{R-\sqrt{D}} \tag{C.9}$$

so that the roots of the equation are given by

$$t_1 = S+T-\frac{a_1}{3} \tag{C.10}$$

$$t_2 = -\frac{S+T}{2}-\frac{a_1}{3}+i\frac{\sqrt{3}}{2}(S-T) \tag{C.11}$$

$$t_3 = -\frac{S+T}{2}-\frac{a_1}{3}-i\frac{\sqrt{3}}{2}(S-T) \tag{C.12}$$

When $D = 0$ there is always one negative real root $t_1$of the equation because $-a_1$and R are negative.

D. THE STEP RESPONSE OF THE TWO REGION MODEL

First consider the two well mixed regions without the liquid film around the bubble, shown enclosed in box in Fig. D.1.The non-dimensionalised simultaneous equations to solve for this model are:

$$\frac{\partial \bar{c}_1}{\partial t} = \frac{d\ A_f}{V_1}(1-\bar{c}_1) - \frac{Sh}{Pe}\frac{d\ A_s}{V_1}(\bar{c}_1-\bar{c}_2) \tag{D.1}$$

$$\frac{\partial \bar{c}_2}{\partial t} = \frac{Sh}{Pe}\frac{d\ A_s}{V_2}(\bar{c}_1-\bar{c}_2) \tag{D.2}$$

where V_1 is the volume of the film, V_2 is the volume of the vortex region, A_s is the surface area available for film to vortex mass transfer and A_f is the cross sectional area of the liquid film surrounding the bubble. The characteristic concentration used for non-dimensionalisation is c_{in}.

The initial conditions are:

$$\bar{c}_1(0) = \bar{c}_2(0) = 0 \tag{D.3}$$

This gives the response:

$$\bar{c}_1(\bar{t}) = 1 + \frac{e^{-\frac{1}{2}(\zeta+\alpha+\beta+\gamma)\bar{t}}(-\zeta-\alpha+\beta+\gamma)}{2\zeta} - \frac{e^{\left[\zeta-\frac{1}{2}(\zeta+\alpha+\beta+\gamma)\right]\bar{t}}(\zeta-\alpha+\beta+\gamma)}{2\zeta} \tag{D.4}$$

$$\bar{c}_2(\bar{t}) = 1 + \frac{e^{-\frac{1}{2}(\zeta+\alpha+\beta+\gamma)\bar{t}}(-\zeta+\alpha+\beta+\gamma)}{2\zeta} - \frac{e^{\left[\zeta-\frac{1}{2}(\zeta+\alpha+\beta+\gamma)\right]\bar{t}}(\zeta+\alpha+\beta+\gamma)}{2\zeta} \tag{D.5}$$

where:

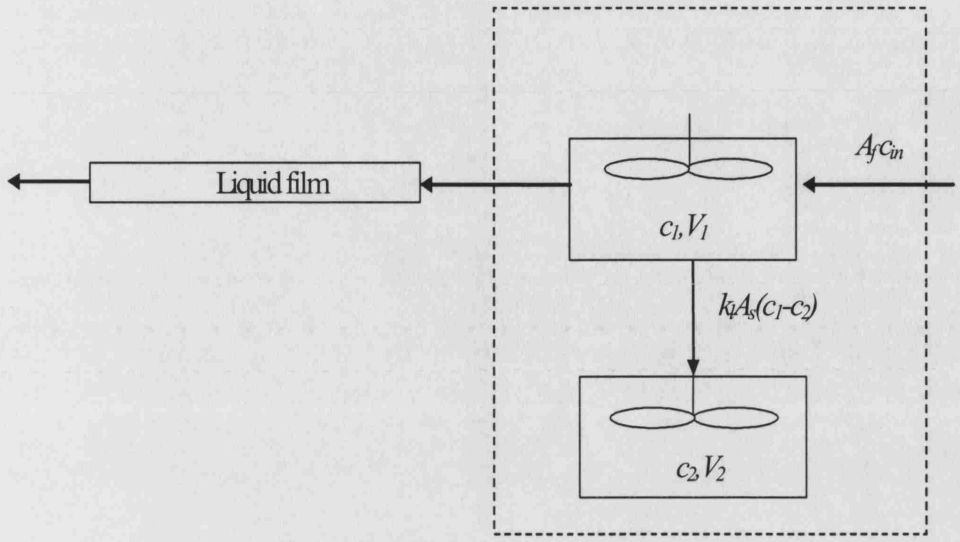

Fig. D.1: Schematic for two region model

$$\zeta = \sqrt{(\alpha+\beta+\gamma)^2 - 4\alpha\gamma} \tag{D.6}$$

$$\alpha = \frac{A_f}{V_1}\frac{d}{} \tag{D.7}$$

$$\beta = \frac{Sh}{Pe}\frac{A_s d}{V_1} \tag{D.8}$$

$$\gamma = \frac{Sh}{Pe}\frac{A_s d}{V_2} \tag{D.9}$$

The introduction of the liquid film surrounding the bubble results in the introduction of a delay between output and input given by the time constant of that film: $t_p = V_{film}/A_f U_b = L_b/U_b$.

$$\bar{c}_1(\bar{t}) = \begin{cases} 1 + \frac{e^{-\frac{1}{2}(\zeta+\alpha+\beta+\gamma)(\bar{t}-\bar{t}_p)}(-\zeta-\alpha+\beta+\gamma)}{2\zeta} & \bar{t} \geq \bar{t}_p \\ -\frac{e^{\left[\zeta-\frac{1}{2}(\zeta+\alpha+\beta+\gamma)\right](\bar{t}-\bar{t}_p)}(\zeta-\alpha+\beta+\gamma)}{2\zeta} & \\ 0 & \bar{t} < \bar{t}_p \end{cases} \tag{D.10}$$

The Residence time distribution curve can be obtained easily by differentiating the expression for $\bar{c}_1(t)$:

$$\bar{c}_1'(\bar{t}) = \begin{cases} -\dfrac{e^{-\frac{1}{2}(\zeta+\alpha+\beta+\gamma)(\bar{t}-\bar{t}_p)}(-\zeta-\alpha+\beta+\gamma)(\zeta+\alpha+\beta+\gamma))}{4\zeta} & \bar{t} \geq \bar{t}_p \\ -\dfrac{e^{\left[\zeta-\frac{1}{2}(\zeta+\alpha+\beta+\gamma)\right](\bar{t}-\bar{t}_p)}(\zeta-\alpha+\beta+\gamma)\left[\zeta-\frac{1}{2}(\zeta+\alpha+\beta+\gamma)\right]}{2\zeta} & \\ 0 & \bar{t} < \bar{t}_p \end{cases} \tag{D.11}$$

E. ESTIMATING THE LIQUID SLUG FILM VOLUME

The liquid enters the reactor through the film of width $\bar{\delta}$. This film then expands to attain, if the flow inside becomes a fully developed parabolic profile a thickness $\bar{\delta}_f$ in expression (A2.1) [83].

$$\bar{\delta}_f = \frac{1}{2} - \frac{\sqrt{2-\psi}}{2} = \frac{1}{2}\left(1 - \sqrt{2 - \frac{1^2}{4\left(\frac{1}{2} - \delta\right)^2}}\right) \tag{A2.1}$$

Hence the film region volume is bracketed between the two values:

$$\bar{V}_{\bar{\delta}} = \pi\left(\bar{R}^2 - \bar{R}_b^2\right)\left(L_s + 2\bar{R}_b\right) \tag{E.1}$$

$$\bar{V}_{\bar{\delta}_f} = \frac{\pi\left(\bar{R}^2 - 2\bar{R}_b^2\right)\left(4\bar{R}^4 - 8\bar{R}_b^4 - \bar{R}_b^2\bar{R}\left(3Ls + 4\bar{R}_b\right) + 6\bar{R}\left(2\bar{R}_b^2 - \bar{R}^2\right)^{3/2}\right)}{3\bar{R}_b^3} \tag{E.2}$$

For thin liquid films, see Fig. E.1, it makes no significant difference which is used.

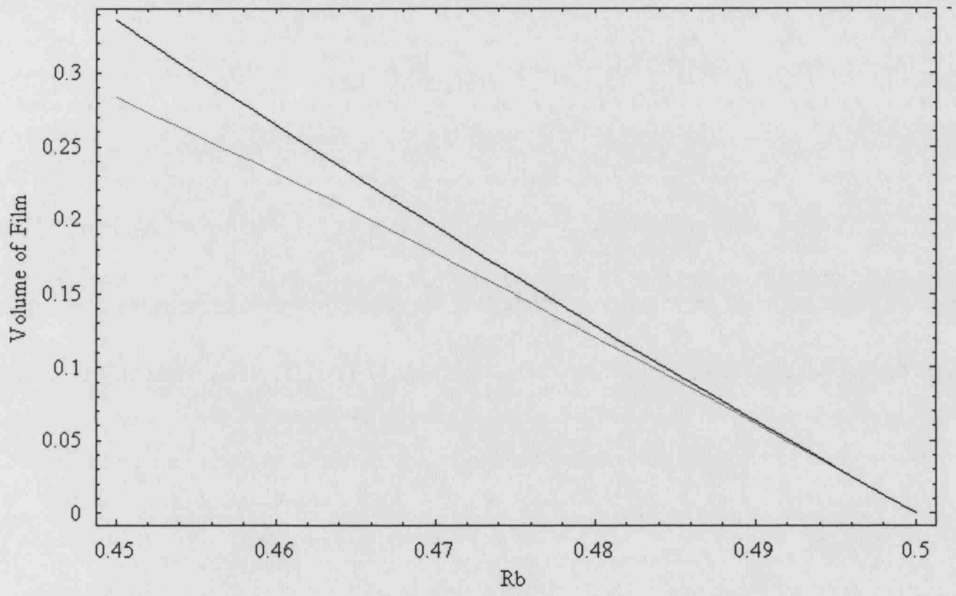

Fig. E.1: Variation of the film region volume from that based on thickness of liquid film surrounding the bubble (red) to a thickness based on a fully developed velocity profile (black).

F. MATLAB PROGRAM FOR ESTIMATING RTD OF A REACTOR AT LOW PECLET NUMBERS

```
% script file result.m
    lbd= parametricval(6); %diameter dimensionless bubble length
    lsd= parametricval(7); %diameter dimensionless slug length
    Dimensionalreactorlength=parametricval(11); %dimensional reactor length
    Reactorradiusd=parametricval(2); %diameter dimensionless reactor radius
    Rbd=parametricval(9);                %diameter dimensionless bubble radius
    Ped=parametricval(5);
    Diameter=parametricval(1); %dimensional diameter
    Volumed=pi*(Reactorradiusd^2*(lsd+2*Rbd)-(4/3)*Rbd^3) %diameter dimensionless
volume
    Aread =pi*(Reactorradiusd^2-Rbd^2);
    VoA=Volumed/Aread*(1/lbd);
    nca=5;
    ncb=50;
    n=nca+ncb+1;
    int=250;
    k=0.10/4;
    tmax=6;
    theta=1;
    Pe=Ped*lbd;
    lb=lbd/lbd;
    ls=lsd/lbd;
    Volumed=(Reactorradiusd^2*(lsd+2*Rbd)-(4/3)*Rbd^3); %diameter dimensionless vol-
ume
    Aread=Reactorradiusd^2-Rbd^2;
    VoA=Volumed/Aread*(1/lbd)
    Dimensionlessreactorlength=Dimensionalreactorlength/(lbd*Diameter);

    % dimensionless with respect to bubblelength.
    disp('press any key to continue');
```

```
pause
true=1;
false=0;
if abs(Ped)<=100
    R=1;
    F=Pe;
    check=1;
else
    R=1/Pe;
    F=1;
    check=0;
end
[barvalues,variationwithlength,filmprofile,tmax,timestepmat,u,timevalue,newvalue]=
    imass(nca,ncb,int,k,Dimensionlessreactorlength,tmax,lb,ls,theta,VoA,F,R,check);
[mean,sd,mean2,sd2]=param(barvalues,lb,(lb+ls),n);
figure(3);
plot(timevalue,newvalue);


function variable=parametricval(variablenumber)
values=zeros(16,1);
% Problem parameters
format long
tolerance=1.0e-7;
nmax=10000; % Number of iterations for correlation root.
values(1)=300e-6; % Value of real diameter
values(2)=0.5; % Value of R
values(3)=1e-5; % Value of Capillary number defined with the average slug velocity
values(4)=0.88396; % Values of the Reynolds number
values(5)=11; % Value of Peclet number
values(6)=1.10; % Bubble length (dimensionless)
values(7)=0.25; % Slug length (dimensionless)
values(13)=3.15e-01; % Froude Number
values(11)=1.0; % Value of Reactor Length Dimensional
% Calculating the capillary number for the film thickness
Ca=values(3);
if ((Ca<1.9) & (Ca>=1.0e-2));
    psinew=1;
    psiold=0;
```

```
    n=1;
    while ((abs(psiold-psinew)>tolerance) & (n < nmax));
        psiold=psinew;
        psinew=(1-2*0.36*(1-exp(-3.08*(Ca/psiold)^0.54)))^2;
        n=n+1;
        if n==nmax
            disp('maximum number of iterations has been reached');
        end
    end
    psival=psiold;
    delta=0.36*(1-exp(-3.08*(Ca/psival)^0.54))/2; % Irandoust and Andersson
elseif ((Ca<1e-2) & (Ca>=3e-4));
    psivalue=1-1.29*(3*Ca)^(2/3); % Bretherton(1961)
    delta=1/2*(1-sqrt(psivalue));
elseif ((Ca<3e-4) & (Ca>=5e-5));
    delta=0.25*(1-sqrt(1-2*Ca^0.5)); %Chen 1986
elseif ((Ca<5e-5) & (Ca>=0));
    psival=1-1.29*(3*Ca)^(2/3); % Bretherton(1961)
    delta=1/2*(1-sqrt(psival));
end
R=values(2);
values(8)= delta; % Film Thickness
values(9)= R-delta; % Value of Rb
Rb=values(9);
psi=((pi*(R^2))/(pi*(Rb^2)))-1;
values(10)=psi; % Value of dimensionless bubble velocity
DimensionlessReactorlength=values(11)/values(1)+(values(6)+values(7)); %treactor+tcell
values(12)=DimensionlessReactorlength;
%output the values
variable=values(variablenumber);

function [alpha,beta,gamma]=adjustkparam(totalpoints,k,h,theta,ae,aw,ap,VoA,L,n)
a=-aw*(k/h)*theta;
b=(1-(k/h)*theta*ap);
c=-ae*(k/h)*theta;
a2=-aw*(k/h)*(1-theta);
b2=(1-(k/h)*(1-theta)*ap);
c2=-ae*(k/h)*(1-theta);
% define the extra coefficient for the slug point
```

```
bslug=(VoA-k*theta*ap);
for j=0:n;
    for i=(2+j*L):(j+1)*L;
        % For tridiagonal solver
        alpha(i)=a;
        beta(i)=b;
        gamma(i)=c;
    end
    if j~=n;
        alpha((j+1)*L+1)=a*h;
        beta((j+1)*L+1)=bslug;
        gamma((j+1)*L+1)=c*h;
    end
end
% Derichlet boundary condition coefficients
alpha(1)=0;
beta(1)=1;
gamma(1)=0;
alpha(totalpoints)=0;
beta(totalpoints)=1;
gamma(totalpoints)=0;


function [barvalues,variationwithlength,filmprofile,tmax,timestepmat,u,timevalue,newvalue]=
imass(nca,ncb,int,k,lreactor,tmax,lb,ls,theta,VoA,F,R,Pcheck)
%
%Program for IMPLICIT and CRANK-NICOLSON methods for Ut=R*Uxx-F*U*Ux
note (-F) in equation
% the one dimensional convection diffusion equation.
%
%Input nca, number of cells upstream (integer)
% ncb, number of cells downstream (integer)
% int, number of x-subintervals (integer)
% k, time step size (real)
% TMAX, maximum computational time (real)
% lb, bubble length
% lreactor, reactor length
% theta, theta=1 for IMPLICIT, theta=0.5 for CRANK-NICOLSON (real)
% R, Diffusivity
```

```
% F, Convection
% VoA, Volume of a single slug / Cross sectional area of the film.
%
% Rb, is the radius of the bubble
% ls, slug length
%
% also needed are functions:
% p(t), left boundary condition
% q(t), right boundary condition
% init(x), initial condition
%
% OUTPUT
% barvalues: the concentrations in the slug series.
% variationwithlength : concentrations changing with length
% filmprofile : The concentration profiles in the film
% Initialise logic variable for old matlab versions.
true=1;
false=0;

% Initialise Tolerence values
conctol=1e-4; % Tolerance at which concentration is considered negligible.
ttol=1e-5;
countchange=5; % Number of steps before the time step is varried.
% Check time values to use, depending on the Peclet number values.
if Pcheck
    disp('Pe<=100')
    tcell=(lb+ls)/F
    treactor=lreactor/F
    tbubble=lb/F
else
    disp('Pe>100')
    tcell=(lb+ls)
    treactor=lreactor
    tbubble=lb
end;
format long;
disp('tcell , treactor , tbubble ');
disp([tcell,treactor,tbubble]);
newvalue=[];
```

```
timevalue=[];

% Check the entred value of the maximum time to see if less than maximum possible
time allowed
% for the axial mixing to be analysied.
if tmax<(treactor+(ncb+1)*tcell)
    disp('time entered is too short, continue or change to default')
    userinput1=input('press 1 to continue, and any other number to revert to default:
')
    if userinput1==1
        tmax=tmax;
        disp('tmax');
        disp(tmax);
        disp('press any key to continue');
        pause
    else
        tmax=(treactor+(ncb+1)*tcell);
        disp('tmax');
        disp(tmax);
        disp('press any key to continue');
        pause
    end
end
disp('nca,ncb');
disp([nca,ncb]);
kmax=tcell*2; % defines the maximum time step size
if k>kmax
    k=kmax;
    disp('stepsizevalue has been changed to tcell*2');
    disp(k);
end
x1=0;
x2=lb;
flag1=true; % flag for checking if the first non zero cell is seen.
flag2=false;
override=false;
%Define the Peclet number for a unit cell as Patankar
h=(x2-x1)/int;
Pe=(F/R)*h;
```

```
n=nca+ncb+1; % This gives the total number of cell considered
% initialising values
t=0;
pointnumber=int+1; %number of points to consider if it where a single channel being
modelled.
totalpoints=(n+1)*(pointnumber-1)+1; %number of points in the entire system.
% initialising processing abscessa
% gives the abscessas of all the points
grid=[];
for i=0:n;
    templinspace=linspace(x1+ls*i,x2+ls*i,pointnumber);
    if i~=n
        templinspace=templinspace(1:length(templinspace)-1);
    end
    grid=[grid,templinspace];
end
clear templinspace;
% initialising matricies of the system.
%solution space vector
u=zeros(1,totalpoints);
u2=zeros(1,totalpoints);
% This is set the coefficients for exponential method of Patankar
[ae,aw,ap]=discretexp(Pe,F);
% Solving the system
%-------------------------------
% Set initial condition
%-------------------------------
u=initial(grid,nca,totalpoints,pointnumber);
% Use algorithm to define tridiagonal linear system
L=int;
[alpha,beta,gamma]=adjustkparam(totalpoints,k,h,theta,ae,aw,ap,VoA,L,n);
% initialise boundaries
u(1)=p(t);
u(totalpoints)=q(t);
% initialise the adaption parameter u2.
u2=u;
%-------------------
% Time Steps
%-------------------
```

```
% Start of timesteps solutions
count=0;
totalsteps=0;
timestepmat=[];
t=0;
restore=false;
while (abs(tmax-t)>(k/2)); % stopping criteria
    totalsteps=totalsteps+1;
    if (t>(treactor-(nca+2)*tcell)) %Adjust the step size (necessary for geometric
resolution)
        if (k>(tcell-tbubble)/10)
            k=(tcell-tbubble)/10;
            [alpha,beta,gamma]=adjustkparam(totalpoints,k,h,theta,ae,aw,ap,VoA,L,n);
            disp('stepsizevalue has been changed to tslug / 10');
            disp(k);
            % disp('time is');
            % disp(t);
        end
    end
    %-----------------------------------
    % Check for the concentration at reactor exiting
    %-----------------------------------
    if (t>(treactor-(nca+1)*tcell))
        [slugnumber,slugconc]=slugexiting(t,treactor,tcell,tbubble,nca,n,pointnumber,u);
        timevalue=[timevalue;t];
        newvalue=[newvalue;slugconc];
    end
    %-------------------------
    % Check for the first exiting cell
    %-------------------------
    if ((t>=(treactor-nca*tcell)) & flag1)& ~override
        % Triggering the output check if flag1 is set as true
        % and the cells are exiting
        % Calculate the position of the first non zero cell.
        [cellnumber,cellconcen,difference]=cellexiting(t,treactor,tcell,nca,n,pointnumber,u);
        if (cellconcen >= conctol);
            disp('cellconcen >= conctol')
            disp('ratio of difference to stepsize is');
            disp(difference/k)
```

```
        if (difference/k)<=1;
            % This section alters the stepsize to make the exit
            % time correspond to a timestep.
            kstored=k;
            restore=true;
            k=abs(difference);
            [alpha,beta,gamma]=adjustkparam(totalpoints,k,h,theta,ae,aw,ap,VoA,L,n);
            disp('stepsizevalue has been changed to equal the difference');
            disp(k);
            flag1=false;
            disp('cell counting trigerred');
            disp('first cell with concentration to exit is');
            disp(cellnumber);
            barvalues=cellvalues(u,pointnumber,n);
            disp(barvalues);
        end
    end
end
%-------------------------
% Check for the last exiting cell
%-------------------------
if (~flag1 & ~override) %Triggering the output
    [cellbar,cellconcen,difference]=cellexiting(t,treactor,tcell,nca,n,pointnumber,u);
    if ((cellconcen < conctol));
        disp('cellconcen <conctol')
        disp('ratio of difference to stepsize is');
        disp(difference/k);
        if (abs(difference/k)<=1);
            % This section alters the stepsize to make the exit
            % time correspond to a timestep.
            k=abs(difference);
            [alpha,beta,gamma]=adjustkparam(totalpoints,k,h,theta,ae,aw,ap,VoA,L,n);
            disp('stepsizevalue has been changed to equal the difference');
            disp(k);
            flag2=true;
        end
        tmax=(treactor+(cellbar-nca)*tcell);
        disp('The new maximum time is');
        disp(tmax)
```

```
        end
    end
    sensflag=false; %sensflag trigger flag
    % if a fixed time step is to be used.
    if ~sensflag
        % disp(t);
        v=definev(totalpoints,L,k,h,theta,ae,ap,aw,u,VoA,n,t);
        % solving the system of equations to obtain the values at the new time step
u
        u=tridiag1(alpha(2:totalpoints),beta,gamma(1:totalpoints-1),v);
        t=t+k;
    end
    % if an adaptive time step is to be used.
    while sensflag
        % Setting same starting values.
        u2=u;
        % Single Step
        v=definev(totalpoints,L,k,h,theta,ae,ap,aw,u,VoA,n,t+k);
        u=tridiag1(alpha(2:totalpoints),beta,gamma(1:totalpoints-1),v);
        % Double Step
        kstor=k;
        k=k/2;
        [alpha,beta,gamma]=adjustkparam(totalpoints,k,h,theta,ae,aw,ap,VoA,L,n);
        for countsense=1:2
            v2=definev(totalpoints,L,k,h,theta,ae,ap,aw,u2,VoA,n,(t+countsense*k));
% note k/2
            % solving the system of equations to obtain the values at the new time
step u2
            u2= tridiag1(alpha(2:totalpoints),beta,gamma(1:totalpoints-1),v2);
        end
        k=kstor;
        [alpha,beta,gamma]=adjustkparam(totalpoints,k,h,theta,ae,aw,ap,VoA,L,n);
        % Comparison of two step sizes.
        if max(abs(u2-u))>conctol
            k=k/2;
            [alpha,beta,gamma]=adjustkparam(totalpoints,k,h,theta,ae,aw,ap,VoA,L,n);
            disp('k too large')
            disp(k)
        elseif ((max(abs(u2-u))<conctol)& (t<(treactor-(nca+1)*tcell)))
```

```
            t=t+k;
            count=count+1;
            if count>countchange
                k=min(k*2,kmax);
                [alpha,beta,gamma]=adjustkparam(totalpoints,k,h,theta,ae,aw,ap,VoA,L,n);
                count=0;
                % disp('k increased')
                % disp('time, k')
                % disp([t,k])
                % timestepmat=[timestepmat;[t,k]];
            end
            u=u2;
            sensflag=false;
        elseif ((max(abs(u2-u))<conctol)& (t>(treactor-(nca+1)*tcell)))
            t=t+k;
            count=count+1;
            if count>countchange
                k=min(k*2,tcell/2);
                [alpha,beta,gamma]=adjustkparam(totalpoints,k,h,theta,ae,aw,ap,VoA,L,n);
                count=0;
                % disp('system exiting and k increased')
                % disp('time, k')
                % disp([t,k])
                % timestepmat=[timestepmat;[t,k]];
            end
            u=u2;
            sensflag=false;
        end
    end
    if restore
        k=kstored;
        restore=false;
        [alpha,beta,gamma]=adjustkparam(totalpoints,k,h,theta,ae,aw,ap,VoA,L,n);
    end
end
disp('totalsteps')
disp(totalsteps)
% initialising output abscessa
functiongrid=[];
```

```
for i=0:n-1;
    functiongrid=[functiongrid,linspace(x1+(x2+ls)*i,x2+(x2+ls)*i,pointnumber)];
end
% Start output values
functionvalue=[];
for j=0:n-1;
    functionvalue=[functionvalue,u(1+j*(pointnumber-1):1+j*(pointnumber-1)+L)];
end
% figure output, variation of concentration with length
figure(1);
plot(functiongrid,functionvalue);
%output the results in lengthdependent form
variationwithlength=[functiongrid;functionvalue];
barvalues=cellvalues(u,pointnumber,n)
% figure output, cell concentration output
figure(2);
bar(barvalues);
%output the filmresults
filmprofile=[grid;u];
function [ae,aw,ap]=discretexp(Pe,F)

% This function returns the space descritisation coefficients ae,aw,ap
% using the exponential method for one dimension as specified by Patankar
if abs(Pe)<=100
    ae=+F/(exp(Pe)-1);
    aw=+F*exp(Pe)/(exp(Pe)-1);
    ap=-ae-aw;
elseif Pe>100
    ae=0;
    aw=+F;
    ap=-ae-aw;
elseif Pe<100
    ae=-F;
    aw=0 ;
    ap=-ae-aw;
end

function initial=initial(x,nca,totalpoints,pointnumber);
% This funciton gives the initial condition of the system.
```

```
MagnitudeofPulse=1;
base=zeros(1,totalpoints);
for i=(nca)*(pointnumber-1)+2:(nca+1)*(pointnumber-1)+1
    base(i)=MagnitudeofPulse;
end
base((nca+1)*(pointnumber-1)+1)=MagnitudeofPulse;
initial=base;
%initial=a*exp(c*x);
function p=p(t)
% function wich gives the LEFT BOUNDARY CONDITION
p=0;

function q=q(t)
% function wich gives the LEFT BOUNDARY CONDITION
q=0;

function [alpha,beta,gamma]=adjustkparam(totalpoints,k,h,theta,ae,aw,ap,VoA,L,n)
a=-aw*(k/h)*theta;
b=(1-(k/h)*theta*ap);
c=-ae*(k/h)*theta;
a2=-aw*(k/h)*(1-theta);
b2=(1-(k/h)*(1-theta)*ap);
c2=-ae*(k/h)*(1-theta);
% define the extra coefficient for the slug point
bslug=(VoA-k*theta*ap);
for j=0:n;
    for i=(2+j*L):(j+1)*L;
        % For tridiagonal solver
        alpha(i)=a;
        beta(i)=b;
        gamma(i)=c;
    end
    if j~=n;
        alpha((j+1)*L+1)=a*h;
        beta((j+1)*L+1)=bslug;
        gamma((j+1)*L+1)=c*h;
    end
end
% Derichlet boundary condition coefficients
```

```
alpha(1)=0;
beta(1)=1;
gamma(1)=0;
alpha(totalpoints)=0;
beta(totalpoints)=1;
gamma(totalpoints)=0;
function [cellout,cellconc,difference]=cellexiting(t,treactor,tcell,nca,n,pointnumber,u)
% Get cell concentrations
cellout=0;
barvalues=cellvalues(u,pointnumber,n);
% Calculating the concentration of the exiting cells.
for i=1:n
    if (t>(treactor+(i-1-nca)*tcell)&(t<=treactor+(i-nca)*tcell));
        cellout=i;
        cellconc=barvalues(cellout);
        break
    else
        cellout=0;
        cellconc=0;
        difference=0;
    end
end
difference=(treactor+(cellout-nca)*tcell)-t;

function barvalues=cellvalues(u,pointnumber,n)
% obtain values of concentrations in the cells
barvalues=[];
for i=0:(n-1)
    barvalues=[barvalues,u(pointnumber+i*(pointnumber-1))];
end

function [slugexiting,slugconc]=slugexiting(t,treactor,tcell,tbubble,nca,n,pointnumber,u)
% Get cell concentrations
barvalues=cellvalues(u,pointnumber,n);
% Calculating the concentration of the exiting cells.
for i=1:n
    if ((t>(treactor+(i-1-nca)*tcell)+tbubble)&(t<=treactor+(i-nca)*tcell));
        slugexiting=i;
        slugconc=barvalues(slugexiting);
```

```
            break
        else
            slugexiting=0;
            slugconc=0;
        end
    end
    function v=definev(totalpoints,L,k,h,theta,ae,ap,aw,u,VoA,n,t)
    v=zeros(1,totalpoints);
    for j=0:n;
        for i=(2+j*L):(j+1)*L;
            v(i)=-(k/h)*(1-theta)*ae*u(i+1) + (1-(k/h)*ap*(1-theta))*u(i)-aw*(1-theta)*(k/h)*u(i
1);
        end
        %
        if j~=n;
            v((j+1)*L+1)=-k*(1-theta)*ae*u((j+1)*L+2) + (VoA-k*ap*(1-theta))*u((j+1)*L+1)-
aw*(1-theta)*k*u((j+1)*L);
        end
    end
    %substituting the boundary conditions
    v(1)= p(t);
    v(totalpoints)= q(t);

    function [out,sd,out2,sd2]=param(barvalues,lb,lcell,n)
    x1=zeros(1,n);
    x2=zeros(1,n);
    total=0;
    sd2=0;
    for i=1:n
        x1(i)=lb+(i-1)*lcell;
        x2(i)=i*lcell;
    total=total+i*barvalues(i);
    end

    val1=0.5.*((x2.^2)-(x1.^2))*barvalues';
    val2=(x2-x1)*barvalues';
    out=val1/val2;
    discreatmean=total/sum(barvalues);
    out2=discreatmean*(lcell);
```

```
sd=((((x2-out).^3)-((x1-out).^3))/3)*barvalues';
for i=1:n
    sd2=sd2+((lcell/2+(i-1)*lcell-out2)^2)*barvalues(i);
end
% for i=1:n
% sd2=sd2+((i-discreatmean)^2)*barvalues(i);
% end


function [x, alpha, beta, ier] = tridiag(a,b,c,f,n,iflag)
% function [x, alpha, beta, ier] = tridiag(a,b,c,f,n,iflag)
%
% Solve a tridiagonal linear system M*x=f
%
% INPUT:
% The order of the linear system is given in n.
% The subdiagonal, diagonal, and superdiagonal of M are given
% by the arrays a,b,c, respectively. More precisely,
% M(i,i-1) = a(i), i=2,...,n
% M(i,i) = b(i), i=1,...,n
% M(i,i+1) = c(i), i=1,...,n-1
% iflag=0 means that the original matrix M is given as specified above.
% iflag=1 means that the LU factorization of M is already known and is
% stored in a,b,c. This will have been accomplished by a previous call
% to this routine. In that case, the vectors alpha and beta should
% have been substituted for a and b in the calling sequence.
%
% OUTPUT:
% Upon exit, the LU factorization of M is already known and is stored
% in alpha,beta,c. The solution x is given as well.
% ier=0 means the program was completed satisfactorily.
% ier=1 means that a zero pivot element was encountered and the
% solution process was abandoned.
a(1) = 0;
if iflag == 0
    % Compute LU factorization of matrix M.
    for j=2:n
        if b(j-1) == 0
```

```
            ier = 1;
        return
        end
        a(j) = a(j)/b(j-1);
        b(j) = b(j) - a(j)*c(j-1);
    end
    if b(n) == 0
        ier = 1;
        return
    end
end
% Compute solution x to M*x = f.
% Do forward substitution to solve lower triangular system.
for j=2:n
    f(j) = f(j) - a(j)*f(j-1);
end
% Do backward substitution to solve upper triangular system.
f(n) = f(n)/b(n);
for j=n-1:-1:1
    f(j) = (f(j) - c(j)*f(j+1))/b(j);
end
% Set output variables.
ier = 0;
x = f;
alpha = a; beta = b;
```

BIBLIOGRAPHY

[1] http://media.wiley.com/product_data/excerpt/00/04714881/0471488100-3.pdf viewed 1/5/2005

[2] C. de Bellefon, 2003, New Gas-Liquid-Solid microreactors for the investigation of Catalysis, Book of abstracts of IMRET7 7th international conference on microreactor technology, Sept 7-10, Lausanne, Switzerland.

[3] C. de Bellefon, N. Pestre, T. Lamouille, P. Grenouillet, V. Hessel, 2003, Microreactors for dynamic high throughput screening of Fluid/Liquid molecular catalysts, Angewandte Chemie International Edition, 39, 3442

[4] C. de Bellefon, R. Abdallah, T. Lamouille, N. Pestre, S. Caravieilhes, P. Grenouillet, 2002, High throughput screening of molecular catalysts using automated liquid handlin, injection and microdevices, Chimia, 56 [11], 621

[5] V. Hessel, W. Ehrfeld, K. Golbig, V. Haverkamp, H. Lowe, T. Richter, 1998, Gas/Liquid dispersion process in Micromixers: The hexagonal flow, Proceedings of 2nd International Conference on Microreaction Technology: IMRET 2, February, New Orleans,LA.

[6] C. de Bellefon, N. Pestre, T. Lamouille, P. Grenouillet, V. Hessel, 2003, High throughput kinetic investigations of Asymmetric Hydrogenations with Microdevices, Advanced Synthesis and Catalysis, 345[1-2], 190

[7] T. Fukuyama, M. Shinmen, S. Nishitani, M. Sato, I. Ryu, 2002, A copper-free Sonogashira coupling reaction in Ionic liquid and its application to a microflow system for efficient catalysis recycling, Organic Letters, 4, 10, 1691

[8] H.A. Stone, A.D. Stroock, A. Ajdari, 2004, Engineering flows in small devices: Microfluidics towards a Lab-on-a-Chip, Annual Review of Fluid Mechanics, 36, 381

[9] D.Y.C. Chan, R.G. Horn, 1985, The drainage of thin liquid films between solid surfaces, Journal of Chemical Physics, 83, 10, 5311

[10] M. Gee, P. McGuiggan, J. Israelachvili, 1990, Liquid to solid like transitions of molecularly thin films under shear, Journal of chemical physics, 93, 3, 1895

[11] P.W. Atkins, J. de Paula, 2002, Atkins' Physical chemistry, 7th ed. Oxford ,Oxford University Press.

[12] P. Tabeling, 2001, Some basic problems of microfluidics, 14^{th} Australasian Fluid Mechanics Conference, Adelaide University, Adelaide, Australia.

[13] J. Koplik, J. R. Banavar, J.L. Willemsen, 1988, Molecular dynamics of poiseuille flow and moving contact lines, Physical Review Letters, 60,13, 1282

[14] P.A. Thompson, M.O. Robins, 1990, Shear flow near solids: Epitaxial order and flow boundary conditions, Physical Review A., 41, 12, 6830

[15] J. Barrat, L. Bocquet, 1999, Large Slip Effect at a Nonwetting Fluid-Solid Interface, Physical Review Letters, 82,23, 4671

[16] C. Cottin-Bizonne, J. Barrat, L. Bocquet, E. Charlaix, 2003, Low friction liquid flows at nanopatterned interfaces, Nature materials, 2, 237

[17] J.M. Georges, S. Millot, L. Loubet, A. Tonck, 1983, Drainage of thin liquid films between relatively smooth surfaces, Journal of Chemical Physics, 98,9, 7345

[18] R. Pit, H. Hervet, L. Lėger, 2000, Direct experimental evidence of slip in Hexadecane: Solid interfaces, Physical Review Letters, 85, 5, 980-083.

[19] J. Baudry, E. Charlaix, Q. Tonck, D. Mazuyer, 2001, Experimental evidence for a large slip effect at a nonwetting fluid-solid interface, Langmuir, 17, 5232

[20] Y.X. Zhu, S. Granicks, 2002, Limits of the hydrodynamic no-slip boundary condition, Physical Review Letters, 99, 106102.

[21] P.A. Thompson, S.M. Troian, 1997, A general boundary condition for liquid flow at solid surfaces, Nature, 389, 360

[22] J.W. Tyrrell, P. Attard, 2001, Images of Nanobubbles on hydrophobic surfaces and their interactions, Physical review Letters, 87,17, 176104.

[23] L. Pismen, 2002, Mesoscopic hydrodynamics of contact line motion, Colloids and surfaces A: Physiochemical and Engineering Aspects, 206, 11

[24] H.A. Stone, 1990, A simple derivation of the time-dependent convection-diffusion equation for surfactant transport along a deforming interface, Physics of Fluids A, 2, 111

[25] S.N. Ghadiali and D.P. Gaver III, The influence of non-equilibrium surfactant dynamics on the flow of a semi-infinite bubble in a rigid cylindrical capillary tube, Journal of Fluid Mechanics, 478, 165.

[26] V.B. Fainerman, R. Miller, H.Mőhwald, 2002, General relationships of the adsorption behavior of Surfactants at the water/air interface, Journal of Physical Chemistry B., 106, 809

[27] M. Severino, M.D. Giavedoni, F.A. Saita, 2003, A gas phase displacing a liquid with soluble surfactants out of a small conduit: The plane case, Physics of fluids, 15[10], 2961

[28] P.M.Chung, , M. Kawaji, , 2004, The effect of channel diameter on adiabatic two-phase flow characteristics in microchannels, International Journal of Multiphase Flow, 30, 735

[29] W.L. Chen, M.C. Twu, C. Pan, 2002, Gas-liquid two-phase flow in microchannels, International Journal of Multiphase Flow, 28, 1235

[30] C. Yang, C. Shieh, 2001, Flow pattern of air-water and twophase R-134a in small circular tubes, International Journal of Multiphase Flow, 27, 1163

[31] K.A.Triplett, S.M. Ghiaasiaan, S.I. Abdel-Khalik, D. L. Sadowski, 1999a, Gas-liquid two-phase flow in microchannels Part I: two-phase flow patterns. International Journal of Multiphase Flow 25[3], 377

[32] M. Suo, P.Griffith, 1964, Two-phase flow in capillary tubes, Journal of Basic Engineering, 86,576

[33] Simmons, M.J., D.C.Y. Wong, P.J. Travers, J.S. Rothwell, 2003, Bubble behaviour in three phase capillary microreactors, International Journal of Chemical Reactor Engineering, 1, Article A30.

[34] G. Wolk , M. Dreyer , H.J. Rath, 2000, Flow patterns in small diameter vertical non-circular channels, International Journal of Multiphase Flow, 26, 1037

[35] W.L. Chen, M.C. Twu, C. Pan,, 2002, Gas-liquid two phase flow in microchannels, International Journal of Multiphase Flow, 28, 1235-1247.

[36] I. Chen, K. Yang, Y. Chang, C. Wang, Two-phase pressure drop of air-water and R-410A in small horizontal tubes, International Journal of Multiphase Flow 27, 1293

[37] Zhao, T.S., Bi, Q.C., 2001, Pressure drop characteristics of gas-liquid two-phase flow in vertical miniature triangular channels, International Journal of Heat and Mass Transfer, 44, 2523

[38] K.A. Triplett, S.M. Ghiaasiaan, S.I. Abdel-Khalik, A. LeMouel, B.N.McCord, 1999b, Gas-liquid two-phase flow in microchannels Part II: void fraction and pressure drop. International Journal of Multiphase Flow 25[3], 395

[39] N. Brauner, D. Moalem-Maron, 1992, Identification of the range of 'small diameters' conduits, regarding two-phase flow pattern transitions. Interantional communication in heat and mass transfer 19, 29

[40] F.P. Bretherton, 1961, The motion of long bubbles in tubes. Journal of Fluid Mechanics 10, 166

[41] L. Zhao, K.S.Rezkallah, 1993, Gas-liquid flow patterns at microgravity conditions, International Journal of Multiphase Flow, 19, 751

[42] K.S. Rezkallah, L. Zhao, 1995, A flow pattern map for two-phase liquid-gas flows under reduced gravity conditions. Adv. Space Res., 16, 133

[43] K.S. Rezkallah, 1996. Weber number based flow-pattern maps for liquid-gas flows at microgravity. Int. J. Multiphase Flow 22, 1265-1270.

[44] D.C. Lowe, K.S. Rezkallah, 1999, Flow regime identification in microgravity two-phase flow using void fraction signals, International Journal of Multiphase Flow, 25, 433

[45] J.F. Zhao, J.C. Xie, H. Lin, W.R. Hu, A.V. Ivanov, A.Yu. Belyaev, , 2001, Experimental studies on two-phase flow patterns aboard the Mir space station, International Journal of Multiphase Flow, 27, 1931

[46] M.K. Akbar, D.A. Plummer, S.M.Ghiaasiaan, , 2003, On gas-liquid two-phase regimes in microchannels, International Journal of Multiphase Flow, 29, 855

[47] A. Kawahara, P.M.-Y.Chung, M. Kawaji, 2002, International Journal of Multiphase Flow, 28, 1411

[48] A.M. Barajas, R.L. Panton, 1993, The effect of contact angle on two phase flow in capillary tubes. International Journal of Multiphase flow, 19, 337

[49] A. Serizawa, Z. Feng, Z. Kawara, 2002, Two-phase flow in microchannels, Experimental Thermal and Fluid Science, 26, 703

[50] R. Dreyfus, P. Tabeling, H. Willaime, 2003, Ordered and disordered patterns in two-phase flows in microchannels, Physical review letters, 90, 14

[51] Cubaud, T., Ulmanella, U., Ho, C.H., 2004, Two-Phase flow in Microchannels with Surface Modifications, 5th International Conference on Multiphase Flow, ICMF'04, Yokohama Japan.

[52] J. Prothero, A.C. Burton, 1961, The physics of blood flow in capillaries, Journal of Biophysics, 2, 525

[53] W.L. Olbricht, 1996, Pore-scale prototypes of multiphase flow in porous media, Annual Review of Fluid Mechanics, 28, 187

[54] T.A. Nijhuis, M.T. Kreutzer, A.C. J. Romijn, F. Kapteijn, J.A. Moulijn, 2001, Monolithic catalysts as efficient three-phase reactors, Chemical Engineering Science, 56, 823

[55] K. Jähnisch, M. Baerns, V. Hessel, W. Ehrfeld, V. Haverkamp, H. löwe, Ch. Wille, A. Guber, 2000, Direct fluorination of toluene using elemental fluorine in gas/liquid microreactors, Journal of Fluorine Chemistry, 105, 117.

[56] A. de Ryck, 2002, The effect of weak inertia on the emptying of a tybe, Physics of Fluids, 14,7, 2102

[57] E.T. White, R.H. Beardmore, 1962, The velocity of rise of single cylindrical air bubbles through liquids contained in vertical tubes. Chemical Engineering Science 17, 351

[58] G. B. Wallis, 1969, One-dimensional two-phase flow. New York: McGraw Hill.

[59] J. Fabre, A. Liné, 1992, Modeling of two-phase slug flow. Annual Review of Fluid Mechanics 24, 21

[60] T. B. Benjamin, 1968, Gravity currents and related phenomena, Journal of Fluid Mechanics,31[2], 209

[61] E.E. Zukoski, 1965, Influence of viscosity, surface tension, and inclination angle on motion of long bubbles in closed tubes, Journal of Fluid Mechanics 25 (4), 821

[62] Q.C. Bi, T.S. Zhao, 2001, Taylor bubbles in miniaturized circular and noncircular channels, International Journal of Multiphase Flow 27[3], 561

[63] F. Fairbrother, A.E. Stubbs, 1935, Studies in electro-endosmosis -VII, the "bubble tube" method of measurement, Journal of Chemical Society 1, 527

[64] B.G. Cox, 1964, An experimental investigation of the streamlines in viscous fluid expelled from a tube. Journal of Fluid Mechanics 20, 193

[65] J.D. Chen, 1986, Measuring the film thickness Surrounding a bubble inside a capillary, Journal of Colloid and Interface Science 109[2], 341

[66] R.N. Marchessault, S.G. Mason, 1960, Flow of entrapped bubbles through a capillary, Industrial Engineering Chemistry, 52(1),79.

[67] S. Irandoust, B. Andersson, 1989, Liquid-film in taylor flow through a capillary. Industrial & Engineering Chemistry Research 28[11], 1684

[68] P. Aussillous, D. Quéré, 2000, Quick deposition of a fluid on the wall of a tube, Physics of Fluids, 12,10, 2367

[69] K. Bendiksen, 1984, An experimental investigation of the Motion of long bubbles in inclined tubes. International Journal of Multiphase Flow 10[4], 467

[70] D.A. Reinelt, P.G. Saffman, 1985, The penetration of a finger into a viscous fluid in a channel and tube. Journal of Science Statistics.Computation 6, 542

[71] E. Shen, K. Udell, 1985, A finite-Element study of low Reynolds-number 2-phase flow in cylindrical-tubes. Journal of Applied Mechanics-Transactions of the ASME 52[2], 253

[72] W.Q. Lu, H.C. Chang, 1988, An extension of the biharmonic boundary integral method to free surface flow in channels, Journal of computational physics,77, 430

[73] M.J. Martinex, K. Udell, 1989, Boundary integral analysis of the creeping flow of long bubbles in capillaries, Transaction of the ASME, Jouranl of Applied Mechanics, 56, 211.

[74] H. Wesborg, O. Hassager, 1989, Creeping motion of long bubbles and drops in capillary tubes, Journal of Colloid and Interface Science,133 [1], 135

[75] J. Ratulowski, H.C. Change, 1989, Transport of Gas Bubblies in Capillaries, Physics of Fluids A1, 10, 1642

[76] R.K. Edvinsson, S. Irandoust, 1996, Finite-element analysis of Taylor flow. AIChE Journal 42[7], 1815

[77] M.D. Giavedoni, F.A. Saita, 1997, The axisymmetrical and plane cases of gas phase steadily displacing a Newtonian liquid- A simultaneous solution of the governing equations, Physics of Fluids, 9 [8], 2420

[78] M.D. Giavedoni, F.A. Saita, 1998, The rear meniscus of a long bubble steadily displacing a Newtonian liquid in a capillary tube, 11 [4], 786

[79] W. L. Olbricht, D. M. Kung, 1992, Deformation and breakup of liquid drops in low Reynolds number flow through a capillary, Physics of Fluids A, 4, 1347.

[80] M. Heil, 2001, Finite Reynolds number effects in the Bretherton problem, Physics of Fluids, 13[9], 2517

[81] G. I. Taylor, 1960, Deposition of viscous fluid on the wall of a tube. Journal of Fluid Mechanics 10, 161

[82] B.G. Cox, 1962, On driving a viscous fluid out of a tube, Journal of Fluid Mechanics, 14, 81

[83] T.C. Thulasidas, M.A. Abraham, R.L. Cerro, 1997, Flow patterns in liquid slugs during bubble-train flow inside capillaries. Chemical Engineering Science 52[17], 2947

[84] L. Schwartz, H. Princen, A. Kiss, 1986, On the motion of bubbles in capillary tubes. Journal of Fluid Mechanics 172, 259

[85] G.M. Ginley, C.J. Radke, 1988, Influence of a soluble surfactant on the flow of long bubbles through a cylindrical capillary, ACS Symp. Ser. 396,480.

[86] J. Ratulowski, H.C. Chang, 1990 Maragoni effects of trace impurities on the motion of long gas bubbles in capillaries. Journal of Fluid Mechanics 210, 303

[87] C.W. Park, 1992, Influence of soluble surfactants on the motion of a finite bubble in capillary tube, Physics of Fluids A, 5, 1533.

[88] K.J. Stebe, D. Barthès-Biesel, 1995, Marangoni effects of adsorption-desorption controlled surfactants on the leading end of an infinitely long bubble in a capillary, Journal of Fluid Mechanics, 286,25.

[89] X. Geng, H. Yuan, H.N. Oğuz ,A. Prosperetti, 1999, The oscillation of gas bubbles in tubes: Experimental results, Journal of the accostic society of America, 106, 2, 674

[90] M.J. Jensen, 2002, Bubbles in microchannels, MSc Thesis, Mikroelektronic Centret (MIC), Technical University of Denmark.

[91] A. Serizawa, Z. Feng, Z. Kawara, Two phase flow in microchannels, Experimental Thermal and fluid sciences, 26, 703

[92] H.J. Schulze, K.W. Stőckelhuber, A. Wenger, The influence of acting forces on the rupture mechanism of wetting films-nucleation or capillary waves, Colloids and surfaces, 192, 61

[93] T.C. Thulasidas, M.A. Abraham, R.L. Cerro, 1997, Flow patterns in liquid slugs during bubble-train flow inside capillaries, Chemical Engineering Science 52[17], 2947

[94] S. Irandoust, B. Andersson, 1988, Mass-Transfer And Liquid-Phase Reactions In A Segmented 2-Phase Flow Monolithic Catalyst Reactor, Chemical Engineering Science 43[8], 1983

[95] T.C. Thulasidas, M.A. Abraham , R.L. Cerro, 1999, Dispersion during bubble-train flow in capillaries. Chemical Engineering Science 54, 61

[96] W. Salman, A. Gavriilidis, P. Angeli, 2004, A model for predicting axial mixing during gas-liquid Taylor flow in microchannels at low Bodenstein numbers, Chemical Engineering Journal, 101, 391

[97] G. Berčic, A. Pintar, 1997, The role of gas bubbles and liquid slug lengths on mass transport in the Taylor flow through capillaries, Chemical Engineering Science 52, 3709

[98] M. Kreutzer, 2003. Hydrodynamics of Taylor flow in capillaries and monolith reactors. Delft University Press.

[99] T.C. Thulasidas, M.A. Abraham, R.L. Cerro, 1995. Bubble-train flow in capillaries of circular and square cross section. Chemical Engineering Science 50, 183

[100] R. Kumar, N.R. Kuloor , 1990. The formation of bubbles and drops, Vol. 8, Academic Press, New York.

[101] R. Clift, J.R. Grace, M.E. Weber, 1978. Bubbles, drops and particles, Academic Press, New York.

[102] O. Pamperin, H. Rath , 1995, Influence of buoyancy on bubble formation at submerged orifices, Chemical Engineering Science, 50, 3009

[103] I.H. Kim, Y. Kamotani, S. Ostrach, 1994, Modeling bubble and drop formation in flowing liquids in Microgravity, AIChE 40, 19

[104] H.K. Nahra, Y. Kamotani, 2003, Prediction of bubble diameter at detachment from a wall orifice in liquid cross-flow under reduced and normal gravity conditions, Chemical Engineering Science, 58, 55

[105] A. Bhunia, S.C. Pais, Y. Kamotani , I.H. Kim, 1998, Bubble formation in a coflowconfiguration in normal and reduced gravity. AIChE, 44, 1499

[106] H.N. Oğuz, J. Zeng, 1998, Production of gas bubbles in reduced-g environments, Proceeding of the fourth microgravity fluids physics and transport phenomena conference, August 12-14 Cleveland Ohio.

[107] R. Chebbi, 2003, Deformation of advancing gas-liquid interfaces in capillary tubes, Journal of Colloid and Interface Science, 265, 166

[108] S. Irandoust, B. Andersson, 1988, Mass-transfer and liquid-phase reactions in a segmented 2-phase flow monolithic catalyst reactor. Chemical Engineering Science 43[8], 1983

[109] S. Irandoust, B. Andersson, 1989, Simulation of flow and mass-transfer in Taylor flow through a capillary. Computers & Chemical Engineering 13[4-5], 519

[110] G. Berčic, 2001, Influence of operating conditions on the observed reaction rate in the single channel monolith reactor. Catalysis Today 69, 147

[111] C.A. Lucy, B.P. Hausermann, 1995, Co-current chromatography: A new mode of liquid-liquid chromatography, Analytica Chimica Acta, 307, 173

[112] T.C. Thulasidas, M.A. Abraham, R.L. Cerro, 1999, Dispersion during bubble-train flow in capillaries. Chemical Engineering Science 54, 61

[113] L.J. Skeggs, 1957, An automatic method for calorimetric analysis, American Journal for Clinical Pathology, 28, 311

[114] C. Amador, W. Salman, S. Sanguanpiyapan, A. Gavriilidis, P. Angeli, 2004, Effect of gas-inlet conditions on the mechanism of Taylor flow formation, 5th International Conference on Multiphase Flow, ICMF'04, Yokohama, Japan, paper No. 515.

[115] A. Serizawa, Z. Feng, Z. Kawara, 2002, Two-phase flow in microchannels, Experimental Thermal and Fluid Science, 26, 703

[116] R.E. Thiers, A.H. Reed, K. Delander, 1971, Origin of the lag phase of continuous-Flow Analysis Curves, Clinical Chemistry, Vol 17[1], 42

[117] H. Pedersen, C. Hovarth, 1981, Axial dispersion in a segmented gas-liquid flow. Industrial & Engineering Chemistry Fundamentals 20, 181

[118] C. Hovarth, B. Solomon, J. Engasser, Measure of radial transport in slug flow using enzyme tubes, Industrial Engineering Chemistry Fundamentals, 12[4], 431

[119] R.Gruber, T. Melin, T., 2003, Radial mass transfer enhancement in bubble train flow, International Journal of Heat and Mass Transfer, 46, 2799

[120] T. Taha, Z.F. Cui, 2004, Hydrodynamics of slug flow inside capillaries, Chemical Engineering Science, 59, 1181

[121] Femlab ver 2.3 software, COMSOL Inc., 1 New England Executive Park, Suite 350, Burlington, MA 01803

[122] R.L. Burden, D.J., Faires, A.C. Reynolds, 1978, Numerical analysis [Natural Cubic Spline Algorithm], Prindle, Weber, and Schmidt, Boston, 120

[123] http://library.wolfram.com/infocenter/MathSource/699/ viewed 9/2003

[124] E.B. Nauman, B.A. Buffman, 1983, Mixing in continuous flow systems, John Wiley & Sons.

[125] P.P. Valkó, J. Abate, 2003, Comparison of sequence accelerators for the Gaver method of numerical Laplace Transform inversion, Computers and Mathematics with Applications, 48, 629

[126] http://library.wolfram.com/database/MathSource/4738/ viewed 9/2003.

[127] O. Levenspiel, 1999, Chemical Reaction Engineering, 3rd ed., John Wiley, New York.

[128] H. Song, D. Joshua, R.F. Ismagilov, 2003, A microfluidic system for controlling reaction netweork in time, Angewandte Chemie International edition., 42, 7, 767

[129] M.A. Burns, C.H. Mastrangelo, T.S. Sammarco, F.P. Man, JR.Webster, 1996, Microfabricated structures for integrated DNA analysis, Proceedings of the National Academy of Science, USA , 93, 5556

[130] C. de Bellefon, N. Pestre, T. Lamouille, P. Grenouillet, V. Hessel, 2003, High throughput kinetic investigations of asymmetric hydrogenations with microdevices, Advanced Synthesis and Catalysis, 345, 190

[131] H. Pennemann, V. Hessel, J. Kost, H. Löwe, C. de Bellefon, 2004, Investigations on pulse broadening for catalyst screening in Gas/Liquid Systems, AIChE Journal, 50, 8, 1814

[132] O. Levenspiel, 1990, Chemical Reaction Engineering, John Wiley, New York.

[133] S.V. Patankar, 1980, Numerical heat transfer and fluid flow, McGraw-Hill Book Company.

[134] I. Boztosun, A. Charafi , M. Zerroukat and K. Djidjeli, 2002, Thin-Plate spline radial basis function scheme for advection-diffusion Problems, Electronic Journal of Boundary Elements, Vol. BETEQ 2001[2], 267.

[135] W.K. Lewis, W.G. Whitman, 1924,Principles of gas adsorption, Industrial and Engineering Chemistry, 16, 1215

[136] W.G. Whitman, 1925, A Preliminary Experimental Confirmation of the Two-Film-Theory of Gas Adsorption Chemical Metallurgical Engineering, 29, 146

[137] R. Higbie, 1983, The rate of absorption of a pure gas into a still liquid during short periods of exposure. Transactions of the AIChE. 31, 365

[138] P.V. Danckwertz, 1951, Significance of liquid-film coefficients in gas absorption, Industrial and Engineering Chemistry, 43,6, 1460

[139] G. Astarita, 1967, Mass Transfer with Chemical Reaction, Elsevier publishing Company, London.

[140] R.Clift, J.R. Grace, M.E. Weber, 1978, Bubbles, drops and particles, Academic Press, New York.

[141] J. M. van Baten, R. Krishna, 2004, CFD simulations of mass transfer from Taylor bubbles rising in circular capillaries, Chemical Engineering Science, 59, 2535

[142] T.K. Sherwood, R.L. Pigford, C.R. Wilke, 1975, Mass Transfer, McGraw-Hill, Inc.

[143] S. Irandoust, S. Ertle, B. Andersson,1992b, Gas-Liquid mass transfer in Taylor flow through a capillary. Canadian Journal of Chemical Engineering 70[1], 115

[144] P. Assilous, D. Quère, 2000, Quick deposition of a fluid on the wall of a tube, Physics of Fluids 12[10], 2367

[145] FIDAP ver. 6.2 software, Fluent Europe Ltd, Sheffield Business Park, Europa Link, Sheffield S9 1XU